TESIS DE LA UNIVERSIDAD DE ZARAGOZA

2022 48

Eduardo Moya Lasheras

Soft-Landing Control of Short-Stroke Reluctance Actuators

Director/es
Sagües Blazquiz, Carlos

ISSN 2254-7606

Prensas de la Universidad
Universidad Zaragoza

ISSN 2254-7606

Universidad Zaragoza
1542

Tesis Doctoral

SOFT-LANDING CONTROL OF SHORT-STROKE RELUCTANCE ACTUATORS

Autor

Eduardo Moya Lasheras

Director/es

Sagües Blazquiz, Carlos

UNIVERSIDAD DE ZARAGOZA
Escuela de Doctorado

2021

PhD Thesis

Soft-Landing Control of Short-Stroke Reluctance Actuators

Eduardo Moya Lasheras

Supervisor: Carlos Sagüés Blázquiz

Universidad de Zaragoza

March 4, 2021

Resumen

Los actuadores de reluctancia se utilizan ampliamente debido a sus altas densidades de fuerza y baja disipación de calor. En particular, los actuadores de reluctancia simples de una sola bobina de carrera corta, como los relés electromecánicos y las electroválvulas, son la mejor opción para operaciones de conmutación de encendido y apagado en muchas aplicaciones debido a su bajo coste, tamaño y masa. Sin embargo, un inconveniente importante es el fuerte impacto al final de cada conmutación, que provoca rebotes, desgaste mecánico y ruido acústico. Son fenómenos muy indeseables que restan valor a las ventajas evidentes de estos actuadores y limitan su rango de aplicaciones potenciales.

Esta tesis se centra en el desarrollo y estudio de soluciones de control de aterrizaje suave para actuadores de reluctancia de carrera corta, con el objetivo de minimizar sus velocidades de impacto. Es importante indicar que la eficiencia de dichos dispositivos se produce a costa de serios retos teóricos y prácticos en cuanto a su control, por ejemplo, dinámicas rápidas, híbridas y altamente no lineales, fenómenos electromagnéticos complejos, variabilidad entre unidades y falta de medidas de posición durante el movimiento.

El punto de partida es la modelización del sistema, teniendo en cuenta sus subsistemas interconectados eléctricos, magnéticos y mecánicos. El objetivo principal de los modelos es servir para el desarrollo de métodos de control y estimación. Por lo tanto, se trata de modelos de parámetros concentrados expresados como representaciones del espacio de estados. Se especifican diferentes fenómenos electromagnéticos, con especial atención a la histéresis magnética. Se proponen dos tipos de modelos de diferente complejidad según se incorpore o se desprecie el fenómeno de la histéresis magnética.

El primer enfoque para el control del aterrizaje suave es el diseño óptimo de las trayectorias de posición y sus correspondientes señales de entrada. La propuesta tiene en cuenta la incertidumbre en la posición del contacto y, por tanto, las soluciones obtenidas son más robustas. Mientras que las señales de entrada generadas son eficaces para las estrategias de control en lazo abierto, las trayectorias de posición generadas pueden utilizarse controles de prealimentación o de retroalimentación.

Para mejorar la robustez de los controladores de lazo abierto, también proponemos una estrategia *run-to-run* que adapta iterativamente las señales de entrada. En concreto,

está diseñada para trabajar conjuntamente con un controlador de prealimentación basado en las mencionadas trayectorias de posición construidas de forma óptima. Para el algoritmo de aprendizaje ciclo a ciclo, se elige una técnica de optimización, se ajusta y se compara con dos alternativas.

Otro enfoque explorado es el control de retroalimentación para el seguimiento de trayectorias predefinidas de posición. La solución propuesta es un controlador estrictamente conmutativo en modo deslizante. Está enfocado en la simplicidad para facilitar su implementación, al tiempo que se tiene en cuenta la dinámica híbrida. Los análisis teóricos y simulados demuestran que el aterrizaje suave es posible con tasas de muestreo razonables.

Los controladores de retroalimentación y otros controladores de seguimiento requieren mediciones o estimaciones precisas de la posición. Como la medición de la posición raramente es práctica, parte de la investigación se dedica al diseño de estimadores de estado. La principal propuesta es un suavizador Rauch-Tung-Striebel ampliado para sistemas no lineales, que incluye varias ideas nuevas relacionadas con el modelo discreto, las entradas y las salidas. Los análisis simulados demuestran que el efecto combinado de las nuevas adiciones da lugar a mucho mejores estimaciones de la posición.

Abstract

Reluctance actuators are widely used due to their high force densities and low heat dissipation. In particular, simple short-stroke single-coil reluctance actuators, such as electromechanical relays and solenoid valves, are the best choice for on-off switching operations in many applications because of their low cost, size and mass. However, a major drawback is the strong impact at the end of each commutation, which provokes bouncing, mechanical wear and acoustic noise. They are very undesirable phenomena that detract from the evident advantages of these actuators and limit their range of potential applications.

This thesis focuses on the development and study of soft-landing control solutions for short-stroke reluctance actuators, aiming at minimizing their impact velocities. It is important to indicate that the efficiency of the aforementioned devices comes at the cost of serious theoretical and practical challenges regarding their control, e.g., fast, hybrid and highly nonlinear dynamics, complex electromagnetic phenomena, unit-to-unit variability and lack of position measurements during motion.

The starting point is the system modeling, accounting for their interconnected electrical, magnetic and mechanical subsystems. The main purpose of the models is to be used for the development of control and estimation methods. Therefore, they are lumped-parameter models expressed as state-space representations. Different electromagnetic phenomena are specified, with special attention to the magnetic hysteresis. Two model types of different complexities are proposed depending on whether the magnetic hysteresis phenomenon is incorporated or neglected.

The first approach for soft-landing control is the optimal design of position trajectories and their corresponding input signals. The proposal considers uncertainty in the contact position, and hence, the obtained solutions are more robust. While the generated input signals are effective for open-loop control strategies, the generated position trajectories can be used in feedforward or feedback control.

In order to improve the robustness of open-loop controllers, we also propose a run-to-run strategy that iteratively adapts the input signals. Specifically, it is designed to work in conjunction with a feedforward controller based on the aforementioned opti-

mally constructed position trajectories. For the cycle-to-cycle learning algorithm, an optimization technique is chosen, adjusted and compared to two alternatives.

Another explored approach is feedback control for tracking predefined position trajectories. The proposed solution is a purely switching sliding-mode controller. The focus is on simplicity to facilitate its implementation, while also taking into account the hybrid dynamics. Theoretical and simulated analyses show that soft landing is achievable with reasonable sampling rates.

Feedback and other tracking controllers require accurate measurements or position estimations. As measuring the position is rarely practical, part of the research is devoted to the design of state estimators. The main proposal is an extended Rauch–Tung–Striebel smoother, which includes several new ideas regarding the discrete model, the inputs and the outputs. Simulated analyses demonstrate that the combined effect of the novel additions results in much better position estimations.

Contents

List of Figures

List of Tables

Nomenclature

Acronyms

BO	Bayesian optimization
BVP	Boundary value problem
EOS	Energy-optimal solution
ERTSS	Extended Rauch–Tung-Striebel smoother
EKF	Extended Kalman filter
FEM	Finite element model
FK	Fröhlich–Kennelly
GPM	Generalized Preisach model
ILC	Iterative learning control
JA	Jiles–Atherton
KF	Kalman filter
MEC	Magnetic equivalent circuit
NM	Nelder–Mead
NRMSE	Normalized root-mean-square error
PDF	Probability density function
POS	Probability-based optimal solution
PS	Pattern search
R2R	Run-to-run
R2R-BO	Run-to-run based on Bayesian optimization
R2R-NM	Run-to-run based on Nelder–Mead search
R2R-PS	Run-to-run based on pattern search
RAM-FK	Reluctance actuator model based on Fröhlich–Kennelly
RAM-GP	Reluctance actuator model based on the generalized Preisach model
RAM-JA	Reluctance actuator model based on Jiles–Atherton
SMC	Sliding-mode control
wNRMSE	Weighted normalized root-mean-square error

Latin symbols

A	Cross-sectional area
$\boldsymbol{A}$	Quadratic programming matrix
a	Acceleration
A_b, a_b	Bounced acceleration (random variable or function)
A_c	Cross-sectional area of the core
A_g	Effective cross-sectional area of the gap
$A_{\mathrm{g},0}$	Effective cross-sectional area of the gap as $z \to 0$
B	Magnetic flux density
$\boldsymbol{B}$, B_ϕ, B_a	Vector or scalar coefficients of dynamical equation
b	Langevin function constant
$\boldsymbol{b}$	Quadratic programming vector
B_c	Average flux density in the core
B_e	Effective flux density
c	Reversibility factor
c_1, c_2	Fröhlich–Kennellyconstants
c_con	Contraction coefficient
c_exp	Expansion coefficient
c_f	Friction or damping coefficient
C_q	Flow set
c_ref	Reflection coefficient
c_shrink	Shrinkage coefficient
$\mathcal{D}$	Data set
d	Dimension of decision vector
$\boldsymbol{d}$	Disturbance vector
D_q	Jump set
$\boldsymbol{D}_{\boldsymbol{\chi}}$	Smoothed variation of $\boldsymbol{\chi}_\mathbf{best}$
E	Expected value
e_F	Force error (auxiliary variable)
e_ι	Current error (auxiliary variable)
E_s	Signal energy
$\boldsymbol{F}$	State transition matrix
$\mathcal{F}$	Magnetomotive force
f	Bayesian optimization random variable
$\mathbf{f}$	Transition function of the discrete model
$\boldsymbol{f}$, f_a, $f_{\mathcal{F}_\mathrm{c}}$, $\boldsymbol{f}_{\boldsymbol{\mathcal{F}}_\mathbf{c}}$, $\boldsymbol{f}_q$, f_v, f_λ, f_ϑ, $\boldsymbol{f}_{\boldsymbol{\vartheta}}$, f_ϕ	Dynamical functions or flow maps

f_{acqn}	Acquisition function
$\mathcal{F}_{\text{c}}$, $\boldsymbol{\mathcal{F}}_{\mathbf{c}}$	Magnetomotive forces in the core
f_{iJA},	Inverse Jiles–Atherton function
f_{JA}	Jiles–Atherton function
F_{mag}	Magnetic force
f_{n}	Normalization of f
F_{pas}	Passive force
$\boldsymbol{G}$	Smoother gain
$\mathcal{GP}$	Gaussian process
$\boldsymbol{G}_q$	Jump map
H	Magnetic field strength
$\boldsymbol{H}$	Observation matrix
$\mathcal{H}$	Hamiltonian
h	Output function
h	Observation function of the discrete model
H_{c}	Magnetic field strength in the core
H_f	Differential entropy of f
I	Improvement
i	Index
I_{mov}	Moment of inertia
I_{net}	Net improvement
J	Current density (Chapter 2)
$J, \mathcal{J}$	Cost functional or function (Chapters 3 and 4)
$\boldsymbol{J}$	Jacobian
j	Index
J_{free}	Free current density
$\boldsymbol{K}$	Kalman gain
$\mathbf{K}$, $\mathbf{k}$, k	Kernel matrix, vector or function
k	Index
k_1, k_2	Gap reluctance constants
k_{eddy}	Eddy current constant
k_{sp}	Spring stiffness constant
L	Inductance
$\boldsymbol{L}$	Bound length vector
l	Length
$\boldsymbol{l}$	Vector of length scales
l_{c}	Core length
l_{g}	Gap length
l_{w}	Coil winding length
l_z	Travel distance

M	Magnetization
m, $\mathbf{m}$	Gaussian process mean
M_{an}	Anhysteretic magnetization
M_{c}	Magnetization of the core
M_{irr}	Irreversible magnetization
m_{mov}	Moving mass
N	Number of turns of the coil
$\mathcal{N}$	Normal distribution
n	Order of dynamical system
n	Number of the simulation run (Section 4.5.3)
n_{g}	Number of position-dependent gaps
$\mathcal{O}$	Observability matrix
$\boldsymbol{p}$	Parameter vector
P	Probability
$\boldsymbol{P}$	Estimated state covariance
P_{c}	Probability of contact
$\mathrm{P}_{\mathcal{N}_{\mathrm{S}}}$	Standard normal cumulative distribution function
q	Discrete state
$\boldsymbol{Q}$	Process noise covariance
R	Internal resistance of the coil
$\boldsymbol{R}$	Observation noise covariance
$\mathcal{R}$	Magnetic reluctance
r	Radius
$\mathcal{R}_{\mathrm{c}}$	Magnetic reluctance of the core
$\mathcal{R}_{\mathrm{c},0}$	Core reluctance for $\phi = 0$
$\mathcal{R}_{\mathrm{g}}$	Magnetic reluctance of the gap
$\mathcal{R}_{\mathrm{g},0}$	Gap reluctance for $z = 0$
$\mathcal{R}'_{\mathrm{g},0}$	Gap reluctance derivative for $z = 0$
R_{real}	Real resistance
R_{shunt}	Shunt resistance
S	Surface
$\boldsymbol{S}$	Path constraint function
$\boldsymbol{\mathcal{S}}$	Constraint function of decision vector
s	Sliding surface
s	Nelder–Mead step (Appendix A.2)
T	Temperature
$\boldsymbol{T}$	Final state constraint function
T_{c}	Contact instant (random variable)
t	Time
T_{s}	Sampling period

t_{trig}	Trigger instant
U, $\boldsymbol{U}$	Input function
$\mathcal{U}$	Set of permissible inputs
u, $\boldsymbol{u}$	Input variable or vector
u_{hybrid}	Control action accounting for the full hybrid dynamics
u_{motion}	Control action accounting for the motion dynamics
unif	Continuous uniform distribution
V	Volume (Chapter 4 and Appendix A.2)
V	Lyapunov function (Chapter 5)
$\mathcal{V}$	Cost functional integrand
v	Velocity
v_{b}	Bounced velocity
$\mathcal{V}_{\mathrm{b}}$	Set of feasible bounced velocities
V_{c}	Contact velocity (random variable)
v_{c}	Simulated contact velocity
$v_{\mathrm{c}}^{\mathrm{eq}}$	Equivalent contact velocity
w	Process noise
$\boldsymbol{x}$	Continuous state vector
$\mathbf{X}$	Matrix of decision vectors
y, $\boldsymbol{y}$	Output variable or vector
z	Position of mover or armature
Z_{c}	Contact position (random variable)
z_{sp}	Spring resting position

Greek symbols

α	Interdomain coupling factor
α_R	Resistance temperature coefficient
β, $\boldsymbol{\beta}$	Costate
γ	Coefficient of restitution
δ	Additive effect of disturbance on cost
$\delta\Sigma$	Flux closed path
$\delta\Sigma_{\mathrm{c}}$	Flux path through the core
$\delta\Sigma_{\mathrm{g}}$	Flux path through the gap
ϵ	Parameter relative error
ε	Auxiliary term of the sliding surface expression
$\boldsymbol{\varepsilon}$	Evaluation noise
η	Minimum convergence speed of the sliding surface
$\boldsymbol{\theta}$	Vector of unknown constants
ϑ, $\boldsymbol{\vartheta}$	Additional state variable or vector

ι	Electrical current
ι_{coil}	Electrical current through the coil
ι_{eddy}	Net eddy current
κ	Spinning factor
λ	Flux linkage
λ_{e}	Effective flux linkage
μ	Magnetic permeability (Chapter 2)
μ	Expectation (Chapter 4)
μ_0	Magnetic permeability of free space
μ_z	Expected contact position
ν, $\boldsymbol{\nu}$, ν_ι	Observation error or noise
ρ, $\rho_{\mathcal{N}_{\mathrm{S}}}$ $\rho_{T_{\mathrm{c}}}$, $\rho_{Z_{\mathrm{c}}}$	Probability density functions
ϱ_1, ϱ_2	Sliding surface constants
Σ	Surface enclosed by $\delta\Sigma$
$\boldsymbol{\Sigma}$	Covariance matrix
σ	Conductivity (Chapter 2)
σ, σ_{n}, σ_T, σ_z, σ_ι	Standard deviation
σ_f^2	Characteristic variance of kernel
σ_p	Relative standard deviation of perturbed parameters
ς	Generalized sliding surface
τ	Bound variable for time integration (Chapter 3)
τ	Time interval (Appendix B.1)
τ_{mag}	Magnetic torque
τ_{mov}	Motion duration
τ_{pas}	Passive torque
υ	Voltage
υ_{coil}	Voltage between the coil terminals
$\upsilon_{\mathrm{audio}}$	Voltage signal from the microphone
ϕ	Magnetic flux
φ_ϕ	Alternative dynamical function of ϕ
$\boldsymbol{\chi}$	Decision vector
$\boldsymbol{\chi}_{\mathbf{best}}$	Best decision vector
$\boldsymbol{\chi}_{\mathbf{c}}$	Simplex centroid
χ_{tol}	Tolerance for parameter reduction
$\boldsymbol{\Psi}$	Vector of observed costs
ψ	Observed cost
ψ_{r}	Real cost
ω	Angle

Subscripts

a_0	Initial value
a_b	Breaking operation
a_eq	Equivalent
a_f	Final value
a_i	ith element or column
$a_{i,j}$	Element in the ith row and jth column
$a_{\setminus i}$	Removal of the ith element or column
a_k	kth element or column
$a_{k\|k}$	*A posteriori* (corrected) estimation
$a_{k\|k-1}$	*A priori* estimation
$a_{k\|k_\mathrm{f}}$	Smoothed estimation
a_lb	Lower bound
$a_\mathrm{lb,abs}$	Absolute lower bound
a_m	Making operation
a_max	Maximum
a_min	Minimum
a_ref	Reference value or signal
a_sat	Saturation value
a_ub	Upper bound
$a_\mathrm{ub,abs}$	Absolute upper bound
a_+, a_-	Piece of piece-wise function

Superscripts

a^exp	Experimental
a^i	Value at the ith iteration
$a^{(i)}$	ith time derivative
a^j	Value at the jth iteration
a^nom	Nominal value
a^sim	Simulated
a^+	Right limit
a^-	Left limit
a'	Partial derivative with respect to the position
a^*	Optimal value
$a^\#$	Auxiliary parameter or variable

Accents

$\dot{a}$	Time derivative
$\hat{a}$	Estimated value
$\bar{a}$	Mean value
$\tilde{a}$	Error

Chapter 1

Introduction

1.1 Motivation

Electromagnetic actuators constitute a class of electromechanical devices where the positioning of their movable components rely on forces produced by electrical and magnetic fields. Depending on the working principle of the magnetic forces, they can be classified as Lorentz or reluctance actuators. In particular, reluctance actuators rely on attractive magnetic forces between ferromagnetic movers and stators, which are magnetized by means of current coils and thus become electromagnets. The working principle of the reluctance-based magnetic force is the variation of magnetic reluctance with respect to the relative displacement between movable and fixed magnetic core parts. The main advantage of reluctance over Lorentz actuators is that they can achieve larger forces with lighter cores and reduced heat losses [1]. Thus, there is an increasing interest in incorporating this type of actuators in many applications, for instance, fast tool servos for diamond turning [2], propulsion systems for elevators [3], beam pointing and stabilization in optical systems [4], anti-vibration systems [5], linear compressors [6], or flexure-guided nanopositioning [7].

More specifically, switch-type reluctance actuators are characterized by having constrained motion. They are mostly used for opening and closing electrical, pneumatic or hydraulic circuits. On the one hand, contactors and electromechanical relays are utilized for power switching operations. Some examples of current applications are drive by wire [8], induction heating [9], battery charging [10] and wireless power transfer [11]. On the other hand, solenoid valves are used for fluid flow control in many applications, such as automotive internal combustion engines [12]–[15] or electronic-stability control [16], [17]. A well-known problem of the switching actuation is the strong landing impacts that cause mechanical wear, bouncing and acoustic noise. In addition, in electrical contacts, they may provoke contact welding [18], or arcing that exacerbates the erosion [19].

Thus, there is a great interest in designing and implementing soft-landing controllers to reduce the impact velocities during switching.

The efficiency of reluctance over Lorentz forces comes at the cost of more difficult control. While in Lorenz actuators there is a linear relation between the current and the force [20], reluctance actuators rely on a force that is dependent on both the magnetic flux and the position in a highly nonlinear fashion. Furthermore, regarding the control of reluctance actuators, it is important to distinguish between simple reluctance actuators, with a single-coil and no permanent magnets (see Fig. 1.1a); and more complex actuators, which may include permanent magnets or a second coil (see Figs. 1.1b and 1.1c). The advantage of the first type is its lower cost and size. However, having a single coil is very limiting from a control viewpoint. It can only generate magnetic force in one direction (attractive), which means that the actuator must rely on a source of an uncontrollable force (most commonly a spring) for moving in the opposite direction. Moreover, a second coil would provide more electrical information about the system that could be exploited for more accurate estimation and control of the actuator position. Despite the challenges, the research of soft-landing solutions for simple low-cost actuators is worthwhile, as it potentially extends their service life, makes them operate more quietly, and opens them to a wider range of applications.

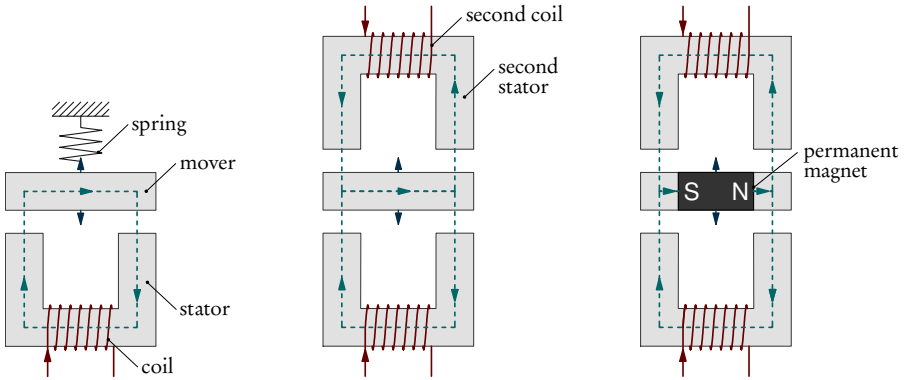

(a) Simple actuator. **(b)** Double actuator. **(c)** Hybrid actuator.

Figure 1.1: Schematic diagrams of short-stroke reluctance actuators with different complexities.

This thesis is framed in the context of collaboration between the University of Zaragoza and BSH Home Appliances Group. The shared goal lies in the research and development of technologies for the products of the company. In a process of continued improvement, BSH intends to put in the market home appliances with a wide range of prices and features, covering the needs of the biggest spectrum of users, while maintaining or extending their useful life and quality. In that regard, the study of soft-landing control strategies for simple short-stroke actuators is aligned with the interests of BSH. On the one hand, electromechanical relays are essential components in many home ap-

pliances (Fig. 1.2), but, due to their mechanical operation, these devices are subject to the deterioration of their contacts, whose main cause is the impact forces during each commutation. In some cases, these devices are gradually being replaced by semiconductor devices, which have no mechanical components and can perform similar functions. However, the relays still have advantages over semiconductor components: they are cheaper, have a lower cost power dissipation, admit voltages and currents in both directions, have no leakage currents when they open the circuit, and provide galvanic isolation between the activation and the power circuits. Therefore, improving their performance during switching while maintaining their advantages is of great interest. On the other hand, solenoid valves are primarily used as safety elements in gas stoves (Fig. 1.3), to stop the gas output in case there is no flame. The mitigation of switching impacts and bounces may open solenoid valves to applications that require a higher number of commutations, such as the regulation of the gas flow.

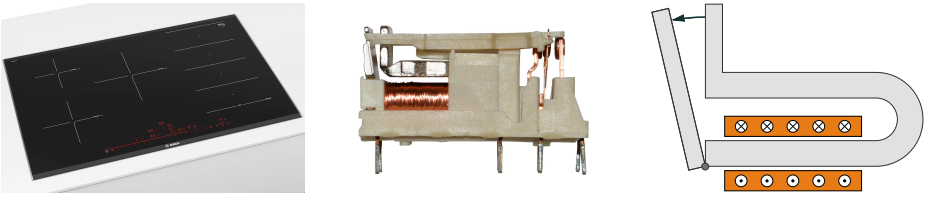

(a) Induction cooktop. **(b)** Electromechanical relay. **(c)** Relay diagram.

Figure 1.2: Electromechanical relays are used in electric appliances, such as induction cooktops.

(a) Gas cooktop. **(b)** Solenoid valve. **(c)** Valve diagram.

Figure 1.3: Solenoid valves are used in gas appliances, such as gas cooktops.

In any case, most of the presented work has been generalized, so that it can be applied to any simple short-stroke reluctance actuator, regardless of its type and intended application. Furthermore, even though the focus is on the simplest reluctance actuators, which present the most obvious challenges regarding their control, most solutions of this thesis are also valid for many other more complex and expensive actuators.

1.2 Objectives

The research aim of this thesis is the proposal of soft-landing solutions for short-stroke reluctance actuators, based on theory of control systems. More specifically, we focus on the control of single-coil actuators with no permanent magnets, such as electromechanical relays and solenoid valves. To achieve the main goal, several objectives are formulated:

1. **Dynamical modeling**. The starting point should be the design of dynamical models of reluctance actuators, accounting for their interconnected mechanical and electromagnetic systems, with their nonlinear relations and discontinuities. The purpose is to use the models for the development of control and estimation methods and, given the typically fast dynamics of reluctance actuators, special emphasis is devoted to the trade-off between accuracy and computational efficiency. In that regard, there is an interest in the design and comparison of models with varying levels of complexity and accuracy, considering or neglecting different phenomena.
2. **Identification**. For validation and comparison purposes, the models should be particularized to a real actuator. Many parameters and variables cannot be measured or directly estimated, which complicates the adjustment of the model. Thus, it is convenient to reduce the number of parameters, ideally without further simplifications of the dynamical system. It is also necessary to perform tests and adjust the parameter values from the available information (mainly electrical measurements) through optimization methods.
3. **Control**. As the main research focus, control strategies will be developed in order to reduce impact velocities during commutations and, as a consequence, the acoustic noise and the mechanical wear. An important effort will be made to propose and evaluate control strategies, from conventional open-loop and feedback control techniques to more specialized alternatives. Given the repetitive nature of the switching actuation, iterative techniques will be taken into consideration.
4. **Estimation**. Robust control strategies require information of the state of the system for feedback. The most important variable for motion control is the position of the movable part, especially for closed-loop controllers. Considering that position sensors are most commonly unavailable for low-cost actuators, another relevant research objective is the design and analysis of position estimators.

1.3 Thesis outline

The main content of the thesis has been divided into seven chapters. Chapter 1 is the current introduction, while Chapter 7 includes the main conclusions drawn from the investigation, as well as recommendations for continuing it. The main body is composed of five chapters, each one focusing on one research topic:

- In Chapter 2, the modeling of reluctance actuators is discussed. Firstly, the generalized differential equations for the electromagnetic and mechanical dynamics are derived. Then, the model is specified by including different electromagnetic phenomena—flux fringing, magnetic saturation and magnetic hysteresis—as well as the hybrid dynamics of the mechanical subsystem—combining behavior from continuous and discrete dynamical systems. Consequently, different models can be constructed depending on the selected specifications. For control purposes, the dynamical models are expressed as state-space representations. In particular, two main model types are considered, depending on whether the magnetic hysteresis phenomenon is incorporated or neglected. After that, model reductions are proposed for the electromagnetic subsystem of both types, thus decreasing the number of parameters and making them identifiable from easily measurable electrical signals. Lastly, the models are fitted to measurements from a real actuator and compared with respect to a more complex state-of-the-art model.

- Chapter 3 focuses on the optimal design of position trajectories for soft landing, and their corresponding input signals. Firstly, the problem is formulated as an optimal control problem and transformed into a two-point boundary value problem for its numerical resolution. On the one hand, the generated input signals are useful for open-loop control strategies. Simulated and experimental tests are performed using a dynamical model and a commercial short-stroke solenoid valve, comparing the open-loop proposal with a state-of-the-art alternative. On the other hand, the generated position trajectories are useful for other types of control, such as feedforward and feedback, which are presented in the following chapters.

- A run-to-run (R2R) strategy is proposed in Chapter 4. This type of control method exploits the repetitive functioning of the devices to adapt and improve a noncyclic controller, e.g. open-loop, feedforward or feedback controller. Specifically, it is designed to work in conjunction with a feedforward controller based on the position trajectories previously designed in Chapter 3. Moreover, a method is proposed for reducing the dimension of the decision vectors, thus simplifying and expediting the convergence. For the cycle-to-cycle learning algorithm, an optimization technique is chosen, adjusted and compared with Monte Carlo simulations to two alternatives. To further validate the proposal, experimental results are presented as well.

  This thesis also includes appendices that provide additional information in relation to the R2R control. Specifically, in Appendix A, the alternative R2R search functions are described. In Appendix B, an alternative input generation is presented. It is valid for R2R voltage control. The resulting R2R strategies are tested and compared through a Monte Carlo method. Lastly, in Appendix C, the application of the proposed R2R dimension reduction algorithm is detailed. In addition, a simulated comparison is included to showcase the advantage of reducing the number of decision variables.

- Chapter 5 explores the possibility of real-time tracking of the position with a feedback controller for soft landing. The proposed solution is a sliding-mode controller (SMC), whose design is focused on simplicity to facilitate its implementation, while taking into account the hybrid nature of the system dynamics. Then, theoretical and simulation analyses are presented to demonstrate its convergence and its performance in terms of the sampling rate.

- Chapter 6 deals with the state estimation, with special attention to the position. It is required for tracking control in many cases, as measuring the position during motion is rarely practical. Firstly, an efficient discrete model is constructed, based on the simplest model from Chapter 2. Then, the state estimation algorithm is presented. It is a smoother, which is divided into two parts: the first one is a forward filter, which serves as a conventional observer for real-time control; while the second part is a backward filter, which corrects past data and is very useful for cycle-to-cycle learning-type controllers. Finally, different states estimators are compared through a Monte Carlo method in which the simulations incorporate modeling and measurement errors.

1.4 Contributions and publications

Most contributions are the result of research work carried out in the Department of Computer Science and Systems Engineering, in the School of Engineering and Architecture of the University of Zaragoza; and in the BSH Competence Center for Induction Development in Zaragoza, Spain. Additional contributions originated from a three-month research stay that was conducted at the Department of Electrical Engineering of the Eindhoven University of Technology, in the Netherlands.

For clarity, the main contributions are divided into categories corresponding to different chapters of the thesis:

2 System modeling. Two model types have been proposed. On the one hand, the first model was proposed for the first time and presented at the 56th IEEE Conference on Decision and Control [21]. The main contribution regarding this model is the system representation with a hybrid automaton which accounts for the discrete behavior of the mechanical dynamics. On the other hand, the second model was proposed in a paper that has been accepted for its publication in Mechatronics [22]. The main contributions of the second proposal are the gap reluctance function and, most notably, the dynamical equation of the magnetomotive force in the core, which characterizes magnetic hysteresis and saturation phenomena. Another idea is the model reduction, which transforms the electromagnetic subsystem and ensures that their parameters are identifiable from measurements of electrical signals.

3 **Optimal control design**. On the one hand, our main optimal control proposal is published in the IEEE Transactions on Control Systems Technology [23]. The primary contribution is the addition of probability functions in the problem formulation. Specifically, uncertainty in the contact position is included and the soft-landing optimal control is formulated in order to minimize the expectations of the contact velocity and acceleration. Furthermore, the advantages of utilizing the electrical current as the control input for reluctance actuators are discussed and, in consequence, the optimization of the current signal is included in the formulation of the problem. On the other hand, we have also collaborated on the design of open-loop control signals solving deterministic optimal control problems. The contribution is the analysis of the open-loop control strategies on perturbed systems via a Monte Carlo method. It has been presented at the 17th European Control Conference [24].

4 **Run-to-run control**. The first main contribution of the R2R proposal is the search algorithm, based on Bayesian optimization. In the preliminary proposal, presented at the 17th European Control Conference [25], several adjustments are introduced to the algorithm: the limitation of the number of stored data by means of the combination or removal of observations, and the definition of a new acquisition function. For the final proposal, published in the IEEE/ASME Transactions on Mechatronics [26], new ideas are introduced regarding the search function, e.g. adaptive search bounds and an improved acquisition function. Moreover, as the second main contribution, the input signals are parameterized based on a feedforward controller, which relates the decision variables to parameters of the dynamical model. It exploits the flatness property of the dynamical model to derive a simple algebraic expression to calculate the input signal from the model parameters.

5 **Sliding-mode control**. A robust SMC controller has been developed for reluctance actuators and presented at the 21st IFAC World Congress [27]. The first contribution is the design of the controller as a switching model-free SMC, which works for every dynamic mode of the system. The second contribution is the analysis of the influence of the sampling rate on the impact velocities.

6 **State estimation**. The final contribution of the aforementioned paper presented at the 56th IEEE Conference on Decision and Control [21] is a stochastic state observer based on a discretized version of one of the proposed models and the unscented Kalman filter. Two patent applications have been submitted in relation to its application for electromechanical relays [28] and solenoid valves [29] in cooking appliances. Moreover, the stochastic observer has served as the foundation for the main estimation proposal. It is described in a manuscript, which is under review at the time of writing [30]. It introduces two ideas that have not been previously explored for this class of actuators. Firstly, the state estimation is approached as a smoothing problem of a stochastic process, in which the state

at a given time is refined by using future observation samples. Regarding the second main contribution, the estimator is designed using a novel set of observable variables. In addition to the electrical signals, commonly considered as the input and output of the system, the proposed estimator directly exploits discrete information related to its state, in particular, whether the mover is resting at one of the contacts or moving. In the context of state estimation, we have also collaborated on the development of two novel techniques to estimate in real time the magnetic flux and other electromagnetic variables of reluctance actuators. They have been published in the IEEE Transactions on Industrial Electronics [31].

Journal articles

1. E. Ramirez-Laboreo, E. Moya-Lasheras, and C. Sagues, "Real-Time Electromagnetic Estimation for Reluctance Actuators," *IEEE Transactions on Industrial Electronics*, vol. 66, no. 3, pp. 1952–1961, Mar. 2019. DOI: 10.1109/TIE.2018.2838077.

2. E. Moya-Lasheras, E. Ramirez-Laboreo, and C. Sagues, "Probability-Based Optimal Control Design for Soft Landing of Short-Stroke Actuators," *IEEE Transactions on Control Systems Technology*, vol. 28, no. 5, pp. 1956–1963, Sep. 2020, DOI: 10.1109/TCST.2019.2918479.

3. E. Moya-Lasheras and C. Sagues, "Run-to-Run Control With Bayesian Optimization for Soft Landing of Short-Stroke Reluctance Actuators," *IEEE/ASME Transactions on Mechatronics*, vol. 25, no. 6, pp. 2645–2656, Dec. 2020. DOI: 10.1109/TMECH.2020.2987942.

4. E. Moya-Lasheras, C. Sagues, and S. Llorente, "An Efficient Dynamical Model of Reluctance Actuators with Flux Fringing and Magnetic Hysteresis," *Mechatronics*, vol. 74, Apr. 2021. DOI: 10.1016/j.mechatronics.2021.102500.

5. E. Moya-Lasheras, J. M. Schellekens, and C. Sagues, "Rauch–Tung–Striebel Smoother for Control of Short-Stroke Reluctance Actuators," under review.

International peer-reviewed conferences

6. E. Moya-Lasheras, C. Sagues, E. Ramirez-Laboreo, and S. Llorente, "Nonlinear Bounded State Estimation for Sensorless Control of an Electromagnetic Device," in *2017 IEEE 56th Annual Conference on Decision and Control (CDC)*, Melbourne, Australia, Dec. 2017, pp. 5050–5055, DOI: 10.1109/CDC.2017.8264407.

7. E. Moya-Lasheras, E. Ramirez-Laboreo, and C. Sagues, "A Novel Algorithm Based on Bayesian Optimization for Run-to-Run Control of Short-Stroke Reluctance Actuators," in *2019 18th European Control Conference (ECC)*, Naples, Italy, Jun. 2019, pp. 1103–1109, DOI: 10.23919/ECC.2019.8795949.

8. E. Ramirez-Laboreo, E. Moya-Lasheras, and C. Sagues, "Optimal Open-Loop Control Policies for a Class of Nonlinear Actuators," in *2019 18th European Control Conference (ECC)*, Naples, Italy, Jun. 2019, pp. 3261–3266, DOI: 10.23919/ECC.2019.8795785.

9. E. Moya-Lasheras, E. Ramirez-Laboreo, and C. Sagues, "Model-Free Sliding-Mode Controller for Soft Landing of Reluctance Actuators," *21st IFAC World Congress 2020*, Berlin, Germany, Jul. 2020.

Patent applications

10. S. Llorente Gil, E. Moya Lasheras, E. J. Ramirez Laboreo, and C. Sagües Blázquiz, "Domestic appliance device," WO/2019/106488, 2019.

11. J. Ballester Castañer, J. Corral Ricalde, S. Llorente Gil, E. Moya Lasheras, J. S. Ochoa Torres, E. Placer Maruri, E. J. Ramirez Laboreo, J. Rivera Peman, C. Sagües Blázquiz, and D. Serrano García, "Gas cooking appliance device," WO/2019/220247, 2019.

Chapter 2

System Modeling

Two dynamical models of different complexities are proposed. Different electromagnetic phenomena are specified, with special attention to the magnetic hysteresis. Equivalent models with fewer parameters are also presented. They are identifiable from electrical measurements. Lastly, the models are fitted and compared.

2.1 Introduction

Dynamical modeling is an essential step in the design of controllers and estimators. Concerning electromagnetic modeling, there are two main approaches. On the one hand, finite element models (FEM) [14], [32]–[34] allow representing the dynamic behavior of these devices with great accuracy, but they are too computationally demanding for control applications. On the other hand, although analytical lumped-parameter models are less accurate, they are much less complex and thus may be suitable for real-time estimation and control.

There is considerable literature concerning the representation of reluctance actuators with lumped-parameter models. Most works neglect the effect of the magnetic hysteresis [35]–[38]. Some works do propose hysteresis models for actuators but neglect the motion dynamics [39]–[41]. Recently, Ramirez-Laboreo et al. [42] proposed a model of the mechanical and electromagnetic dynamics, with special emphasis on the derived hysteresis solution based on the generalized Preisach model (GPM) to characterize the magnetic hysteresis. This state-of-the-art approach is treated as the reference point, and it is used for comparison.

The major drawback of the GPM is its computational complexity. It requires numerical integration in each time step, even if it is implemented in an efficient state-space form [43]. A simpler and, thus, more efficient dynamical model will give relevant advantages for control applications. From a more general perspective, there are numerous hysteresis models in the literature for ferromagnetic materials, e.g. Jiles–Atherton (JA)

model [44], play and stop models [45], or the generalized positive-feedback model [46]. The JA model is one of the most widespread physics-inspired techniques. It is a relatively simple macromagnetic model, only requiring five parameters to describe the hysteresis phenomenon [47]. Regarding control applications, it has been used for hysteresis compensation of electromagnets [43]. However, to the best of the authors' knowledge, the JA solution has not yet been incorporated in a dynamical model of reluctance actuators.

In this chapter, two types of hybrid lumped-parameter models are presented for characterizing the dynamics of reluctance actuators. The first model includes the simplest electromagnetic phenomena (eddy currents, flux fringing, magnetic saturation), while the second one also incorporates magnetic hysteresis. Then, equivalent models are derived with a reduced number of parameters, ensuring that they are identifiable solely from measurements of electrical signals. Lastly, the models are fitted and compared with the state-of-the-art alternative.

2.2 General dynamical equations

In this section, the generalized dynamical model is presented, which serves as the basis for the more specific models presented in Section 2.3.

2.2.1 Description of reluctance actuators

The devices under study are simple low-cost actuators, with a single coil and no permanent magnets. For example, Fig. 2.1 depicts schematic representations of some of these actuators. For each one, the magnetic core is divided into two parts: a fixed part (stator) and a movable part (mover or armature). The air gaps between the core parts are dependent on the position of the mover z, which is restricted between a lower and an upper limit. The motion may be linear (Figs. 2.1a and 2.1b) or angular (Fig. 2.1c).

The electrical current through the coil ι_{coil} generates a magnetic flux ϕ through the core parts and the air gaps between them, which results in a magnetic force. With a single coil and no permanent magnets, it is only possible to generate a magnetic force in one direction. Consequently, there are two asymmetrical types of operation depending on the movement direction. On the one hand, in a making (closing) operation, the coil is energized to increase the magnetic force and attract the mover toward the stator. On the other hand, in a breaking (opening) operation, the magnetic force is reduced so that passive—most commonly elastic—forces move the armature in the opposite direction.

In order to derive computationally efficient lumped-parameter models, the complex distributed system must be approximated by a limited set of time-dependent scalar variables. On the one hand, any movable part is assumed a rigid body, defined by its position z and velocity v. On the other hand, the magnetic flux density is assumed to be constant within each core and gap section normal to the magnetic field lines. In other words, even

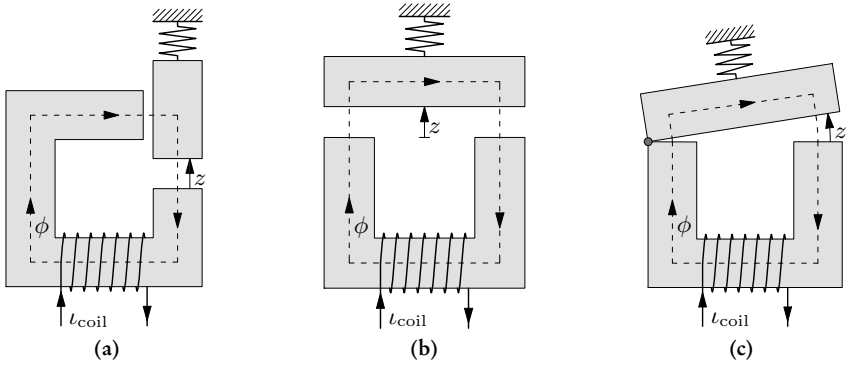

Figure 2.1: Schematic representation of single-coil reluctance actuators.

if the area of the cross-section varies along the magnetic field path, the magnetic flux is uniform within it.

2.2.2 Electromagnetic subsystem

The magnetic equivalent circuit (MEC) approach [48], [49] provides the perfect baseline for modeling the electromagnetic subsystem with lumped parameters. A MEC is analogous to an electrical circuit, in which the current, electromotive force and resistance are replaced by the magnetic flux, magnetomotive force and reluctance, respectively. In this approximation, it is assumed that the magnetic flux strictly follows a path along the core and air gaps (see Fig. 2.2). In other words, flux leakage is neglected. It is a reasonable and widely accepted assumption, especially if the air gaps are small because the ferromagnetic core has a much greater magnetic permeability than the air around it.

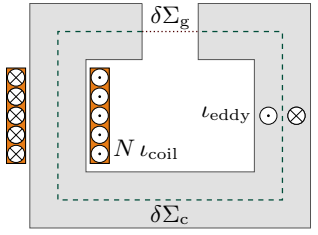

Figure 2.2: Schematic representation of the electromagnetic subsystem. The flux path is divided into $\delta\Sigma_\mathrm{c}$ (dashed line) and $\delta\Sigma_\mathrm{g}$ (dotted line).

The electromagnetic subsystem represented in Fig. 2.2 is governed by two main equations. The first one is the electrical circuit equation of the coil,

$$\upsilon_\mathrm{coil} = R\,\iota_\mathrm{coil} + N\,\dot{\phi}, \tag{2.1}$$

where υ_{coil}, ι_{coil}, R and N are the coil voltage, current, resistance and number of turns, respectively. The second equation is Ampère's circuital law, which relates the total free current density J_{free} passing through a surface Σ with the magnetic field strength H across its closed boundary curve $\delta\Sigma$. Formally, it can be expressed as

$$\iint_{\Sigma} J_{\text{free}} \, \mathrm{d}S = \oint_{\delta\Sigma} H \, \mathrm{d}l, \tag{2.2}$$

being J_{free} the free current density. Note that the original Ampère's law, as presented above, is only correct in a magnetostatic scenario. Nonetheless, it is a valid approximation for relatively low frequencies—around 1 MHz, which is orders of magnitude higher than the dynamics of this type of actuators [50].

By defining $\delta\Sigma$ as the path of the magnetic flux (see Fig. 2.2), the left-hand side of (2.2) is

$$\iint_{\Sigma} J_{\text{free}} \, \mathrm{d}S = N \, \iota_{\text{coil}} + \iota_{\text{eddy}}, \tag{2.3}$$

where ι_{eddy} is the net eddy current through the core. To model the eddy currents, it is assumed that the magnetic flux is uniform within the cross section of the core. This first-order approximation results in eddy currents proportional to the time derivative of the magnetic flux,

$$\iota_{\text{eddy}} = -k_{\text{eddy}} \, \dot{\phi}, \tag{2.4}$$

in which k_{eddy} is a positive constant that depends on the geometry and conductivity of the core. For detailed derivations of (2.4), see Section 6.3 of [50] and Section 2.7 of [51].

Regarding the right hand of (2.2), it is convenient to separate the integral into two components,

$$\oint_{\delta\Sigma} H \, \mathrm{d}l = \int_{\delta\Sigma_{\text{g}}} H \, \mathrm{d}l + \int_{\delta\Sigma_{\text{c}}} H \, \mathrm{d}l, \tag{2.5}$$

because the model must take into account different magnetic phenomena in the air and the core. Note that there may be several air gaps across $\delta\Sigma$ but, for convenience, they are grouped together as in Fig. 2.2

In general, the relation between the magnetic field strength and the flux density is given by the magnetic permeability μ,

$$B = \mu \, H. \tag{2.6}$$

This relation is analogous to the microscopic Ohm's law in electrical circuits $J = \sigma \, E$ (being J, σ and E the current density, conductivity and electric field, respectively). As in Ohm's law, there is also a macroscopic relation for magnetic circuits, known as Hopkinson's law,

$$\mathcal{F} = \mathcal{R} \, \phi, \tag{2.7}$$

where $\mathcal{F}$ is the magnetomotive force and $\mathcal{R}$ is the magnetic reluctance (counterparts of the electromotive force and resistance in electrical circuits, respectively). The magnetomotive force is defined in terms of the magnetic field strength as follows:

$$\mathcal{F} = \int H \,\mathrm{d}l. \tag{2.8}$$

In consequence, the reluctance term must be

$$\mathcal{R} = \frac{\int H \,\mathrm{d}l}{\phi} = \int \frac{\mathrm{d}l}{\mu\, A}, \tag{2.9}$$

where A is the cross-sectional area. Note that, under the assumption that the magnetic flux is uniform, $\phi = B\, A$.

In the air gaps, the length of $\delta\Sigma_\mathrm{g}$ depends on the position of the mover. Additionally, the magnetic permeability can be considered constant ($\mu \approx \mu_0 \approx 4\,\pi \times 10^{-7}\,\mathrm{N\,H/m}$). Then, Hopkinson's law results in

$$\int_{\delta\Sigma_\mathrm{g}} H \,\mathrm{d}l = \mathcal{R}_\mathrm{g}(z)\,\phi, \tag{2.10}$$

where the magnetic reluctance of the air gaps $\mathcal{R}_\mathrm{g}$ depends solely on the mover position z.

Regarding the core term from (2.5), the relation between the magnetic flux and the field strength is not only nonlinear, but it presents also a hysteretic behavior. Thus, Hopkinson's law can only be applied if the magnetic hysteresis phenomenon is neglected. For now, the integral is simplified to a sum of an arbitrary number of different magnetomotive force terms $\mathcal{F}_{\mathrm{c}i}$, where each term corresponds to a core part with a length $l_{\mathrm{c}i}$ and cross-sectional area $A_{\mathrm{c}i}$, such that its average magnetic field strength is $H_{\mathrm{c}i}$

$$\int_{\delta\Sigma_\mathrm{c}} H \,\mathrm{d}l = \sum_i H_{\mathrm{c}i}\, l_{\mathrm{c}i} = \sum_i \mathcal{F}_{\mathrm{c}i}. \tag{2.11}$$

The characterization of $\mathcal{F}_{\mathrm{c}i}$ will be detailed in Section 2.3.2.

Finally, substituting (2.3), (2.4), (2.5), (2.7) into (2.3), and isolating $\dot{\phi}$, the following differential equation is derived,

$$\dot{\phi} = -\frac{\mathcal{R}_\mathrm{g}(z)\,\phi + \sum_i \mathcal{F}_{\mathrm{c}i}}{k_\mathrm{eddy}} + \frac{N}{k_\mathrm{eddy}}\,\iota_\mathrm{coil}, \tag{2.12}$$

where ι_coil would be the input.

However, it is more common to control the actuators with υ_coil. Then, from (2.1) and (2.12),

$$\dot{\phi} = -\frac{R\left(\mathcal{R}_\mathrm{g}(z)\,\phi + \sum_i \mathcal{F}_{\mathrm{c}i}\right)}{N^2 + R\,k_\mathrm{eddy}} + \frac{N}{N^2 + R\,k_\mathrm{eddy}}\,\upsilon_\mathrm{coil}. \tag{2.13}$$

Regardless of the chosen input, the dynamics of the magnetic flux is given by an input-affine nonlinear function, denoted as f_ϕ,

$$\dot{\phi} = f_\phi(z, \phi, \boldsymbol{\mathcal{F}}_\mathbf{c}, u). \tag{2.14}$$

Note that, for simplifying this and subsequent expressions, the variables $\mathcal{F}_{\mathrm{c}i}$ are grouped in the vector $\boldsymbol{\mathcal{F}}_\mathbf{c} = \begin{bmatrix}\mathcal{F}_{\mathrm{c}1} & \mathcal{F}_{\mathrm{c}2} & \cdots\end{bmatrix}^\mathsf{T}$.

Once the input is selected, the other electrical variable may be considered the system output. If υ_{coil} is the input, the output ι_{coil} is calculated as

$$\iota_{\mathrm{coil}} = \frac{N\left(\mathcal{R}_{\mathrm{g}}(z)\,\phi + \sum_i \mathcal{F}_{\mathrm{c}i}\right)}{N^2 + R\,k_{\mathrm{eddy}}} + \frac{k_{\mathrm{eddy}}}{N^2 + R\,k_{\mathrm{eddy}}}\,\upsilon_{\mathrm{coil}}. \tag{2.15}$$

If, instead, ι_{coil} is the input, the output υ_{coil} is

$$\upsilon_{\mathrm{coil}} = -\frac{N\left(\mathcal{R}_{\mathrm{g}}(z)\,\phi + \sum_i \mathcal{F}_{\mathrm{c}i}\right)}{k_{\mathrm{eddy}}} + \frac{N^2 + R\,k_{\mathrm{eddy}}}{k_{\mathrm{eddy}}}\,\iota_{\mathrm{coil}}. \tag{2.16}$$

In any case, the output equation can be expressed as

$$y = h(z, \phi, \boldsymbol{\mathcal{F}}_\mathbf{c}, u), \tag{2.17}$$

being y the output and h the output function.

2.2.3 Mechanical subsystem

During motion, the dynamical equation of the armature is given by Newton's second law,

$$m_{\mathrm{mov}}\,\ddot{z} = F_{\mathrm{pas}}(z, \dot{z}) + F_{\mathrm{mag}}(z, \phi), \tag{2.18}$$

where m_{mov} is the movable mass. Notice that total force is separated into the magnetic force F_{mag}, and the passive total force F_{pas}, which encompasses the rest of the forces acting on the mover. The passive force may include elastic, gravitational and friction forces. Regarding the friction, it can be approximated as an ideal Coulomb or viscous friction. Alternatively, if deemed necessary, more complex models can be used [52].

The only controllable force—albeit in an indirect way—is the magnetic force, which mainly depends on the magnetic flux. The magnetic force may be derived through an energy balance (see Chapter 2.8 of [51]), resulting in the following equation:

$$F_{\mathrm{mag}}(z, \phi) = -\frac{1}{2}\,\mathcal{R}'_{\mathrm{g}}(z)\,\phi^2, \tag{2.19}$$

where $\mathcal{R}'_{\mathrm{g}}(z)$ represents the partial derivative of the magnetic reluctance of the gap with respect to the position,

$$\mathcal{R}'_{\mathrm{g}}(z) = \frac{\partial \mathcal{R}_{\mathrm{g}}(z)}{\partial z}. \tag{2.20}$$

In general, the magnetic force tends to attract the mover toward the position of minimum reluctance which, in the majority of simple reluctance actuators, corresponds to the minimum air gap. Note that the direction of the magnetic force cannot be controlled, because it depends on the square of the magnetic flux. To be able to move the armature in the opposite direction to the magnetic force, passive forces are essential (e.g., elastic forces).

In the case of angular motion, the dynamics are given by a completely analogous equation,

$$I_{\mathrm{mov}}\,\ddot{\omega} = \tau_{\mathrm{pas}}(\omega,\dot{\omega}) + \tau_{\mathrm{mag}}(\omega,\phi), \qquad \tau_{\mathrm{mag}}(\omega,\phi) = -\frac{1}{2}\,\frac{\partial \mathcal{R}_{\mathrm{g}}(\omega)}{\partial \omega}\,\phi^2, \tag{2.21}$$

where ω, I_{mov}, τ_{pas}, τ_{mag} are the angular position, the moment of inertia, the passive torque and the magnetic torque, respectively. Regardless, to unify the expressions, the dynamical equation for angular motion may be transformed into (2.18) by defining the position z as the arc length with radius r, i.e. $z = \omega\, r$. Then, the equivalent moving mass and forces are defined as follows:

$$m_{\mathrm{mov}} = \frac{I_{\mathrm{mov}}}{r^2}, \quad F_{\mathrm{pas}}(z,\dot{z}) = \frac{\tau_{\mathrm{mag}}(z/r,\dot{z}/r)}{r}, \quad F_{\mathrm{mag}}(z,\phi) = \frac{\tau_{\mathrm{pas}}(z/r,\phi)}{r}. \tag{2.22}$$

Note that, in this case, m_{mov} does not represent the actual moving mass, but a lumped mass concentrated at the point corresponding to the angle ω and radius r. Accordingly, F_{pas} and F_{mag} are not the forces acting on the moving mass but instead represent forces perpendicular to ω and directed to the point with concentrated mass m_{mov}.

Following a state-space representation, both the position z and velocity v are treated as state variables. Then, their dynamical equations during motion are

$$\dot{z} = v, \tag{2.23}$$

$$\dot{v} = f_v(z,v,\phi) = \frac{1}{m_{\mathrm{mov}}}\,\big(F_{\mathrm{pas}}(z,v) + F_{\mathrm{mag}}(z,\phi)\big). \tag{2.24}$$

Note, however, that the position of this class of actuators is restricted between a lower and an upper limit ($z \in [z_{\min},\, z_{\max}]$). Evidently, when the armature reaches one of its limits, a normal force acts on the armature due to contact. Furthermore, there is a velocity change at impact that is almost instantaneous—i.e. the elasto-plastic dynamics of the collision is much faster than the dynamics of the armature during unconstrained motion—therefore it is reasonable to characterize it as a discrete event. In general, the velocity jump (from v to v^+) due to a collision can be modeled in terms of the coefficient of restitution $\gamma = \gamma(v) \in [0,1]$,

$$v^+ = -\gamma(v)\, v, \tag{2.25}$$

where $\gamma = 0$ would indicate a perfectly inelastic collision, with no bouncing, and $\gamma = 1$ would indicate a perfectly elastic collision, with no energy losses due to the impact. The

bouncing is in fact one of the main motivations for the research of soft-landing solutions for this class of actuators. Nevertheless, in most cases, modeling this phenomenon is not necessary because the intention is to control the actuator before the first impact in order to reduce the velocity at that event. Then, reduction of the impact velocities leads to a reduction of bouncing and subsequent impact velocities. Furthermore, the effect of the bouncing is barely appreciable in the output (current or voltage). Hence, a position sensor would be required to properly characterize the function γ. This would unnecessarily complicate the models and their identification. In consequence, for the most of this thesis, the collisions are assumed perfectly inelastic.

The mechanical subsystem is hybrid, as it is a combination of both continuous and discrete-time dynamics. Specifically, this type of hybrid system can be represented as a hybrid automaton, which separates the state into a continuous and a discrete state [53]. The diagram is presented in Fig. 2.3. It has three dynamic modes, which correspond to the lower limit, motion and upper limit, respectively. On the one hand, the continuous state variables are the position z and velocity v, whose continuous dynamics must be specified for each mode. On the other hand, the discrete state is $q \in \{1, 2, 3\}$, which designates the dynamic mode. The possibility of bouncing is determined by the guard conditions and reset rules of the transitions from the motion mode ($q = 2$), which depend on the coefficient of restitution.

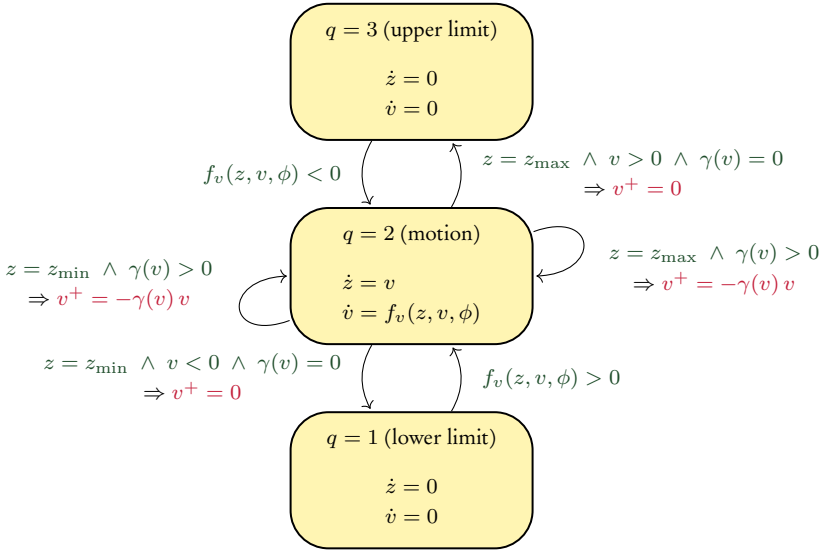

Figure 2.3: Diagram of the hybrid automaton modeling the mechanical subsystem of reluctance actuators. Each transition between modes (yellow blocks) occurs when the corresponding guard condition (green text) is satisfied. In some transitions, the continuous state jumps according to the corresponding reset rule (red text).

2.3 Specifications

This section presents specific expressions for the magnetic reluctance of the gap and the magnetomotive force of the core, considering different electromagnetic phenomena. They are required for fully defining the dynamical equation of the magnetic flux (2.12) or (2.13), as well as the output equation (2.15) or (2.16).

2.3.1 Magnetic reluctance of the air gaps

For the calculation of the total gap reluctance, the integral (2.9) can be approximated by a sum of different reluctance terms, corresponding to different air gaps,

$$\mathcal{R}_{\mathrm{g}}(z) = \sum_i \frac{l_{\mathrm{g}_i}(z)}{\mu_0 \, A_{\mathrm{g}_i}(z)}, \tag{2.26}$$

where the gap lengths l_{g_i} may depend on the mover position, and each effective area A_{g_i} augments with its corresponding gap length. This is due to the flux fringing effect, in which the flux spreads out in the air gaps because there is no magnetic core to provide a path with high permeability. It can be approximated using fringing flux factors for each gap, such as McLyman's [54],

$$A_{\mathrm{g}_i}(z) = A_{\mathrm{g},0_i} \left(1 + \frac{l_{\mathrm{g}_i}(z)}{\sqrt{A_{\mathrm{g},0_i}}} \ln\!\left(\frac{2\, l_{\mathrm{w}}}{l_{\mathrm{g}_i}(z)} \right) \right), \tag{2.27}$$

where each $A_{\mathrm{g},0_i}$ is the effective area when the gap length tends to zero, and l_{w} is the coil winding length.

The resulting function of the gap reluctance (2.26) and (2.27) cannot be simplified further without loss of generality. Still, we propose a simplification that is useful for characterizing most reluctance actuators. It is assumed that all position-dependent gaps are identical and proportional to the position,

$$A_{\mathrm{g},0_i} = A_{\mathrm{g},0}, \qquad\qquad l_{\mathrm{g}_i} = l'_{\mathrm{g}}\, z, \tag{2.28}$$

being l'_{g} a positive constant. The assumption holds for most linear-travel reluctance actuators—e.g., Figs. 2.1a and 2.1b. Furthermore, it may be a good approximation for short-stroke actuators with angular positioning—e.g., Fig. 2.1c—because the angles are very small and the motion is almost linear.

Then, their total reluctance is equal to

$$\sum_{i=1}^{n_{\mathrm{g}}} \mathcal{R}_{\mathrm{g}_i}(z) = n_{\mathrm{g}} \, \frac{l'_{\mathrm{g}}\, z}{\mu_0 \left(1 + \dfrac{l'_{\mathrm{g}}\, z}{\sqrt{A_{\mathrm{g},0}}} \ln\!\left(\dfrac{2\, l_{\mathrm{w}}}{l'_{\mathrm{g}}\, z} \right) \right)}, \tag{2.29}$$

where n_g is the number of position-dependent gaps. On the other hand, there may be gaps that are not dependent on the mover position. In that case, their reluctance terms can be grouped in the constant $\mathcal{R}_{\mathrm{g},0}$. Then, by combining all constant parameters from (2.29) and adding $\mathcal{R}_{\mathrm{g},0}$, the total gap reluctance is expressed as

$$\mathcal{R}_\mathrm{g}(z) = \mathcal{R}_{\mathrm{g},0} + \sum_{i=1}^{n_\mathrm{g}} \mathcal{R}_{\mathrm{g}_i}(z) = \mathcal{R}_{\mathrm{g},0} + \frac{\mathcal{R}'_{\mathrm{g},0}\, z}{1 + k_1\, z\, \ln(k_2/z)}, \tag{2.30}$$

where

$$\mathcal{R}'_{\mathrm{g},0} = \frac{n_\mathrm{g}\, l'_\mathrm{g}}{\mu_0}, \qquad k_1 = \frac{l'_\mathrm{g}}{\sqrt{A_{\mathrm{g},0}}}, \qquad k_2 = \frac{2\, l_\mathrm{w}}{l'_\mathrm{g}}. \tag{2.31}$$

The constants $\mathcal{R}_{\mathrm{g},0}$, $\mathcal{R}'_{\mathrm{g},0}$, k_1 and k_2 are to be fitted through identification from experimental or FEM data.

Note that the partial derivative of the gap reluctance, necessary for determining the magnetic force (see Section 2.2.3), can be easily derived from (2.30),

$$\mathcal{R}'_\mathrm{g}(z) = \frac{\partial \mathcal{R}_\mathrm{g}(z)}{\partial z} = \frac{\mathcal{R}'_{\mathrm{g},0}\,(1 + k_1\, z)}{\big(1 + k_1\, z\, \ln(k_2/z)\big)^2}. \tag{2.32}$$

Note also that (2.30) and (2.32) are indeterminate for $z = 0$ so, in that event, $\mathcal{R}_\mathrm{g}$ and $\mathcal{R}'_\mathrm{g}$ must be calculated in the limit from the right,

$$\lim_{z \to 0^+} \mathcal{R}_\mathrm{g}(z) = \mathcal{R}_{\mathrm{g},0}, \qquad \lim_{z \to 0^+} \mathcal{R}'_\mathrm{g}(z) = \mathcal{R}'_{\mathrm{g},0}. \tag{2.33}$$

2.3.2 Magnetomotive forces in the core

Regarding the definition of the magnetomotive forces, two solutions are proposed. The first one is simpler. It takes into account the magnetic saturation in the core, but neglects entirely the magnetic hysteresis phenomenon. The second one is more complete, but also much more complex. It also takes into account the magnetic hysteresis phenomenon.

Magnetic saturation

In this subsection, we derive a relation between the force and the magnetic flux ϕ based on the Fröhlich–Kennelly(FK) equation [55]. In the following reformulation of the original FK equation, the magnetic flux density B is defined in terms of the field strength H,

$$B = \frac{c_1\, H}{1 + c_2\, |H|}, \tag{2.34}$$

where c_1 and c_2 are positive constants. This alternative FK equation includes an absolute value in the denominator, making it an odd function ($B(-H) = -B(H)$) and thus extending its domain from the positive to the whole real number line [37]. The function is represented in 2.4a.

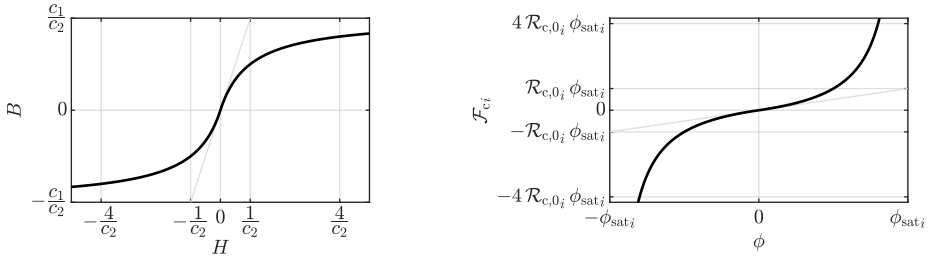

(a) Magnetic flux density. **(b)** Magnetomotive force.

Figure 2.4: General B–H and $\mathcal{F}_{\mathrm{c}i}$–$\phi$ curves with saturation.

Then, taking into account that $\mathrm{sgn}(H) = \mathrm{sgn}(B)$, the magnetic permeability μ can be defined as a function of the magnetic flux density B,

$$\mu = \frac{B}{H} = \frac{c_1}{1 + c_2\,|B|/\mu} \;\Rightarrow\; \mu = c_1 - c_2\,|B|. \tag{2.35}$$

From there, an inverse version of the FK equation (2.34) is derived,

$$H = \frac{B}{\mu} = \frac{B}{c_1 - c_2\,|B|}, \tag{2.36}$$

Having an explicit definition of the magnetic permeability, H may now be directly related to the state variable ϕ. For consistency, Hopkinson's law (2.7) may be used again to obtain the macroscopic counterpart, resulting in the following relation:

$$\mathcal{F}_{\mathrm{c}i} = \mathcal{F}_{\mathrm{c}i}(\phi) = \mathcal{R}_{\mathrm{c}i}(\phi)\,\phi, \qquad\qquad \mathcal{R}_{\mathrm{c}i}(\phi) = \frac{\mathcal{R}_{\mathrm{c},0_i}}{1 - |\phi|/\phi_{\mathrm{sat}_i}}, \tag{2.37}$$

where each $\mathcal{R}_{\mathrm{c}i}$ is the magnetic reluctance of a core part, whose parameters are

$$\mathcal{R}_{\mathrm{c},0_i} = c_1\,\frac{l_{\mathrm{c}i}}{A_{\mathrm{c}i}}, \qquad\qquad \phi_{\mathrm{sat}_i} = \frac{c_1}{c_2}\,A_{\mathrm{c}i}. \tag{2.38}$$

The reluctance parameters have an intuitive meaning: each $\mathcal{R}_{\mathrm{c},0_i}$ represents the core reluctance when $\phi = 0$, while each ϕ_{sat_i} represents the saturation value of the magnetic flux, ensuring that $|\phi| < \phi_{\mathrm{sat}_i}$ (see Fig. 2.4b).

Finally, the magnetic flux dynamical equation which incorporates magnetic saturation is fully defined by replacing (2.37) into the corresponding function f_ϕ (2.12)—if $u = \iota_{\mathrm{coil}}$—or (2.13)—if $u = \upsilon_{\mathrm{coil}}$. Note that, with the chosen formulation, the total reluctance has been partitioned into a term that is dependent on the position—$\mathcal{R}_{\mathrm{g}}(z)$—and one or more terms that are dependent on the magnetic flux—$\mathcal{R}_{\mathrm{c}i}(\phi)$.

Magnetic hysteresis

In the previous approach, the B–H relation is assumed one-to-one. It is sufficient for modeling magnetic saturation. However, for modeling the magnetic hysteresis phenomenon, a surjective mapping $H \mapsto B$ cannot be constructed, so the concepts of magnetic permeability and reluctance must be discarded.

A different type of model is proposed, based on the JA theory. The original formulation [44] permits calculating the magnetization M from its field strength H. Specifically, an ordinary differential equation of the form

$$\frac{\mathrm{d}M}{\mathrm{d}H} = f_{\mathrm{JA}}(M, H, \dot{H}) = \begin{cases} f_{\mathrm{JA}+}(M, H), & \text{if } \dot{H} \geq 0 \\ f_{\mathrm{JA}-}(M, H), & \text{if } \dot{H} < 0 \end{cases} \tag{2.39}$$

is solved to obtain M. Then, by definition, B can be calculated from M and H,

$$B = \mu_0 \, (H + M). \tag{2.40}$$

However, in this case, it is more appropriate to determine H from B. Thus, the inverse JA model [56] is used, in which an alternative differential equation is proposed, which can be expressed compactly as

$$\frac{\mathrm{d}M}{\mathrm{d}B} = f_{\mathrm{iJA}}(M, B, \dot{B}) = \begin{cases} f_{\mathrm{iJA}+}(M, B), & \text{if } \dot{B} \geq 0 \\ f_{\mathrm{iJA}-}(M, B), & \text{if } \dot{B} < 0 \end{cases}. \tag{2.41}$$

The complete process is described below.

The effective flux density B_{e} is defined as

$$B_{\mathrm{e}} = \mu_0 \, (H + \alpha \, M), \tag{2.42}$$

where the constant α represents the interdomain coupling. The effective flux density B_{e} depends on both the core field strength H and magnetization M, which can be obtained from (2.40), resulting in the following equation:

$$B_{\mathrm{e}} = B - \mu_0 \, (1 - \alpha) \, M. \tag{2.43}$$

Then, the anhysteretic magnetization of the core M_{an} and its derivative are obtained by using a modified Langevin function [57],

$$M_{\mathrm{an}} = M_{\mathrm{sat}} \left(\coth\!\left(\frac{B_{\mathrm{e}}}{b} \right) - \frac{b}{B_{\mathrm{e}}} \right), \tag{2.44}$$

$$\frac{\mathrm{d}M_{\mathrm{an}}}{\mathrm{d}B_{\mathrm{e}}} = \frac{M_{\mathrm{sat}}}{b} \left(1 - \coth^2\!\left(\frac{B_{\mathrm{e}}}{b} \right) + \left(\frac{b}{B_{\mathrm{e}}} \right)^2 \right), \tag{2.45}$$

where M_{sat} and b are positive constants, which determine the saturation value of M_{an} and the initial value of $\mathrm{d}M_{\mathrm{an}}/\mathrm{d}B_{\mathrm{e}}$, as can be seen in Fig. 2.5. Note that the functions are indeterminate for $B_{\mathrm{e}} = 0$, so they should be calculated as limits,

$$\lim_{B_{\mathrm{e}} \to 0} M_{\mathrm{an}} = 0, \qquad \lim_{B_{\mathrm{e}} \to 0} \frac{\mathrm{d}M_{\mathrm{an}}}{\mathrm{d}B_{\mathrm{e}}} = \frac{M_{\mathrm{sat}}}{3\,b}. \tag{2.46}$$

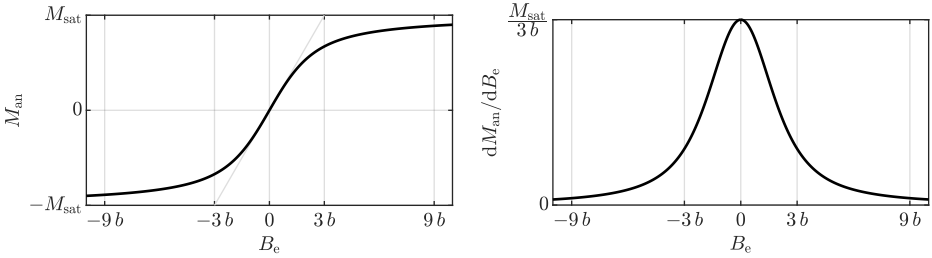

(a) Anhysteretic magnetization. **(b)** Derivative of anhysteretic magnetization.

Figure 2.5: Anhysteretic magnetization and its derivative as functions of the effective flux density.

Secondly, the irreversible magnetization M_{irr} is given by the following differential equation,

$$\frac{\mathrm{d}M_{\mathrm{irr}}}{\mathrm{d}B_{\mathrm{e}}} = \frac{M_{\mathrm{an}} - M_{\mathrm{irr}}}{\mu_0\,\kappa}\ \mathrm{sgn}\left(\dot{B}\right), \tag{2.47}$$

where κ is the spinning factor.

Thirdly, the total magnetization M can be expressed as a weighted sum depending on the reversibility factor c,

$$M = (1 - c)\,M_{\mathrm{irr}} + c\,M_{\mathrm{an}}. \tag{2.48}$$

Then, the differential equation (2.41) is given by

$$\frac{\mathrm{d}M}{\mathrm{d}B} = f_{\mathrm{iJA}}(M, B, \dot{B}) = \frac{\mathrm{d}M/\mathrm{d}B_{\mathrm{e}}}{\mathrm{d}B/\mathrm{d}B_{\mathrm{e}}}, \tag{2.49}$$

where $\mathrm{d}M/\mathrm{d}B_{\mathrm{e}}$ and $\mathrm{d}B/\mathrm{d}B_{\mathrm{e}}$ are obtained by deriving (2.48) and (2.43), respectively,

$$\frac{\mathrm{d}M}{\mathrm{d}B_{\mathrm{e}}} = (1 - c)\,\frac{\mathrm{d}M_{\mathrm{irr}}}{\mathrm{d}B_{\mathrm{e}}} + c\,\frac{M_{\mathrm{an}}}{B_{\mathrm{e}}}, \tag{2.50}$$

$$\frac{\mathrm{d}B}{\mathrm{d}B_{\mathrm{e}}} = 1 + \mu_0\,(1 - \alpha)\,\frac{\mathrm{d}M}{\mathrm{d}B_{\mathrm{e}}}. \tag{2.51}$$

Note that the resulting differential equation can be used to obtain M from B. This is not directly applicable to the proposed models, which depend on macroscopic variables

ϕ and $\mathcal{F}_{\mathrm{c}i}$. Nonetheless, each $\mathcal{F}_{\mathrm{c}i}$ can be defined in terms of the corresponding magnetic flux density $B_{\mathrm{c}i}$ and magnetization $M_{\mathrm{c}i}$,

$$\mathcal{F}_{\mathrm{c}i} = H_{\mathrm{c}i}\, l_{\mathrm{c}i} = \left(\frac{B_{\mathrm{c}i}}{\mu_0} - M_{\mathrm{c}i} \right) l_{\mathrm{c}i}. \tag{2.52}$$

Then, the time derivative of each $\mathcal{F}_{\mathrm{c}i}$ can be defined following the same structure as the magnetic flux differential equation (2.14),

$$\dot{\mathcal{F}}_{\mathrm{c}i} = f_{\mathcal{F}_{\mathrm{c}i}}(z, \phi, \boldsymbol{\mathcal{F}}_{\mathbf{c}}, u) = \left(\frac{1}{\mu_0} - f_{\mathrm{iJA}}(M_{\mathrm{c}i}, B_{\mathrm{c}i}, \dot{B}_{\mathrm{c}i}) \right) l_{\mathrm{c}i}\, \dot{B}_{\mathrm{c}i}, \tag{2.53}$$

where

$$B_{\mathrm{c}i} = \frac{\phi}{A_{\mathrm{c}i}}, \qquad M_{\mathrm{c}i} = \frac{\phi}{\mu_0\, A_{\mathrm{c}i}} - \frac{\mathcal{F}_{\mathrm{c}i}}{l_{\mathrm{c}i}}, \qquad \dot{B}_{\mathrm{c}i} = \frac{f_\phi(z, \phi, \boldsymbol{\mathcal{F}}_{\mathbf{c}}, u)}{A_{\mathrm{c}i}}. \tag{2.54}$$

2.3.3 State-space representation

Full state-space hybrid models can be constructed by incorporating the derived expressions for the magnetic reluctance of the gap (Section 2.3.1) and the magnetomotive forces of the core (Section 2.3.2). Following a state-space representation, any dynamical model is expressed compactly with a dynamical and an output equation,

$$\begin{cases} \dot{\boldsymbol{x}} = \boldsymbol{f}_q(\boldsymbol{x}, u), \\ y = h(\boldsymbol{x}, u). \end{cases} \tag{2.55}$$

The complete continuous state vector is represented by $\boldsymbol{x}$, and its dynamical function—i.e., flow map—is $\boldsymbol{f}_q$, where q is the discrete state variable presented in Section 2.2.3. On the other hand, y and h are the output and its corresponding function, respectively. The input u is an argument of both functions $\boldsymbol{f}_q$ and h.

The models can be categorized based on the characterization of $\mathcal{F}_{\mathrm{c}}$ (Section 2.3.2). Then, the dynamic and output equations (2.55) are specified for each alternative.

Reluctance actuator model based on Fröhlich–Kennelly (RAM-FK)

The first model accounts for magnetic saturation in the core by means of the ϕ—$\mathcal{F}_{\mathrm{c}i}$ relation derived from the FK expression (see Section 2.3.2). This results in the simplest solution, where the state vector is

$$\boldsymbol{x} = \begin{bmatrix} z \\ v \\ \phi \end{bmatrix}. \tag{2.56}$$

The dynamical functions for the motion ($q = 2$) and resting positions ($q = 1$ or $q = 3$) must be

$$\boldsymbol{f}_q(\boldsymbol{x}, u) = \begin{bmatrix} v \\ f_v(z, v, \phi) \\ f_\phi(z, \phi, \boldsymbol{\mathcal{F}}_\mathbf{c}(\phi), u) \end{bmatrix}, \quad \text{if } q = 2, \tag{2.57a}$$

$$\boldsymbol{f}_q(\boldsymbol{x}, u) = \begin{bmatrix} 0 \\ 0 \\ f_\phi(z, \phi, \boldsymbol{\mathcal{F}}_\mathbf{c}(\phi), u) \end{bmatrix}, \quad \text{if } q \neq 2. \tag{2.57b}$$

where the function f_v is described in (2.24), and f_ϕ is (2.12) or (2.14), depending on the input choice.

Then, with some abuse of notation for convenience, the output function in this state-space representation is defined based on its generalized form (2.17),

$$h(\boldsymbol{x}, u) = h\big(z, \phi, \boldsymbol{\mathcal{F}}_\mathbf{c}(\phi), u\big). \tag{2.58}$$

Reluctance actuator model based on Jiles–Atherton (RAM-JA)

A more complete model can be constructed by incorporating the expressions derived from the JA model (see Section 2.3.2), thus accounting for the magnetic hysteresis in the core. Note that, in this case, there is not a one-to-one relation between the magnetomotive forces in the core $\mathcal{F}_{\mathrm{c}i}$ and the magnetic flux ϕ. Instead, all of these terms must be treated as state variables. Thus, the complete continuous state vector is

$$\boldsymbol{x} = \begin{bmatrix} z \\ v \\ \phi \\ \boldsymbol{\mathcal{F}}_\mathbf{c} \end{bmatrix}, \tag{2.59}$$

where the dimension of $\boldsymbol{\mathcal{F}}_\mathbf{c} = \begin{bmatrix} \mathcal{F}_{\mathrm{c}1} & \mathcal{F}_{\mathrm{c}2} & \cdots \end{bmatrix}^\mathsf{T}$ corresponds to the number of distinct core elements, with different cross-sectional areas $A_{\mathrm{c}i}$ and their corresponding lengths $l_{\mathrm{c}i}$.

Consequently, the flow maps for every dynamic mode ($q \in \{1, 2, 3\}$) are

$$\boldsymbol{f}_q(\boldsymbol{x}, u) = \begin{bmatrix} v \\ f_v(z, v, \phi) \\ f_\phi(z, \phi, \boldsymbol{\mathcal{F}}_\mathbf{c}, u) \\ \boldsymbol{f}_{\boldsymbol{\mathcal{F}}_\mathbf{c}}(z, \phi, \boldsymbol{\mathcal{F}}_\mathbf{c}, u) \end{bmatrix}, \quad \text{if } q = 2, \tag{2.60a}$$

$$\boldsymbol{f}_q(\boldsymbol{x}, u) = \begin{bmatrix} 0 \\ 0 \\ f_\phi(z, \phi, \boldsymbol{\mathcal{F}}_\mathbf{c}, u) \\ \boldsymbol{f}_{\boldsymbol{\mathcal{F}}_\mathbf{c}}(z, \phi, \boldsymbol{\mathcal{F}}_\mathbf{c}, u) \end{bmatrix}, \quad \text{if } q \neq 2. \tag{2.60b}$$

where $\boldsymbol{f}_{\boldsymbol{\mathcal{F}}_\mathrm{c}} = \begin{bmatrix} f_{\mathcal{F}_{\mathrm{c}1}} & f_{\mathcal{F}_{\mathrm{c}2}} & \cdots \end{bmatrix}^\mathsf{T}$. Lastly, analogously to (2.58), the output function depends on every state variable except the velocity,

$$h(\boldsymbol{x}, u) = h\big(z, \phi, \boldsymbol{\mathcal{F}}_\mathbf{c}, u\big). \tag{2.61}$$

Both models allow separating the core into multiple parts to calculate their corresponding magnetomotive forces. However, given its increased complexity, its identification and subsequent design and implementation of control strategies is much more challenging. Thus, going forward, only the simpler scenario is considered, in which the core geometry is simplified into a single part, with a total length l_c and an average area A_c, resulting in a single scalar magnetomotive force $\mathcal{F}_\mathrm{c}$.

2.4 Model reduction and identifiability

Although the presented characterization of the magnetic hysteresis is simpler than other state-of-the-art alternatives, the more complete model (RAM-JA) is much more complex than analogous lumped-parameter models that neglect this phenomenon, and the number of parameters is quite large. In order to fit the model to any device, the parameters must be estimated using data from different sources, e.g., measured electrical signals, FEM simulations, or direct measurements of parameters.

Ultimately, identification with only electrical signals is not possible, as even the simpler model (RAM-FK) is over-parameterized. However, by performing various manipulations to the dynamical equations, it is possible to derive equivalent models that depend on smaller sets of parameters, i.e. reduced models.

2.4.1 Reduced models

For these equivalent models, the voltage v_coil and current $\imath_\mathrm{coil}$, being the measurable electrical signals, must remain as input and output—or vice versa. In addition, for convenience, the variables of interest for control applications, the position z and velocity v, are kept as state variables. By contrast, the magnetic flux ϕ and magnetomotive force $\mathcal{F}_\mathrm{c}$ are replaced by auxiliary variables that permits simplifying the dynamical equations.

To improve the readability, the parameters of the electromagnetic models, and their corresponding reduced forms, are summarized in Table 2.1. The superscript $\#$ is used for indicating auxiliary parameters of the reduced models, which replace the corresponding ones from the original models. For clarity, the auxiliary parameters that are identical to the original ones are denoted without the aforementioned superscript.

Table 2.1: Parameters of the electromagnetic subsystem: summary.

(a) RAM-FK.

Original	Reduced
R	R
k_{eddy}	$k^{\#}_{\mathrm{eddy}} = k_{\mathrm{eddy}}/N^2$
$\mathcal{R}_{\mathrm{g},0}$	$\mathcal{R}^{\#}_{\mathrm{g},0} = \mathcal{R}_{\mathrm{g},0}/N^2$
$\mathcal{R}'_{\mathrm{g},0}$	$\mathcal{R}'^{\#}_{\mathrm{g},0} = \mathcal{R}'_{\mathrm{g},0}/N^2$
k_1	k_1
k_2	k_2
$\mathcal{R}_{\mathrm{c},0}$	$\mathcal{R}^{\#}_{\mathrm{c},0} = \mathcal{R}_{\mathrm{c},0}/N^2$
ϕ_{sat}	$\lambda_{\mathrm{sat}} = N\,\phi_{\mathrm{sat}}$
N	

(b) RAM-JA.

Original	Reduced
R	R
k_{eddy}	$k^{\#}_{\mathrm{eddy}} = k_{\mathrm{eddy}}/N^2$
$\mathcal{R}_{\mathrm{g},0}$	$\mathcal{R}^{\#}_{\mathrm{g},0} = \big(\mathcal{R}_{\mathrm{g},0} + l_{\mathrm{c}}/(\mu_0\,A_{\mathrm{c}})\big)/N^2$
$\mathcal{R}'_{\mathrm{g},0}$	$\mathcal{R}'^{\#}_{\mathrm{g},0} = \mathcal{R}'_{\mathrm{g},0}/N^2$
k_1	k_1
k_2	k_2
M_{sat}	$M^{\#}_{\mathrm{sat}} = l_{\mathrm{c}}\,M_{\mathrm{sat}}/N$
b	$b^{\#} = N\,A_{\mathrm{c}}\,b$
c	c
κ	$\kappa^{\#} = N\,A_{\mathrm{c}}\,\kappa$
α	$\alpha^{\#} = N^2\,A_{\mathrm{c}}\,(1-\alpha)/l_{\mathrm{c}}$
N	
A_{c}	
l_{c}	

Reduction of RAM-FK

Regarding the basic model (Section 2.3.3), we propose to replace ϕ with the flux linkage λ. It is a widely used extension of the magnetic flux, and particularly useful for multi-turn coils. It is defined as follows:

$$\lambda = N\,\phi. \tag{2.62}$$

Then, the dynamical equation of the flux linkage is derived from (2.12) or (2.13), depending on the input choice,

$$\dot{\lambda} = f^{\#}_{\lambda}(z,\lambda,u) = -\frac{\big(\mathcal{R}^{\#}_{\mathrm{g}}(z) + \mathcal{R}^{\#}_{\mathrm{c}}(\lambda)\big)\,\lambda}{k^{\#}_{\mathrm{eddy}}} + \frac{1}{k^{\#}_{\mathrm{eddy}}}\,\iota_{\mathrm{coil}}, \tag{2.63}$$

$$\dot{\lambda} = f^{\#}_{\lambda}(z,\lambda,u) = -\frac{R\,\big(\mathcal{R}^{\#}_{\mathrm{g}}(z) + \mathcal{R}^{\#}_{\mathrm{c}}(\lambda)\big)\,\lambda}{1 + R\,k^{\#}_{\mathrm{eddy}}} + \frac{1}{1 + R\,k^{\#}_{\mathrm{eddy}}}\,\upsilon_{\mathrm{coil}}, \tag{2.64}$$

where $u = \iota_{\mathrm{coil}}$ or $u = \upsilon_{\mathrm{coil}}$, respectively. Note that $k^{\#}_{\mathrm{eddy}}$ is a new parameter, defined in Table 2.1. Notice also the dependence on the new functions $\mathcal{R}^{\#}_{\mathrm{g}}$ and $\mathcal{R}^{\#}_{\mathrm{c}}$, related to the reluctance definitions (2.30) and (2.37). Both are defined following the same structure as their standard counterparts,

$$\mathcal{R}^{\#}_{\mathrm{g}}(z) = \mathcal{R}^{\#}_{\mathrm{g},0} + \frac{\mathcal{R}'^{\#}_{\mathrm{g},0}\,z}{1 + k_1\,z\,\ln(k_2/z)}, \qquad \mathcal{R}^{\#}_{\mathrm{c}}(\lambda) = \frac{\mathcal{R}^{\#}_{\mathrm{c},0}}{1 - \lambda/\lambda_{\mathrm{sat}}}. \tag{2.65}$$

Note that the counterpart of ϕ_{sat} is precisely the saturation value of the flux linkage λ, thus it is denoted as λ_{sat}.

With respect to the mechanical part, the dynamical equation of the velocity (2.24) must be modified considering that ϕ and $\mathcal{R}_\mathrm{g}(z)$ have been replaced by λ and $\mathcal{R}_\mathrm{g}^\#(z)$, respectively. The derived expression is

$$\dot{v} = f_v^\#(z, v, \lambda) = \frac{F_\mathrm{pas}(z, v) + F_\mathrm{mag}^\#(z, \lambda)}{m_\mathrm{mov}}, \tag{2.66}$$

where

$$F_\mathrm{mag}^\#(z, \lambda) = -\frac{1}{2}\,\mathcal{R}_\mathrm{g}'^\#(z)\,\lambda^2, \qquad \mathcal{R}_\mathrm{g}'^\#(z) = \frac{\partial \mathcal{R}_\mathrm{g}^\#(z)}{\partial z}. \tag{2.67}$$

Lastly, the new output function is obtained from (2.15) or (2.16), depending on the input choice,

$$y = h^\#(z, \lambda, u) = -\frac{\left(\mathcal{R}_\mathrm{g}^\#(z) + \mathcal{R}_\mathrm{c}^\#(\lambda)\right)\lambda}{k_\mathrm{eddy}^\#} + \frac{1 + R\,k_\mathrm{eddy}^\#}{k_\mathrm{eddy}^\#}\,\iota_\mathrm{coil}, \tag{2.68}$$

$$y = h^\#(z, \lambda, u) = \frac{\left(\mathcal{R}_\mathrm{g}^\#(z) + \mathcal{R}_\mathrm{c}^\#(\lambda)\right)\lambda}{1 + R\,k_\mathrm{eddy}^\#} + \frac{k_\mathrm{eddy}^\#}{1 + R\,k_\mathrm{eddy}^\#}\,\upsilon_\mathrm{coil}, \tag{2.69}$$

where $u = \iota_\mathrm{coil}$ and $y = \iota_\mathrm{coil}$, or $u = \upsilon_\mathrm{coil}$ and $y = \iota_\mathrm{coil}$, respectively.

As a result of the above manipulations, the number of parameters in the dynamical equations of the electromagnetic system (2.64) and (2.63) and output equations (2.68) and (2.69) is reduced. In this simple case, every parameter from the original model has a counterpart in the reduced form, except for the number of coil turns N.

Reduction of RAM-JA

For the reduction of the complete model (Section 2.3.2), we propose to replace the electromagnetic state variables ϕ and $\mathcal{F}_\mathrm{c}$ with the flux linkage λ and the new auxiliary variable $M_\mathrm{c}^\#$, respectively,

$$\lambda = N\,\phi, \qquad M_\mathrm{c}^\# = \frac{l_\mathrm{c}}{N}\,M_\mathrm{c}. \tag{2.70}$$

Analogously to (2.63) or (2.64), the dynamical equation of flux linkage is

$$\dot{\lambda} = f_\lambda^\#(z, \lambda, M_\mathrm{c}^\#, u) = -\frac{\mathcal{R}_\mathrm{g}^\#(z)\,\lambda - M_\mathrm{c}^\#}{k_\mathrm{eddy}^\#} + \frac{1}{k_\mathrm{eddy}^\#}\,\iota_\mathrm{coil}, \tag{2.71}$$

$$\dot{\lambda} = f_\lambda^\#(z, \lambda, M_\mathrm{c}^\#, u) = -\frac{R\left(\mathcal{R}_\mathrm{g}^\#(z)\,\lambda - M_\mathrm{c}^\#\right)}{1 + R\,k_\mathrm{eddy}^\#} + \frac{1}{1 + R\,k_\mathrm{eddy}^\#}\,\upsilon_\mathrm{coil}, \tag{2.72}$$

where the input is $u = \iota_{\mathrm{coil}}$ or $u = v_{\mathrm{coil}}$, respectively. Notice again the auxiliary parameter $k^{\#}_{\mathrm{eddy}}$ and function $\mathcal{R}^{\#}_{\mathrm{g}}$, which are defined in the same way. However, in this case, the constant $\mathcal{R}^{\#}_{\mathrm{g},0}$ is defined differently (see Table 2.1).

Furthermore, the equations (2.44)–(2.53) are tweaked to obtain the dynamical equation of the auxiliary variable $M^{\#}_{\mathrm{c}}$, resulting in the following function:

$$\dot{M}^{\#}_{\mathrm{c}} = f^{\#}_{M_{\mathrm{c}}}(z, \lambda, M^{\#}_{\mathrm{c}}, u) = \frac{\mathrm{d}M^{\#}_{\mathrm{c}}}{\mathrm{d}\lambda}\, f^{\#}_{\lambda}(z, \lambda, M^{\#}_{\mathrm{c}}, u), \tag{2.73}$$

where the intermediary steps are

$$\lambda_{\mathrm{e}} = \lambda - \mu_0\, \alpha^{\#}\, M^{\#}_{\mathrm{c}}, \tag{2.74a}$$

$$M^{\#}_{\mathrm{an}} = M^{\#}_{\mathrm{sat}} \left(\coth\!\left(\frac{\lambda_{\mathrm{e}}}{b^{\#}}\right) - \frac{b^{\#}}{\lambda_{\mathrm{e}}} \right), \tag{2.74b}$$

$$\frac{\mathrm{d}M^{\#}_{\mathrm{an}}}{\mathrm{d}\lambda_{\mathrm{e}}} = \frac{M^{\#}_{\mathrm{sat}}}{b^{\#}} \left(1 - \coth^2\!\left(\frac{\lambda_{\mathrm{e}}}{b^{\#}}\right) + \left(\frac{b^{\#}}{\lambda_{\mathrm{e}}}\right)^2 \right), \tag{2.74c}$$

$$M^{\#}_{\mathrm{irr}} = \frac{M^{\#}_{\mathrm{c}} - c\, M^{\#}_{\mathrm{an}}}{1 - c}, \tag{2.74d}$$

$$\frac{\mathrm{d}M^{\#}_{\mathrm{irr}}}{\mathrm{d}\lambda_{\mathrm{e}}} = \frac{M^{\#}_{\mathrm{an}} - M^{\#}_{\mathrm{irr}}}{\mu_0\, \kappa^{\#}}\, \mathrm{sgn}(\dot{\lambda}), \tag{2.74e}$$

$$\frac{\mathrm{d}M^{\#}_{\mathrm{c}}}{\mathrm{d}\lambda_{\mathrm{e}}} = (1 - c)\, \frac{\mathrm{d}M^{\#}_{\mathrm{irr}}}{\mathrm{d}\lambda_{\mathrm{e}}} + c\, \frac{\mathrm{d}M^{\#}_{\mathrm{an}}}{\mathrm{d}\lambda_{\mathrm{e}}}, \tag{2.74f}$$

$$\frac{\mathrm{d}\lambda}{\mathrm{d}\lambda_{\mathrm{e}}} = 1 + \mu_0\, \alpha^{\#}\, \frac{\mathrm{d}M^{\#}_{\mathrm{c}}}{\mathrm{d}\lambda_{\mathrm{e}}}, \tag{2.74g}$$

$$\frac{\mathrm{d}M^{\#}_{\mathrm{c}}}{\mathrm{d}\lambda} = \frac{\mathrm{d}M^{\#}_{\mathrm{c}}/\mathrm{d}\lambda_{\mathrm{e}}}{\mathrm{d}\lambda/\mathrm{d}\lambda_{\mathrm{e}}}, \tag{2.74h}$$

which, in turn, depend on new auxiliary parameters $M^{\#}_{\mathrm{sat}}$, $b^{\#}$, $\kappa^{\#}$ and $\alpha^{\#}$. Note that these intermediary steps consist in the calculation of values and derivatives of new time-dependent variables: the effective flux linkage,

$$\lambda_{\mathrm{e}} = N\, A_{\mathrm{c}}\, B_{\mathrm{e}}; \tag{2.75}$$

and scaled versions of the anhysteretic and irreversible magnetization,

$$M^{\#}_{\mathrm{an}} = \frac{l_{\mathrm{c}}}{N}\, M_{\mathrm{an}}, \qquad\qquad M^{\#}_{\mathrm{irr}} = \frac{l_{\mathrm{c}}}{N}\, M_{\mathrm{irr}}. \tag{2.76}$$

In relation to the mechanical subsystem, the resulting equations are exactly the same as in the reduction of RAM-FK (2.66) and (2.67). And, finally, the new output function

is, depending on the input choice,

$$y = h^{\#}(z, \lambda, M_{\mathrm{c}}^{\#}, u) = -\frac{\mathcal{R}_{\mathrm{g}}^{\#}(z)\,\lambda - M_{\mathrm{c}}^{\#}}{k_{\mathrm{eddy}}^{\#}} + \frac{1 + R\,k_{\mathrm{eddy}}^{\#}}{k_{\mathrm{eddy}}^{\#}}\,\iota_{\mathrm{coil}}, \tag{2.77}$$

$$y = h^{\#}(z, \lambda, M_{\mathrm{c}}^{\#}, u) = \frac{\mathcal{R}_{\mathrm{g}}(z)\,\lambda - M_{\mathrm{c}}^{\#}}{1 + R\,k_{\mathrm{eddy}}^{\#}} + \frac{k_{\mathrm{eddy}}^{\#}}{1 + R\,k_{\mathrm{eddy}}^{\#}}\,\upsilon_{\mathrm{coil}}, \tag{2.78}$$

where $u = \iota_{\mathrm{coil}}$ and $y = \iota_{\mathrm{coil}}$, or $u = \upsilon_{\mathrm{coil}}$ and $y = \iota_{\mathrm{coil}}$, respectively.

As a consequence, the number of parameters in the dynamical equations of the electromagnetic system (2.71) and (2.72) and output equations (2.77) and (2.78) is reduced by three. Specifically, the number of coil turns N, the average core section area A_{c} and the core length l_{c} are used for defining new auxiliary parameters, but they do not have counterparts in the reduced model.

2.4.2 Identifiability analyses

A local structural identifiability analysis is performed to demonstrate that the reduced models are identifiable with only electrical signals, and no further reductions are possible. The models are quite complex for this type of analysis, so it is convenient to separate them into the electromagnetic and mechanical subsystems. As the novel ideas of the proposal are in the electromagnetic subsystem, this analysis is focused on that part. Thus, the position is assumed to be fixed, effectively nullifying the mechanical subsystem[1].

For a local identifiability analysis, an observability-identifiability matrix is constructed. For a given instant, output derivatives are derived as functions of the variables, parameters, and input derivatives.

Identifiability of RAM-FK

Formally, the expression for each output derivative can be obtained recursively.

$$y^{(i+1)} = \frac{\partial y^{(i)}}{\partial \lambda}\, f_{\lambda}^{\#}(\cdot) + \sum_{j=1}^{i} \frac{\partial y^{(i)}}{\partial u^{(j)}}\, u^{(j)}, \tag{2.79}$$

being $y^{(0)} = h^{\#}(\cdot)$ from (2.68) or (2.69). Then, a vector of outputs is constructed,

$$Y(\boldsymbol{\theta}) = \begin{bmatrix} y^{(0)} & y^{(1)} & \cdots & y^{(5)} \end{bmatrix}^{\mathsf{T}}, \tag{2.80}$$

where $\boldsymbol{\theta}$ is the vector of unknown variables and parameters,

$$\boldsymbol{\theta} = \begin{bmatrix} \lambda & R & k_{\mathrm{eddy}}^{\#} & \mathcal{R}_{\mathrm{c},0}^{\#} & \lambda_{\mathrm{sat}} & \mathcal{R}_{\mathrm{g}}^{\#} \end{bmatrix}^{\mathsf{T}}. \tag{2.81}$$

[1]Note that the gap reluctance depends on the position. In practice, to fully identify that part of the model, the identification process should be performed for several fixed positions.

Note that, as the position is assumed to be fixed, the gap reluctance $\mathcal{R}_\mathrm{g}$ is considered here an unknown constant. Then the Jacobian $\boldsymbol{J}$ of Y (2.80) should be constructed, where each element is

$$J_{ij}(\boldsymbol{\theta}) = \frac{\partial Y_i}{\partial \theta_j}, \tag{2.82}$$

Then the model is locally identifiable for $\boldsymbol{\theta}^*$ if the Jacobian $\boldsymbol{J}$, evaluated at $\boldsymbol{\theta} = \boldsymbol{\theta}^*$ has full rank. Using a computer algebra system, the full-rank condition of the symbolic matrix can be checked, concluding that the reduced electromagnetic model is structurally locally identifiable. Furthermore, for a specific case, values can be given to the variables and parameters to numerically check the rank of $\boldsymbol{J}$.

Identifiability of RAM-JA

Analogously to (2.79), the time-derivatives of the output are derived recursively as follows:

$$y^{(i+1)} = \frac{\partial y^{(i)}}{\partial \lambda}\, f_\lambda^\#(\cdot) + \frac{\partial y^{(i)}}{\partial M_\mathrm{c}^\#}\, f_{M_\mathrm{c}}^\#(\cdot) + \sum_{j=1}^{i} \frac{\partial y^{(i)}}{\partial u^{(j)}}\, u^{(j)}, \tag{2.83}$$

being $y^{(0)} = h^\#(\cdot)$ from (2.77) or (2.78). Then, a vector of outputs is constructed,

$$Y(\boldsymbol{\theta}) = \begin{bmatrix} y^{(0)} & y^{(1)} & \cdots & y^{(9)} \end{bmatrix}^\mathsf{T}, \tag{2.84}$$

where $\boldsymbol{\theta}$ is the vector of unknown variables and parameters.

$$\boldsymbol{\theta} = \begin{bmatrix} \lambda & M_\mathrm{c}^\# & R & k_\mathrm{eddy}^* & M_\mathrm{sat}^* & b^* & c & \kappa^* & \alpha^* & \mathcal{R}_\mathrm{g}^* \end{bmatrix}^\mathsf{T}. \tag{2.85}$$

As before, the rank of a Jacobian of Y (2.84) should be evaluated. However, constructing and evaluating the rank of such a large matrix is intractable. To circumvent this problem, the particularities of the proposed model can be exploited to reduce the complexity of the problem.

The electromagnetic variables are λ and $M_\mathrm{c}^\#$. While $M_\mathrm{c}^\#$ is a hidden variable, λ can be assumed known because it can be directly estimated from the electrical signals, as explained in [21] and [31].

Then, it is easy to prove that the internal resistance of the coil R is identifiable independently of the other model parameters. Assuming that υ_coil, ι_coil, $\dot{\lambda}$ are known, it can be directly calculated from (2.1). E.g., in a steady state, it is simply

$$R = \upsilon_\mathrm{coil}/\iota_\mathrm{coil}, \qquad \text{if } \dot{\lambda} = 0. \tag{2.86}$$

Moreover, consider the following differential equation, derived from the output function $h^\#$:

$$\mathrm{d}y = \left(\frac{\partial h^\#}{\partial \lambda}\, f_\lambda^\#(\cdot) + \frac{\partial h^\#}{\partial M_\mathrm{c}^\#}\, f_{M_\mathrm{c}}^\#(\cdot) \right) \mathrm{d}t + \frac{\partial h^\#}{\partial u}\, \mathrm{d}u. \tag{2.87}$$

Evidently, a step in the input results in a step in the output, dependent only on the second addend. This can be checked in the limit as $\mathrm{d}t$ tends to zero. Then, from (2.77) or (2.78), R and $k^{\#}_{\mathrm{eddy}}$ can be related to the ratio of steps in the voltage and current, regardless on the input choice. Specifically,

$$\lim_{\mathrm{d}t\to 0} \frac{\mathrm{d}v_{\mathrm{coil}}}{\mathrm{d}\iota_{\mathrm{coil}}} = \frac{1 + R\, k^{\#}_{\mathrm{eddy}}}{k^{\#}_{\mathrm{eddy}}}. \tag{2.88}$$

Therefore, the value of $k^{\#}_{\mathrm{eddy}}$ can be uniquely calculated from the electrical signals and R, which is also known.

As R, $k^{\#}_{\mathrm{eddy}}$ and λ are assumed known, the new parameter vector has seven elements,

$$\boldsymbol{\theta}' = \begin{bmatrix} M^{\#}_{\mathrm{c}} & M^{\#}_{\mathrm{sat}} & b^{\#} & c & \kappa^{\#} & \alpha^{\#} & \mathcal{R}^{\#}_{\mathrm{g}} \end{bmatrix}^{\mathsf{T}}. \tag{2.89}$$

Still, the symbolic computation of seven consecutive derivatives is memory intensive. To further simplify the process, we can consider that there is one step in the input so that the flux changes direction. Formally, it can be expressed as

$$y^{\pm} = h^{\#}(z, \lambda, M^{\#}_{\mathrm{c}}, u^{\pm}), \qquad \operatorname{sgn}(\dot{\lambda}^{-}) \neq \operatorname{sgn}(\dot{\lambda}^{+}), \tag{2.90}$$

where $u^{\pm}$, $y^{\pm}$ and $\lambda^{\pm}$ are the input, output and flux linkage derivative immediately before $(-)$ and after $(+)$ the step. This distinction is usually useless for identifiability analysis of dynamical models, as they do not add new information to determine the unknown parameters and variables. However, in this case, the dynamic behavior of M_{c} changes with the sign of the magnetic flux (2.47). Thus, it is possible to construct an output vector with smaller derivatives,

$$Y^{\pm}(\boldsymbol{\theta}') = \begin{bmatrix} y^{+(0)} & y^{-(1)} & y^{+(1)} & y^{-(2)} & y^{+(2)} & y^{-(3)} & y^{+(3)} \end{bmatrix}^{\mathsf{T}}. \tag{2.91}$$

Then the model is locally identifiable for $\boldsymbol{\theta}^*$ if the Jacobian $\boldsymbol{J}$,

$$J_{ij}(\boldsymbol{\theta}') = \frac{\partial Y^{\pm}_i}{\partial \theta'_j}, \tag{2.92}$$

evaluated in $\boldsymbol{\theta}' = \boldsymbol{\theta}^*$, has full rank. Given the proposed simplifications, this can be checked easily by using a computer algebra system. Equivalently to RAM-FK, the symbolic matrix is full-rank, so the proposed reduced electromagnetic model is structurally locally identifiable.

2.5 Model fitting and comparison

The presented models introduce two new ideas with respect to previous works: the gap reluctance approximation, and the characterization of the magnetic hysteresis. To show

the adequacy of these proposals, they are identified using data from an actual reluctance actuator, and the results are evaluated with respect to a state-of-the-art alternative [42].

The device is a plunger-type solenoid valve, as shown in Fig. 2.6. It has a cylindrically symmetrical steel core, where the fixed part is the stator and the plunger is the mover. There are essentially two gaps between these parts: one below the plunger—whose length is equal to the plunger position—and one around the plunger—whose length is constant. It has a single copper coil wrapped around the core, whose current generates a magnetic flux through the core parts and the air gap between them that, in turn, generates a magnetic force. It also has a coil spring designed for compression, which generates an elastic force. These forces act in opposing directions, resulting in two types of operation: in a making operation, the gap is closed via the magnetic force; whereas in a breaking operation, the gap is opened by reducing the magnetic force and allowing the spring force to move the plunger.

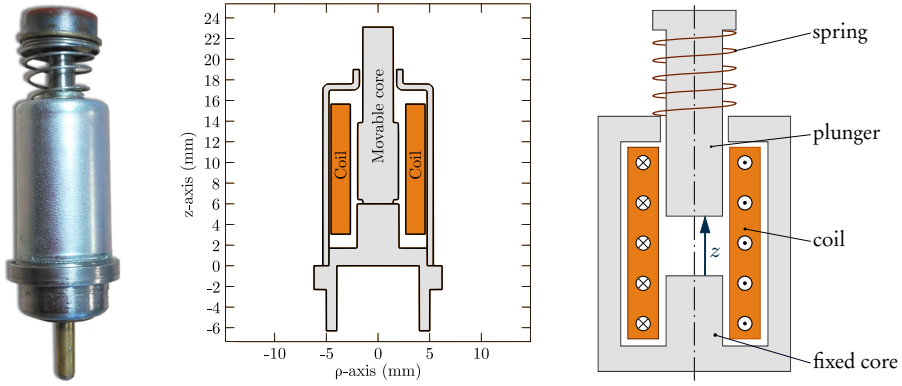

(a) Photo. **(b)** Longitudinal section. **(c)** Schematic representation.

Figure 2.6: Solenoid valve.

Regarding the fitting process and comparison, only the parameters related to the gap reluctance and the magnetization curve are estimated, while the common mechanical and electromagnetic parameters of all models are assumed to be known (see Table 2.2). For this device, the passive force is primarily generated by a spring. Then, assuming an ideal spring, it is defined as

$$F_{\mathrm{pas}}(z, v) = k_{\mathrm{sp}}\,(z - z_{\mathrm{sp}}), \tag{2.93}$$

where k_{sp} and z_{sp} is the spring stiffness and resting position, respectively.

Note that, in this case, identifying the original models is equivalent to identifying the reduced models because there are enough known parameters. Thus, for clarity, the fitting process is performed for the original model forms, as presented in Sections 2.2 and 2.3.

Table 2.2: Known parameters.

Parameter	Value	
N	1200	
k_{eddy}	1630	Ω^{-1}
l_{c}	0.055	m
A_{c}	1.26×10^{-5}	m^2
γ	0	

Parameter	Value	
m_{mov}	1.6×10^{-3}	kg
k_{sp}	55	N/m
z_{sp}	0.015	m
$z_{\min}$	0	m
$z_{\max}$	9×10^{-4}	m

2.5.1 Gap reluctance

The gap reluctance and its derivative have been previously characterized for different positions from FEM simulations using the software COMSOL Multiphysics and the geometry presented in Fig. 2.6b [34]. In order to make use of these data in simulations with the dynamical model, the reluctance for any feasible position can be approximated through some type of interpolation. Alternatively, the proposed algebraic expression (2.30) can be used. In that case, its parameters must be fitted.

Given the parameter vector,

$$\boldsymbol{\theta} = \begin{bmatrix} \mathcal{R}_{\text{g},0} & \mathcal{R}'_{\text{g},0} & k_1 & k_2 \end{bmatrix}^{\mathsf{T}}, \tag{2.94}$$

the objective is to find the one that minimizes the errors of both $\mathcal{R}_{\text{g}}$ and $\mathcal{R}'_{\text{g}}$. Formally, it is expressed as

$$\min_{\boldsymbol{\theta}} \Big({\text{NRMSE}_{\mathcal{R}_{\text{g}}}}^2 + {\text{NRMSE}_{\mathcal{R}'_{\text{g}}}}^2 \Big), \tag{2.95}$$

where $\text{NRMSE}_{\mathcal{R}_{\text{g}}}$ is the normalized root-mean-square error of the simulated values ${\mathcal{R}_{\text{g}}}^{\text{sim}}$ with respect the experimental ones ${\mathcal{R}_{\text{g}}}^{\text{exp}}$,

$$\text{NRMSE}_{\mathcal{R}_{\text{g}}} = \sqrt{\frac{\sum_i \left({\mathcal{R}_{\text{g}}}_i^{\text{sim}} - {\mathcal{R}_{\text{g}}}_i^{\text{exp}} \right)^2}{\sum_i \left({\mathcal{R}_{\text{g}}}_i^{\text{exp}} \right)^2}}, \tag{2.96}$$

and $\text{NRMSE}_{\mathcal{R}'_{\text{g}}}$ is defined in an equivalent manner. The optimized parameters are presented in Table 2.3.

Table 2.3: Estimated parameters of the gap reluctance model.

Parameter	Value	
$\mathcal{R}_{\text{g},0}$	5.594×10^6	H^{-1}
$\mathcal{R}'_{\text{g},0}$	1.105×10^{11}	H^{-1}/m
k_1	1318	m^{-1}
k_2	9.735×10^{-3}	m

Fig. 2.7 shows that the algebraic expression with the fitted parameters matches very well the experimental data. Specifically, the errors are

$$\mathrm{NRMSE}_{\mathcal{R}_\mathrm{g}} = 0.436\,\%, \qquad \mathrm{NRMSE}_{\mathcal{R}'_\mathrm{g}} = 0.226\,\%. \tag{2.97}$$

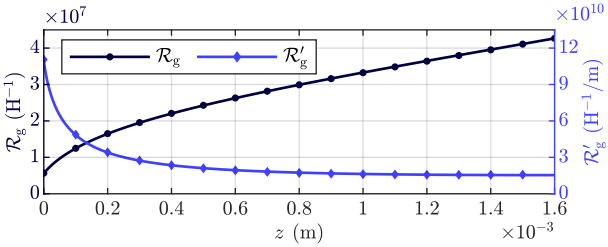

Figure 2.7: Gap reluctance and its derivative with respect to the armature position. The markers represent the experimental data and the lines represent the approximated results.

2.5.2 Magnetic hysteresis and saturation

The most novel modeling idea is the characterization of the magnetic hysteresis and saturation in RAM-JA. To identify this part of the model, the curve ι_coil–λ is fitted using the same measurements as [42]. The experimental setup consists of a 4-quadrant power supplier (Toellner TOE 7621), a current probe (Tektronix TCP312A) with its corresponding amplifier (TCPA300), a USB oscilloscope with an arbitrary waveform generator (Picoscope 4824), a computer with MATLAB and the Instrument Control Toolbox installed, and the solenoid valve (Fig. 2.6). As only the electromagnetic subsystem is being fitted, the plunger position of the valve is fixed ($z = z_\mathrm{min}$). Voltage signals are constructed in MATLAB, which are then sent out to the waveform generator of the USB oscilloscope. The generated signal is amplified by the power supplier and applied to the solenoid valve. The applied signals are pulse waves with a frequency of 10 Hz and several amplitudes (1 V, 2 V, 4 V, 6 V, 9 V). The applied voltage and current signals are measured with the oscilloscope at a sampling rate of 100 kHz and sent to the computer. They are depicted in Fig. 2.8. Then, from those measurements, the magnetic flux is estimated following the method presented in [31].

Given the vector of parameters,

$$\boldsymbol{\theta} = \begin{bmatrix} M_\mathrm{sat} & b & c & \kappa & \alpha \end{bmatrix}^\mathsf{T}, \tag{2.98}$$

the objective is to find the one that minimizes the errors of the simulated signals ϕ and ι_coil, which are obtained by using the measured voltage signals as input u. Formally, the optimization problem is formulated as

$$\min_{\boldsymbol{\theta}} \left(\mathrm{wNRMSE}_{\phi,|\dot{\phi}|}{}^2 + \mathrm{wNRMSE}_{\iota_\mathrm{coil},|\dot{\phi}|}{}^2 \right), \tag{2.99}$$

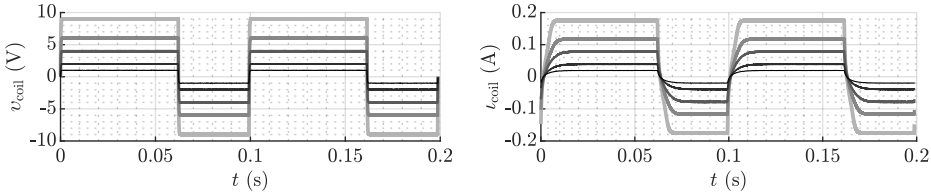

(a) Measured voltage. **(b)** Measured current.

Figure 2.8: Experimental signals used for model fitting.

where $\text{wNRMSE}_{\phi,|\dot{\phi}|}$ is the weighted normalized root-mean-square error of ϕ, with $|\dot{\phi}|$ acting as the weight,

$$\text{wNRMSE}_{\phi,|\dot{\phi}|} = \sqrt{\frac{\sum_i |\dot{\phi}_i^{\text{exp}}| \, (\phi_i^{\text{sim}} - \phi_i^{\text{exp}})^2}{\sum_i |\dot{\phi}_i^{\text{exp}}| \, (\phi_i^{\text{exp}})^2}}, \tag{2.100}$$

and $\text{wNRMSE}_{\iota_{\text{coil}},|\dot{\phi}|}$ is defined equivalently. Note that $|\dot{\phi}|$ is used as the weight in order to avoid overfitting the slowly varying intervals (especially the steady-state intervals in which $\dot{\phi} = 0$).

The optimization process results in the parameter values presented in Table 2.4b. The simulated results fit fairly well the experimental data, as shown in Fig. 2.9b. For a comprehensive comparison, the parameter fitting procedure is executed in the same manner for RAM-FK, resulting in the parameter values of Table 2.4a. As expected, there is a much more noticeable mismatch between the simulated and experimental curves. Notice in Fig. 2.9a that there is an apparent hysteretic behavior. However, it is completely due to the eddy currents, as the model does not include magnetic hysteresis. Lastly, for reference, the GPM from [42], which is much more computationally demanding, has also been fitted using the same procedure, and the simulated data is represented in Fig. 2.9c. There is no significant improvement over the proposed complete model. To summarize the simulation results, the average errors $\text{wNRMSE}_{\lambda,|\dot{\lambda}|}$ and $\text{wNRMSE}_{\iota_{\text{coil}},|\dot{\lambda}|}$ are presented in Table 2.5.

Table 2.4: Estimated parameters of the magnetic saturation and hysteresis models.

(a) RAM-FK.

Parameter	Value
$\mathcal{R}^{\#}_{\text{c},0}$	1.950×10^{6} H^{-1}
ϕ_{sat}	1.907×10^{-5} Wb

(b) RAM-JA.

Parameter	Value
M_{sat}	1.45×10^{6} A/m
b	2.45×10^{-3} T
c	0.736
κ	943 A/m
α	3.66×10^{-3}

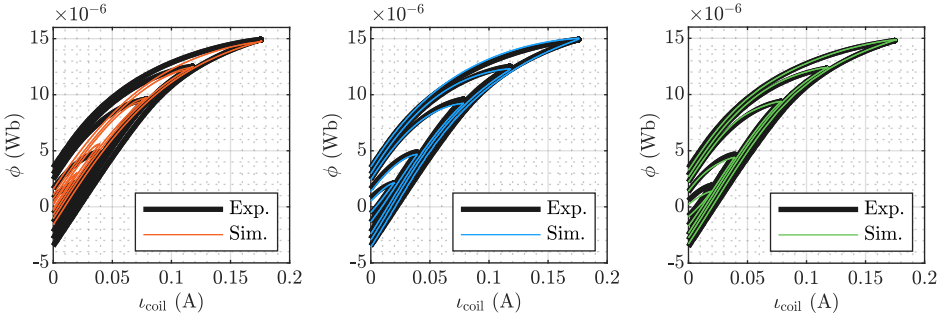

(a) RAM-FK. **(b)** RAM-JA. **(c)** RAM-GP.

Figure 2.9: Experimental and simulated ι_{coil}–ϕ curves.

Table 2.5: Model comparison.

	$\text{NRMSE}_{\lambda,\lvert\dot{\lambda}\rvert}$	$\text{NRMSE}_{\iota_{\text{coil}},\lvert\dot{\lambda}\rvert}$
RAM-FK	9.536 %	11.752 %
RAM-JA	2.055 %	3.218 %
RAM-GP	2.671 %	2.104 %

2.5.3 Model comparison

The main advantage of the proposed models is their low computational requirements. To justify this statement, simulations are performed with the full dynamical models, including their mechanical subsystem. Thus, the plunger is allowed to move between its position limits $z_{\min}$ and $z_{\max}$. Note that the coefficient of restitution is set to zero—in accordance to the discussion in Section 2.2.3—so collisions are assumed to be perfectly inelastic. The proposals RAM-FK and RAM-JA use the reluctance gap approximation presented in Section 2.3.1, while RAM-GP directly interpolates from the experimental data (see Fig. 2.7). For this comparison, the parameters from Table 2.4 are fine-tuned to fit the simulated current and magnetic flux using the RAM-GP (see Fig 2.9c), following the same procedure as in Section 2.5.2.

Then, the simulations are carried out by using as input a voltage signal with four rectangular pulses (see Fig. 2.10a). The current is calculated as the output and plotted in Fig. 2.10b. Then, the state variables magnetic flux, magnetomotive force of the core and plunger position are displayed in Figs. 2.10c, 2.10d and 2.10e, respectively. Note that, for RAM-FK, the magnetomotive force is not a state variable, because it is directly calculated as a function of the magnetic flux. Nonetheless, it is included in Fig 2.10d. As expected, the larger discrepancy corresponds to the RAM-FK simulations with respect to the other more complex models. In contrast, the simulated current and state variables of RAM-JA and RAM-GP match fairly well.

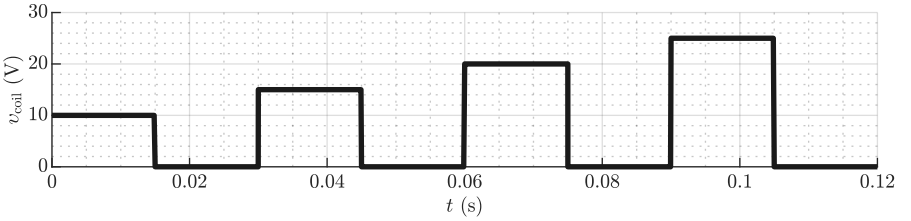

(a) Voltage (input).

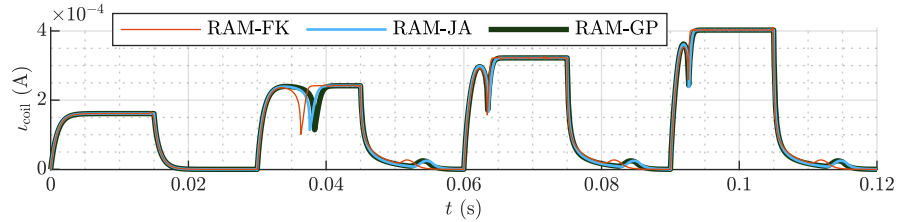

(b) Current (output).

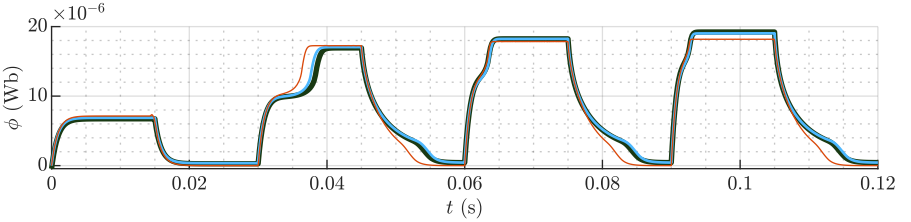

(c) Magnetic flux.

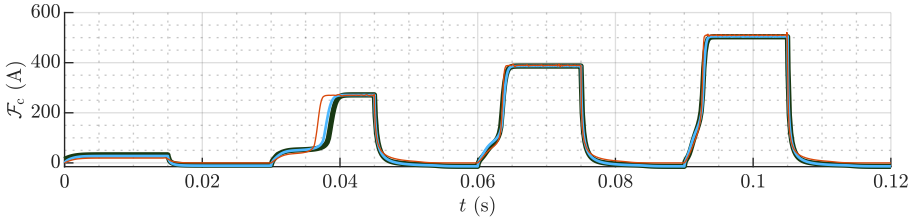

(d) Magnetomotive force in the core.

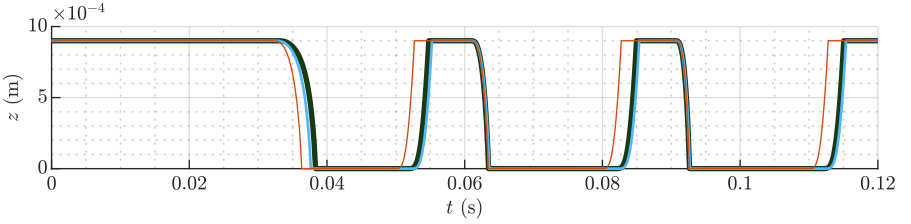

(e) Position.

Figure 2.10: Simulation results. The first voltage pulse is not sufficient to displace the mover.

The simulations are performed using MATLAB standard variable-step ordinary differential equation solver, `ode45`—which uses the Runge–Kutta Dormand–Price method [58]—with default options; and a computer with a 2.4GHz Intel Core i7-5500 CPU. After 1000 repetitions, the mean computation time of RAM-GP is $209.37\,\mathrm{ms}$. In contrast, the mean computation time of RAM-FK and RAM-JA are $14.37\,\mathrm{ms}$ and $26.06\,\mathrm{ms}$, respectively. This last comparison shows the main advantage of RAM-JA over RAM-GP.

2.6 Discussion

We have proposed dynamical models of reluctance actuators, characterizing both mechanical and electromagnetic dynamics. They are lumped-parameter models that account for the most relevant electromagnetic phenomena: magnetic saturation, flux fringing, eddy currents and, optionally, magnetic hysteresis. They are state-space representations, where every differential equation can be computed analytically. Thus, it can be used for designing observers or controllers with state-of-the-art techniques.

After some assumptions and simplifications, the generalized models are reduced to two distinct ones. For the simpler model, the FK relation is adapted, accounting for magnetic saturation, but neglecting magnetic hysteresis. This model is the least accurate one, but its simplicity is advantageous for designing and implementing algorithms, e.g., for identification, estimation or control. On the other hand, the more complete model adapts the JA theory, accounting for both magnetic saturation and hysteresis. It is an efficient alternative to the state-of-the-art reluctance actuator model [42], which adapts the GPM to describe the magnetic hysteresis. In the end, there is always a compromise between computational complexity and accuracy. Thus, the best model choice depends on several factors, e.g., the actuator characteristics, the type of controller or estimator and the implementation requirements.

Chapter 3

Optimal Control Design

This chapter presents a novel design method of position trajectories and input signals for soft-landing control. The solutions are derived from optimal control problems that consider uncertainty in the contact position. The results show a significant improvement relative to past deterministic solutions.

3.1 Introduction

The design of a tracking trajectory and its corresponding input signal is a key point for both feedback and feedforward control. The generation of trajectories is discussed in previous works for different actuators, and it is common to assume that errors in models, observers and measurements are negligible. On that assumption, soft landing is achieved by setting the final velocity and acceleration to zero, as bound conditions. Trajectory planning is therefore focused on finding feasible solutions [59]–[61] or on optimizing some particular variables, e.g. transition time [62] or mean power consumption [63]. However, in practice, and especially for low-cost actuators, the system representation is not perfect and therefore the generated optimal input signals do not result in real soft landing when the control is implemented.

In this chapter, a novel approach for soft-landing trajectory design and open-loop control is developed. Probability functions are incorporated in the optimal control problem for trajectory planning. Specifically, the contact position is assumed to be a random variable, and the soft-landing optimal control is formulated in order to minimize the expectations of the contact velocity and acceleration. Furthermore, the advantages of utilizing the electrical current as the control input for reluctance actuators are discussed and, in consequence, the optimization of the current signal is included in the formulation of the problem. Simulated and experimental tests have been carried out to analyze the applicability of the designed trajectories in an open-loop controller and the improvement due to the inclusion of uncertainty.

3.2 Problem statement

The first step of the proposed method is the definition of the motion dynamics. The proposed representation is a generalized lumped parameter model, accounting for the mechanical subsystem and additional dynamics influencing the system. It is expressed as a set of two or more differential equations,

$$\dot{z} = v, \tag{3.1a}$$

$$\dot{v} = f_v(z, v, \boldsymbol{\vartheta}, \boldsymbol{u}), \tag{3.1b}$$

$$\dot{\boldsymbol{\vartheta}} = \boldsymbol{f}_{\boldsymbol{\vartheta}}(z, v, \boldsymbol{\vartheta}, \boldsymbol{u}), \tag{3.1c}$$

where z and v are the position and velocity of the movable part. Additional state variables are condensed in the vector $\boldsymbol{\vartheta} \in \mathbb{R}^{n-2}$, being $n \geq 2$ the order of the dynamical system. The input vector $\boldsymbol{u}$ may affect directly the acceleration $\dot{v}$ or the dynamics of $\boldsymbol{\vartheta}$, which in turn influences $\dot{v}$. Note that the model is general enough to represent a wide range of switch-type devices. For example, apart from reluctance actuators, this model form can be used for microelectromechanical system switches, for which there is also a great interest and extensive literature regarding soft landing [64]–[68].

To simplify later expressions, the set of equations (3.1) is expressed compactly as

$$\dot{\boldsymbol{x}} = \boldsymbol{f}(\boldsymbol{x}, \boldsymbol{u}), \tag{3.2}$$

where the state vector $\boldsymbol{x} \in \mathbb{R}^n$ is

$$\boldsymbol{x} = \begin{bmatrix} z \\ v \\ \boldsymbol{\vartheta} \end{bmatrix}. \tag{3.3}$$

Secondly, the soft-landing trajectory planning is formulated as a standard optimal control problem, where the cost is a functional of a scalar function $\mathcal{V}$ of the state and the input, i.e.

$$J = \int_{t_0}^{t_\mathrm{f}} \mathcal{V}\big(\boldsymbol{x}(t), \boldsymbol{u}(t)\big)\, \mathrm{d}t, \tag{3.4}$$

where t_0 and t_f are the initial and final time, respectively. The definition of $\mathcal{V}$ for soft landing is specified in Section 3.3. The optimization problem is then solved via Pontryagin's Minimum Principle [69]. Provided that $\boldsymbol{\beta} \in \mathbb{R}^n$ is the costate vector and the Hamiltonian is

$$\mathcal{H}\big(\boldsymbol{x}, \boldsymbol{\beta}, \boldsymbol{u}\big) = \mathcal{V}(\boldsymbol{x}, \boldsymbol{u}) + \boldsymbol{\beta}^\mathsf{T} \boldsymbol{f}\big(\boldsymbol{x}, \boldsymbol{u}\big), \tag{3.5}$$

the optimal control $\boldsymbol{u}^*$ must satisfy the following condition:

$$\boldsymbol{u}^* = \boldsymbol{u}^*\big(\boldsymbol{x}^*, \boldsymbol{\beta}^*\big) \quad \text{such that } \mathcal{H}\big(\boldsymbol{x}^*, \boldsymbol{\beta}^*, \boldsymbol{u}^*\big) \leq \mathcal{H}\big(\boldsymbol{x}^*, \boldsymbol{\beta}^*, \boldsymbol{u}\big),\ \forall \boldsymbol{u} \in \boldsymbol{\mathcal{U}}, \tag{3.6}$$

where $\boldsymbol{x}^*$ and $\boldsymbol{\beta}^*$ are the optimal state and costate vectors, and $\boldsymbol{\mathcal{U}}$ is the set of permissible values for $\boldsymbol{u}$. Then, the optimal control problem is reformulated as a two-point boundary

value problem (BVP), with the differential equations for the optimal state and costate vectors,

$$\dot{\boldsymbol{x}}^* = \boldsymbol{f}\big(\boldsymbol{x}^*, \boldsymbol{u}^*(\boldsymbol{x}^*, \boldsymbol{\beta}^*)\big), \qquad \dot{\boldsymbol{\beta}}^* = -\frac{\partial \mathcal{H}\big(\boldsymbol{x}^*, \boldsymbol{\beta}^*, \boldsymbol{u}^*(\boldsymbol{x}^*, \boldsymbol{\beta}^*)\big)}{\partial \boldsymbol{x}^*}, \tag{3.7a}$$

subject to a set of $2\,n$ boundary conditions. The initial time t_0 is defined as the beginning of the motion (takeoff) from the initial position z_0. So, the corresponding boundary conditions must be

$$z(t_0) = z_0, \qquad \dot{z}(t_0) = v(t_0) = 0, \qquad \ldots, \qquad z^{(n-1)}(t_0) = 0. \tag{3.8}$$

Given the assumption that the model is a perfect representation of the dynamical system, soft landing could be achieved by setting to zero the final velocity $v(t_\mathrm{f})$—and higher position derivatives if $n > 2$—as boundary conditions. However, the model is always a simplification of the system. To account for expected uncertainty and obtain a more conservative trajectory, the actual contact position is assumed a random variable Z_c. Since the contact position is random, so it is the contact instant T_c, velocity V_c and other state variables, and hence they cannot be set as boundary conditions. Therefore, the boundary conditions for $t = t_\mathrm{f}$ correspond to a free-final state, except for the final position, which is set to z_f,

$$z(t_\mathrm{f}) = z_\mathrm{f}, \qquad \beta_2(t_\mathrm{f}) = 0, \qquad \ldots, \qquad \beta_n(t_\mathrm{f}) = 0. \tag{3.9}$$

As the actual contact position is unknown, the solution does not terminate when $z = Z_\mathrm{c}$. Instead, the choice of z_f establishes the probability that the contact occurs before t_f. For example, in the case that the contact position is a normal deviate ($Z_\mathrm{c} \sim \mathcal{N}(\mu_z, \sigma_z^2)$), the final position could be set as its expectation μ_z, which means that there would be a $50\,\%$ probability of $T_\mathrm{c} \leq t_\mathrm{f}$. Alternatively, setting $z_\mathrm{f} = \mu_z + 3\,\mathrm{sgn}(V_\mathrm{c})\,\sigma_z$ would guarantee a contact with a $99.87\,\%$ confidence. This is preferable because, by definition, the trajectories beyond t_f are not optimized. Note also that the differential equation (3.2) represents the unconstrained system dynamics assuming the contact has not happened yet ($t < T_\mathrm{c}$). As the contact velocity is not affected by the dynamics after that event, there is no need to consider the dynamical system for the case $t > T_\mathrm{c}$. In other words, it is not necessary to take into account the hybrid dynamics of the switch-type actuator, as in Section 2.2.3.

3.3 Soft-landing cost functional

In this section, a cost J is defined to obtain an optimal position trajectory and its correspondent input signal, given the assumption that the contact position is random. The total cost functional is divided into several terms J_i,

$$J = \sum_i J_i = \sum_i \int_{t_0}^{t_\mathrm{f}} \mathcal{V}_i\big(\boldsymbol{x}(t), \boldsymbol{u}(t)\big)\,\mathrm{d}t, \tag{3.10}$$

and each function $\mathcal{V}_i$ is defined in Sections 3.3.1, 3.3.2 and 3.3.3.

In many devices, there are two asymmetrical switching operations, depending on the direction of movement. The optimal control problem is formulated to be solved separately for each operation type. Nevertheless, the following reasoning and expressions are generalized in order to be used for both.

3.3.1 Expected contact velocity

In an elastic collision, the bouncing velocity depends on the velocity just before contact. Therefore, to reduce both impact forces and bouncing, the contact velocity should be minimized. The contact velocity is a function of a random variable, and thus its actual value is unknown. However, its expected value can be expressed as a conditional expectation and calculated based on some reasonable assumptions.

Assumption 3.1. *The actual contact position is a random variable Z_c with a probability density function (PDF) ρ_{Z_c} that is continuously differentiable on the time interval,*

$$\exists\, \frac{\partial^2 \rho_{Z_\mathrm{c}}(z)}{\partial z^2},\ \forall z(t) \quad \text{such that } t \in [t_0,\, t_\mathrm{f}]. \tag{3.11}$$

Assumption 3.2. *The position is a monotonic function of time during the interval. Specifically, it may be nondecreasing,*

$$z(t_1) \leq z(t_2),\ \forall t_1, t_2 \quad \text{such that } t_0 \leq t_1 \leq t_2 \leq t_\mathrm{f}, \tag{3.12}$$

or nonincreasing,

$$z(t_1) \geq z(t_2),\ \forall t_1, t_2 \quad \text{such that } t_0 \leq t_1 \leq t_2 \leq t_\mathrm{f}, \tag{3.13}$$

Assumption 3.2 might seem restrictive, but it is completely reasonable. If it is not satisfied, there would be at least one time interval in which the movable part goes backward, away from the final position. This is clearly not an expected behavior in an optimal trajectory.

Lemma 3.1. *The contact instant T_c is a random variable whose PDF is*

$$\rho_{T_\mathrm{c}}(t) = \big|v(t)\big|\, \rho_{Z_\mathrm{c}}\big(z(t)\big). \tag{3.14}$$

Proof. Since the contact position is a random variable, the contact instant T_c is also random,

$$T_\mathrm{c} = \big(t \mid z(t) = Z_\mathrm{c}\big). \tag{3.15}$$

Thus, its PDF must be related to the PDF of the contact position. As an intermediary step, we define P_c as the probability that at an arbitrary instant $t \geq t_0$ the contact has

already occurred,

$$P_{\mathrm{c}}(t) = \left| \int_{z(t_0)}^{z(t)} \rho_{Z_{\mathrm{c}}}(z)\,\mathrm{d}z \right|. \tag{3.16}$$

Depending on the motion direction, $z(t) \leq z(t_0)$ or $z(t) \geq z(t_0)$. Thus, the absolute value simply ensures that the probability is nonnegative for both cases. Moreover, integration by substitution permits transforming (3.16) into a time integral,

$$P_{\mathrm{c}}(t) = \left| \int_{t_0}^{t} \rho_{Z_{\mathrm{c}}}\big(z(\tau)\big)\,\dot{z}(\tau)\,\mathrm{d}\tau \right|. \tag{3.17}$$

Note that the PDF is nonnegative by definition. In addition, according to Assumption 3.2, the time derivative of the position is always nonnegative or nonpositive. Then, the integrand is always nonnegative or nonpositive and, consequently, the absolute value can be moved inside the integral,

$$P_{\mathrm{c}}(t) = \int_{t_0}^{t} \left| \rho_{Z_{\mathrm{c}}}\big(z(\tau)\big)\,\dot{z}(\tau) \right| \mathrm{d}\tau. \tag{3.18}$$

From (3.18) and (3.1a), the PDF $\rho_{T_{\mathrm{c}}}$ can be calculated as

$$\rho_{T_{\mathrm{c}}}(t) = \frac{\mathrm{d}P_{\mathrm{c}}(t)}{\mathrm{d}t} = \big|v(t)\big|\,\rho_{Z_{\mathrm{c}}}\big(z(t)\big). \tag{3.19}$$

□

Proposition 3.1. *The contact velocity V_{c} is a random variable whose expectation is*

$$\mathrm{E}[V_{\mathrm{c}}] = \int_{t_0}^{t_{\mathrm{f}}} \frac{1}{\mathrm{P}(t_0 \leq T_{\mathrm{c}} \leq t_{\mathrm{f}})}\, v(t)\,\big|v(t)\big|\,\rho_{Z_{\mathrm{c}}}\big(z(t)\big)\,\mathrm{d}t. \tag{3.20}$$

Proof. The contact velocity is a function of the contact instant

$$V_{\mathrm{c}} = v(T_{\mathrm{c}}). \tag{3.21}$$

Thus, its expected value can be expressed as a conditional expectation,

$$\mathrm{E}[V_{\mathrm{c}}] = \mathrm{E}\big[v(T_{\mathrm{c}}) \mid t_0 \leq T_{\mathrm{c}} \leq t_{\mathrm{f}}\big], \tag{3.22}$$

which can be calculated as

$$\mathrm{E}[V_{\mathrm{c}}] = \frac{1}{\mathrm{P}(t_0 \leq T_{\mathrm{c}} \leq t_{\mathrm{f}})} \int_{t_0}^{t_{\mathrm{f}}} v(t)\,\rho_{T_{\mathrm{c}}}(t)\,\mathrm{d}t. \tag{3.23}$$

Then, based on Lemma 3.1, the PDF of the contact instant can be related to the PDF of the contact position which, according to Assumption 3.1, is known. The resulting expression is

$$\mathrm{E}[V_\mathrm{c}] = \frac{1}{\mathrm{P}(t_0 \leq T_\mathrm{c} \leq t_\mathrm{f})} \int_{t_0}^{t_\mathrm{f}} v(t) \left|v(t)\right| \rho_{Z_\mathrm{c}}\big(z(t)\big)\, \mathrm{d}t. \tag{3.24}$$

Note that $\mathrm{P}(t_0 \leq T_\mathrm{c} \leq t_\mathrm{f})$ is a probability constant, so it can be moved inside the integral, as in (3.20). □

The derived expression for the expected contact velocity (3.20) has the form of a standard optimal control performance index. Since the goal is to minimize the absolute value of the contact velocity, the proposed cost functional J_1 is defined as proportional to the expectation of $|V_\mathrm{c}|$, and as the velocity cannot change sign (Assumption 3.2), it can be expressed as

$$J_1 = w_1 \,\mathrm{E}\big[|V_\mathrm{c}|\big] = w_1 \,\mathrm{sgn}(V_\mathrm{c})\,\mathrm{E}[V_\mathrm{c}], \tag{3.25}$$

where w_1 is a weight constant. This constant and the following ones determine the importance of each cost functional and should be chosen accordingly. Substituting (3.20) from Proposition 3.1 into (3.25) the final expression is obtained,

$$J_1 = \int_{t_0}^{t_\mathrm{f}} \mathcal{V}_1\big(\boldsymbol{x}(t)\big)\, \mathrm{d}t, \qquad \mathcal{V}_1(\boldsymbol{x}) = \frac{w_1}{P(t_0 \leq T_\mathrm{c} \leq t_\mathrm{f})}\, v^2\, \rho_{Z_\mathrm{c}}(z). \tag{3.26}$$

Note that the absolute values are removed because $\mathrm{sgn}(v) = \mathrm{sgn}(V_c)$ except when $v = 0$, and then $\mathcal{V}_1 = 0$.

3.3.2 Expected bounced acceleration

In the case that the system is second order ($n = 2$), the acceleration can be directly controlled by the input $\boldsymbol{u}$, and therefore it is sufficient to minimize the expected contact velocity. However, in most cases, $n > 2$ and position derivatives of higher order (acceleration, jerk, jounce...) should be minimized as well to achieve soft landing. The reason is that, if their sign is opposite to the motion direction, they tend to separate the movable part from the final position, even in a completely inelastic collision. In this subsection, the cost functional for the minimization of the bounced acceleration is derived. In the rare cases in which $n > 3$, the same line of reasoning should be followed for higher-order derivatives of the position.

As stated in (3.1b), the acceleration $\dot{v}$ may depend on the velocity, which can change abruptly in the contact instant. Thus, the bounced acceleration a_b after contact should be calculated from the bounced velocity v_b,

$$a_\mathrm{b}(z, v_\mathrm{b}, \boldsymbol{\vartheta}, \boldsymbol{u}) = f_v(z, v_\mathrm{b}, \boldsymbol{\vartheta}, \boldsymbol{u}). \tag{3.27}$$

If contact occurs at t, the bounced velocity, in the most general form, is a function of the state and the input at that instant. In the case there is no accurate model of the bouncing phenomenon, it is possible to conservatively estimate v_b as

$$\hat{v}_\mathrm{b}(\boldsymbol{x}, \boldsymbol{u}) = \underset{v_\mathrm{b} \in \mathcal{V}_\mathrm{b}}{\arg\max} \; -\mathrm{sgn}(V_\mathrm{c})\, a_\mathrm{b}(z, v_\mathrm{b}, \boldsymbol{\vartheta}, \boldsymbol{u}), \tag{3.28}$$

where $\mathcal{V}_\mathrm{b}$ is the set of possible bouncing velocities. For the worst-case scenario, it is defined as

$$\mathcal{V}_\mathrm{b} = \big\{ -\gamma\, v \mid \gamma \in [0, 1] \big\}, \tag{3.29}$$

where γ represents the coefficient of restitution, as in Section 2.2.3.

It is important to notice that the bounced acceleration is only detrimental in the direction that separates the armature from the final position. In other words, in the opposite direction of the velocity. Taking that into account, the saturated bounced acceleration $a_{\mathrm{b,sat}}$ is defined as an auxiliary variable, in the case of contact,

$$a_{\mathrm{b,sat}}(\boldsymbol{x}, \boldsymbol{u}) = \begin{cases} a_\mathrm{b}(z, \hat{v}_\mathrm{b}, \boldsymbol{\vartheta}, \boldsymbol{u}), & V_\mathrm{c}\, a_\mathrm{b}(z, \hat{v}_\mathrm{b}, \boldsymbol{\vartheta}, \boldsymbol{u}) \leq 0 \;\; \text{(take off)} \\ 0, & V_\mathrm{c}\, a_\mathrm{b}(z, \hat{v}_\mathrm{b}, \boldsymbol{\vartheta}, \boldsymbol{u}) > 0 \;\; \text{(hold)} \end{cases}. \tag{3.30}$$

Note that the saturation is required for calculating the cost functional. The unconstrained acceleration $\dot{v}$ is still calculated from (3.1b). Furthermore, to numerically solve the problem, $a_{\mathrm{b,sat}}$ should be differentiable. This condition is not satisfied in (3.30), thus a smooth saturation function should be used instead.

Proposition 3.2. *The saturated bounced acceleration at contact A_b is a random variable whose expectation is*

$$\mathrm{E}[A_\mathrm{b}] = \int_{t_0}^{t_\mathrm{f}} \frac{1}{\mathrm{P}(t_0 \leq T_\mathrm{c} \leq t_\mathrm{f})}\, |v(t)|\, a_{\mathrm{b,sat}}\big(\boldsymbol{x}(t), \boldsymbol{u}(t)\big)\, \rho_{Z_\mathrm{c}}\big(z(t)\big)\, \mathrm{d}t. \tag{3.31}$$

Proof. The bounced acceleration depends on the contact instant,

$$A_\mathrm{b} = a_{\mathrm{b,sat}}\big(\boldsymbol{x}(T_\mathrm{c}), \boldsymbol{u}(T_\mathrm{c})\big). \tag{3.32}$$

As was the case for the contact velocity in Section 3.3.1, its expected value can be defined as a conditional expectation,

$$\mathrm{E}[A_\mathrm{b}] = \mathrm{E}\big[a_{\mathrm{b,sat}}\big(\boldsymbol{x}(T_\mathrm{c}), \boldsymbol{u}(T_\mathrm{c})\big) \mid t_0 \leq T_\mathrm{c} \leq t_\mathrm{f}\big], \tag{3.33}$$

which can be computed as

$$\mathrm{E}[A_\mathrm{b}] = \frac{1}{\mathrm{P}(t_0 \leq T_\mathrm{c} \leq t_\mathrm{f})} \int_{t_0}^{t_\mathrm{f}} a_{\mathrm{b,sat}}\big(\boldsymbol{x}(t), \boldsymbol{u}(t)\big)\, \rho_{T_\mathrm{c}}(t)\, \mathrm{d}t. \tag{3.34}$$

Then, the ρ_{T_c} expression (3.14) from Lemma 3.1 is substituted in (3.34),

$$\mathrm{E}[A_\mathrm{b}] = \frac{1}{\mathrm{P}(t_0 \leq T_\mathrm{c} \leq t_\mathrm{f})} \int_{t_0}^{t_\mathrm{f}} a_{\mathrm{b,sat}}\big(\boldsymbol{x}(t), \boldsymbol{u}(t)\big)\, |v(t)|\, \rho_{Z_\mathrm{c}}\big(z(t)\big)\, \mathrm{d}t. \tag{3.35}$$

Finally, in an equivalent manner to Section 3.3.1, the constant probability $\mathrm{P}(t_0 \leq T_\mathrm{c} \leq t_\mathrm{f})$ can be moved inside the integral, resulting in (3.31). □

In this case, the objective is to minimize the absolute value of A_b. In consequence, the cost functional term should be

$$J_2 = w_2\, \mathrm{E}\big[|A_\mathrm{b}|\big] = -w_2\, \mathrm{sgn}(V_\mathrm{c})\, \mathrm{E}[A_\mathrm{b}], \tag{3.36}$$

where w_2 is the corresponding weight term. Substituting (3.31) from Proposition 3.2 into (3.36), the final expression is obtained,

$$J_2 = \int_{t_0}^{t_\mathrm{f}} \mathcal{V}_2\big(\boldsymbol{x}(t), \boldsymbol{u}(t)\big)\, \mathrm{d}t, \tag{3.37a}$$

$$\mathcal{V}_2(\boldsymbol{x}, \boldsymbol{u}) = -\frac{w_2}{\mathrm{P}(t_0 \leq T_\mathrm{c} \leq t_\mathrm{f})}\, v\, a_{\mathrm{b,sat}}(\boldsymbol{x}, \boldsymbol{u})\, \rho_{Z_\mathrm{c}}\big(z\big). \tag{3.37b}$$

3.3.3 Regularization terms

Many switch-type systems are input-affine, including the dynamical models of reluctance actuators presented in the previous chapter[1]. For this class of systems, the cost functional terms $\mathcal{V}_1$ and $\mathcal{V}_2$ are also input-affine, which means that, until this point, the Hamiltonian (3.5) would also be affine with respect to the input $\boldsymbol{u}$. Thus, the optimal control $\boldsymbol{u}^*$ (3.6) would have discontinuities, which means the problem is ill-defined, complicating its numerical resolution. A simple and common workaround, firstly introduced by Jacobson et al. [70], is to add as a regularization term a quadratic expression with respect to $\boldsymbol{u}$, making the optimal control continuous. We propose the following alternative:

$$J_3 = \int_{t_0}^{t_\mathrm{f}} \mathcal{V}_3\big(\boldsymbol{x}(t), \boldsymbol{u}(t)\big)\, \mathrm{d}t, \qquad \mathcal{V}_3(\boldsymbol{x}, \boldsymbol{u}) = w_3 \left(\frac{\mathrm{d}h^{\#}(\boldsymbol{x})}{\mathrm{d}t}\right)^2, \tag{3.38}$$

where w_3 is the corresponding weight term and $h^{\#}(\boldsymbol{x})$ is an auxiliary output signal whose quadratic derivative is minimized. The cost functional term can be expressed as

$$\mathcal{V}_3(\boldsymbol{x}, \boldsymbol{u}) = w_3 \left(\frac{\partial h^{\#}(\boldsymbol{x})}{\partial \boldsymbol{x}}\, \boldsymbol{f}(\boldsymbol{x}, \boldsymbol{u})\right)^2. \tag{3.39}$$

[1]More rigorously, the dynamical function of the complete model (RAM-JA) is a piece-wise function where each of the two pieces is input-affine, and there is no discontinuity between them.

In general, it serves as a regularization term because it is not an affine function of $\boldsymbol{u}$. However, note that a regularization term is only strictly required for the cases in which $\boldsymbol{f}$ is input-affine with respect to $\boldsymbol{u}$. In that case, $\mathcal{V}_3$ is quadratic with respect to u, which greatly simplifies the calculation of the optimal control $\boldsymbol{u}^*$ from (3.6).

In particular, for reluctance actuators, $h^{\#}(\boldsymbol{x})$ can be the current ι_{coil}. Reducing its time derivative would be advantageous if its optimal signal is used as reference or input. (The motivation for using the current as input is discussed in Section 3.4.1). The signal $h^{\#}(\boldsymbol{x})$ obtained this way is less steep and therefore easier to follow accurately in the implementation. Therefore, $\mathcal{V}_3$ is not only useful for the numerical resolution of the problem, because reducing $h^{\#}(\boldsymbol{x})$ may be also desirable from a theoretical or from an implementation perspective. Note, however, that it is not possible to minimize simultaneously the output signal derivative and the expected values of the contact velocity and acceleration. There is a trade-off that depends on the chosen cost weights w_1, w_2 and w_3.

3.4 Application

As an example, and for later analysis, the proposed optimal control problem is solved for a dynamical model based on a real reluctance actuator. The details are presented in this section.

3.4.1 Actuator description and dynamical model

The actuator is a small solenoid valve (Fig. 3.1a). It is slightly different from the one used for model fitting and comparison in Section 2.5. Most distinctively, it has a plastic ring between the plunger and the spring, in order to limit the minimum gap $z_{\min}$ to $0.4\,\mathrm{mm}$.

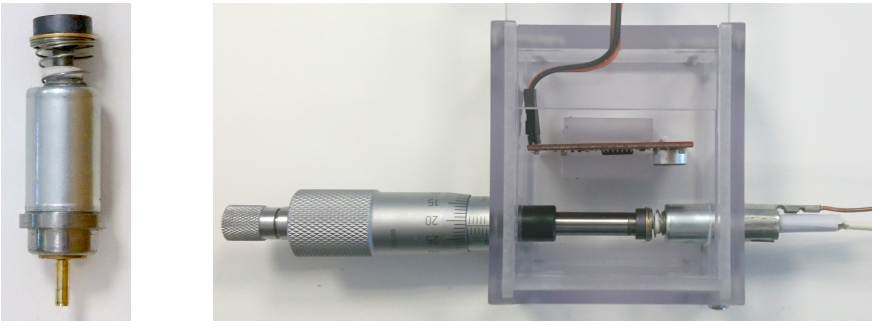

(a) Valve. **(b)** Experimental setup.

Figure 3.1: Linear-travel short-stroke solenoid valve and experimental setup with the valve, a micrometer to limit the maximum gap and an electret microphone to measure the impact noise.

Regarding the state-space differential equations from (3.1), they are particularized for this device based on the basic model (RAM-FK) with the voltage as input, as presented in Chapter 2. Thus, $\boldsymbol{\vartheta}$ and $\boldsymbol{f_\vartheta}$ correspond to the magnetic flux ϕ and its dynamical function f_ϕ, respectively. To be consistent with the previous and following chapters, the later notation is chosen to represent the third state variable. The dynamical functions are defined as follows:

$$f_v(z, v) = \frac{1}{m_{\mathrm{mov}}}\left(k_{\mathrm{sp}}\,(z_{\mathrm{sp}} - z) - c_{\mathrm{f}}\,v - \frac{1}{2}\,\frac{\partial \mathcal{R}_{\mathrm{g}}(z)}{\partial z}\,\phi^2\right), \tag{3.40a}$$

$$f_\phi(z, \phi, u) = -\frac{R\left(\mathcal{R}_{\mathrm{g}}(z) + \mathcal{R}_{\mathrm{c}}(\phi)\right)}{N^2 + R\,k_{\mathrm{eddy}}}\,\phi + \frac{N}{N^2 + R\,k_{\mathrm{eddy}}}\,u, \tag{3.40b}$$

where the gap and core reluctance terms are

$$\mathcal{R}_{\mathrm{g}}(z) = \mathcal{R}_{\mathrm{g},0} + \frac{\mathcal{R}'_{\mathrm{g},0}\,z}{1 + k_1\,z\,\ln(k_2/z)}, \qquad \mathcal{R}_{\mathrm{c}}(\phi) = \frac{\mathcal{R}_{\mathrm{c},0}}{1 - |\phi|/\phi_{\mathrm{sat}}}. \tag{3.41}$$

Note that the mechanical subsystem is modeled as a mass-spring-damper system, with the newly defined damping coefficient c_{f} to model the frictional losses. Furthermore, the estimated bounced velocity (3.28)—needed only for the calculation of the expected bounced acceleration—is chosen conservatively. From (3.40a), it is easy to see that the acceleration increases if the velocity decreases, so the worst-case scenario corresponds to $\gamma = 0$, so that $\hat{v}_{\mathrm{b}} = 0$. All the model parameters are specified in Table 3.1.

Table 3.1: Solenoid valve parameters.

Parameter	Nominal value		Parameter	Nominal value	
R	50	Ω	N	1200	
k_{eddy}	1630×10^3	Ω^{-1}	m_{mov}	1.63×10^{-3}	kg
$\mathcal{R}_{\mathrm{c},0}$	4.41×10^6	H^{-1}	k_{sp}	61.8	N/m
ϕ_{sat}	2.63×10^{-5}	Wb	z_{sp}	1.92×10^{-2}	m
$\mathcal{R}_{\mathrm{g},0}$	5.594×10^6	H^{-1}	c_{f}	0.806	Ns/m
$\mathcal{R}'_{\mathrm{g},0}$	1.105×10^{11}	H^{-1}/m	$z_{\min}$	3.99×10^{-4}	m
k_1	1318	m^{-1}	$z_{\max}$	1.60×10^{-3}	m
k_2	9.735×10^{-3}	m	γ	0	

To justify the use of the current as the control input (see Section 3.3.3), notice that the dynamical equation of the magnetic flux ϕ with voltage as input (3.40b) depends on the internal resistance R of the copper coil, which in turn depends greatly on temperature. Typically, the resistance dependence on temperature is negligible during an operation but not after a large number of operation cycles. This means that the control with the voltage as input is not robust, i.e., a supplied voltage signal that achieves the desired behavior at a certain temperature is not guaranteed to work when that temperature changes. On the

other hand, the relation between the current and the state of the device does not depend on the resistance,

$$\iota_{\mathrm{coil}} = \frac{\mathcal{R}_{\mathrm{g}}(z) + \mathcal{R}_{\mathrm{c}}(\phi)}{N}\,\phi + k_{\mathrm{eddy}}\,\dot{\phi}. \tag{3.42}$$

Therefore, we propose to control the actuator by applying an optimal current signal. It is important to remark that the optimal control problem is still solved with the voltage as the control signal. The optimal current signal can then be easily calculated. Notice that the current derivative depends on $\ddot{\phi}$ so, in order to accurately calculate it, an auxiliary variable $\vartheta_2 = \dot{\phi}$ should be added to the state vector $\boldsymbol{x}$. Alternatively, it can be approximated by setting $k_{\mathrm{eddy}} = 0$. Thus, the auxiliary output function is defined as

$$h^{\#}(z, \phi) = \frac{\mathcal{R}_{\mathrm{g}}(z) + \mathcal{R}_{\mathrm{c}}(\phi)}{N}\,\phi. \tag{3.43}$$

As the effect of the eddy currents is neglected, the solution is suboptimal. The error of the approximation will be illustrated in the following section. Note that this approximation only affects the output function used in the cost term $\mathcal{V}_3$, the dynamical function f_ϕ (3.40b) still considers the eddy current phenomenon due to the parameter k_{eddy}.

Although not required for solving the optimal control problem, a model for simulations must also consider the position constraints between $z_{\min}$ and $z_{\max}$. This is accomplished by defining a hybrid automaton, as in Section 2.2.3. Note that, as the generated magnetic force is an even function of the magnetic flux (see (2.19)), there is no need to work with negative values of magnetic flux. Moreover, in most control strategies, it is advantageous to restrict the current and thus the magnetic flux to nonnegative values. In practice, this would be implemented with diodes, which only allow one current flow direction. In the model, this is achieved by the addition of dynamic modes in which the magnetic flux is static. Ultimately, the automaton presents six dynamic modes, with the corresponding guard conditions and reset rules, as illustrated in Fig. 3.2. The discrete state $q \in \{1, 2, \ldots, 6\}$ designates the dynamic mode: positive current and plunger in the lower limit, motion or the upper limit ($q = 1$, 2 or 3, respectively); or current saturated to zero and plunger in the lower limit, motion or the upper limit ($q = 4$, 5 or 6, respectively).

Notice that the automaton includes two additional functions: h and φ_ϕ. On the one hand, h represents the output function (2.15), where the output is the current. Particularizing to the RAM-FK reluctance model, it is defined as

$$\iota_{\mathrm{coil}} = h(z, \phi, u) = \frac{N\left(\mathcal{R}_{\mathrm{g}}(z) + \mathcal{R}_{\mathrm{c}}(\phi)\right)}{N^2 + R\,k_{\mathrm{eddy}}}\,\phi + \frac{k_{\mathrm{eddy}}}{N^2 + R\,k_{\mathrm{eddy}}}\,u. \tag{3.44}$$

On the other hand, φ_ϕ represents the dynamical function of the magnetic flux when the current is saturated to zero. It is derived from (3.42) by setting $\iota_{\mathrm{coil}} = 0$,

$$\varphi_\phi(z, \phi) = -\frac{\mathcal{R}_{\mathrm{g}}(z) + \mathcal{R}_{\mathrm{c}}(\phi)}{k_{\mathrm{eddy}}}\,\phi. \tag{3.45}$$

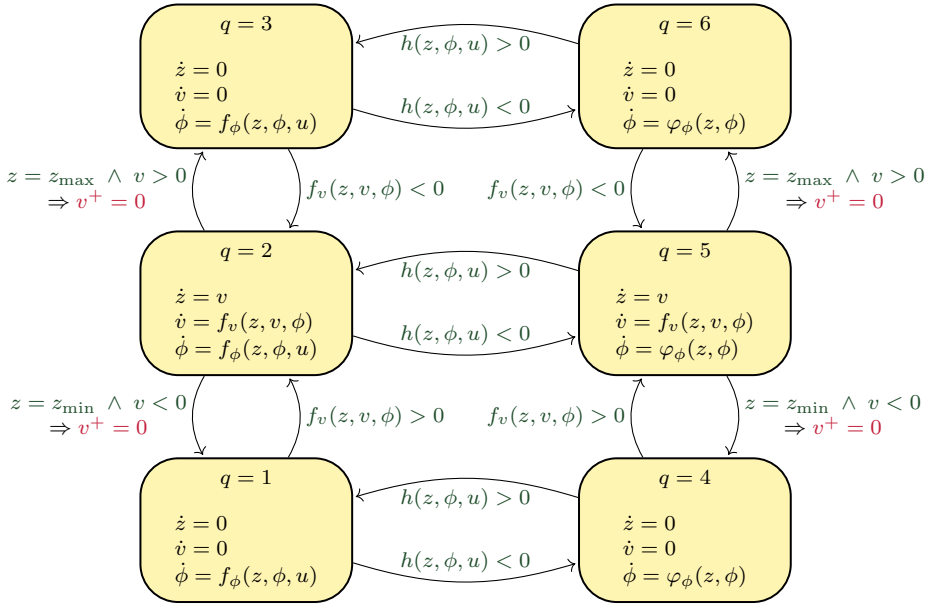

Figure 3.2: Diagram of the hybrid automaton modeling the full system of the actuator, including the output saturation to zero. Each transition between modes (yellow blocks) occurs when the corresponding guard condition (green text) is satisfied. In some transitions, the continuous state jumps according to the corresponding reset rule (red text).

3.4.2 Optimal voltage signal

According to (3.6), the optimal control u^* for this particular case is defined as

$$u^*(\boldsymbol{x}^*, \boldsymbol{\beta}^*) = \underset{u_{\text{lb}} \le u \le u_{\text{ub}}}{\arg\min} \ \mathcal{H}(\boldsymbol{x}^*, \boldsymbol{\beta}^*, u), \tag{3.46}$$

where u_{lb} and u_{ub} are the lower and upper limits of the optimal voltage input. In the case the voltage is used as the input in the implementation, they could be set directly to $u_{\min}$ and $u_{\max}$ respectively, which represent the minimum and maximum supply voltage. However, if the current is used as input, the real voltage changes with the resistance, as noted in Section 3.4.1. This means that the values of u_{lb} and u_{ub} must be selected conservatively to guarantee that the designed current is actually obtainable with a voltage between $u_{\min}$ and $u_{\max}$ and a real resistance R_{real} ranging from $R_{\min}$ to $R_{\max}$.

Assumption 3.3. *The current is always nonnegative, as in the dynamical model presented in Section 3.4.1.*

Assumption 3.4. *The voltage and real resistance are bounded as follows:*

$$v_{\text{coil}} \in [u_{\min}, \, u_{\max}], \qquad R_{\text{real}} \in [R_{\min}, \, R_{\max}]. \tag{3.47}$$

Proposition 3.3. *If the lower and upper limits of the optimal voltage input satisfy*

$$u_{\mathrm{ub}} \leq \frac{R}{R_{\max}}\, u_{\max}, \qquad\qquad u_{\mathrm{lb}} \geq \frac{R - R_{\min}}{R}\, u_{\mathrm{ub}} + u_{\min}, \tag{3.48}$$

where R is the resistance used in the optimal control equations, then the designed current is actually obtainable with an arbitrary voltage v_{coil} and any resistance R_{real}.

Proof. Given the electrical circuit equation,

$$u = R\,\iota_{\mathrm{coil}} + N\,\dot{\phi}, \tag{3.49}$$

it is possible to determine the worst-case scenarios, according to Assumption 3.47,

$$-\,R_{\mathrm{real}}\,\iota_{\mathrm{coil}} + u_{\min} \leq -R\,\iota_{\mathrm{coil}} + u^* \leq -R_{\mathrm{real}}\,\iota_{\mathrm{coil}} + u_{\max}. \tag{3.50}$$

Then, the bounding condition of the optimal input u^* is

$$u_{\min} + \max\big((R - R_{\mathrm{real}})\,\iota_{\mathrm{coil}}\big) \leq u^* \leq u_{\max} + \min\big((R - R_{\mathrm{real}})\,\iota_{\mathrm{coil}}\big). \tag{3.51}$$

Note that, considering that the current must be nonnegative (Assumption 3.3), the lower and upper bounds of u^* must satisfy

$$u_{\mathrm{ub}} \leq u_{\max} + (R - R_{\max})\,\iota_{\max}, \qquad u_{\mathrm{lb}} \geq u_{\min} + (R - R_{\min})\,\iota_{\max}. \tag{3.52}$$

Moreover, the maximum value fo the current can be conservatively calculated as $\iota_{\max} = u_{\mathrm{ub}}/R$. With some manipulations, the derived conditions are (3.48). □

Then, to solve (3.46) algebraically, an auxiliary variable is defined,

$$u^{\#}(\boldsymbol{x}^*, \boldsymbol{\beta}^*) = \arg\min_{u}\, \mathcal{H}(\boldsymbol{x}^*, \boldsymbol{\beta}^*, u) = u \quad \text{such that } \frac{\partial \mathcal{H}(\boldsymbol{x}^*, \boldsymbol{\beta}^*, u)}{\partial u} = 0, \tag{3.53}$$

which is unique and easily solvable because $\partial\mathcal{H}/\partial u$ is an affine function of u.

Proposition 3.4. *The optimal control u^* can be obtained by simply saturating $u^{\#}$ between the control limits,*

$$u^* = u^*(\boldsymbol{x}^*, \boldsymbol{\beta}^*) = \begin{cases} u_{\mathrm{lb}}, & u_{\mathrm{lb}} > u^{\#}(\boldsymbol{x}^*, \boldsymbol{\beta}^*) \\ u^{\#}(\boldsymbol{x}^*, \boldsymbol{\beta}^*), & u_{\mathrm{lb}} \leq u^{\#}(\boldsymbol{x}^*, \boldsymbol{\beta}^*) \leq u_{\mathrm{ub}} \\ u_{\mathrm{ub}}, & u^{\#}(\boldsymbol{x}^*, \boldsymbol{\beta}^*) > u_{\mathrm{ub}} \end{cases}. \tag{3.54}$$

Proof. Notice that $u^{\#}$ is the global minimum of $\mathcal{H}$ and $\partial^2\mathcal{H}/\partial u^2$ does not depend on u. Therefore, $\partial\mathcal{H}/\partial u > 0$ for any $u < u^{\#}$ and $\partial\mathcal{H}/\partial u < 0$ for any $u > u^{\#}$. Thus, for any $u \in (u_{\mathrm{lb}},\, u_{\mathrm{ub}})$ and $u^{\#} \notin [u_{\mathrm{lb}},\, u_{\mathrm{ub}}]$,

$$u^{\#} < u_{\mathrm{lb}} < u \quad \Rightarrow \quad \mathcal{H}(\boldsymbol{x}^*, \boldsymbol{\beta}^*, u_{\mathrm{lb}}) < \mathcal{H}(\boldsymbol{x}^*, \boldsymbol{\beta}^*, u) \quad \Leftrightarrow \quad u^* = u_{\mathrm{lb}}, \tag{3.55a}$$

$$u^{\#} > u_{\mathrm{ub}} > u \quad \Rightarrow \quad \mathcal{H}(\boldsymbol{x}^*, \boldsymbol{\beta}^*, u_{\mathrm{ub}}) < \mathcal{H}(\boldsymbol{x}^*, \boldsymbol{\beta}^*, u) \quad \Leftrightarrow \quad u^* = u_{\mathrm{ub}}. \tag{3.55b}$$

□

Analogously to the acceleration in Section 3.3.2, the saturation of $u^{\#}$ in (3.54) should be approximated with a differentiable function.

3.4.3 Compared solutions

The optimal control problem may be solved for both operation types: making ($z_\mathrm{f} < z_0$) and breaking ($z_\mathrm{f} > z_0$). The common parameters are specified in Table 3.2. To account for the uncertainty, the contact position Z_c is considered a normal random variable,

$$Z_\mathrm{c} \sim \mathcal{N}\big(\mu_z,\, \sigma_z^2\big), \tag{3.56}$$

where μ_z is the expected contact position and σ_z is its standard deviation. The probability density is therefore

$$\rho_{Z_\mathrm{c}}(z) = \frac{1}{\sigma_z\,\sqrt{2\pi}}\,\exp\!\left(-\frac{(z-\mu_z)^2}{2\,\sigma_z^2}\right). \tag{3.57}$$

Then, the initial and expected contact positions are defined as follows:

$$z_0 = z_\mathrm{max}, \qquad \mu_z = z_\mathrm{min}, \qquad \text{(making operation)} \tag{3.58}$$

$$z_0 = z_\mathrm{min}, \qquad \mu_z = z_\mathrm{max}. \qquad \text{(breaking operation)} \tag{3.59}$$

Table 3.2: Optimization parameters.

Parameter	Value	
u_lb	-45	V
u_ub	45	V
t_0	0	s
t_f	3.5×10^{-3}	s

Parameter	Value
σ_z	$2 \times 10^{-5}\,\mathrm{m}^2$
w_1	10^6
w_2	10^3
w_3	1000

To analyze the probability-based optimal solutions (POS), they are compared with an energy-optimal solution (EOS) for soft landing with no uncertainty considerations. For the latter case, there are essentially two differences: the boundary conditions for t_f, which force the velocity and acceleration to be zero,

$$f_v\big(z(t), v_\mathrm{b}(t), \phi(t), u(t)\big) = 0, \qquad v(t_\mathrm{f}) = 0; \tag{3.60}$$

and the cost functional, which corresponds to an energy-optimal control problem,

$$J = \int_{t_0}^{t_\mathrm{f}} u^2(t)\,\mathrm{d}t. \tag{3.61}$$

Then, to make a fair comparison between EOS and POS, we set $z_\mathrm{f} = \mu_z$. This means that, for both solutions, there is a 50 % probability of no contact in the optimal control time interval, i.e.,

$$\mathrm{P}(t_0 \le T_\mathrm{c} \le t_\mathrm{f}) = 0.50. \tag{3.62}$$

3.5 Analyses

In this section, simulated and experimental tests are performed to compare our proposed POS with the state-of-the-art EOS in which the position randomness is not taken into account. The trajectories are obtained by solving the BVP with MATLAB function `bvp4c` [71], integrating with an adaptive step size.

3.5.1 Theoretical comparison

The simulated results of EOS and POS are presented in Fig. 3.3 for the making (left-hand side) and breaking (right-hand side) operations. Although our trajectory-optimal proposal presents a term for the minimization of the current derivative, its weight is purposely set to be much smaller than the others, in order to prioritize the minimization of the expected contact velocity and acceleration. For that reason, the current (Figs. 3.3c and 3.3d), as well as the voltage signals (Figs. 3.3a and 3.3b), are steeper than the ones from EOS. Note also that both voltage signals saturate to $u_{\mathrm{lb}} = -45\,\mathrm{V}$ and $u_{\mathrm{ub}} = 45\,\mathrm{V}$.

Although the model takes into account the eddy currents, they are neglected in the calculation of $\mathcal{V}_3$ (3.39). In Figs. 3.3c and 3.3d, the auxiliary output $h^{\#}(\boldsymbol{x})$ (3.43) is compared against the current (3.44). There is a noticeable discrepancy, but it is small enough to justify the approximation.

As seen in Figs. 3.3k and 3.3l, the position of the EOS has a steadier transition than POS, which shifts abruptly toward the final position, but slows down quickly when the probability of contact stops being negligible. This can be checked as well in the velocity (Figs. 3.3i and 3.3j) and acceleration (Figs. 3.3g and 3.3h) plots. The expectations of the velocity and acceleration in the case of contact are therefore smaller in absolute value (see Table 3.3). This improvement comes at the expense of an energy consumption increase during motion, which may be relevant for applications with very high switching frequencies, but, otherwise, can be neglected.

Table 3.3: Comparison of optimal control solutions: summary.

(a) Making operation.

	$\mathrm{E}\big[\lvert V_{\mathrm{c}}\rvert\big]$	$\mathrm{E}\big[\lvert A_{\mathrm{b}}\rvert\big]$	Energy
EOS	$0.0989\,\mathrm{m/s}$	$353.6439\,\mathrm{m/s^2}$	$0.0467\,\mathrm{J}$
POS	$0.0463\,\mathrm{m/s}$	$75.1087\,\mathrm{m/s^2}$	$0.0524\,\mathrm{J}$

(b) Breaking operation.

	$\mathrm{E}\big[\lvert V_{\mathrm{c}}\rvert\big]$	$\mathrm{E}\big[\lvert A_{\mathrm{b}}\rvert\big]$	Energy
EOS	$0.1183\,\mathrm{m/s}$	$516.0612\,\mathrm{m/s^2}$	$0.0298\,\mathrm{J}$
POS	$0.0470\,\mathrm{m/s}$	$78.4155\,\mathrm{m/s^2}$	$0.0355\,\mathrm{J}$

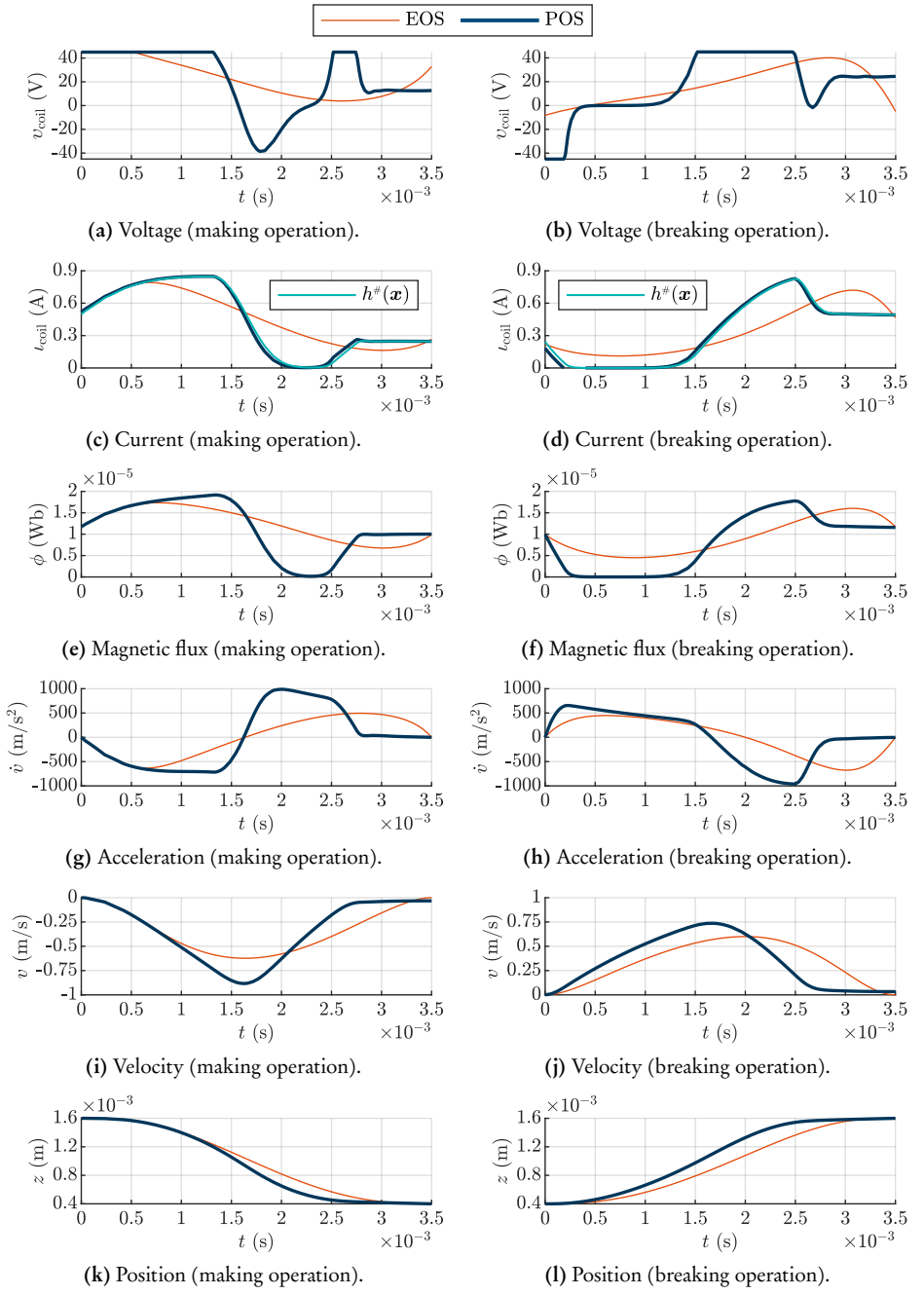

(a) Voltage (making operation).

(b) Voltage (breaking operation).

(c) Current (making operation).

(d) Current (breaking operation).

(e) Magnetic flux (making operation).

(f) Magnetic flux (breaking operation).

(g) Acceleration (making operation).

(h) Acceleration (breaking operation).

(i) Velocity (making operation).

(j) Velocity (breaking operation).

(k) Position (making operation).

(l) Position (breaking operation).

Figure 3.3: Comparison of simulated results from EOS and POS.

To better comprehend the advantage of our proposal, it is useful to visualize the velocity v and acceleration $a_{\mathrm{b,sat}}$ trajectories with respect to position z, as in the state planes presented in Fig. 3.4. The arrows show the direction of their evolution over time, as z approaches z_{f}. Notice that only a small interval of z is shown in each graphic (around $z = z_{\min}$ and $z = z_{\max}$ for the making and breaking operations, respectively) because for other positions the probability of contact is negligible. Note also that acceleration $a_{\mathrm{b,sat}}$ (Figs. 3.4c and 3.4d) is saturated to zero, as explained in Section 3.3.2. These graphics represent the contact velocity and bounced acceleration for every possible contact position. The probability density function of the contact position for each operation is also presented in Figs. 3.4e and 3.4f. The EOS velocity and acceleration are exactly zero in the expected contact position, $z = \mu_z$, but their values change steeply as the position does. POS, instead, keeps a small and steady velocity and acceleration in the position interval in which the probability of contact is significant. This behavior results in considerably better expectations of the contact velocity and bounced acceleration.

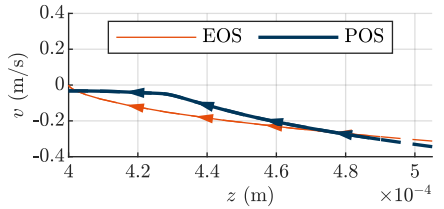

(a) Contact velocity (making operation).

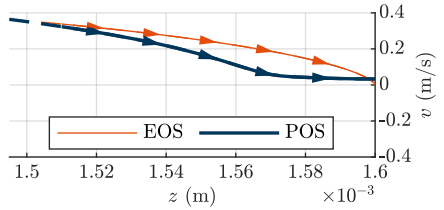

(b) Contact velocity (breaking operation).

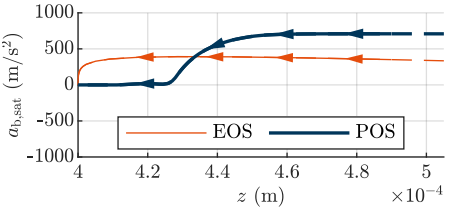

(c) Bounced acceleration (making operation).

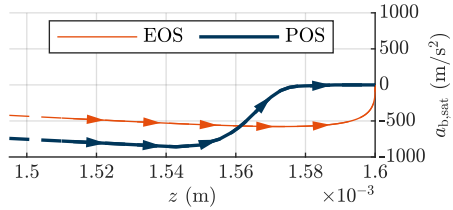

(d) Bounced acceleration (breaking operation).

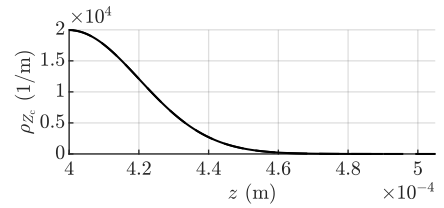

(e) Contact position PDF (making operation).

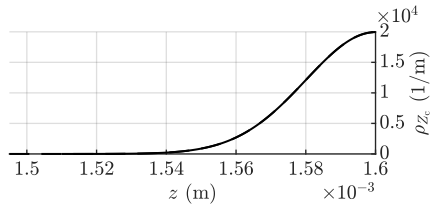

(f) Contact position PDF (breaking operation).

Figure 3.4: Contact velocity, bounced acceleration and PDF in terms of the contact position.

Additionally, to make a more complete comparison, multiple simulations are performed by modifying the contact position variance, while the rest of the parameters are

kept as specified in Section 3.4.3. As the range of standard deviations utilized in the simulations is very wide, the horizontal axis is presented in a logarithmic scale. The results, displayed in Fig. 3.5, show a persistent improvement of POS in the expected velocities and accelerations with respect to EOS, for both types of operations. Unsurprisingly, as the uncertainty decreases, i.e., σ_z is reduced, the expectations of velocity and acceleration in the contact tend to zero for both solutions. This is more prominent in the case of the expected contact velocities, which are very close to zero for both methods if $\sigma_z < 10^{-7}\,\mathrm{m}$ (see Figs. 3.5a and 3.5b). However, the expected accelerations from the EOS solutions are still substantial for small values of σ_z, whereas the ones from the proposed solutions are insignificant (see Figs. 3.5c and 3.5d).

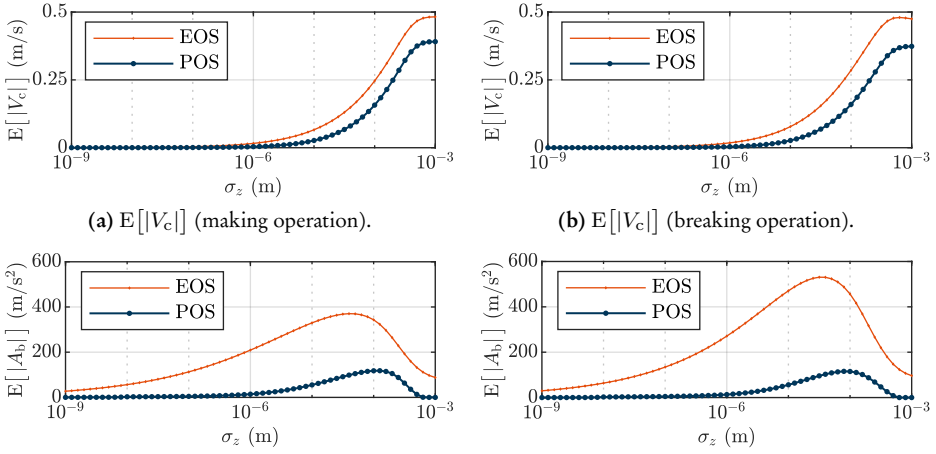

(a) $\mathrm{E}[|V_c|]$ (making operation).

(b) $\mathrm{E}[|V_c|]$ (breaking operation).

(c) $\mathrm{E}[|A_b|]$ (making operation).

(d) $\mathrm{E}[|A_b|]$ (breaking operation).

Figure 3.5: Absolute values of expected contact velocities and bounced accelerations for different standard deviations σ_z.

3.5.2 Comparison via a Monte Carlo method

The most straightforward application of the optimal control design is open-loop control strategies, in which the input signal is directly applied to the actuators to achieve soft landing. The main disadvantage of open-loop control compared to other more complex and expensive alternatives is the lack of any feedback or adaptation loop to correct disturbances. Thus, to analyze this type of control, modeling errors are taken into account.

Firstly, complete input signals are constructed based on the optimal control solutions and are presented in Fig. 3.6. They correspond to a making and breaking cycle. With regards to the voltage signal (Fig. 3.6a), there is an interval previous to the start of motion in which the voltage is constant (u_{ub} and u_{lb} for the making and breaking

operations, respectively). It is necessary for increasing or decreasing the magnetic force so it balances the spring force and the plunger can take off and start the motion. The time interval required cannot be calculated analytically, so the differential equation is solved by numerical integration. There is also an interval at the end of each operation with constant voltage (u_{ub} and 0 for the making and breaking operations, respectively), which is large enough to ensure that the armature always reaches the desired position. On the other hand, the corresponding current signal (3.6b) is calculated by integrating the state vector with the voltage as input, based on the hybrid automaton from Fig. 3.2 and then using the output function (3.44). For these and the following simulations, the initial state is initialized assuming a de-energized coil,

$$\boldsymbol{x}(0) = \begin{bmatrix} z_{\max} \\ 0 \\ 0 \end{bmatrix}, \qquad q(0) = 6. \tag{3.63}$$

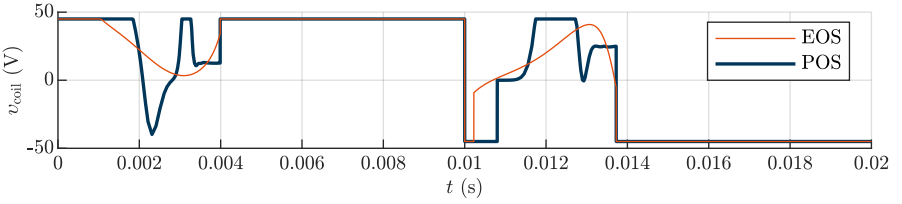

(a) Voltage.

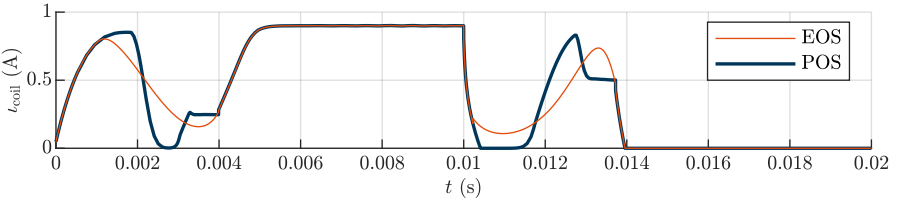

(b) Current.

Figure 3.6: Open-loop soft-landing control signals for making and breaking cycles.

Monte Carlo simulations are performed to analyze the performance of the control strategies. They serve to demonstrate the improvement of our proposal over the standard solution in a more realistic scenario. They are also used to show the advantage of using the current as the input of the open-loop control, instead of the voltage. We perform 50 000 simulations of making and breaking commutations for each case. The simulations depend on the parameter vector $\boldsymbol{p}$, which is defined as

$$\boldsymbol{p} = \begin{bmatrix} z_{\min} & z_{\max} & k_{\mathrm{sp}} & z_{\mathrm{sp}} & c_{\mathrm{f}} & N & \mathcal{R}_{\mathrm{c},0} & \phi_{\mathrm{sat}} & k_{\mathrm{eddy}} & m_{\mathrm{mov}} \end{bmatrix}^{\mathsf{T}}. \tag{3.64}$$

To emulate unit-to-unit variability, the model parameters are perturbed. Specifically,

each parameter p_i is defined as a normal deviate,

$$p_i \sim \mathcal{N}\Big(p_i^{\mathrm{nom}},\ \big((z_{\min}^{\mathrm{nom}} - z_{\max}^{\mathrm{nom}})\,\sigma_p\big)^2\Big) \tag{3.65}$$

if p_i is $z_{\max}$ or $z_{\min}$; otherwise,

$$p_i \sim \mathcal{N}\big(p_i^{\mathrm{nom}}, (p_i^{\mathrm{nom}}\,\sigma_p)^2\big), \tag{3.66}$$

where the superscript nom is used for denoting the corresponding nominal value, as specified in Table 3.2. The relative standard deviation is set as $\sigma_p = 0.01$ and serves to emulate the unit-to-unit variation. The resistance R is also perturbed, but it is considered a special case because its variation is predominantly caused by temperature changes in a single device, instead of unit-to-unit variability in the coil characteristics. Thus, the perturbed resistance for each nth run is defined as the following normal deviate:

$$R \sim \mathcal{N}\big(R^{\mathrm{nom}}, (\alpha_R\,\sigma_T)^2\big), \tag{3.67}$$

where α_R is the temperature coefficient of the copper coil resistance ($\alpha_R = 0.004\,\mathrm{K}^{-1}$) and σ_T is the standard deviation of the temperature, assuming a normal distribution. Simulations are performed for different σ_T to see its influence when controlling with the voltage. Note that, when controlling with the current, the position trajectory is independent on the resistance.

To summarize the simulated results, an equivalent contact velocity is calculated for each commutation, as suggested in [24]. It is defined as follows:

$$v_{\mathrm{c,eq}} = \sqrt{\frac{m_{\mathrm{mov}}}{m_{\mathrm{mov}}^{\mathrm{nom}}} \sum_i {v_{\mathrm{c}i}}^2}, \tag{3.68}$$

where $\{v_{\mathrm{c}i}\}$ is the set of contact velocities. Note that $v_{\mathrm{c,eq}}$ corresponds to the contact velocity of the nominal system that would result in the same dissipated kinetic energy as the perturbed system on all the bounces. Note also that, although the dynamical model does not incorporate elastic bounces by means of a coefficient of restitution, there may be several bounces if the acceleration at contact is positive (for making operations) or negative (for breaking operations). This is the motivation for incorporating the expected bounced acceleration in the cost functional, as discussed in 3.3.2.

The results are presented in Fig. 3.7 for the making operations and in Fig. 3.8 for the breaking operations. For any input choice and temperature variance, the results with POS are considerably better than EOS. This indicates that, even though POS only theoretically accounts for uncertainty in the contact position, the resulting input signals are more robust to errors of other parameters. Additionally, notice in the histograms that the cases with no bounces (light areas) are separated from the ones with bounces (dark areas). In average, the simulations in which there are bounces are notably worse. In this respect, there is also a clear advantage of POS over EOS, as the proportion of results in which there are no bounces is larger for any case. This is an expected consequence of minimizing a cost functional with a term related to the bounced accelerations.

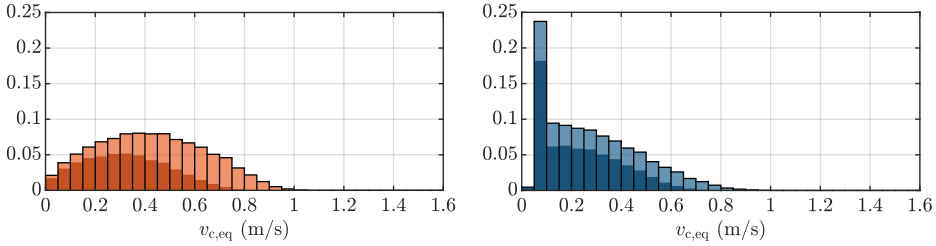

(a) EOS ($u = v_{coil}$, $\sigma_T = 0$).

(b) POS ($u = v_{coil}$, $\sigma_T = 0$).

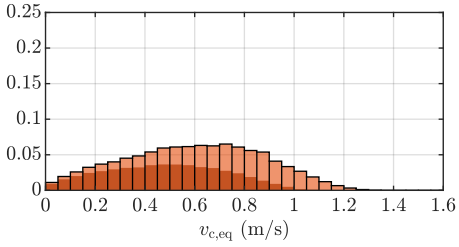

(c) EOS ($u = v_{coil}$, $\sigma_T = 5\,^\circ$C).

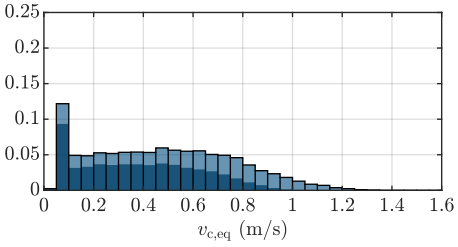

(d) POS ($u = v_{coil}$, $\sigma_T = 5\,^\circ$C).

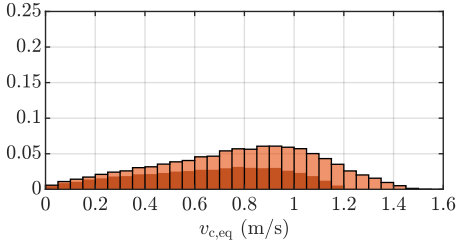

(e) EOS ($u = v_{coil}$, $\sigma_T = 10\,^\circ$C).

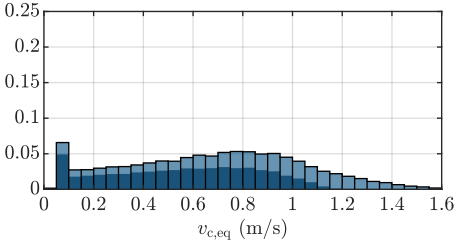

(f) POS ($u = v_{coil}$, $\sigma_T = 10\,^\circ$C).

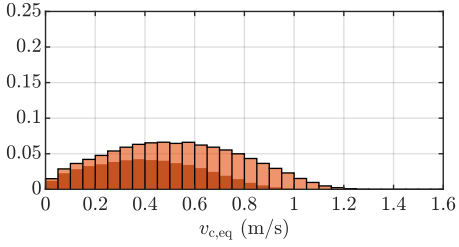

(g) EOS ($u = \iota_{coil}$).

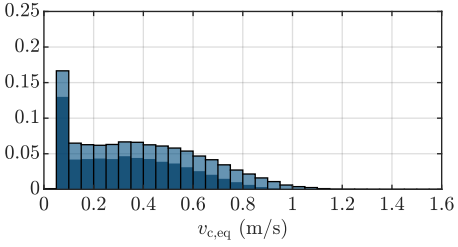

(h) POS ($u = \iota_{coil}$).

Figure 3.7: Relative frequency histograms of the equivalent velocities of the optimal control EOS and POS for the making operation. The dark areas of the histograms correspond to the cases with no bounces.

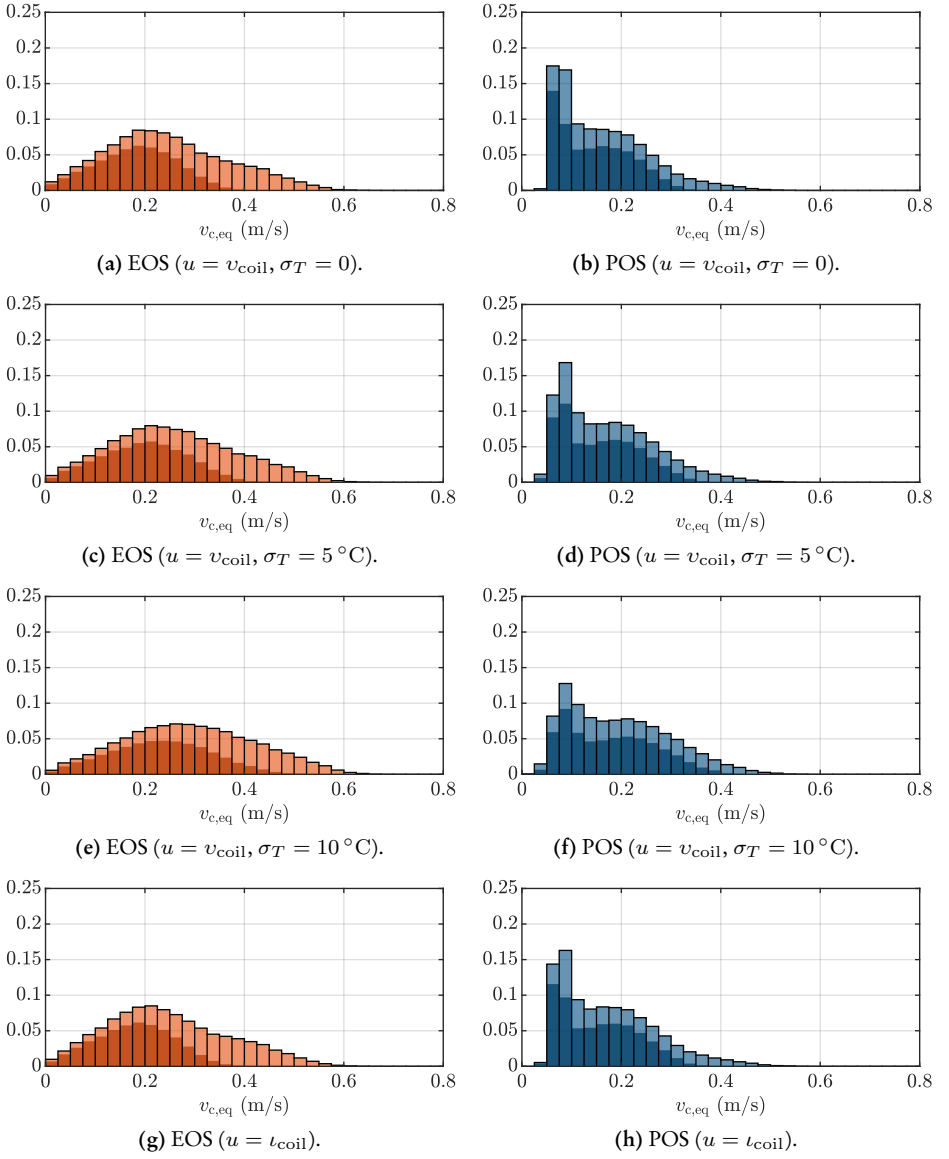

(a) EOS ($u = v_{\text{coil}}$, $\sigma_T = 0$).

(b) POS ($u = v_{\text{coil}}$, $\sigma_T = 0$).

(c) EOS ($u = v_{\text{coil}}$, $\sigma_T = 5\,^{\circ}\text{C}$).

(d) POS ($u = v_{\text{coil}}$, $\sigma_T = 5\,^{\circ}\text{C}$).

(e) EOS ($u = v_{\text{coil}}$, $\sigma_T = 10\,^{\circ}\text{C}$).

(f) POS ($u = v_{\text{coil}}$, $\sigma_T = 10\,^{\circ}\text{C}$).

(g) EOS ($u = \iota_{\text{coil}}$).

(h) POS ($u = \iota_{\text{coil}}$).

Figure 3.8: Relative frequency histograms of the equivalent velocities of the optimal control EOS and POS for the breaking operation. The dark areas of the histograms correspond to the cases with no bounces.

Focusing on the making operations (Fig. 3.7), the best results are obtained with the voltage as input and no temperature changes (Figs. 3.7b and 3.7a). However, there is a worsening trend as the temperature variance increases, while the results with current as input remain unchanged by definition (Figs. 3.7h and 3.7g). For deviations of $5°\mathrm{C}$ or larger, which are completely reasonable, the current is a better input. Notice also that there is a significant fraction of commutations with bounces due to the bounced acceleration and, as expected, their results are worse in average. This is more prominent in the EOS cases, as the expected bounced acceleration is not included in the cost functional. Regarding the breaking operations (Fig. 3.8), the results are much better in general, with smaller $v_{\mathrm{c,eq}}$. Nonetheless, the conclusions related to the choice of input and optimal control solution are analogous.

3.5.3 Experimental comparison

To validate the improvement in a real application, the optimal solutions are applied to the solenoid valve presented in Section 3.4.1. The lack of a position sensor is an important limitation for the experimental testing, but instead, it is possible to measure the impact noises. Thus, the experimental setup incorporates an electret microphone, as can be seen in Fig. 3.1b.

Three different current signals for the making operation are alternately applied to the valve, 500 times each. The first one is simply set to $0.8\,\mathrm{A}$ (no control) and serves as a reference for the other two. The second and third ones correspond to the EOS and POS current signals (see Fig. 3.9). For each one, there is a constant-slope transition from $0\,\mathrm{A}$ to the initial current value in $2\,\mathrm{ms}$ and another constant-slope transition from the final current value to $0.8\,\mathrm{A}$ in $2\,\mathrm{ms}$. The current is then kept at $0.8\,\mathrm{A}$ for a sufficiently long time interval to ensure the commutation and to completely measure the audio with the microphone. We focus on the making operations, which present the most notable impact noises in this device.

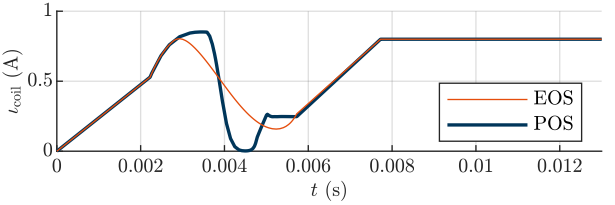

Figure 3.9: Open-loop soft-landing control signals for making operations in experimental tests.

For supplying the desired current signals to the device, we use in our experiments a voltage to current converter. The diagram is presented in Fig. 3.10. The actuator coil is represented by the resistance R in series with the inductance L. The shunt resistor is $R_{\mathrm{shunt}} = 2\,\Omega$, the input is a voltage proportional to the desired current

$v_{\text{ref}} = R_{\text{shunt}}\, \iota_{\text{coil}}$, and the operational amplifier is an Apex PA92, with supply voltages of -60 and $+60\,\text{V}$.

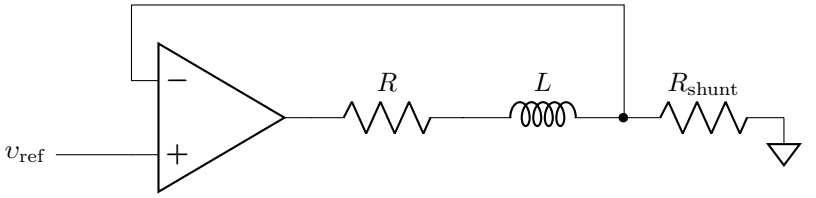

Figure 3.10: Circuit diagram of the voltage to current converter used in the experiments.

To process the voltage signals from the microphone, the following energy is obtained for each one,

$$E_{\text{s}} = \int_{t_{\text{trig}}}^{t_{\text{trig}}+\Delta t} {v_{\text{audio}}}^2(t)\,\text{d}t, \tag{3.69}$$

where t_{trig} is established as the first instant t where $v_{\text{audio}}(t) > \max(v_{\text{audio}})/5$ and $\Delta t = 0.01\,\text{s}$. The energies are then normalized by dividing each one by $1.52\times10^{-3}\,\text{V}^2\,\text{s}$, which is the average of the 500 runs with no control (its relative standard deviation is 0.1561).

The results from the optimal control solutions are summarized in the histograms shown in Fig. 3.11. Both reduce considerably the impact sound with respect to the average operation with no control. The results from POS are appreciably better, with an average of 0.161 and a standard deviation of 0.0795, in contrast with the average of 0.2242 and standard deviation of 0.0947 from the energy-optimal solution.

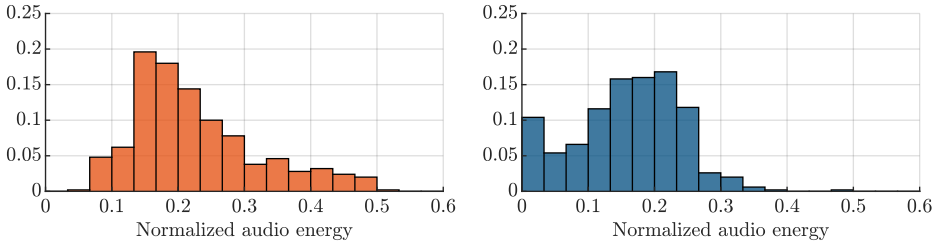

(a) EOS. **(b)** POS.

Figure 3.11: Relative frequency histograms of the normalized energies from the audio signals.

3.6 Discussion

In this chapter, we have proposed a new optimal approach to design soft-landing trajectories of reluctance actuators. For the case of reluctance actuators, the advantage of using the current as input has been discussed and a term has been added to the cost functional to minimize the square of the current derivative. The choice of the current as input is also validated by the results of the Monte Carlo simulations.

Note that, although only the contact position is considered a random variable in the optimal control design, the overall solution is able to compensate for uncertainty of other model parameters. This is also demonstrated in the experimental results, which show the improvement of considering uncertainty in the contact position, even though there are other sources of uncertainty. Additionally, the aforementioned results help to highlight how challenging these types of devices are to soft-landing control when there is no position sensor or observer. Notice that, even though the same current signal is applied to the device repeatedly, the resulting impact noise has a notable dispersion.

The designed input signals has been proven advantageous for open-loop control implementations. Furthermore, the position trajectories are also useful for other types of control, such as the ones explored in the following chapters: run-to-run adaptive feedforward control (Chapter 4) and position-tracking feedback control (Chapter 5).

Chapter 4

Run-to-Run Control

A run-to-run control is proposed for soft landing. The search method is based on Bayesian optimization, and several ideas are introduced for its application in run-to-run strategies. Additionally, methods for the input parametrization and dimension reduction are presented. Lastly, the control is analyzed through simulated and experimental tests.

4.1 Introduction

Cycle-to-cycle learning-type strategies may be used for improving the robustness of open-loop or feedforward soft-landing controllers by taking advantage of the repetitive functioning of these switching devices and adapting the input profiles. Examples of proposals found in the literature include iterative learning [13], [72] and extremum seeking controllers [73], [74]. Run-to-run (R2R) control, in contrast with other learning-type strategies, only requires one evaluation value for each cycle [75]. The most popular application is semiconductor manufacturing [76], [77] for the control of properties that cannot be measured during each operation, e.g. wafer thickness. It is also suitable for controlling low-cost reluctance actuators because, although it is difficult to measure the position in real time, other variables can be measured or derived to evaluate each cycle, for example, the duration of the bouncing [78] or the sound intensity of the impact.

R2R controllers can be classified as direct and indirect. In direct R2R methods, the input is directly calculated in an optimization process of the evaluation variable [79], [80]. On the other hand, indirect R2R consists in calculating some decision variables that indirectly affects the system input. For example, the decision variables may be used to determine the reference [81], parameters of an online feedback controller [82], time intervals of an open-loop input profile [15], [78] or an input offset [83]. This chapter focuses on the design of indirect R2R strategies. It allows separating the optimization process from the input generation.

The optimization problem can be formulated as the minimization of a cost function,

which maps the decision (input) with the evaluation (output) variables. In that regard, an important distinction is between implicit and explicit methods [84]. On the one hand, an explicit optimization depends on a process model, which may be fixed or refined in each iteration. On the other hand, an implicit method treats the cost function as a black box. Designing a model-based R2R strategy for reluctance actuators is very challenging, as it needs an explicit definition of the cost function to be optimized. Therefore, the R2R strategies that are studied in this chapter are implicit. Without an explicit definition of the cost function, each evaluation must be performed on the real device. Hence, the optimization convergence speed is of great importance. As stated by Srinivasan et al.[84], the gradient of the cost function can be approximated by disturbing the d decision variables. However, the estimated derivatives are very sensitive to noise and need at least $d+1$ function evaluations in each iteration. A better solution for this type of problem, proposed by Ramirez-Laboreo et al. [78], is based in a derivative-free pattern search (PS) method [85]. However, the optimization still requires several function evaluations in each iteration.

Besides the optimization algorithm, the input signal selection is critical for the control performance. Furthermore, the signal must be parametrized in a way that permits modifying it in each iteration from a limited set of decision variables. If the voltage is chosen as the input, open-loop bang-bang or bang-bang-off signals are adequate for soft landing and very easily parametrizable. On the other hand, controllers with the current as input are more robust to changes in the temperature, as shown in Chapter 3. However, the parametrization of open-loop current signals is more challenging because of its relatively slow dynamics, which is comparable to the mechanical dynamics.

The main proposal presented in this chapter is an R2R strategy with a search function based on Bayesian optimization (BO) and a flatness-based feedforward controller for the input generation. To demonstrate the effectiveness of the proposal, multiple simulations are performed with a dynamical model that fits a commercial solenoid valve, as in Chapter 3. The proposed R2R control is compared with two alternatives. The first one uses a PS method and was previously proposed for bounce reduction of relays [78]. The second one uses a Nelder–Mead (NM) search method, which requires fewer function evaluations in each iteration than the PS method. Then, to validate the control applicability in real devices, the R2R strategies are applied to solenoid valves using an experimental setup.

4.2 Problem statement

Most commonly in R2R optimization problems, the system dynamics is formulated with a conventional state-space representation [86], but it is not accurate enough in this scenario. As mentioned in previous chapters, switch-type actuators have three different dynamic modes, corresponding to the upper and lower position boundaries and the motion between those limits. Furthermore, other dynamical or output variables may also

have discrete behaviors. Therefore, the dynamical system cannot be considered a continuous dynamical system, but a hybrid automaton. Similarly to the generalized form presented in [53], it can be formulated as

$$\frac{\mathrm{d}}{\mathrm{d}t}\,\boldsymbol{x}^j(t) = \boldsymbol{f}_q\big(\boldsymbol{x}^j(t),\, \boldsymbol{u}^j(t),\, \boldsymbol{d}^j(t)\big), \qquad \boldsymbol{x}^j(t) \in C_q, \tag{4.1}$$

$$\big(\boldsymbol{x}^j(t^+),\, q^j(t^+)\big) = \boldsymbol{G}_q\big(\boldsymbol{x}^j(t)\big), \qquad \boldsymbol{x}^j(t) \in D_q, \tag{4.2}$$

$$\big(\boldsymbol{x}^j(0),\, q^j(0)\big) = (\boldsymbol{x}_0,\, q_0), \tag{4.3}$$

where $\boldsymbol{x}^j(t)$ the continuous state vector, $q^j(t) \in \{1,\, 2,\, \ldots\}$ the discrete state, $\boldsymbol{u}^j(t)$ the input vector, $\boldsymbol{d}^j(t)$ the disturbance vector, $\boldsymbol{f}_q$ the flow map, $\boldsymbol{G}_q$ the jump map, C_q the flow set, D_q the jump set, and $(\boldsymbol{x}_0,\, q_0)$ the initial states. Note that, for cycle-to-cycle controllers, it is important to explicitly discern between iterations, hence the superscript j represents the iteration number. Note also that, to simplify the problem statement, the usual continuous output vector is not directly defined. It can be included in—or derived from—$\boldsymbol{x}^j(t)$, so there is no loss of generality.

Secondly, the input signal is parameterized into a discrete set of decision variables, as is required for R2R control. For any instant t, the input is obtained as

$$\boldsymbol{u}^j(t) = \boldsymbol{U}\big(\boldsymbol{\chi}^j,\, t\big), \tag{4.4}$$

where $\boldsymbol{\chi}^j \in \mathbb{R}^d$ is the decision vector and $\boldsymbol{U}$ is the function that generates the input signals.

Thirdly, the variable to be optimized in each repeated cycle is defined. It is obtained directly or indirectly from measurements, which means the optimization problem is measurement-based. This variable may be related to the impact noise level, the bouncing duration, the transient time, or a combination of them. It can be defined as a terminal cost ψ_{r}^j to be optimized,

$$\psi_{\mathrm{r}}^j = J\big(\boldsymbol{x}^j(t_{\mathrm{f}})\big), \tag{4.5}$$

being J the cost function and t_{f} the operation final time.

The optimization process exploits the stored data from previous iterations, which are the decision vectors $\boldsymbol{\chi}^i$ and their corresponding observed costs ψ^i, for all $i = 1,\, 2,\, \ldots,\, j-1$. Note that, due to possible measurement errors, there is a distinction between *observed* costs ψ^i and *real* ones ψ_{r}^i.

Finally, the general measurement-based terminal-cost optimization under uncer-

tainty can be formulated as follows:

$$\begin{aligned}
\min_{\boldsymbol{\chi}^j} \quad & \psi_{\mathrm{r}}^j = J\big(\boldsymbol{x}^j(t_{\mathrm{f}})\big), && (4.6)\\
\text{such that} \quad & (4.1) - (4.4), \\
& \boldsymbol{S}\big(\boldsymbol{x}^j(t),\, \boldsymbol{u}^j(t),\, q^j(t)\big) \leq \mathbf{0}, && (4.7)\\
& \boldsymbol{T}\big(\boldsymbol{x}^j(t_{\mathrm{f}}),\, q^j(t_{\mathrm{f}})\big) \leq \mathbf{0}, && (4.8)\\
\text{given} \quad & \mathcal{D}^{j-1} = \big\{(\boldsymbol{\chi}^i, \psi^i) \mid i = 1,\, 2,\, \ldots,\, j-1\big\}, && (4.9)\\
\text{where} \quad & \psi^i = \psi_{\mathrm{r}}^i + \nu^i, && (4.10)
\end{aligned}$$

being $\boldsymbol{S}$ and $\boldsymbol{T}$ the path and final state constraint functions, $\boldsymbol{\mathcal{D}}^{j-1}$ the data set composed of the previous decision vectors and observed costs, ν^i the ith observation noise, and $\mathbf{0}$ a column vector of all zeros.

As an implicit R2R optimization, the cost function and system dynamics are treated as a black box. To simplify the optimization formulation, the input generation may be included in the black-box function, resulting in the following reformulation,

$$\begin{aligned}
\min_{\boldsymbol{\chi}^j} \quad & \psi_{\mathrm{r}}^j = \mathcal{J}\big(\boldsymbol{\chi}^j\big) + \delta^j, && (4.11)\\
\text{such that} \quad & \boldsymbol{\mathcal{S}}\big(\boldsymbol{\chi}^j\big) \leq \mathbf{0}, && (4.12)\\
\text{given} \quad & \mathcal{D}^{j-1} = \big\{(\boldsymbol{\chi}^i, \psi^i) \mid i = 1,\, 2,\, \ldots,\, k-1\big\}, && (4.13)\\
\text{where} \quad & \psi^i = \psi_{\mathrm{r}}^i + \nu^i, && (4.14)
\end{aligned}$$

where the new black-box cost function $\mathcal{J}$ maps the decision vector to the cost, δ^j is the additive effect of the disturbance $\boldsymbol{d}^j(t)$ from (4.1), and the new constraint function $\boldsymbol{\mathcal{S}}$ acts as a replacement of $\boldsymbol{S}$ and $\boldsymbol{T}$.

4.3 Run-to-run algorithm

This section presents the R2R control strategy with the proposed search method.

4.3.1 Main algorithm

Firstly, the generalized R2R control algorithm is presented. It must be iterative to account for and exploit the cyclic operations. In particular, reluctance actuators are characterized by having two distinct operation types depending on the motion direction: making and breaking. These two operation types act alternatively, which means that a complete commutation cycle consists of one operation of each.

The R2R solution (see Algorithm 4.1) consists in a loop in which every iteration j comprises the generation of the input signals for the making and breaking operations

($\boldsymbol{u}_{\mathbf{m}}^{j}$ and $\boldsymbol{u}_{\mathbf{b}}^{j}$, respectively) from their corresponding decision vectors ($\boldsymbol{\chi}_{\mathbf{m}}^{j}$ and $\boldsymbol{\chi}_{\mathbf{b}}^{j}$), the application of these signals and the observation of the costs (ψ_{m}^{j} and ψ_{b}^{j}), and lastly, the optimization process in which the next decision vectors ($\boldsymbol{\chi}_{\mathbf{m}}^{j+1}$ and $\boldsymbol{\chi}_{\mathbf{b}}^{j+1}$) are obtained from previous data ($\mathcal{D}_{\mathrm{m}}^{j}$ and $\mathcal{D}_{\mathrm{b}}^{j}$).

Algorithm 4.1 Run-to-run control

Initialize: $\boldsymbol{\chi}_{\mathbf{m}}^{1}$, $\boldsymbol{\chi}_{\mathbf{b}}^{1}$
for $j \leftarrow 1$ **to** num. commutations **do**
  $\boldsymbol{u}_{\mathbf{m}}^{j}(t) \leftarrow$ GENERATE INPUT($\boldsymbol{\chi}_{\mathbf{m}}^{j}$)
  $\boldsymbol{u}_{\mathbf{b}}^{j}(t) \leftarrow$ GENERATE INPUT($\boldsymbol{\chi}_{\mathbf{b}}^{j}$)
  Apply $\boldsymbol{u}_{\mathbf{m}}^{j}(t)$ and measure ψ_{m}^{j}
  Apply $\boldsymbol{u}_{\mathbf{b}}^{j}(t)$ and measure ψ_{b}^{j}
  $\boldsymbol{\chi}_{\mathbf{m}}^{j+1} \leftarrow$SEARCH($\mathcal{D}_{\mathrm{m}}^{j}$)
  $\boldsymbol{\chi}_{\mathbf{b}}^{j+1} \leftarrow$SEARCH($\mathcal{D}_{\mathrm{b}}^{j}$)
end for

Notice that the frequency of the cycles is limited by the computation time of the functions GENERATE INPUT and SEARCH. If that time is not small enough, it will be necessary to adapt the algorithm to work around this issue, e.g. by commuting the device several times in each iteration without updating the decision vectors, or by computing in parallel the function algorithms for the making and breaking operations.

While the function GENERATE INPUT must be specifically defined for each situation, the following description of optimization function SEARCH is generalized for any actuator.

4.3.2 Optimization method

Different optimization methods have been explored for the SEARCH function. While alternatives are described in Appendix A, this section focuses on explaining the main proposal. It is based on BO, which is a well-known method of black-box global optimization, and has proven to be effective in real-time control applications, e.g. maximum power point tracking [87], or altitude optimization of airborne wind energy systems [88]. In each iteration, it approximates the black-box function with a random process regressor—which is typically Gaussian [89]—depending on data from previous iterations. Through the regressor, it predicts the output for any point $\boldsymbol{\chi}$. Then, through the maximization of a utility or acquisition function f_{acqn} of the predicted output, it selects the following points to be evaluated $\boldsymbol{\chi}^{j+1}$.

The proposed function is described in Algorithm 4.2. Its inputs are the current point (decision vector $\boldsymbol{\chi}^{j}$), which has been obtained in the previous iteration, and its evaluation ψ^{j}. Its output is the next point $\boldsymbol{\chi}^{j+1}$. Some parameters are set as constant (for

Algorithm 4.2 Optimization

function SEARCH($\boldsymbol{\chi}^j$, ψ^j)
  Constant: σ_{n}^2, d, $k_{\max}$
  Persistent: $\mathbf{X}$, $\boldsymbol{\Psi}$, $\boldsymbol{\Sigma}$, k
  ▷ Learning
  $k \leftarrow k + 1$
  $(\mathbf{X}_k, \Psi_k, \boldsymbol{\Sigma}_{k,k}) \leftarrow \left(\boldsymbol{\chi}^j, \psi^j, \sigma_{\mathrm{n}}^2\right)$
  ▷ Data size constraining
  $(\mathbf{X}, \boldsymbol{\Psi}, \boldsymbol{\Sigma}, k) \leftarrow$ MERGE($\mathbf{X}$, $\boldsymbol{\Psi}$, $\boldsymbol{\Sigma}$, k)
  $(\boldsymbol{\chi}_{\mathbf{lb}}, \boldsymbol{\chi}_{\mathbf{ub}}) \leftarrow$ BOUNDS($\mathbf{X}$, $\boldsymbol{\Psi}$, $\boldsymbol{\Sigma}$)
  if $k > k_{\max}$ **then**
    $(\mathbf{X}, \boldsymbol{\Psi}, \boldsymbol{\Sigma}, k) \leftarrow$ REMOVE($\mathbf{X}$, $\boldsymbol{\Psi}$, $\boldsymbol{\Sigma}$, k, $\boldsymbol{\chi}_{\mathbf{lb}}$, $\boldsymbol{\chi}_{\mathbf{ub}}$)
  end if
  ▷ Acquisition
  $\boldsymbol{\chi}^{j+1} \leftarrow \arg\max_{\boldsymbol{\chi}_{\mathbf{lb}} \leq \boldsymbol{\chi} \leq \boldsymbol{\chi}_{\mathbf{ub}}} f_{\mathrm{acqn}}(\boldsymbol{\chi} \mid \mathbf{X}, \boldsymbol{\Psi}, \boldsymbol{\Sigma})$
  return $\boldsymbol{\chi}^{j+1}$
end function

example, the observation noise variance σ_{n}^2). Also, there are some persistent variables (for example, the number of stored points k), which are changed inside the function but are not required outside of it. Note that these variables are different for each operation type, but, for the sake of simplicity, that distinction is omitted. For clarity, the algorithm is divided into three steps:

1. **Learning**. Updating the stored points $\mathbf{X} \in \mathbb{R}^{d \times k}$ and their evaluations $\boldsymbol{\Psi} \in \mathbb{R}^{1 \times k}$ by the addition of the jth decision vector $\boldsymbol{\chi}^j$ and its cost ψ^j. The variance of the last observation σ_{n}^2 is added to the covariance $\boldsymbol{\Sigma}$.

2. **Data size constraining** ($k \leq k_{\max}$). Observations are merged or removed if necessary. Furthermore, the search space lower and upper bounds ($\boldsymbol{\chi}_{\mathbf{lb}}$ and $\boldsymbol{\chi}_{\mathbf{ub}}$, respectively) are modified in each iteration. These processes are further discussed in Section 4.3.4.

3. **Acquisition**. Selection of next decision vector $\boldsymbol{\chi}^{j+1}$ by maximizing an acquisition function, given the previous data ($\mathbf{X}$, $\boldsymbol{\Psi}$ and $\boldsymbol{\Sigma}$). The search is restricted between the lower bound $\boldsymbol{\chi}_{\mathbf{lb}}$ and the upper bound $\boldsymbol{\chi}_{\mathbf{ub}}$. The proposed acquisition function is defined in Section 4.3.5.

4.3.3 Prior and posterior distributions

The selected model for regression is the Gaussian process. It is the most popular one in the context of BO because it only requires algebraic operations to determine the corre-

sponding posterior distribution. In general, it is completely specified by a mean function $\mathrm{m}(\boldsymbol{\chi})$ and covariance or kernel function $\mathrm{k}(\boldsymbol{\chi}, \boldsymbol{\chi}')$ [89],

$$f(\boldsymbol{\chi}) \sim \mathcal{GP}\big(\mathrm{m}(\boldsymbol{\chi}),\, \mathrm{k}(\boldsymbol{\chi}, \boldsymbol{\chi}')\big). \tag{4.15}$$

For convenience, m is assumed to be constant. On the other hand, the chosen covariance function is squared exponential,

$$\mathrm{k}(\boldsymbol{\chi}, \boldsymbol{\chi}') = \sigma_f^2 \exp\!\left(-\frac{1}{2}\,(\boldsymbol{\chi} - \boldsymbol{\chi}')^{\mathsf{T}}\, \mathrm{diag}(\boldsymbol{l})^{-2}\,(\boldsymbol{\chi} - \boldsymbol{\chi}')\right), \tag{4.16}$$

where σ_f^2 is the characteristic variance and $\mathrm{diag}(\boldsymbol{l}) \in \mathbb{R}^{d\times d}$ is a diagonal matrix with the length scales for each dimension.

In a given iteration, we have the training outputs $\boldsymbol{\Psi} = f(\mathbf{X}) + \boldsymbol{\varepsilon}$. The output noise $\boldsymbol{\varepsilon}$ is an independently distributed Gaussian random vector whose covariance is the diagonal matrix $\boldsymbol{\Sigma}$. Given the properties of Gaussian processes, the joint distribution of $\boldsymbol{\Psi}$ and an output f for an arbitrary $\boldsymbol{\chi}$ is multivariate normal,

$$\begin{bmatrix} \boldsymbol{\Psi}^{\mathsf{T}} \\ f \end{bmatrix} \sim \mathcal{N}\!\left(\mathbf{m},\, \begin{bmatrix} \mathbf{K} + \boldsymbol{\Sigma} & \mathbf{k} \\ \mathbf{k}^{\mathsf{T}} & \mathrm{k}(\boldsymbol{\chi}, \boldsymbol{\chi}) \end{bmatrix}\right), \tag{4.17}$$

where the mean vector $\mathbf{m} \in \mathbb{R}^{(k+1)\times 1}$, kernel matrix $\mathbf{K} \in \mathbb{R}^{k\times k}$ and kernel vector $\mathbf{k} \in \mathbb{R}^{k\times 1}$ are

$$\mathbf{m}_i = \mathrm{m}, \qquad \mathbf{K}_{i,i'} = \mathrm{k}(\mathbf{X}_i, \mathbf{X}_{i'}), \qquad \mathbf{k}_i = \mathrm{k}(\mathbf{X}_i, \boldsymbol{\chi}), \qquad \forall i, i' \leq k. \tag{4.18}$$

The posterior predictive distribution for f is also Gaussian,

$$f \mid \mathbf{X}, \boldsymbol{\Psi}, \boldsymbol{\chi} \sim \mathcal{N}(\mu,\, \sigma^2), \tag{4.19}$$

where the mean μ and variance σ^2 depend on previous data,

$$\mu = \mu(\boldsymbol{\chi}) = (\boldsymbol{\Psi} - \mathbf{m})\,(\mathbf{K} + \boldsymbol{\Sigma})^{-1}\,\mathbf{K} + \mathrm{m}, \tag{4.20}$$

$$\sigma^2 = \sigma^2(\boldsymbol{\chi}) = \mathrm{k}(\boldsymbol{\chi}, \boldsymbol{\chi}) - \mathbf{k}^{\mathsf{T}}\,(\mathbf{K} + \boldsymbol{\Sigma})^{-1}\,\mathbf{k}. \tag{4.21}$$

4.3.4 Data size constraining

For the application of the optimization method for cycle-to-cycle learning type control, it is imperative to constrain the size of stored data in order to prevent the ceaseless increase of computational requirements. For that purpose, three adjustments are introduced, corresponding to the functions in Algorithm 4.2.

Merge

The first measure considers that, if two or more observations are performed for the same input, there is no need to store them separately. By using Bayesian inference, those cost evaluations can be merged and the equivalent cost mean and variance are obtained.

Assumption 4.1. *The ith and kth columns of* $\mathbf{X}$ *are equal (*$\mathbf{X}_i = \mathbf{X}_k$*).*

Proposition 4.1. *Their corresponding costs are* Ψ_i *and* Ψ_k*, with variances* $\Sigma_{i,i}$ *and* $\Sigma_{k,k}$ *are equivalent to* ψ_{eq} *and* σ^2_{eq} *respectively, which are defined as*

$$\psi_{\text{eq}} = \frac{\Sigma_{k,k}\,\Psi_i + \Sigma_{i,i}\,\Psi_k}{\Sigma_{i,i} + \Sigma_{k,k}}, \qquad \sigma^2_{\text{eq}} = \frac{\Sigma_{i,i}\,\Sigma_{k,k}}{\Sigma_{i,i} + \Sigma_{k,k}}. \tag{4.22}$$

Proof. From the first observation $(\Psi_i, \Sigma_{i,i})$, the prior probability density for an arbitrary ψ is proportional to

$$\rho(\psi) \propto \exp\left(-\frac{(\psi - \Psi_i)^2}{2\,\Sigma_{i,i}}\right), \tag{4.23}$$

and the likelihood of the second observation $(\Psi_k, \Sigma_{k,k})$ given ψ is proportional to

$$\rho(\Psi_k \mid \psi) \propto \exp\left(-\frac{(\Psi_k - \psi)^2}{2\,\Sigma_{k,k}}\right). \tag{4.24}$$

Therefore, the posterior probability density is proportional to

$$\begin{aligned}\rho(\psi \mid \Psi_k) &\propto \rho(\psi)\,\rho(\Psi_k|y) \\ &\propto \exp\left(-\frac{(\psi - \Psi_i)^2}{2\,\Sigma_{i,i}} - \frac{(\Psi_k - \psi)^2}{2\,\Sigma_{k,k}}\right) \\ &\propto \exp\left(-\frac{(\psi - \psi_{\text{eq}})^2}{2\,\sigma^2_{\text{eq}}}\right),\end{aligned} \tag{4.25}$$

where the mean ψ_{eq} and variance σ^2_{eq} correspond to (4.22). □

As Bayesian inference is used, the substitution of $(\Psi_i, \Sigma_{i,i})$ with $(\psi_{\text{eq}}, \sigma^2_{\text{eq}})$ and the removal of $(\Psi_k, \Sigma_{k,k})$ will result in the same posterior Gaussian probability distribution (see (4.19)) for the optimization phase. Note that the condition $\mathbf{X}_k = \mathbf{X}_i$ can be relaxed to allow some tolerance. A straightforward and effective way is to round all decision vectors, so two points that are very close together are treated as equal.

Bounds

The second idea is making the search space adaptive, closing around the best point $\boldsymbol{\chi}_{\mathbf{best}}$ when it does not change in consecutive runs, and expanding otherwise. The function is described in Algorithm 4.3. The space expansion in an iteration j is related to the variation of $\boldsymbol{\chi}_{\mathbf{best}}$ from the previous iteration $j-1$. Firstly, the current one $\boldsymbol{\chi}^{j}_{\mathbf{best}}$ is selected based on its mean value (see (4.20)). Secondly, the variations are filtered with an exponentially weighted moving average (EWMA), where $w \in (0,1)$ is the filtering factor. Thirdly, the bound length vector $\boldsymbol{L} \in \mathbb{R}^d$ is updated in each iteration, shrinking if $\boldsymbol{D}_{\boldsymbol{\chi}}$ is small and expanding otherwise (where $c_{\text{shrink}} \in (0,1)$ is the shrinkage coefficient, $|\boldsymbol{D}_{\boldsymbol{\chi}}|$ is the element-wise absolute value, and $\text{sat}^{\boldsymbol{L}_{\mathbf{min}}}_{\boldsymbol{L}_{\mathbf{max}}}$ denotes an element-wise saturation function between the chosen $\boldsymbol{L}_{\mathbf{min}}$ and $\boldsymbol{L}_{\mathbf{max}}$). Finally, the bounds $\boldsymbol{\chi}_{\mathbf{lb}}$ and $\boldsymbol{\chi}_{\mathbf{ub}}$ are calculated around the best point $\boldsymbol{\chi}^{j}_{\mathbf{best}}$, ensuring that they do not surpass the absolute ones $\boldsymbol{\chi}_{\mathbf{lb,abs}}$ and $\boldsymbol{\chi}_{\mathbf{ub,abs}}$.

Algorithm 4.3 Adaptive search bounds

function BOUNDS($\mathbf{X}$, $\boldsymbol{\Psi}$, $\boldsymbol{\Sigma}$)
  Constant: $\boldsymbol{\chi}_{\mathbf{lb,abs}}$, $\boldsymbol{\chi}_{\mathbf{ub,abs}}$, w, c_{shrink}
  Persistent: $\boldsymbol{L}$, $\boldsymbol{D}_{\boldsymbol{\chi}}$, $\boldsymbol{\chi}^{j}_{\mathbf{best}}$
  $\boldsymbol{\chi}^{j-1}_{\mathbf{best}} \leftarrow \boldsymbol{\chi}^{j}_{\mathbf{best}}$
  $\boldsymbol{\chi}^{j}_{\mathbf{best}} \leftarrow \mathbf{X}_i \quad$ such that $i = \arg\min_{i'} \boldsymbol{\mu}(\mathbf{X}_{i'})$
  $\boldsymbol{D}_{\boldsymbol{\chi}} \leftarrow (1-w)\,\boldsymbol{D}_{\boldsymbol{\chi}} + w\left(\boldsymbol{\chi}^{j}_{\mathbf{best}} - \boldsymbol{\chi}^{j-1}_{\mathbf{best}}\right)$
  $\boldsymbol{L} \leftarrow \text{sat}^{\boldsymbol{L}_{\mathbf{max}}}_{\boldsymbol{L}_{\mathbf{min}}}\left(c_{\text{shrink}}\left(\boldsymbol{L} + |\boldsymbol{D}_{\boldsymbol{\chi}}|\right)\right)$
  $\boldsymbol{\chi}_{\mathbf{lb}} \leftarrow \max(\boldsymbol{\chi}_{\mathbf{lb,abs}},\ \boldsymbol{\chi}^{j}_{\mathbf{best}} - \boldsymbol{L})$
  $\boldsymbol{\chi}_{\mathbf{ub}} \leftarrow \min(\boldsymbol{\chi}_{\mathbf{ub,abs}},\ \boldsymbol{\chi}^{j}_{\mathbf{best}} + \boldsymbol{L})$
  return $\boldsymbol{\chi}_{\mathbf{lb}}$, $\boldsymbol{\chi}_{\mathbf{ub}}$
end function

Remove

Merging observations does not guarantee that the size of data history is bounded. Thus, in the case that the number of stored points k surpasses a chosen limit $k_{\max}$, the third measure consists in a two-step removal of points. For the first step, note that the effect of points that are far away from the bounded space—depending on the characteristic length scales $\boldsymbol{l}$ (see (4.16))—can be considered negligible. Thus, any point $\mathbf{X}_i$ that does not meet

$$\boldsymbol{\chi}_{\mathbf{lb}} - 3\,\boldsymbol{l} \leq \mathbf{X}_i \leq \boldsymbol{\chi}_{\mathbf{ub}} + 3\,\boldsymbol{l} \tag{4.26}$$

is removed. The shrinkage and removal of distant points are especially useful for high-dimensional inputs, in which the limited number of stored data is not enough to generate

a regressor of the entire search space. However, in any case, the data size constraining is still not guaranteed. Then, as the second step, a removal criterion is defined to ensure that $k \leq k_{\max}$. One way of approximating the Gaussian process for large data sets is by selecting a subset. The selection criterion introduced by Lawrence et al. [90] aims at keeping the most information of the function by maximizing the differential entropy. However, in the presented problem, only one point at most is needed to be removed from the set in each iteration. Consequently, instead of a selection criterion, it is more straightforward and computationally efficient to define a removal criterion. Considering that, the objective is to find the index i which minimizes the increment of entropy due to the removal of $\mathbf{X}_i$ from $\mathbf{X}$,

$$\arg\min_i \Big(H_f\big(\sigma^2_{\setminus i}\big) - H_f\big(\sigma^2_i\big) \Big), \tag{4.27}$$

being $H_f(\sigma^2_i)$ and $H_f(\sigma^2_{\setminus i})$ the entropy values of f (4.19) before and after the removal of $\mathbf{X}_i$ from $\mathbf{X}$, respectively. Note that the differential entropy of a normal distribution depends solely on the variance,

$$H_f(\sigma^2) = \frac{1}{2}\Big(1 + \ln\big(2\,\pi\,\sigma^2\big)\Big). \tag{4.28}$$

Furthermore, there is no need to evaluate the differential entropy functions for every i. If $\mathbf{X}_i$ were removed, for any i, the resulting posterior variance $\sigma^2_{\setminus i}$ would increase, depending on the observation noise $\Sigma_{i,i}$,

$$\sigma^2_{\setminus i} = \frac{\Sigma_{i,i}\,\sigma^2_i}{\Sigma_{i,i} - \sigma^2_i}. \tag{4.29}$$

By disregarding the constants, the derived entropy increment is proportional to

$$H_f(\sigma^2_{\setminus i}) - H_f(\sigma^2_i) \propto \ln\left(\frac{\sigma^2_{\setminus i}}{\sigma^2_i}\right) \propto -\ln\left(1 - \frac{\sigma^2_i}{\Sigma_{i,i}}\right), \tag{4.30}$$

which monotonically increases with respect to $\sigma^2_i/\Sigma_{i,i}$. Also, for each point $\mathbf{X}_i$, the posterior variance is calculated as $\sigma^2_i = \sigma^2(\mathbf{X}_i)$ from (4.21). Therefore, the index to be removed is simply obtained as follows:

$$\arg\min_i \left(\frac{\sigma^2(\mathbf{X}_i)}{\Sigma_{i,i}}\right). \tag{4.31}$$

4.3.5 Acquisition

The last step is the selection of the next point $\boldsymbol{\chi}^{j+1}$ to evaluate, with a trade off between obtaining the most information of the function (exploration) and attempting to minimize it (exploitation). As f is a random variable, the selection of $\boldsymbol{\chi}^{j+1}$ must be carried

out by the maximization of an acquisition function dependent on μ and σ^2, defined in (4.20) and (4.21). One of the most common acquisition functions is the expected improvement, which is appropriate in regular optimization problems, as it manages to balance exploration and exploitation.

Firstly, the improvement of the Gaussian random variable f can be expressed as a function,

$$I(f) = \max(\mu_{\min} - f,\, 0), \tag{4.32}$$

where $\mu_{\min}$ is the best observation so far, according to their predictive posterior mean values,

$$\mu_{\min} = \min_i \mu(\mathbf{X}_i). \tag{4.33}$$

The expected improvement is the mean of $I(f)$, which can be expressed as

$$\mathrm{E}[I(f)] = \sigma\left(\rho_{\mathcal{N}_\mathrm{S}}(f_\mathrm{n}) + f_\mathrm{n}\,\mathrm{P}_{\mathcal{N}_\mathrm{S}}(f_\mathrm{n})\right), \qquad f_\mathrm{n} = \frac{\mu_{\min} - \mu}{\sigma}, \tag{4.34}$$

where $\rho_{\mathcal{N}_\mathrm{S}}$ and $\mathrm{P}_{\mathcal{N}_\mathrm{S}}$ are the standard probability density and cumulative distribution functions, respectively,

$$\rho_{\mathcal{N}_\mathrm{S}}(f_\mathrm{n}) = \frac{1}{\sqrt{2\,\pi}}\,\exp\!\left(-\frac{{f_\mathrm{n}}^2}{2}\right), \tag{4.35}$$

$$\mathrm{P}_{\mathcal{N}_\mathrm{S}}(f_\mathrm{n}) = \frac{1}{2} + \frac{1}{\sqrt{2\,\pi}}\int_0^{f_\mathrm{n}} \exp\!\left(-\frac{f^2}{2}\right)\mathrm{d}f. \tag{4.36}$$

The reasoning behind (4.32) is that, if the obtained cost f is worse than the best $\mu_{\min}$, there is no improvement but also no loss, so $I(f)$ is zero. This is suitable for optimization problems in which there is no regret. However, for R2R control, there must be a penalty for obtaining worse outputs than $\mu_{\min}$, as this is conducted in real time. Assuming that there are Δj remaining commutations, an improvement over $\mu_{\min}$ would mean a potential improvement for the remaining Δj commutations. On the other hand, a worsening over $\mu_{\min}$ would only mean a worsening for the next commutation, because in the following one it would be possible to commute with an expected cost of $\mu_{\min}$. Taking that into consideration, the *net* improvement is defined,

$$I_{\mathrm{net}}(f) = \begin{cases} \Delta j\,(\mu_{\min} - f), & \text{if } f \le \mu_{\min} \\ \mu_{\min} - f, & \text{if } f > \mu_{\min} \end{cases}. \tag{4.37}$$

Then, the expected net improvement is derived, which can be expressed in relation to the expected improvement $\mathrm{E}[I(f)]$,

$$\mathrm{E}[I_{\mathrm{net}}(f)] = \mu_{\min} - \mu + (\Delta j - 1)\,\mathrm{E}[I(f)]. \tag{4.38}$$

Note that, if $\Delta j = 1$, the maximization of $\mathrm{E}[I_{\mathrm{net}}(f)]$ is equivalent to the minimization of μ. As Δj decreases, the acquisition favors exploitation over exploration, which is the intended behavior. Also, notice that as Δj increases, $\mathrm{E}[I_{\mathrm{net}}(f)]/\Delta j$ tends to $\mathrm{E}[I(f)]$, which would correspond to a regret-free optimization. Moreover, if the number of commutations is not known, Δj can be set as an expectation.

In this control problem, the objective is to minimize a cost related to absolute or nonnegative values, e.g. contact velocities, impact sound intensities, or bouncing durations. Taking that into account, the acquisition function can be further improved. For convenience, f is kept as a Gaussian random variable given by (4.19) and an auxiliary variable f_{sat} is defined by saturating f and ensuring its nonnegativity,

$$f_{\mathrm{sat}} = \max(f, 0). \tag{4.39}$$

Substituting f with f_{sat} in (4.37), the net improvement of the saturated f_{sat} is

$$I_{\mathrm{net}}(f_{\mathrm{sat}}) = \begin{cases} \Delta j\, \mu_{\min}, & \text{if } 0 < f \\ \Delta j\, (\mu_{\min} - f), & \text{if } 0 \leq f \leq \mu_{\min} \\ \mu_{\min} - f, & \text{if } \quad f > \mu_{\min} \end{cases}. \tag{4.40}$$

and its expected value, which is the proposed acquisition function f_{acqn}, can be expressed in terms of the already defined $\mathrm{E}[I_{\mathrm{net}}(f)]$,

$$f_{\mathrm{acqn}} = \mathrm{E}[I_{\mathrm{net}}(f_{\mathrm{sat}})] = \mathrm{E}[I_{\mathrm{net}}(f)] - \Delta j\, \sigma \left(\rho_{\mathcal{N}_{\mathrm{S}}}\left(-\frac{\mu}{\sigma}\right) - \frac{\mu}{\sigma}\, \mathrm{P}_{\mathcal{N}_{\mathrm{S}}}\left(-\frac{\mu}{\sigma}\right) \right). \tag{4.41}$$

Note that the subtracting term is always positive, i.e. $\mathrm{E}[I_{\mathrm{net}}(f_{\mathrm{sat}})] < \mathrm{E}[I_{\mathrm{net}}(f)]$, and increases with respect to the variance, prioritizing exploitation over exploration.

4.4 Input definition

The input function (4.4) must be defined, relating the decision vector $\boldsymbol{\chi}$ to the continuous input signal $\boldsymbol{u}(t)$. Using the current as input is more robust to temperature variations, as shown in Chapter 3, but its parametrization is more challenging. When using the voltage as input, bang-bang signals can be constructed from the time intervals, which would act as the decision variables. For more details about the voltage parametrization, see Appendix B.1. In contrast, the current dynamics is slower, and must be taken into account. Therefore, this section presents a model-based feedforward controller, exploiting its flatness property.

4.4.1 Flatness-based feedforward control

Flatness is a structural property of nonlinear dynamical systems, which may be regarded as an extension of Kalman's controllability of linear systems [91]. (A linear system

is flat if and only if it is controllable). Proving that a system is flat simplifies greatly the design of many types of controllers. Regarding feedforward control, the flatness property implies that both the state and input variables can be expressed as an algebraic function of a fictitious (flat) output and a finite number of its derivatives [92]. This is extremely useful if the flat output trajectory is set as the reference because the input can be calculated without the numerical integration of any differential equation.

The goal of the proposed feedforward controller is to calculate the input signal (current) from a reference trajectory (desired position). The motion dynamics of a generic reluctance actuator must be represented by a flat system. For this purpose, we select the dynamical function of RAM-FK, as defined in Section 2.3.3. Then, the system is defined by three dynamical functions,

$$\dot{z} = v, \tag{4.42a}$$

$$\dot{v} = \frac{F_{\mathrm{pas}}(z, v) + \mathcal{R}'_{\mathrm{g}}(z)\,\phi^2/2}{m_{\mathrm{mov}}}, \tag{4.42b}$$

$$\dot{\phi} = -\frac{\mathcal{R}_{\mathrm{c}}(\phi) + \mathcal{R}_{\mathrm{g}}(z)}{k_{\mathrm{eddy}}}\,\phi + \frac{N}{k_{\mathrm{eddy}}}\,u, \tag{4.42c}$$

while the fictional output is the reference,

$$y = z. \tag{4.43}$$

To prove the flatness property, the state variables are defined as functions of the output and a finite number of its derivatives. Through simple manipulations of (4.42) and (4.43), the following relations are derived:

$$z = y, \tag{4.44a}$$

$$v = \dot{y}, \tag{4.44b}$$

$$\phi = \phi(y, \dot{y}, \ddot{y}) = \sqrt{\frac{2\left(F_{\mathrm{pas}}(y, \dot{y}) - m_{\mathrm{mov}}\,\ddot{y}\right)}{\mathcal{R}'_{\mathrm{g}}(y)}}. \tag{4.44c}$$

Note that there are theoretically two ϕ solutions, but only one is necessary, so the positive one is selected. Furthermore, the input can be defined in the same manner,

$$u = u\Big(y, \dot{y}, \ddot{y}, y^{(3)}\Big) = \frac{\mathcal{R}_{\mathrm{c}}(\phi) + \mathcal{R}_{\mathrm{g}}(y)}{N}\,\phi + \frac{k_{\mathrm{eddy}}}{N}\,\dot{\phi} \tag{4.45}$$

where ϕ is replaced by its function from (4.44c). Similarly, the function for $\dot{\phi}$ can be obtained by calculating the time derivative of (4.42b) and isolating it,

$$\begin{aligned}\dot{\phi} &= \dot{\phi}\Big(y, \dot{y}, \ddot{y}, y^{(3)}\Big) \\ &= \frac{1}{\mathcal{R}'_{\mathrm{g}}(y)\,\phi}\left(\frac{\partial F_{\mathrm{pas}}(y, \dot{y})}{\partial y}\,\dot{y} + \frac{\partial F_{\mathrm{pas}}(y, \dot{y})}{\partial \dot{y}}\,\ddot{y} - m_{\mathrm{mov}}\,y^{(3)} - \frac{1}{2}\,\mathcal{R}''_{\mathrm{g}}(y)\,\dot{y}\,\phi^2\right).\end{aligned} \tag{4.46}$$

Thus, for the system to be flat, F_{pas} must be differentiable and $\mathcal{R}_{\text{g}}$ twice differentiable. There are also singularities for $\phi = 0$ and $\mathcal{R}'_{\text{g}}(y) = 0$. Overall, the flatness condition is

$$\begin{aligned} \frac{F_{\text{pas}}(y,\dot{y}) - m_{\text{mov}}\,\ddot{y}}{\mathcal{R}'_{\text{g}}(y)} > 0 \quad \wedge \quad \exists\, \frac{\partial^2 \mathcal{R}_{\text{g}}(y)}{\partial y^2},\, \frac{\partial F_{\text{pas}}(y,\dot{y})}{\partial y},\, \frac{\partial F_{\text{pas}}(y,\dot{y})}{\partial \dot{y}}, \\ \forall\, y(t),\, \dot{y}(t),\, \ddot{y}(t) \quad \text{such that } \; t \in [t_0,\, t_{\text{f}}], \end{aligned} \tag{4.47}$$

where the times t_0 and t_{f} correspond to the motion start and end, respectively.

We propose to define the predefined position trajectory $z(t)$ as the reference for each operation type. The trajectories can be designed by solving a soft-landing optimal control problem, as in Chapter 3. They can also be established in any other way, as long as they are feasible. Then, they are modified with computationally efficient linear transformations to obtain the output. The first parameters that are considered for decision variables are the initial and final position values, y_0 and y_{f}. Then, the nominal position trajectory $z \in [z_0,\, z_{\text{f}}]$ is linearly transformed into $y \in [y_0,\, y_{\text{f}}]$,

$$y = y'\,(z - z_0) + y_0, \qquad\qquad y' = \frac{\partial y}{\partial z} = \frac{y_{\text{f}} - y_0}{z_{\text{f}} - z_0}, \tag{4.48}$$

where the partial derivative y' is a positive constant. The position derivatives up to the jerk $\dddot{v}$ are transformed as well,

$$\dot{y} = y'\,v, \qquad\qquad \ddot{y} = y'\,\dot{v}, \qquad\qquad y^{(3)} = y'\,\ddot{v}. \tag{4.49}$$

Then, the input can be calculated from (4.45). However, it is possible that, for a poorly chosen set of parameters and position trajectory, the first flatness condition from (4.47) is not guaranteed. That would mean that, in some interval, the required magnetic force is positive, which is not physically possible, or zero, which is a singularity. In those cases, as the closest feasible approximation, ϕ and $\dot{\phi}$ are set to zero. The input definition is finally expressed as

$$u = \begin{cases} \dfrac{\mathcal{R}_{\text{c}}(\phi) + \mathcal{R}_{\text{g}}(y)}{N}\,\phi + \dfrac{k_{\text{eddy}}}{N}\,\dot{\phi}, & \text{if } \phi^2 > 0 \\ 0, & \text{if } \phi^2 \leq 0 \end{cases}, \tag{4.50}$$

where ϕ and $\dot{\phi}$ are calculated from (4.44c) and (4.46), respectively, depending on y and its derivatives.

Thus, the current signal depends on the nominal position trajectory z, its derivatives v, $\dot{v}$, $\ddot{v}$, and the model parameters, including y_0 and y_{f}. On the one hand, the nominal position and its derivatives are established prior to the control. Moreover, depending on the case, some of the parameters are considered constants, because they have been identified accurately and their variability between units is negligible. On the other hand, the

remaining parameters are assumed unknown and will be treated as decision variables, which can be modified in each cycle. As their magnitudes may differ greatly, it is convenient to normalize each one. Consider $\boldsymbol{\theta}$ to be the vector of unknown parameters. Assuming that each parameter is bounded such that $\theta_i \in [\theta_{\mathrm{lb}i},\ \theta_{\mathrm{ub}i}]$, the normalization is achieved through a linear transformation,

$$\chi_i = \frac{2\,\theta_i - \theta_{\mathrm{ub}i} - \theta_{\mathrm{lb}i}}{\theta_{\mathrm{ub}i} - \theta_{\mathrm{lb}i}}. \tag{4.51}$$

Thus, the decision variables are bounded such that $\chi_i \in [-1,\ 1]$.

Note that this resembles an online identification process, as the parameter-related decision variables are optimized in an iterative fashion. However, the parameters are not optimized to reduce estimation errors, but solely to improve the performance, i.e. minimize the defined cost. Thus, the parameters may not converge to their real values if it is not necessary for the control. This is not a limitation but a design choice: the objective is to minimize a certain cost, not to identify the system. Note also that, in an R2R application, the data is very limited (only one cost value per iteration), so it would not be possible to guarantee that the model parameters converge to the real values. Furthermore, the parameter-related decision variables are optimized independently for each operation, so they may be able to correct certain phenomena that are not taken into account by the dynamical model and act differently in each operation type, e.g. magnetic hysteresis.

Note that the input has only been defined for the operations, i.e. during motion. Then, the signal for the complete cycle must be constructed. After each operation, steady current values must be applied to maintain the actuator in its position ($z_{\min}$ after the making operation and $z_{\max}$ after the breaking operation). Also, there need to be feasible transitions between the steady and the operation currents, and vice versa.

4.4.2 Dimension reduction

The convergence rate of the optimization process is strongly dependent on the dimension of the decision vector. Thus, it is highly recommendable to remove redundant decision variables whose effect on the input can be replicated through a combination of other variables. Some of these redundancies may be easy to spot through an examination of the input function (see (4.44c), (4.46) and (4.50)). In that case, through some change of variables, an equivalent input function with fewer parameters can be derived. To ensure that there are no more redundant decision variables, the input function (4.4) can be interpreted as a discrete-time system, where the decision variables constitute the state vector,

$$\begin{cases} \boldsymbol{\chi}(t_{i+1}) = \boldsymbol{\chi}(t_i), \\ u(t_i) = U(\boldsymbol{\chi}(t_i), t_i). \end{cases} \tag{4.52}$$

Then, its local observability matrix $\mathcal{O} \in \mathbb{R}^{d\times d}$ for consecutive time samples t_1, t_2, …, t_d is constructed,

$$\mathcal{O} = \begin{bmatrix} \dfrac{\partial U(\boldsymbol{\chi}, t_1)}{\partial \chi_1} & \dfrac{\partial U(\boldsymbol{\chi}, t_1)}{\partial \chi_2} & \cdots & \dfrac{\partial U(\boldsymbol{\chi}, t_1)}{\partial \chi_d} \\ \dfrac{\partial U(\boldsymbol{\chi}, t_2)}{\partial \chi_1} & \dfrac{\partial U(\boldsymbol{\chi}, t_2)}{\partial \chi_2} & \cdots & \dfrac{\partial U(\boldsymbol{\chi}, t_2)}{\partial \chi_d} \\ \vdots & \vdots & \ddots & \vdots \\ \dfrac{\partial U(\boldsymbol{\chi}, t_d)}{\partial \chi_1} & \dfrac{\partial U(\boldsymbol{\chi}, t_d)}{\partial \chi_2} & \cdots & \dfrac{\partial U(\boldsymbol{\chi}, t_d)}{\partial \chi_d} \end{bmatrix}. \tag{4.53}$$

If the matrix is full-rank—except for singularities—the effect of the decision variables χ_i are independent. Even so, it may be still possible to approximate the effect of one or several decision variables with a combination of the remaining ones. This analysis is very complex, due to the highly nonlinear input function (4.45). Thus, we propose to perform a local sensitivity analysis, at $\boldsymbol{\chi} = \mathbf{0}$, which is equivalent to assuming the errors of the first-order Taylor series negligible,

$$U(\boldsymbol{\chi}, t) - U(\mathbf{0}, t) \approx \sum_{i=1}^{d} \frac{\partial U(\boldsymbol{\chi}, t)}{\partial \chi_i}\bigg|_{\boldsymbol{\chi}=\mathbf{0}} \chi_i = \nabla U(t)\, \boldsymbol{\chi}. \tag{4.54}$$

The sensitivities are set as the partial derivatives of U, which can be calculated for the nominal case $\boldsymbol{\chi} = \mathbf{0}$ for every t. Just by comparing these partial derivatives, it is possible to determine which pair of parameters have very similar effects on the input, or which parameters have a negligible effect. Still, there may be other cases of near collinearity between sensitivities that are not apparent. One relatively simple way to analyze it is to sample the time (t_1, t_2, …) and create a Jacobian matrix such that each ith row is $\nabla U(t_i)$. Then, the rank of the matrix with a chosen tolerance can be calculated and, if the rank is not full, the decision variables to be removed can be detected with a singular value decomposition. However, this method does not take into account the bounds of each parameter. Instead, we propose the following method:

A decision variable χ_i is a candidate for removal if the variation of u due to χ_i is nearly the same as a variation of u with a certain $\boldsymbol{\chi}$, where its ith element is zero. Formally, the set of all possible solutions is

$$\boldsymbol{\mathcal{X}}_{\setminus i} = \Big\{ \boldsymbol{\chi} \mid \chi_i = 0 \wedge \big(\nabla U_i(t) - \nabla U(t)\, \boldsymbol{\chi}\big)^2 \leq {\chi_{\text{tol}}}^2,\ \forall t \Big\}. \tag{4.55}$$

where χ_{tol} is an arbitrary tolerance. If $\boldsymbol{\mathcal{X}}_{\setminus i}$ is empty, the effect of the decision variable χ_i is not redundant and thus it should not be removed. Otherwise, χ_i is a candidate for removal. As the size $\boldsymbol{\mathcal{X}}_{\setminus i}$ may be larger than one—i.e. multiple solutions—we select the

one with the smallest euclidean norm,

$$\boldsymbol{\chi}_{\setminus i} = \underset{\boldsymbol{\chi} \in \boldsymbol{\mathcal{X}}_{\setminus i}}{\arg\min} \|\boldsymbol{\chi}\|_2. \tag{4.56}$$

This is performed for every decision variable χ_i. Then, the one whose $\boldsymbol{\chi}_{\setminus i}$ has the minimum euclidean norm is removed. Note that, due to the removal of a decision variable, the allowed variations of the input are reduced. To be able to vary it as much as before the removal of χ_j, the bounds $\boldsymbol{\theta}_{\mathbf{ub}}$ and $\boldsymbol{\theta}_{\mathbf{lb}}$ of the remaining parameters must be augmented depending on $\boldsymbol{\chi}_{\setminus j}$. Note that ∇U is proportional to $(\boldsymbol{\theta}_{\mathbf{ub}} - \boldsymbol{\theta}_{\mathbf{lb}})$, so it must also be augmented. Note also that the inputs are still normalized ($\chi_i \in [-1, 1]$). The complete method is presented in Algorithm 4.4, which must be performed for the making and breaking inputs separately.

Algorithm 4.4 Dimension reduction

loop
  for $i \leftarrow 1$ **to** d **do**
    Calculate $\boldsymbol{\mathcal{X}}_{\setminus i}$ ▷ Equation (4.55)
  end for
  if $\boldsymbol{\mathcal{X}}_{\setminus i} = \emptyset \ \forall i$ **then**
    break loop
  end if
  Calculate $\boldsymbol{\chi}_{\setminus i}$ ▷ Equation (4.56)
  $j \leftarrow \arg\min_i \|\boldsymbol{\chi}_{\setminus i}\|_2$
  for $i \leftarrow 1$ **to** d **do**
    $\Delta\theta \leftarrow (\theta_{\mathrm{ub}i} - \theta_{\mathrm{lb}i}) \left|(\chi_{\setminus j})_i\right|$
    $\theta_{\mathrm{ub}i} \leftarrow \theta_{\mathrm{ub}i} + \Delta\theta/2$
    $\theta_{\mathrm{lb}i} \leftarrow \theta_{\mathrm{lb}i} - \Delta\theta/2$
    $\nabla U \leftarrow \nabla U \left(1 + \left|(\chi_{\setminus j})_i\right|\right)$
  end for
  $(\boldsymbol{\chi}, \boldsymbol{\theta}_{\mathbf{lb}}, \boldsymbol{\theta}_{\mathbf{lb}}) \leftarrow$ REMOVE$(\chi_j, \theta_{\mathrm{lb},j}, \theta_{\mathrm{ub},j})$
  $d \leftarrow d - 1$
end loop

4.5 Analyses

The run-to-run control with the proposed search function (Section 4.3) is compared with alternatives based on state-of-the-art direct search methods. In a preliminary analysis (Appendix B), we have performed simulations of run-to-run strategies with voltage signals as input, due to their simpler parametrization. This section, however, focuses

on analyzing the main R2R proposal, using the current as input and thus requiring the input definition described in Section 4.4.

4.5.1 Specification of model and input functions

The device used in the tests is the linear-travel solenoid valve specified in Section 3.4.1. The model is characterized in the same way, with equations (3.40) and (3.41), and the hybrid automaton from Fig. 3.2. While the dynamical model during motion is required for particularizing the feedforward control from Section 4.4.1 to the studied device, the entire model presented in the hybrid automaton is also useful for performing analyses through Monte Carlo simulations, similarly to Section 3.5.2. The nominal values of the parameters are directly taken from Table 3.1. The only modification is the position upper limit, which has been set with the micrometer (shown in Fig. 3.1) so that $z_{\max} = 1.4 \times 10^{-3}$ m.

For the feedforward control, the input is parametrized following the process presented in Section 4.4.1. Firstly, the desired position trajectories have been optimally calculated following the procedure presented in Chapter 3, using the same optimization parameters (Table 3.2). Correspondingly, the initial and final position values are $z_0 = z_{\max}$ and $z_{\mathrm{f}} = z_{\min}$ for the making operation, and vice versa for the breaking operation. Fig 4.1 depicts the desired position and the nominal current signals for both operations.

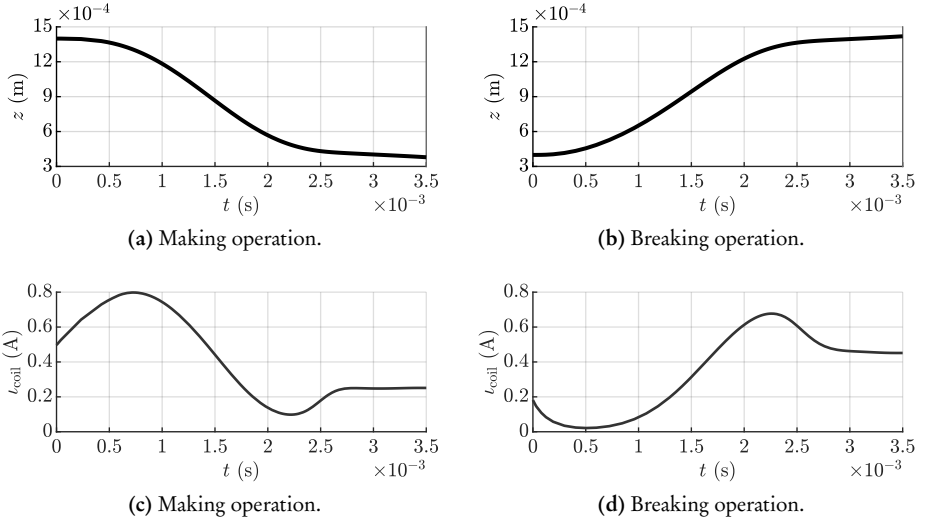

(a) Making operation. **(b)** Breaking operation.

(c) Making operation. **(d)** Breaking operation.

Figure 4.1: Desired position trajectories and nominal current signals.

Secondly, the input function is defined. To simplify the final expression, auxiliary

variable $\phi^{\#} = \phi/\sqrt{m_{\mathrm{mov}}}$ and its derivative are used,

$$u = \begin{cases} \dfrac{\mathcal{R}_{\mathrm{c},0}/(1-\phi^{\#}/\phi^{\#}_{\mathrm{sat}}) + \mathcal{R}_{\mathrm{g}}(y)}{N^{\#}}\,\phi^{\#} + \dfrac{k_{\mathrm{eddy}}}{N^{\#}}\,\dot{\phi}^{\#}, & {\phi^{\#}}^2 > 0 \\ 0, & {\phi^{\#}}^2 \leq 0 \end{cases}, \tag{4.57}$$

being $N^{\#} = N/\sqrt{m_{\mathrm{mov}}}$ and $\phi^{\#}_{\mathrm{sat}} = \phi_{\mathrm{sat}}/\sqrt{m_{\mathrm{mov}}}$ auxiliary parameters. The auxiliary variable $\phi^{\#}$ can be derived from (4.44c),

$$\phi^{\#} = \frac{1}{\sqrt{m_{\mathrm{mov}}}}\,\phi(y,\dot{y},\ddot{y}) = \sqrt{\frac{2\,(k^{\#}_{\mathrm{sp}}\,(z_{\mathrm{sp}}-y) - c^{\#}_{\mathrm{f}}\,\dot{y} - \ddot{y})}{\mathcal{R}'_{\mathrm{g}}(y)}}, \tag{4.58}$$

where $k^{\#}_{\mathrm{sp}} = k_{\mathrm{sp}}/m_{\mathrm{mov}}$ and $c^{\#}_{\mathrm{f}} = c_{\mathrm{f}}/m_{\mathrm{mov}}$. Equivalently, $\dot{\phi}^{\#}$ can be obtained from (4.46),

$$\dot{\phi}^{\#} = \frac{1}{\sqrt{m_{\mathrm{mov}}}}\,\dot{\phi}\Big(y,\dot{y},\ddot{y},y^{(3)}\Big) = -\frac{k^{\#}_{\mathrm{sp}}\,\dot{y} + c^{\#}_{\mathrm{f}}\,\ddot{y} + y^{(3)} + \mathcal{R}''_{\mathrm{g}}(y)\,\dot{y}\,{\phi^{\#}}^2/2}{\mathcal{R}'_{\mathrm{g}}(y)\,\phi^{\#}}. \tag{4.59}$$

Thus, the input depends on these parameters:

$$\boldsymbol{\theta} = \begin{bmatrix} y_0 & y_{\mathrm{f}} & k^{\#}_{\mathrm{sp}} & z_{\mathrm{sp}} & c^{\#}_{\mathrm{f}} & N^{\#} & \mathcal{R}_{\mathrm{c},0} & \phi^{\#}_{\mathrm{sat}} & k_{\mathrm{eddy}} \end{bmatrix}^{\mathsf{T}}, \tag{4.60}$$

which then are normalized (see (4.51)) to obtain the decision vector $\boldsymbol{\chi}$. The parameter bounds are set to $\pm 10\,\%$ of the nominal values θ_i^{nom}. Specifically, if θ_i is z_0 or z_{f},

$$\theta_{\mathrm{lb}\,i} = \theta_i^{\mathrm{nom}} - 0.1\,l_z^{\mathrm{nom}}, \qquad \theta_{\mathrm{ub}\,i} = \theta_i^{\mathrm{nom}} + 0.1\,l_z^{\mathrm{nom}}, \tag{4.61}$$

where $l_z^{\mathrm{nom}} = {z_{\mathrm{max}}}^{\mathrm{nom}} - {z_{\mathrm{min}}}^{\mathrm{nom}}$ is the nominal travel distance. Otherwise,

$$\theta_{\mathrm{lb}\,i} = \theta_i^{\mathrm{nom}} - 0.1\,\theta_i^{\mathrm{nom}}, \qquad \theta_{\mathrm{ub}\,i} = \theta_i^{\mathrm{nom}} + 0.1\,\theta_i^{\mathrm{nom}}. \tag{4.62}$$

Note there was a redundant degree of freedom related to m_{mov}, which has been removed thanks to the change of variables (4.57) and the definition of auxiliary parameters (4.60). Theoretically, there are no other redundancies, because the observability matrix $\mathcal{O}$—as defined in Section 4.4.2—is full-rank. However, there may be some decision variables whose effect can be approximated from a combination of the others. Thus, to detect other candidates for removal, we use Algorithm 4.4, which has been presented in Section 4.4.2. The tolerance is set to $\chi_{\mathrm{tol}} = 10^{-3}\,\mathrm{A}$. Then, the decision variables to be removed are the ones related to $k^{\#}_{\mathrm{sp}}$, $\mathcal{R}_{\mathrm{c},0}$ and k_{eddy}, for both operation types. (A step-by-step description of the algorithm execution is included in Appendix C.1.) Therefore, those parameters are kept constants, and the bounds of the decision variables related to the remaining parameters are augmented to compensate for the removal of degrees of freedom. The dimension of the new decision vectors is $d = 6$.

4.5.2 Compared strategies

The proposed R2R control based on BO is compared with two alternatives. They use the same input definition but different optimization methods.

Run-to-run based on pattern search (R2R-PS)

The first strategy is based on the PS method, a direct-search method previously proposed for soft landing of actuators [78]. The algorithm is described in Appendix A.1. It has the same features as the state-of-the-art approach and also incorporates an additional measure that increases its convergence speed. The function requires evaluating a mesh of $2\,d+1$ points in each iteration (one being the previous best point and the other being around it). The starting meshes $\mathbf{X} \in \mathbb{R}^{d\times(2\,d+1)}$ are equally set for both operations, centered at $\boldsymbol{\chi} = \mathbf{0}$,

$$\mathbf{X} = \begin{bmatrix}\mathbf{0} & \boldsymbol{I} & -\boldsymbol{I}\end{bmatrix}, \tag{4.63}$$

Correspondingly, the rest of persistent variables required in Algorithm A.1 are initialized as

$$\boldsymbol{\chi}_{\mathbf{best}} = \mathbf{0}, \qquad \Delta\mathbf{X} = \begin{bmatrix}\mathbf{0} & \boldsymbol{I} & -\boldsymbol{I}\end{bmatrix}, \qquad k = 1. \tag{4.64}$$

Moreover, the expansion and contraction coefficients are set as follows:

$$c_{\mathrm{exp}} = 2, \qquad c_{\mathrm{con}} = 0.5, \tag{4.65}$$

meaning that the mesh size is halved or doubled if the new best point is the same or not, respectively, as the previous one. The mesh contraction and expansion are restricted by $\Delta\mathbf{X}_{\mathbf{min}}$ and $\Delta\mathbf{X}_{\mathbf{max}}$, respectively. They are set as

$$\Delta\mathbf{X}_{\mathbf{min}} = 10^{-3}\begin{bmatrix}\mathbf{0} & \boldsymbol{I} & -\boldsymbol{I}\end{bmatrix}, \qquad \Delta\mathbf{X}_{\mathbf{max}} = 2\begin{bmatrix}\mathbf{0} & \boldsymbol{I} & -\boldsymbol{I}\end{bmatrix}. \tag{4.66}$$

Run-to-run based on Nelder–Mead (R2R-NM)

The second strategy is based on the NM method, which is also a direct search method [93]. Compared to PS, it requires fewer evaluations per iteration. It has been previously applied for other types of learning controllers, for example, a cyclic adaptive feedforward approach controller for solenoid valves in internal combustion engines [94]. For its application in R2R control, several modifications are introduced to the algorithm: the definition of a minimum simplex volume V_{min}, the modification of the shrink step, and the rearrangement of the algorithm to allow only one evaluation per iteration. For more information about the algorithm, see Appendix A.2. The initial points are set such that they form a regular simplex, centered at $\boldsymbol{\chi} = \mathbf{0}$, with every vertex at a unit distance

from it, and randomly rotated. The simplex is updated depending on three constant coefficients for its reflection, expansion and contraction (c_{ref}, c_{exp} and c_{con} respectively). The constants of the method are set as follows:

$$V_{\min} = 0.005^d, \qquad c_{\mathrm{ref}} = 1, \qquad c_{\mathrm{exp}} = 2, \qquad c_{\mathrm{con}} = 0.5. \tag{4.67}$$

Run-to-run based on Bayesian optimization (R2R-BO)

Concerning our main proposal, the first $2\,d+1$ points are preset as (4.63), gaining some knowledge across the search space before starting the optimization. Regarding the Gaussian process regression, the prior mean values and kernel hyperparameters from (4.16) are specified for each case so the optimization process works efficiently. Then, the following variables are initialized:

$$\boldsymbol{L} = \mathbf{1}, \qquad \boldsymbol{D}_{\boldsymbol{\chi}} = \mathbf{0}, \tag{4.68}$$

where $\mathbf{1}$ denotes a vector of all ones.

Several combinations of the constants c_{shrink} and w have been tested in a preliminary simulated analysis. The selected ones for the final comparison are

$$c_{\mathrm{shrink}} = 0.98, \qquad w = 0.1. \tag{4.69}$$

The remaining constants are set as follows:

$$k_{\max} = 50, \qquad L_{\min i} = 10^{-3}, \qquad L_{\max i} = 2, \qquad \forall i = 1,\, 2,\, \ldots,\, , d. \tag{4.70}$$

Note that the number of stored data $k_{\max}$ depends on the implementation but should be chosen as large as possible. The maximum bound length $\boldsymbol{L}_{\mathbf{max}}$ should be selected conservatively, ensuring that any point is reachable from any other. On the other hand, $\boldsymbol{L}_{\mathbf{min}}$ should be small enough to ensure that the smallest region can be properly approximated with $k_{\max}$ points.

4.5.3 Simulation results

The strategies are compared through a Monte Carlo method, performing 500 simulations of 200 making and breaking commutations for each case. The simulations depend on the parameter vector $\boldsymbol{p}$, which is defined as

$$\boldsymbol{p} = \begin{bmatrix} z_{\min} & z_{\max} & k_{\mathrm{sp}} & z_{\mathrm{sp}} & c_{\mathrm{f}} & N & \mathcal{R}_{\mathrm{c},0} & \phi_{\mathrm{sat}} & k_{\mathrm{eddy}} & m_{\mathrm{mov}} \end{bmatrix}^{\mathsf{T}}. \tag{4.71}$$

Then, to emulate variability, each model parameter p_i is perturbed in every commutation. Thus, for each jth commutation of the nth simulation, the parameter $p_i^{n,j}$ is defined as a random deviate. Specifically,

$$p_i^{n,j} \sim \mathcal{N}\big(\bar{p}_i^{\,n},\, (l_z^{\mathrm{nom}}\, \sigma_p)^2\big), \tag{4.72}$$

if p_i is $z_{\max}$ or $z_{\min}$. Otherwise,

$$p_i^{n,j} \sim \mathcal{N}\big(\bar{p}_i^n,\, (p_i^{\mathrm{nom}}\,\sigma_p)^2\big), \tag{4.73}$$

where the superscript nom is used for denoting the corresponding nominal value (see Table 3.1). The relative standard deviation σ_p serves to emulate the cycle-to-cycle perturbation. Additionally, to emulate unit-to-unit variability, the mean $\bar{\boldsymbol{p}}^n$ is randomly modified in each simulation n, given a continuous uniform distribution,

$$\bar{p}_i^n \sim \mathrm{unif}(p_i^{\mathrm{nom}} - 0.07\,l_z^{\mathrm{nom}},\, p_i^{\mathrm{nom}} + 0.07\,l_z^{\mathrm{nom}}), \tag{4.74}$$

if p_i is $z_{\max}$ or $z_{\min}$. Otherwise,

$$\bar{p}_i^n \sim \mathrm{unif}(0.93\,p_i^{\mathrm{nom}},\, 1.07\,p_i^{\mathrm{nom}}). \tag{4.75}$$

The objective is to minimize the impacts. Therefore, the output or cost ψ is defined as the sum of squared velocities during contact. Note that the elastic bouncing phenomenon is not considered in the proposed model, but bouncing will still occur if the impact acceleration has the opposite sign to the impact velocity. Then, for every simulation, the average cost $\bar{\psi}$ is calculated for each number of commutations j,

$$\bar{\psi} = \frac{1}{j}\sum_{i=1}^{j}\psi^i. \tag{4.76}$$

This way, we determine how good each control is for any number of commutations, and how it improves as the number of commutations increases. In Fig. 4.2, the mean and 25th-75th percentile intervals of $\bar{\psi}$ are represented as functions of the number of commutations. Figs. 4.2a and 4.2b show the average costs for $\sigma_p = 10^{-3}$. Then, σ_p is increased to 2×10^{-3} (Figs. 4.2c and 4.2d), 5×10^{-3} (Figs. 4.2e and 4.2f), and 10^{-2} (Figs. 4.2g and 4.2h). R2R-BO and R2R-PS have the same 13 starting points, so their costs are the same up until that point (the R2R-NM results at the start are also very similar). However, from that point forward the costs from the different strategies start to diverge: the R2R-BO costs are the smallest, following by the costs from R2R-NM, which is still much better than the R2R-PS. As expected, all costs get worse as σ_p increases, and the difference between R2R-BO and R2R-NM augments. In the breaking operations, the costs are generally smaller than in the making operations, and the improvement of R2R-BO over R2R-NM is less significant.

On the one hand, note that R2R-PS and R2R-NM do not require any knowledge of the black-box functions, which makes their implementation for different actuators more straightforward than R2R-BO. They are also more computationally efficient. Between those two, the best strategy is clearly R2R-NM. On the other hand, the best results are obtained with R2R-BO. Moreover, R2R-BO takes into account the stochasticity, so the improvement over R2R-NM is more appreciable for larger cycle-to-cycle variabilities.

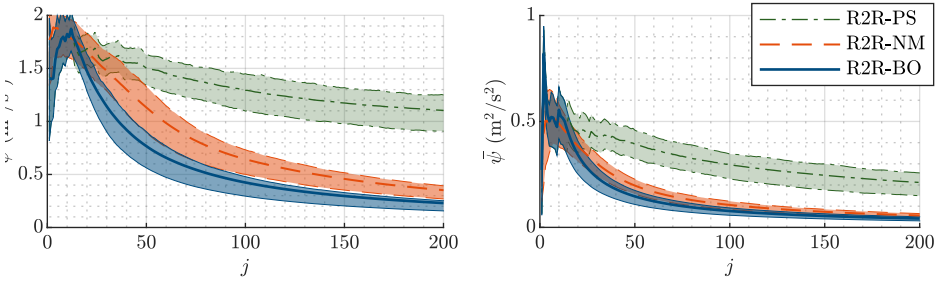

(a) Making operations ($\sigma_p = 10^{-3}$).

(b) Breaking operations ($\sigma_p = 10^{-3}$).

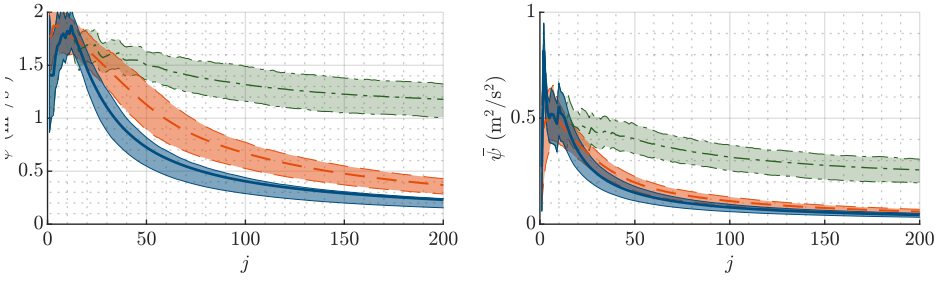

(c) Making operations ($\sigma_p = 2 \times 10^{-3}$).

(d) Breaking operations ($\sigma_p = 2 \times 10^{-3}$).

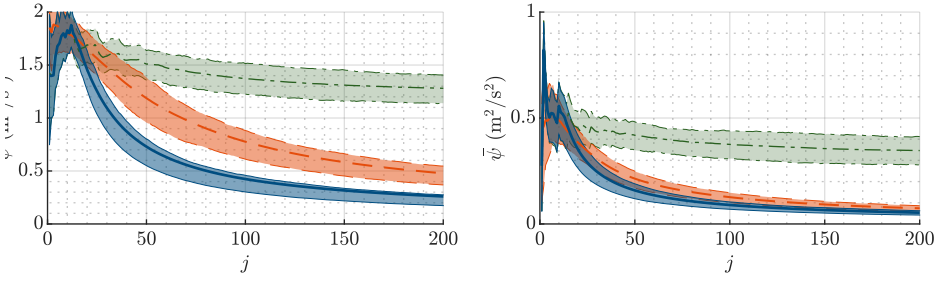

(e) Making operations ($\sigma_p = 5 \times 10^{-3}$).

(f) Breaking operations ($\sigma_p = 5 \times 10^{-3}$).

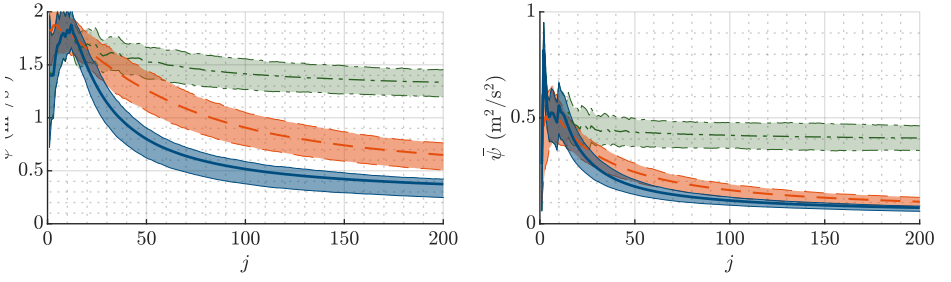

(g) Making operations ($\sigma_p = 10^{-2}$).

(h) Breaking operations ($\sigma_p = 10^{-2}$).

Figure 4.2: Comparison of results (mean values and 25th-75th percentile intervals) from R2R-PS, R2R-NM and R2R-BO, for different σ_p.

4.5.4 Experimental results

To validate the proposed solution for R2R control, experimental testings are performed with five solenoid valves. They are supposedly equal to the one used for identification (see Section 2.2), but unit-to-unit variability is expected. Each control strategy is tested ten times for each device. The impact velocities are unavailable, due to the lack of a position sensor. Instead, an electret microphone is used to measure the impact sound (Fig. 3.1a). The cost is then calculated from the microphone voltage signals,

$$\psi = \int_{t_{\text{trig}}}^{t_{\text{trig}}+\Delta t} {v_{\text{audio}}}^2(t)\,\mathrm{d}t, \tag{4.77}$$

where t_{trig} is established as the first instant t where $v_{\text{audio}}(t) > \max(v_{\text{audio}})/5$ and $\Delta t = 0.01$ s. For reference, a noncontrolled case is also evaluated, with squared voltage signals of 0 and 60 V. Then, the controlled costs y are divided by the average noncontrolled one, resulting in normalized costs. This analysis is focused on the making operations, which present the most notable impact noises. The normalized costs of the making operations are summarized in the histograms from Fig. 4.3.

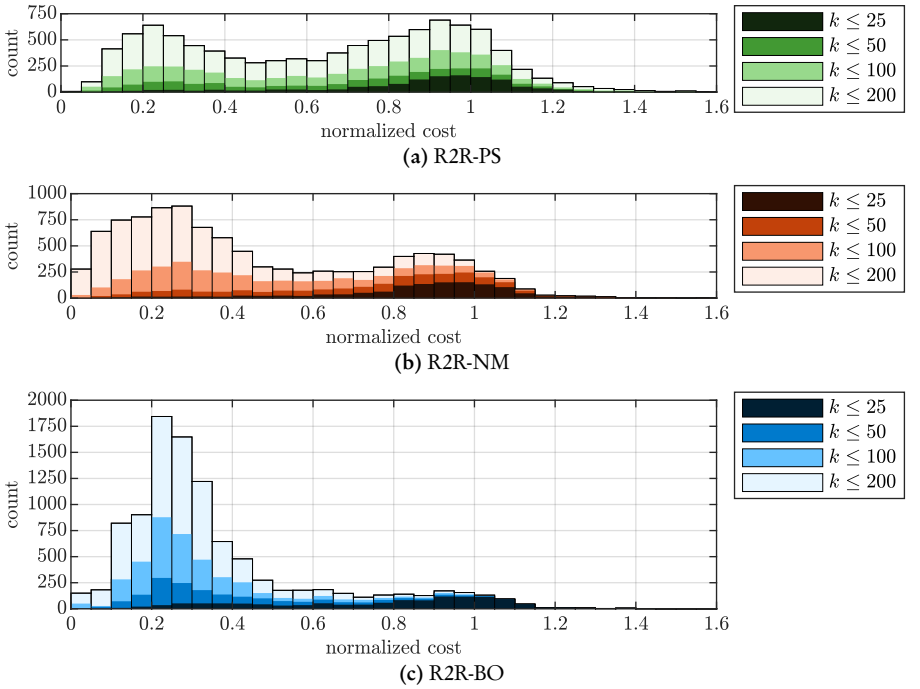

(a) R2R-PS

(b) R2R-NM

(c) R2R-BO

Figure 4.3: Histograms of normalized costs for the first 25, 50, 100 and 200 commutations of each R2R control.

If the control is applied for only 25 commutations, there is a slight improvement over the noncontrolled case: in average 13 % (R2R-PS), 15 % (R2R-NM) and 25 % (R2R-BO). As expected, the results improve as the number of commutations increases. For 200 commutations, the average improvements are 35 % (R2R-PS), 44 % (R2R-NM) and 64 % (R2R-BO). Note that the results of R2R-NM are worse than expected from the simulated analysis. In the fist 100 commutations, the difference between R2R-PS and R2R-NM is not very significant. This indicates that the strategy has a slower convergence rate when applied to the real system. Nevertheless, equivalently to the simulated results, the worst strategy is R2R-PS. Note also that R2R-NM is able to obtain normalized costs below 0.10 more often than R2R-BO, but it also obtains normalized costs larger than 0.35 much more frequently. R2R-BO, on the other hand, is more conservative, keeping most normalized costs around 0.25. Thus, its results are the most robust. Moreover, in average, R2R-BO is better than the other two alternatives for any number of commutations.

4.6 Discussion

R2R control is very useful for cycle-to-cycle adaptation of open-loop and feedforward, allowing the correction of initial discrepancies, due to, for instance, unit-to-unit variability, inaccurate model, or poor identification process. It is also useful for correcting slowly varying perturbations (for instance, mechanical wear), or any kind of perturbation that is replicated in every cycle. We have proposed a new run-to-run strategy based on Bayesian optimization for soft-landing control of short-stroke reluctance actuators. The control does not use position feedback, which makes it useful for applications in which position sensors or observers are not feasible. The complete algorithm has been separated into different parts, most notably the input definition and the search algorithm.

The current has been selected as the input and an input function has been defined. It is a feedforward controller based on a flat dynamical model, so it requires prior knowledge of the system dynamics. Methods for current parametrization and parameter reduction have been proposed for simple reluctance actuators, and they have been put into effect with the dynamical model of a plunger-type solenoid valve. Using the current as input makes the position dynamics independent on the coil resistance. Thus, the controller is more robust to temperature changes. This is an improvement over previous works, which propose to use the voltage as input (see Appendix B).

Although the proposed input definition is based on a model, the cost function is still a black box. Thus, the cycle-to-cycle search process is a black-box optimization. The proposed algorithm is completely generalized. It is based on Bayesian optimization, which has been adapted in several ways for its application in the run-to-run control. The simulated and experimental results show the improvement of our proposal R2R-BO over the alternatives, which use direct search methods (R2R-PS and R2R-NM).

Chapter 5

Sliding-Mode Control

This chapter presents a proposal of a switching model-free sliding-mode controller for position tracking and soft landing, taking into account the hybrid dynamics of short-stroke reluctance actuators. Theoretical and simulated analyses show that soft landing is achievable with reasonable sampling rates.

5.1 Introduction

The main drawback of R2R strategies with open-loop or feedforward controllers is the inability of correcting nonperiodic perturbations. Provided that the actuator position can be measured or estimated in real time, a more robust approach to soft landing is feedback control, in which the position is directly tracked, based on a predefined trajectory.

There is extensive literature regarding position tracking of switch-type reluctance actuators with feedback controllers, although most works deal with more complex and expensive devices, e.g. those having permanent magnets or multiple coils and springs. Many types of controllers have been proposed, such as proportional-integral-derivative [95], proportional-integral with time-varying coefficients [96], linear-quadratic [13], [97], backstepping [98]–[101], or flatness-based feedback linearization [102]–[106].

One important consideration for controlling mass-market single-coil reluctance actuators is the manufacturing variability among devices from the same ensemble. It is especially important for low-cost applications, because the accurate identification of every unit may impose a prohibitive cost. One major approach to deal with model uncertainties is the sliding-mode control (SMC) theory [107]. Several works take this approach. Most commonly, the control law is divided into two terms: an equivalent and a switching control term [108]–[112]. Alternatively, [113] proposed a SMC with only a switching term, which is then approximated to a proportional one. One important aspect that is omitted in these works is the definition of the tracking trajectory, which directly affects the robustness conditions for the SMC. Another important issue is the influence

of the sampling rate. In general, the sliding accuracy is proportional to the square of the switching delay [114]. Still, its effect on the resulting impact velocities needs to be evaluated.

This chapter presents a robust SMC controller for single-coil reluctance actuators. It is initially designed for tracking the position during motion, but it is extended for the entire hybrid system, including the resting positions before and after motion. It is purely a switching controller, which results in a very simple and computationally efficient implementation. Although the resulting controller is model-free—i.e. it does not depend on any model functions or parameters—a dynamical model is required during the design process to guarantee its robustness. A convergence condition is derived, which depends on the system dynamics and the position trajectory. It is then evaluated for a specific dynamical model, based on a commercial solenoid valve, and several trajectories. We also present an analysis of the influence of the sampling rate on the impact velocities.

5.2 Control design

5.2.1 Control for motion dynamics

The controller is initially designed based on the dynamical equations of the motion mode from RAM-FK detailed in Section 2.3.3. For clarity, it is expressed compactly as follows:

$$\dot{\boldsymbol{x}} = \boldsymbol{f}(\boldsymbol{x}) + \boldsymbol{B}\, u, \tag{5.1}$$

where

$$\boldsymbol{x} = \begin{bmatrix} z \\ v \\ \phi \end{bmatrix}, \qquad \boldsymbol{f}(\boldsymbol{x}) = \begin{bmatrix} v \\ f_v(\boldsymbol{x}) \\ f_\phi(\boldsymbol{x}) \end{bmatrix}, \qquad \boldsymbol{B} = \begin{bmatrix} 0 \\ 0 \\ B_\phi \end{bmatrix}, \tag{5.2}$$

and the input u is the voltage. Note that the dynamical system is affine with respect to the input. The functions f_v and f_ϕ and constant B_ϕ are defined as

$$f_v(\boldsymbol{x}) = \frac{F_{\mathrm{pas}}(z, v) + \mathcal{R}'_{\mathrm{g}}(z)\, \phi^2/2}{m_{\mathrm{mov}}}, \tag{5.3a}$$

$$f_\phi(\boldsymbol{x}) = -\frac{R\left(\mathcal{R}_{\mathrm{g}}(z) + \mathcal{R}_{\mathrm{c}}(\phi)\right)\phi}{N^2 + R\, k_{\mathrm{eddy}}}, \tag{5.3b}$$

$$B_\phi = \frac{N}{N^2 + R\, k_{\mathrm{eddy}}}, \tag{5.3c}$$

where the passive force F_{pas} must be a differentiable function of the position and velocity, the gap reluctance $\mathcal{R}_{\mathrm{g}}$ must be a twice-differentiable function of the position, and the core reluctance $\mathcal{R}_{\mathrm{c}}$ must be a differentiable function of the magnetic flux.

As stated in the introduction, our proposal relies on SMC theory. It is assumed that the position z, velocity v, and acceleration a can be obtained either through measurement or estimation. The proposed sliding surface is defined in terms of their errors,

$$s = \left(\varrho_1 + \frac{\mathrm{d}}{\mathrm{d}t}\right)\left(\varrho_2 + \frac{\mathrm{d}}{\mathrm{d}t}\right)\tilde{z} = \tilde{a} + (\varrho_1 + \varrho_2)\,\tilde{v} + \varrho_1\,\varrho_2\,\tilde{z}, \tag{5.4}$$

where ϱ_1 and ϱ_2 are positive constants; and $\tilde{z}$, $\tilde{v}$, and $\tilde{a}$ are the position, velocity and acceleration error, respectively,

$$\tilde{z} = z - z_{\mathrm{ref}}, \qquad \tilde{v} = v - v_{\mathrm{ref}}, \qquad \tilde{a} = a - a_{\mathrm{ref}}. \tag{5.5}$$

Note that the differential equation $s = 0$ from (5.4) has an unique solution, $\tilde{z} = 0$. To achieve that goal, we propose the following model-free control:

$$u_{\mathrm{motion}} = u_{\max}\ \mathrm{sgn}(s)\ \mathrm{sgn}(\phi), \tag{5.6}$$

where $u_{\max}$ is a positive constant.

Proposition 5.1. *If the control* (5.6) *is applied to the system* (5.1) *such that* $u = u_{\mathrm{motion}}$, *and the controller constant* $u_{\max}$ *satisfies*

$$u_{\max} \geq \max\left(\frac{|f_a(\boldsymbol{x}) - \dot{a}_{\mathrm{ref}} + \varepsilon| + \eta}{|B_a(\boldsymbol{x})|}\right), \tag{5.7}$$

where

$$\varepsilon = (\varrho_1 + \varrho_2)\,\tilde{a} + \varrho_1\,\varrho_2\,\tilde{v}, \tag{5.8a}$$

$$f_a(\boldsymbol{x}) = \frac{\partial f_v(\boldsymbol{x})}{\partial \boldsymbol{x}}\,\boldsymbol{f}(\boldsymbol{x}) = \frac{1}{m_{\mathrm{mov}}}\left(\frac{\partial F_{\mathrm{pas}}}{\partial z}(z,v)\,v + \frac{\partial F_{\mathrm{pas}}}{\partial v}(z,v)\,f_v(\boldsymbol{x}) - \frac{1}{2}\,\mathcal{R}_{\mathrm{g}}''(z)\,\phi^2\,v - \mathcal{R}_{\mathrm{g}}'(z)\,\phi\,f_\phi(\boldsymbol{x})\right), \tag{5.8b}$$

$$B_a(\boldsymbol{x}) = -\frac{\partial f_v(\boldsymbol{x})}{\partial \boldsymbol{x}}\,\boldsymbol{B} = \frac{N\,\mathcal{R}_{\mathrm{g}}'(z)\,\phi}{m_{\mathrm{mov}}\,(N^2 + R\,k_{\mathrm{eddy}})}, \tag{5.8c}$$

then the sliding surface s (5.4) *converges to zero in finite time.*

Proof. The following Lyapunov function is defined:

$$V = \frac{1}{2}\,s^2. \tag{5.9}$$

Thus, to ensure that s converges to zero in finite time, the following condition must be satisfied:

$$\dot{V} = s\,\dot{s} \leq -\eta\,|s|, \tag{5.10}$$

being η a positive constant that determines the minimum convergence speed ($|\dot{s}| \geq \eta$). Then, by deriving (5.4) and substituting into (5.10),

$$\dot{V} = s\left(\dot{a} - \dot{a}_{\mathrm{ref}} + (\varrho_1 + \varrho_2)\,\tilde{a} + \varrho_1\,\varrho_2\,\tilde{v}\right), \tag{5.11}$$

where $\dot{a}$ is the jerk and $\dot{a}_{\mathrm{ref}}$ is the reference jerk. The jerk $\dot{a}$ can be derived from the dynamical equations as

$$\dot{a} = \frac{\mathrm{d}f_v(\boldsymbol{x})}{\mathrm{d}t} = \frac{\partial f_v(\boldsymbol{x})}{\partial \boldsymbol{x}}\,\boldsymbol{f}(\boldsymbol{x}) + \frac{\partial f_v(\boldsymbol{x})}{\partial \boldsymbol{x}}\,\boldsymbol{B}\,u = f_a(\boldsymbol{x}) - B_a(\boldsymbol{x})\,u. \tag{5.12}$$

Note that $\dot{a}$ depends on the control u. Thus, the convergence condition (5.10) can be expressed in terms of it,

$$s\left(f_a(\boldsymbol{x}) - \dot{a}_{\mathrm{ref}} + \varepsilon - B_a(\boldsymbol{x})\,u\right) \leq -\eta\,|s|. \tag{5.13}$$

Then, with some manipulations,

$$\mathrm{sgn}(s)\,B_a(\boldsymbol{x})\,u \geq \mathrm{sgn}(s)\,(f_a(\boldsymbol{x}) - \dot{a}_{\mathrm{ref}} + \varepsilon) + \eta. \tag{5.14}$$

Assuming $\mathcal{R}'_{\mathrm{g}}(z) > 0$ for all $z \in [z_{\min}, z_{\max}]$, it is obtained that $\mathrm{sgn}\left(B_a(\boldsymbol{x})\right) = \mathrm{sgn}(\phi)$. Furthermore, if $u = u_{\mathrm{motion}}$, the convergence condition is

$$u_{\max} \geq \frac{\mathrm{sgn}(s)\,(f_a(\boldsymbol{x}) - \dot{a}_{\mathrm{ref}} + \varepsilon) + \eta}{|B_a(\boldsymbol{x})|}, \tag{5.15}$$

which is guaranteed according to (5.7). □

5.2.2 Control for hybrid dynamics

In the previous section, we have proposed a controller and proved its convergence for the motion dynamics. Now, we ensure that it works for the full hybrid system, which is presented in Fig. 5.1. It is assumed that the position trajectory is defined properly before and after the motion. Formally,

$$z_{\mathrm{ref}}(t) = z_0,\ \forall t \leq t_0, \qquad\qquad z_{\mathrm{ref}}(t) = z_{\mathrm{f}},\ \forall t \geq t_{\mathrm{f}}, \tag{5.16}$$

where t_0 and t_{f} represent the initial and final time of the motion, while z_0 and z_{f} are the desired resting positions before and after the motion, respectively.

Tracking the position before motion is quite trivial because it is static when the armature is resting on one of the physical limits. However, in order to start tracking the position at $t = t_0$, the magnetic flux should be ϕ_{ref}, defined as

$$\phi_{\mathrm{ref}} = \phi \quad \text{such that } f_v(z, v, \phi) = 0. \tag{5.17}$$

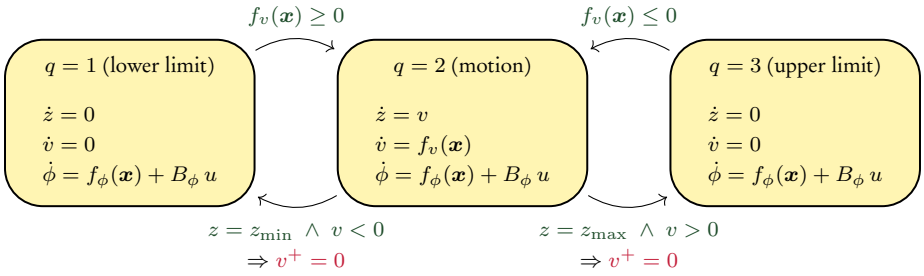

Figure 5.1: Diagram of the hybrid automaton modeling the full dynamical system. Each transition between modes (yellow blocks) occurs when the corresponding guard condition (green text) is satisfied. In each transition from the motion mode, the continuous state jumps according to the corresponding reset rule (red text).

Therefore, the controller should be designed in order to track also the magnetic flux when $t \leq t_0$ so that $\phi = \phi_{\text{ref}}$. For that, we propose the following generalization of the sliding surface s:

$$\varsigma = s + f_v(\boldsymbol{x}) - a = f_v(\boldsymbol{x}) - a_{\text{ref}} + (\varrho_1 + \varrho_2)\,\tilde{v} + \varrho_1\,\varrho_2\,\tilde{z}. \tag{5.18}$$

Note that ς is equal to s in the case of motion, because $a = f_v(\boldsymbol{x})$. In contrast, $\varsigma = f_v(\boldsymbol{x})$ before the start of motion ($t \leq t_0$). Therefore, the sliding condition $\varsigma = 0$ implies that $\phi = \phi_{\text{ref}}$. As a result, if $\varsigma = 0$, the system behaves as desired before and after the start of motion.

Nonetheless, to keep the controller model-free, the proposal cannot use ς due to its dependence on the function f_v. Instead, it should be a function of s. We generalize the proposed control (5.6),

$$u_{\text{hybrid}} = u_{\max}\,\text{sgn}_q(s)\ \text{sgn}(\phi), \tag{5.19}$$

where the new function sgn_q is defined as

$$\text{sgn}_q(s) = \begin{cases} -1, & \text{if } s < 0 \vee (s = 0 \wedge q = 1) \\ +1, & \text{if } s > 0 \vee (s = 0 \wedge q \neq 1) \end{cases}. \tag{5.20}$$

Proposition 5.2. *Consider that the control* (5.19) *is applied to the hybrid system from Fig. 5.1 such that* $u = u_{\text{hybrid}}$*, and that the controller constant* $u_{\max}$ *satisfies* (5.7)*. Then, a sufficient condition for the convergence of* ς *to zero is*

$$\text{sgn}_q(s) = \text{sgn}(\varsigma). \tag{5.21}$$

Proof. The following Lyapunov function is defined:

$$V = \frac{1}{2}\,\varsigma^2. \tag{5.22}$$

Then, following the same line of reasoning as in Section 5.2.1, finite-time convergence to $\varsigma = 0$ requires

$$\operatorname{sgn}(\varsigma)\, B_a(\boldsymbol{x})\, u \geq \operatorname{sgn}(\varsigma)\,(f_a(\boldsymbol{x}) - \dot{a}_{\mathrm{ref}} + \varepsilon) + \eta. \tag{5.23}$$

Moreover, if $u = u_{\mathrm{hybrid}}$, the convergence condition is

$$u_{\max} \operatorname{sgn}_q(s)\, \operatorname{sgn}(\varsigma) \geq \frac{\operatorname{sgn}(\varsigma)\,(f_a(\boldsymbol{x}) - \dot{a}_{\mathrm{ref}} + \varepsilon) + \eta}{|B_a(\boldsymbol{x})|}, \tag{5.24}$$

which is true according to (5.7) and (5.21). □

Based on the sufficient condition (5.21), convergence is studied in three separate cases.

1. If $q = 2$, the convergence condition is directly guaranteed because $s = \varsigma$.

2. If $z = z_{\mathrm{ref}} = z_{\max}$ or $z = z_{\mathrm{ref}} = z_{\min}$, s is always zero, but ς may be not. Note that $a_{\mathrm{ref}} = \tilde{v} = \tilde{z} = 0$. Then,

   $$\operatorname{sgn}(\varsigma) = \operatorname{sgn}\big(f_v(\boldsymbol{x})\big). \tag{5.25}$$

   Note also that $f_v(\boldsymbol{x}) < 0$ if $q = 1$ and $f_v(\boldsymbol{x}) > 0$ if $q = 3$, otherwise the hybrid system would make a transition to $q = 2$ (see guard conditions in Fig. 5.1). Therefore,

   $$\operatorname{sgn}(\varsigma) = \operatorname{sgn}\big(f_v(\boldsymbol{x})\big) = \begin{cases} -1, & \text{if } q = 1 \\ +1, & \text{if } q = 3 \end{cases}. \tag{5.26}$$

   Then, given the proposed definition of $\operatorname{sgn}_q(s)$ (5.20), condition (5.21) holds, so convergence is still guaranteed.

3. We still need to check the convergence of the controller in the case that the position is in one of the limits ($q \neq 2$), but the reference is not. In that event, (5.18) is simplified into

   $$\varsigma = f_v(\boldsymbol{x}) + s, \tag{5.27}$$

   where

   $$s = -a_{\mathrm{ref}} - (\varrho_1 + \varrho_2)\, v_{\mathrm{ref}} - \varrho_1\, \varrho_2\, (z_{\mathrm{ref}} - z). \tag{5.28}$$

   Assuming that the position trajectory is defined smoothly at the start of the movement, condition (5.21) is satisfied because, when $z_0 = z_{\min}$ (breaking operation),

   $$f_v(\boldsymbol{x}) < 0, \qquad (z_{\mathrm{ref}} - z_0),\, v_{\mathrm{ref}},\, a_{\mathrm{ref}} \geq 0. \tag{5.29}$$

   Equivalently, when $z_0 = z_{\max}$ (making operation),

   $$f_v(\boldsymbol{x}) > 0, \qquad (z_{\mathrm{ref}} - z_0),\, v_{\mathrm{ref}},\, a_{\mathrm{ref}} \leq 0. \tag{5.30}$$

On the other hand, at the end of the movement, if z has reached the limit but z_{ref} not yet, the condition is not necessarily satisfied. This may seem like a limitation, but, if the mover has reached the final position prematurely, it is actually preferable keep it in the resting position instead of separating it to continue following the trajectory. Thus, expert rules are added to the controller so the mover is kept at $z_{\mathrm{f}} = z_{\min}$ (making operation) or $z_{\mathrm{f}} = z_{\max}$ (breaking operation),

$$u = \begin{cases} u_{\max}\ \mathrm{sgn}(\phi) & \text{if } z = z_{\mathrm{f}} = z_{\min} \\ 0, & \text{if } z = z_{\mathrm{f}} = z_{\max}\,. \\ u_{\max}\ \mathrm{sgn}_q(s)\ \mathrm{sgn}(\phi), & \text{otherwise} \end{cases} \tag{5.31}$$

5.3 Analyses

5.3.1 Convergence

For the given dynamical model, it is impossible to guarantee convergence in general, for any feasible state. As a clear counterexample, setting $\phi = 0$ makes $B_a(\boldsymbol{x}) = 0$, and the convergence condition (5.7) becomes $u_{\max} \geq \infty$. Therefore, the convergence must be studied for a given trajectory. To illustrate this, three different position trajectories are defined. Each one of them consists of a making operation, followed by a breaking operation. The motion intervals are defined with fifth-degree polynomials, satisfying the boundary conditions

$$\begin{aligned} z_{\mathrm{ref}}(t_0) &= z_0, \qquad v_{\mathrm{ref}}(t_0) = 0, \qquad a_{\mathrm{ref}}(t_0) = 0, \\ z_{\mathrm{ref}}(t_{\mathrm{f}}) &= z_{\mathrm{f}}, \qquad v_{\mathrm{ref}}(t_{\mathrm{f}}) = 0, \qquad a_{\mathrm{ref}}(t_{\mathrm{f}}) = 0. \end{aligned} \tag{5.32}$$

Moreover, for the sake of simplicity, the time intervals are defined in terms of the motion duration $\tau_{\mathrm{mov}} = t_{\mathrm{f}} - t_0$, where $\tau_{\mathrm{mov}} = 3,\ 4,\ 5\,\mathrm{ms}$, for each case. There are also short time intervals equal to $\tau_{\mathrm{mov}}/4$ before and after each operation where $z_{\mathrm{ref}} = z_0$ and $z_{\mathrm{ref}} = z_{\mathrm{f}}$, respectively.

The actuator model is particularized to the commercial solenoid valve depicted in Fig. 3.1a, whose estimated parameters are presented in Table 3.1. To be consistent with Chapter 4, the upper limit is set as $z_{\max} = 1.4 \times 10^{-3}\,\mathrm{m}$. Moreover, the passive force F_{pas} is modeled based on an ideal mass-spring-damper system; whereas the gap and core reluctance terms $\mathcal{R}_{\mathrm{g}}$ and $\mathcal{R}_{\mathrm{c}}$ are modeled as explained in Sections 2.3.1 and 2.3.2,

$$\begin{gathered} F_{\mathrm{pas}}(z, v) = k_{\mathrm{sp}}\,(z_{\mathrm{sp}} - z) - c_{\mathrm{f}}\,v, \\ \mathcal{R}_{\mathrm{g}}(z) = \mathcal{R}_{\mathrm{g},0} + \frac{\mathcal{R}'_{\mathrm{g},0}\,z}{1 + k_1\,z\,\ln(k_2/z)}, \qquad \mathcal{R}_{\mathrm{c}}(\phi) = \frac{\mathcal{R}_{\mathrm{c},0}}{1 - |\phi|/\phi_{\mathrm{sat}}}. \end{gathered} \tag{5.33}$$

The desired position z_{ref} and its derivatives v_{ref} and a_{ref} are displayed in Fig 5.2a,

5.2c and 5.2e, respectively. Three additional useful signals are calculated and shown in Fig. 5.2:

1. The reference magnetic force (Fig. 5.2b), defined as the required magnetic force to track z_{ref},

$$F_{\mathrm{mag,\,ref}} = m_{\mathrm{mov}}\, a_{\mathrm{ref}} - F_{\mathrm{pas}}(z_{\mathrm{ref}}, v_{\mathrm{ref}}). \tag{5.34}$$

2. The absolute value of $B_a(\boldsymbol{x}_{\mathbf{ref}})$ (Fig. 5.2d), where the function B_a is defined in (5.8c) and $\boldsymbol{x}_{\mathbf{ref}}$ is the reference state vector,

$$\boldsymbol{x}_{\mathbf{ref}} = \begin{bmatrix} z_{\mathrm{ref}} \\ v_{\mathrm{ref}} \\ \phi_{\mathrm{ref}} \end{bmatrix}. \tag{5.35}$$

   Note that there are two symmetric ϕ_{ref} solutions (positive and negative),

$$\phi_{\mathrm{ref}} = \pm\sqrt{\frac{2\,F_{\mathrm{mag,\,ref}}}{\mathcal{R}'_{\mathrm{g}}(z_{\mathrm{ref}})}}. \tag{5.36}$$

   They result in two also symmetric solutions of $B_a(\boldsymbol{x}_{\mathbf{ref}})$, because B_a is an odd function with respect to ϕ. Thus, $|B_a(\boldsymbol{x}_{\mathbf{ref}})|$ is unique.

3. The absolute value of the reference action u_{ref} (Fig. 5.2f), which is defined as the action u to be able to track z_{ref} in an ideal scenario (no perturbations or errors),

$$u_{\mathrm{ref}} = \frac{f_a(\boldsymbol{x}_{\mathbf{ref}}) - \dot{a}_{\mathrm{ref}}}{B_a(\boldsymbol{x}_{\mathbf{ref}})}. \tag{5.37}$$

   As $\mathcal{R}_{\mathrm{c}}$ is an even function, f_a (5.8b) is also an even function with respect to the magnetic flux. Therefore, $|u_{\mathrm{ref}}|$ is equal for both ϕ_{ref} solutions.

Note in Fig. 5.2b that, if $\tau_{\mathrm{mov}} = 3$ ms, $F_{\mathrm{mag,\,ref}}$ is positive in a small interval in the breaking operation (around $t/\tau_{\mathrm{mov}} = 2$). Thus, this trajectory is infeasible. This can be checked in Fig. 5.2f as well, where $|u_{\mathrm{ref}}|$ tends to infinity as $F_{\mathrm{mag,\,ref}}$ approaches zero. Then, as the motion duration increases, the requirements are less demanding, because v_{ref} and a_{ref} are reduced. Therefore, the maximum values of u^* are also reduced.

A necessary condition for convergence is $u_{\max} > \max(|u_{\mathrm{ref}}|)$. It is sufficient for perfect tracking in the ideal case, in which $\varepsilon = 0$. Otherwise, in general, a sufficient condition for convergence can be derived from (5.7),

$$u_{\max} \geq \max\left(|u_{\mathrm{ref}}|\right) + \frac{\max\left(|\varepsilon|\right) + \eta}{\min\left(|B_a(\boldsymbol{x}_{\mathbf{ref}})|\right)}, \tag{5.38}$$

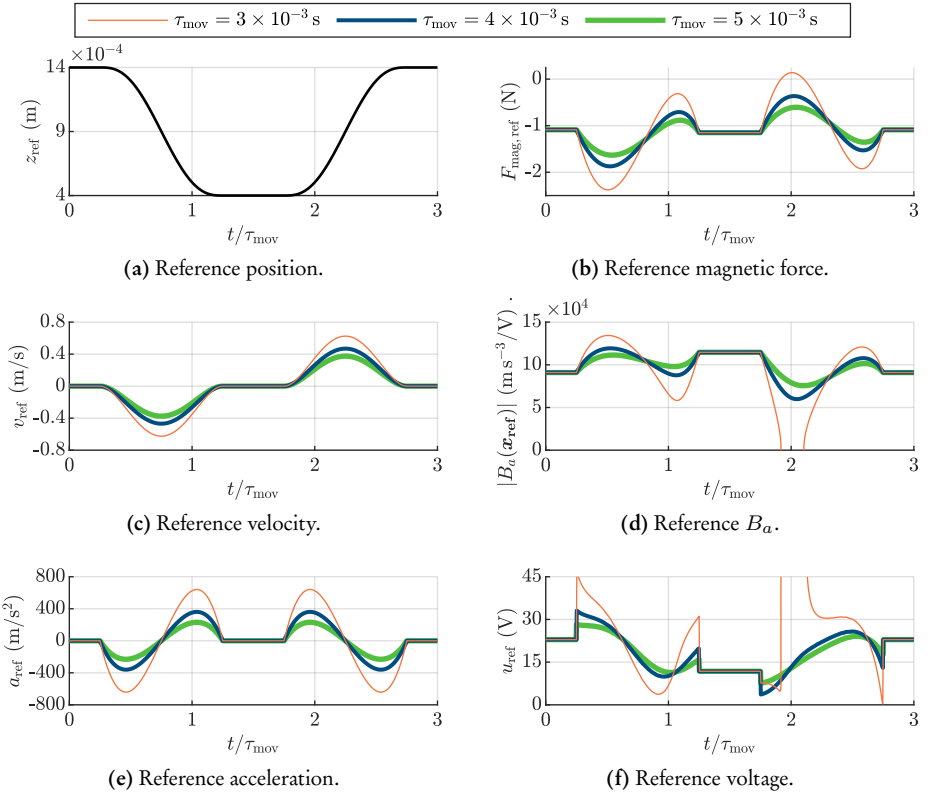

(a) Reference position.

(b) Reference magnetic force.

(c) Reference velocity.

(d) Reference B_a.

(e) Reference acceleration.

(f) Reference voltage.

Figure 5.2: Simulation results. Notice that the time axis is normalized with respect to τ_{mov}.

where ε is bounded, assuming that $\tilde{v}$ and $\tilde{a}$ are bounded,

$$\max\left(|\varepsilon|\right) \leq (\varrho_1 + \varrho_2)\, \max\left(|\tilde{v}|\right) + \varrho_1\, \varrho_2\, \max\left(|\tilde{a}|\right), \tag{5.39}$$

Some assumptions must be made about the bounds of errors $\tilde{v}$ and $\tilde{a}$ to satisfy the previous condition. As an example, the controller constants are set as

$$\varrho_1 = \varrho_2 = 3000\,\text{s}^{-1}, \qquad \eta = 10^5\,\text{m/s}^3. \tag{5.40}$$

And, for the sake of simplicity, very conservative assumptions are made about the error bounds,

$$|\tilde{v}| \leq 0.1\, \max(|v_{\text{ref}}|), \qquad |\tilde{a}| \leq 0.1\, \max(|a_{\text{ref}}|). \tag{5.41}$$

Thus, from (5.38) and (5.39), the convergence condition is $u_{\max} \geq 45.56\,\text{V}$ (if $\tau_{\text{mov}} = 4\,\text{ms}$), or $u_{\max} \geq 35.82\,\text{V}$ (if $\tau_{\text{mov}} = 5\,\text{ms}$). As expected, the condition is less restrictive when the motion duration is increased.

Note that, to ensure that the controller is robust to modeling disturbances, the model parameters used to derive the convergence criteria (5.38) should represent the worst-case scenario, assuming the bounds of each model parameter are known. In practice, however, determining the combination of parameters that results in the worse-case scenario may be too cumbersome, due to the immense number of possibilities. Alternatively, a Monte Carlo evaluation could be performed, permuting all parameters inside their bounds, and then selecting $u_{\max}$ such that (5.38) holds for every case.

5.3.2 Sampling rate analysis

We have proved that convergence can be guaranteed under some reasonable operating conditions. Still, the sampling rate may be a limiting factor, and its influence should be analyzed. Thus, the proposed controller is tested with different sampling periods T_s. As the reference, the second position trajectory from Section 5.3.1 is used ($\tau_\mathrm{mov} = 4\,\mathrm{ms}$). The model parameters and controller constants are set as in Section 5.3.1, with $u_{\max} = 50\,\mathrm{V}$. The dynamical system is simulated using the hybrid automaton from Fig. 2.3.

The impact velocities on contact are obtained for different sampling periods, separating the making and breaking operations. Analogously to (3.68), an equivalent contact velocity is calculated for each case,

$$v_{\mathrm{c,eq}} = \sqrt{\sum_i {v_{\mathrm{c}i}}^2}, \tag{5.42}$$

where $\{v_{\mathrm{c}i}\}$ is the set of contact velocities. The results are depicted in Fig. 5.3.

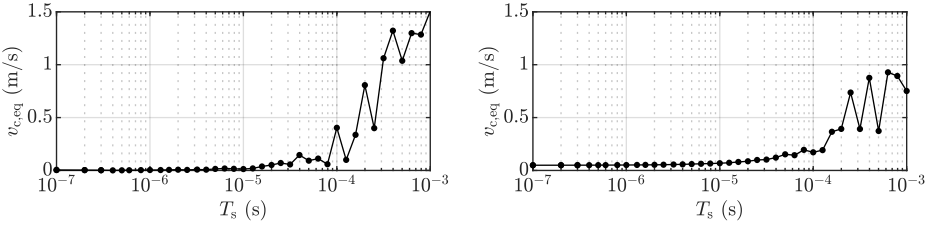

(a) Making operations. **(b)** Breaking operations.

Figure 5.3: Equivalent contact velocities as in terms of the sampling period.

With a sampling rate of 100 kHz, the results are very good, especially in the making operation. For larger sampling periods, the results increasingly worsen. Still, with a sampling rate of only 10 kHz, the impact velocities are better than the ones in a non-controlled scenario. For reference, using a square voltage of 50 V and 0 V, the impact velocities are $-1.572\,\mathrm{m/s}$ and $0.873\,\mathrm{m/s}$, for the making and breaking operations respectively.

Fig. 5.4 presents the resulting state variables for three illustrative sampling periods. With a sampling rate of 1 MHz, the tracking is almost perfect. With a sampling rate of 100 kHz, there is a slight error in the position (almost imperceptible in the graphic presented in Fig. 5.4a), but the impact velocities are appreciably larger (as can be inferred from the velocity graphic in Fig. 5.4b). Still, the performance is very good. With a sampling rate of 10 kHz, the results are much worse. The high ripple of the magnetic flux (represented in Fig. 5.4c) is filtered but leads to significant tracking errors. Even though the position errors may seem small, the velocity errors and, more importantly, the impact velocities are much larger than in the other cases with larger sampling rates.

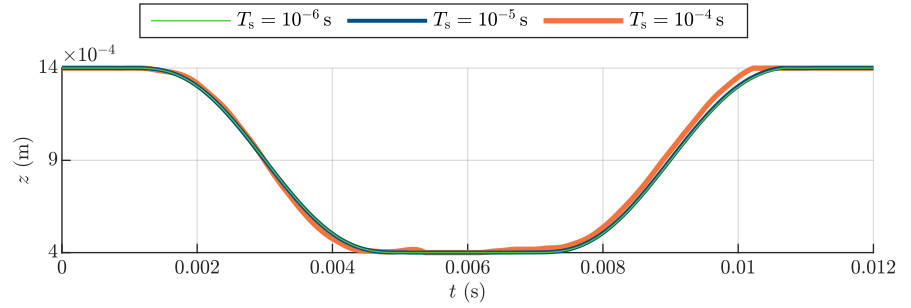

(a) Position.

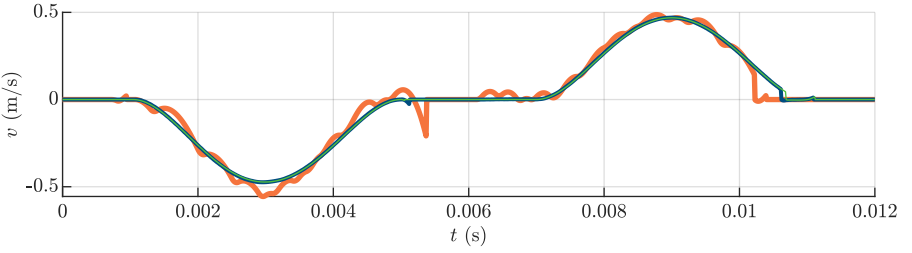

(b) Velocity.

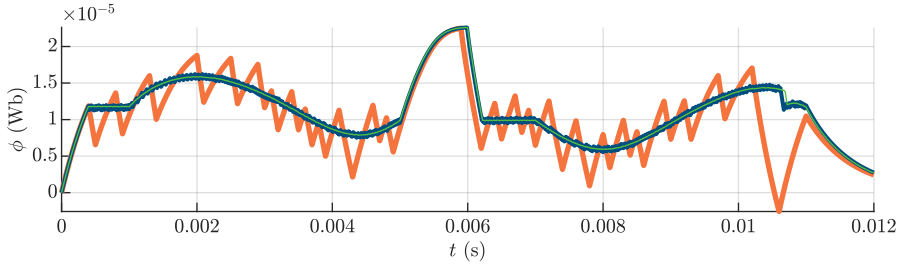

(c) Magnetic flux.

Figure 5.4: Simulated state variables using the controller with three different sampling periods.

5.4 Discussion

We have addressed the soft-landing control of single-coil reluctance actuators, proposing a sliding-mode controller that does not use information about the dynamical system. We have also derived the convergence criteria, based on a generalized dynamical model. This controller requires to know the position and its derivatives, as well as the sign of the magnetic flux. Alternatively, the current through the coil can be restricted to nonnegative values. That way, the magnetic flux is always nonnegative, simplifying the control.

Due to the fast dynamics, the sampling rate must be large enough to track the predefined position and achieve low impact velocities. Note that the position errors may be small with low sampling rates, but the resulting impact velocities are significant. In the end, the sampling rate of the controller itself is not a limiting factor because the designed SMC is very simple. Furthermore, even if a faster control cannot be implemented, the results are still better than in noncontrolled scenarios.

Chapter 6

State Estimation

A novel state estimator is presented for position tracking of reluctance actuators. It is an extended Rauch–Tung–Striebel smoother, which includes several new ideas regarding the discrete model, the inputs and the outputs. The effect of the novel additions is evaluated through a simulated analysis.

6.1 Introduction

Most of the soft-landing solutions for reluctance actuators found in the literature use some kind of position feedback loop [95]–[106], [115]–[119], including the proposal from Chapter 5. However, measuring the position during motion is impractical in many scenarios, especially when using low-cost reluctance actuators. In those cases, position sensors tend to be too expensive in relation to the devices themselves. Alternatively, the position may be estimated from other measurements.

Different estimation techniques have been designed for reluctance actuators. One approach is to estimate the inductance of the coil from the electrical measurements, and then relating it to a certain position using an inverse model [120], a lookup table [121] or a neural network with additional estimated parameters as inputs [122]. A similar idea is calculating the position from a measured current and an estimated magnetic flux [123], or relating the position to the current and its derivative through a polynomial curve fitting technique [124]. These techniques are open loop and rely solely on the characterization of the inductance, magnetic flux or current derivative for every position and current values. Therefore, they are very sensitive to errors in the mapping. Furthermore, generating bijective maps between position and inductance—or flux—is only possible when neglecting certain phenomena, e.g. eddy currents and magnetic hysteresis. Then, some proposals directly account for the motion dynamics by including a model of the mechanical subsystem. These are based on traditional state observers, such as sliding-mode observers [38], or Kalman filter (KF) extensions for nonlinear systems [125]. Nonetheless, these observers still neglect certain electromagnetic phenomena,

most notably the magnetic hysteresis. Still, there are examples of position estimators that take into account this complex phenomenon using heuristic models. For example, Straußberger [126] proposes an open-loop estimator based on a Preisach model.

Nevertheless, designing position estimators for low-cost reluctance actuators is still a very challenging problem. Ideally, they should be based on a complex and accurately identified model. However, as their dynamics are very fast—commutations typically last few milliseconds—, the implementation cost of these complex estimators with a high enough sampling rate is usually prohibitive. Additionally, simplified models are much easier to identify. This is especially relevant for cost-effective manufacturing processes in which each ensemble of actuators has a substantial unit-to-unit variability, which, in turn, implies that model parameters must be estimated or adapted for every single device.

Then, this chapter proposes a novel position estimator for reluctance actuators, introducing two ideas that have not been previously explored for these devices. Firstly, the state estimation is approached as a smoothing problem of a stochastic process, in which the state at a given time is refined by using future observation samples. Secondly, the estimator is designed using a novel set of inputs and outputs. In addition to the electrical signals, the proposed estimator uses discrete information related to its state, in particular whether the armature is resting at one of the contacts, or moving.

6.2 Discrete model for estimation

The complete model presented in Chapter 2 (RAM-JA) is very accurate. It is also computationally efficient compared to other models of similar accuracy (i.e. including magnetic hysteresis, saturation and eddy currents). However, it is still quite complex, with many parameters that need to be identified. Thus, the discrete model used for estimation is based on the basic model (RAM-FK) presented also in the aforementioned chapter.

The number of model parameters are reduced by introducing new auxiliary parameters and variables. The model reduction is similar to the one presented in Section 2.4.1 for the electromagnetic subsystem. In this case, however, the mechanical subsystem is also transformed. For that purpose, the position z and velocity v are normalized,

$$z^{\#} = \frac{z - z_{\min}}{l_z}, \qquad v^{\#} = \frac{\mathrm{d}z}{\mathrm{d}t} = \frac{v}{l_z}, \tag{6.1}$$

where $l_z = z_{\max} - z_{\min}$ is the travel distance. Thus, the new position variable is bounded such that $z^{\#} \in [0, 1]$. Moreover, the flux linkage $\lambda = N\,\phi$ is used as the third state variable. Then, the current is calculated from a simplified output function $h^{\#}$ which neglects both magnetic hysteresis and eddy currents,

$$\iota_{\mathrm{coil}} = h^{\#}(z^{\#}, \lambda, e_\iota) = \left(\mathcal{R}^{\#}_{\mathrm{g}}(z^{\#}) + \mathcal{R}^{\#}_{\mathrm{c}}(\lambda)\right)\lambda + e_\iota, \tag{6.2}$$

where the auxiliary function $\mathcal{R}^{\#}_{\mathrm{g}}(z^{\#}) = \mathcal{R}_{\mathrm{g}}(z)/N^2$ is a scaled reluctance of the gap

(2.30), accounting for magnetic flux fringing; while $\mathcal{R}_{\mathrm{c}}^{\#}(\lambda) = \mathcal{R}_{\mathrm{c}}(\phi)/N^2$ is an scaled reluctance of the core (2.37), accounting for magnetic saturation. Note also the addition of e_ι, which encompasses the modeling errors of the current function.

On the other hand, the dynamics of $v^{\#}$ is based on the acceleration function during motion (2.24),

$$\dot{v}^{\#} = f_v^{\#}(z^{\#}, v^{\#}, \lambda, e_F) = \frac{1}{m_{\mathrm{mov}}^{\#}} \left(F_{\mathrm{pas}}^{\#}(z^{\#}, v^{\#}) - \frac{1}{2}\, \mathcal{R}_{\mathrm{g}}'^{\#}(z^{\#})\, \lambda^2 + e_F \right), \tag{6.3}$$

where the auxiliary parameters and functions are

$$m_{\mathrm{mov}}^{\#} = m_{\mathrm{mov}}\, {l_z}^2, \quad F_{\mathrm{pas}}^{\#}(z^{\#}, v^{\#}) = F_{\mathrm{pas}}(z, v)\, l_z, \quad \mathcal{R}_{\mathrm{g}}'^{\#}(z^{\#}) = \frac{\mathcal{R}_{\mathrm{g}}'(z)\, l_z}{N^2}, \tag{6.4}$$

and the variable e_F is an error term. Note that the $f_v^{\#}$ is only valid during motion, so e_F would include the normal force when the mover is in contact with one of the limits. It can also compensate for modeling errors.

Given the newly defined functions, we express the dynamical system with a discrete-time nonlinear model,

$$\begin{cases} \boldsymbol{x}_k = \mathbf{f}(\boldsymbol{x}_{k-1}, \boldsymbol{u}_k) + \boldsymbol{w}_k, \\ \boldsymbol{y}_k = \mathbf{h}(\boldsymbol{x}_k, \boldsymbol{u}_k) + \boldsymbol{\nu}_k, \end{cases} \tag{6.5}$$

where the subscript k is the sample index; $\boldsymbol{x}_k$, $\boldsymbol{u}_k$ and $\boldsymbol{y}_k$ are the state, input and output vectors; $\boldsymbol{w}_k$ and $\boldsymbol{\nu}_k$ are the process and observation noise vectors; and $\mathbf{f}$ and $\mathbf{h}$ are the transition and observation functions. The noise terms $\boldsymbol{w}_k$ and $\boldsymbol{\nu}_k$ are assumed to be independent zero-mean random vectors. Note that the errors e_ι and e_F may be considered part of those noise terms, but treating them as white noise is a very poor approximation. Instead, they are incorporated to the state vector,

$$\boldsymbol{x}_k = \begin{bmatrix} z_k^{\#} & z_{k-1}^{\#} & \lambda_k & e_{\iota k} & e_{F k} \end{bmatrix}^{\mathsf{T}}. \tag{6.6}$$

Then, for clarity purposes, the elements of $\mathbf{f}$ and $\boldsymbol{w}_k$ are represented based on their corresponding state variables,

$$\mathbf{f}(\cdot) = \begin{bmatrix} \mathrm{f}_{z^{\#}}(\cdot) & \mathrm{f}_{z_{k-1}^{\#}}(\cdot) & \mathrm{f}_{\lambda}(\cdot) & \mathrm{f}_{e_\iota}(\cdot) & \mathrm{f}_{e_F}(\cdot) \end{bmatrix}^{\mathsf{T}}, \tag{6.7}$$

$$\boldsymbol{w}_k = \begin{bmatrix} w_{z^{\#},k} & w_{z_{k-1}^{\#},k} & w_{\lambda,k} & w_{e_\iota,k} & w_{e_F,k} \end{bmatrix}^{\mathsf{T}}. \tag{6.8}$$

To improve the accuracy of the estimator, we propose to use not only the voltage and current but also the contact information. In that case, the input of the estimator may consist of the voltage v_{coil} and the discrete state of the automaton q (see Fig. 2.3),

$$\boldsymbol{u}_k = \begin{bmatrix} v_{\mathrm{coil}\,k} \\ q_k \end{bmatrix}. \tag{6.9}$$

The first element of the state function $\mathbf{f}$ corresponds to the position transition. The discretization is performed using Verlet integration [127]. Then, in the case of $q_k = 1$ or $q_k = 3$, $z_k^\#$ and $v_k^\#$ are replaced by their real values. Consequently, $\mathrm{f}_{z^\#}$ is defined as a piece-wise function,

$$\mathrm{f}_{z^\#}(\boldsymbol{x}_{k-1}, \boldsymbol{u}_k) = \begin{cases} 0 + {T_\mathrm{s}}^2 \, f_v^\#(0, 0, \lambda_{k-1}, e_{F\,k-1}), & \text{if } q_k = 1 \\ 2\, z_{k-1}^\# - z_{k-2}^\# + {T_\mathrm{s}}^2 \, f_v^\#(z_{k-1}^\#, v_{k-1}^\#, \lambda_{k-1}, e_{F\,k-1}), & \text{if } q_k = 2, \\ 1 + {T_\mathrm{s}}^2 \, f_v^\#(1, 0, \lambda_{k-1}, e_{F\,k-1}), & \text{if } q_k = 3 \end{cases} \tag{6.10}$$

where T_s is the sampling period, and $v_{k-1}^\#$ is calculated as the average velocity in the time interval $[t_{k-2},\, t_{k-1}]$,

$$v_{k-1}^\# = \frac{z_{k-1}^\# - z_{k-2}^\#}{T_\mathrm{s}}. \tag{6.11}$$

Note that, as the modeling and discretization errors are accounted for by $e_{F\,k-1}$, there is no need to include an additional process noise, thus $w_{z^\#,k} = 0$ for all k.

The second element of the state function $\mathbf{f}$ corresponds to the transition of the previous position, which is trivial,

$$\mathrm{f}_{z_{k-1}^\#}(\boldsymbol{x}_{k-1}) = z_{k-1}^\#, \qquad\qquad w_{z_{k-1}^\#,k} = 0. \tag{6.12}$$

The third element corresponds to the flux linkage. It is defined by using the forward Euler method to the electrical circuit equation (2.1) and replacing the current with the simplified output equation (6.2),

$$\mathrm{f}_\lambda(\boldsymbol{x}_{k-1}, \boldsymbol{u}_k) = \lambda_{k-1} + T_\mathrm{s} \left(v_{\mathrm{coil}\,k} + R\, h^\#\left(z_{k-1}^\#, \lambda_{k-1}, e_{\iota\,k-1}\right)\right). \tag{6.13}$$

While the modeling errors in the current function are already considered given the state variable $e_{\iota\,k-1}$, the discretization errors of f_λ are accounted for by the process noise $w_{\lambda,k} \neq 0$.

Regarding the auxiliary variables $e_{\iota\,k}$ and $e_{F\,k}$, there is no prior information about their dynamics. The best possible assumption for a generalized case, without increasing the model complexity, is that their expectations are equal to the previous ones,

$$\mathrm{f}_{e_\iota}(\boldsymbol{x}_{k-1}) = e_{\iota\,k-1}, \qquad\qquad \mathrm{f}_{e_F}(\boldsymbol{x}_{k-1}) = e_{F\,k-1}. \tag{6.14}$$

Then, the errors caused by this assumption are accounted for by their process noises $w_{e_\iota,k}$ and $w_{e_F,k}$.

The estimator needs to compare the output of the model with the measured one, and then correct the state vector accordingly. During motion ($q_k = 2$), the only output is the current. On the other hand, if $q_k = 1$ or $q_k = 3$, the contact information can also

be exploited to correct the estimated position. Thus, the observed output vector is

$$\boldsymbol{y}_k = \begin{cases} \begin{bmatrix} \iota_{\text{coil}_k} & 0 \end{bmatrix}^\mathsf{T}, & \text{if } q_k = 1 \\ \iota_{\text{coil}_k}, & \text{if } q_k = 2 \\ \begin{bmatrix} \iota_{\text{coil}_k} & 1 \end{bmatrix}^\mathsf{T}, & \text{if } q_k = 3 \end{cases}. \tag{6.15}$$

Correspondingly, the model-based output function must be

$$\mathbf{h}(\boldsymbol{x}_k, \boldsymbol{u}_k) = \begin{cases} h^{\#}(z_k^{\#}, \lambda_k, e_{\iota k}), & \text{if } q_k = 2 \\ \begin{bmatrix} h^{\#}(z_k^{\#}, \lambda_k, e_{\iota k}) & z_k^{\#} \end{bmatrix}^\mathsf{T}, & \text{if } q_k \neq 2 \end{cases}, \tag{6.16}$$

and the observation noise must be

$$\boldsymbol{\nu}_k = \begin{cases} \nu_{\iota k}, & \text{if } q_k = 2 \\ \begin{bmatrix} \nu_{\iota k} & 0 \end{bmatrix}^\mathsf{T}, & \text{if } q_k \neq 2 \end{cases}, \tag{6.17}$$

where $\nu_{\iota k}$ is the observation error of the current ι_{coil} (not to be confused with the modeling error $e_{\iota k}$). It is noteworthy that the dimension of the output terms depends on the input. Apart from that unconventional aspect, it is a standard discrete-time model that can be used to design estimators.

6.3 Estimation algorithms

Bayesian theory provides a powerful tool for the state estimation of stochastic systems. In the most rigorous way, the complete probability distributions of the state can be recursively calculated through numerical integration. However, this approach is generally intractable in control applications. Therefore, it is necessary to simplify the Bayesian estimation problem and reduce its computational complexity. Specifically, we propose to use an extension of the Rauch–Tung–Striebel smoother [128] for nonlinear systems. This estimator consists of two processes: a forward and a backward filter. Fig. 6.1 presents a diagram for an easier understanding of the processes and the required data for each step.

6.3.1 Forward filter

The forward filter is based on the extended Kalman filter (EKF). The original KF [129] is an algebraic and optimal solution of the Bayesian filtering problem, provided that the system is linear and all the random variables are Gaussian. The EKF, on the other hand, is an approximated extension of the KF for nonlinear systems. It is arguably the most popular stochastic observer for nonlinear systems, due to its simplicity and performance. It may be considered a simplified version of the Bayesian filtering technique, in which the

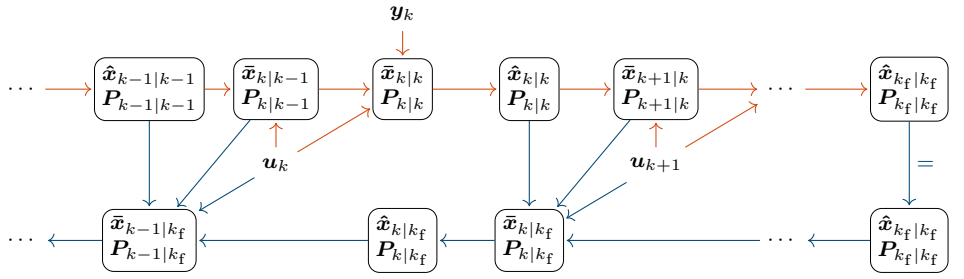

Figure 6.1: Estimator diagram. The forward and backward filters are given by the orange and blue arrows, respectively.

transition and output functions $\mathbf{f}$ and $\mathbf{h}$ are linearized, and the probability distributions are assumed to be normal,

$$(\boldsymbol{x}_k \mid \boldsymbol{u}_1, \ldots, \boldsymbol{u}_k, \boldsymbol{y}_1, \ldots, \boldsymbol{y}_k) \approx \boldsymbol{x}_{k|k}^{\mathrm{EKF}} \sim \mathcal{N}\big(\hat{\boldsymbol{x}}_{k|k}, \boldsymbol{P}_{k|k}\big). \tag{6.18}$$

The algorithm for the forward filter is into three steps:

1. **Prediction**. The kth *a priori* state estimation for $(\bar{\boldsymbol{x}}_{k|k-1}, \boldsymbol{P}_{k|k-1})$ is predicted from the $(k-1)$th projected *a posteriori* state estimation $(\hat{\boldsymbol{x}}_{k-1|k-1}, \boldsymbol{P}_{k-1|k-1})$,

$$\bar{\boldsymbol{x}}_{k|k-1} = \mathbf{f}\big(\hat{\boldsymbol{x}}_{k-1|k-1}, \boldsymbol{u}_k\big), \tag{6.19}$$
$$\boldsymbol{P}_{k|k-1} = \boldsymbol{F}_k \, \boldsymbol{P}_{k-1|k-1} \, \boldsymbol{F}_k^{\mathsf{T}} + \boldsymbol{Q}, \tag{6.20}$$

where $\boldsymbol{F}_k$ is the state transition matrix, obtained from the linearization of $\mathbf{f}$,

$$\boldsymbol{F}_k = \left.\frac{\partial \mathbf{f}}{\partial \boldsymbol{x}}\right|_{\hat{\boldsymbol{x}}_{k-1|k-1}, \boldsymbol{u}_k}, \tag{6.21}$$

and $\boldsymbol{Q}$ is the covariance of the process noise $\boldsymbol{w}_k$.

2. **Update**. The *a priori* prediction is refined by taking into account the observation $\boldsymbol{y}_k$. The updated estimation is the *a posteriori* state $(\bar{\boldsymbol{x}}_{k|k}, \boldsymbol{P}_{k|k})$,

$$\bar{\boldsymbol{x}}_{k|k} = \bar{\boldsymbol{x}}_{k|k-1} + \boldsymbol{K}_k \Big(\boldsymbol{y}_k - \mathbf{h}\big(\bar{\boldsymbol{x}}_{k|k-1}, \boldsymbol{u}_k\big)\Big), \tag{6.22}$$
$$\boldsymbol{P}_{k|k} = \boldsymbol{P}_{k|k-1} - \boldsymbol{K}_k \, \boldsymbol{H}_k \, \boldsymbol{P}_{k|k-1}, \tag{6.23}$$

where $\boldsymbol{H}_k$ is the observation matrix, resulted from the linearization of $\mathbf{h}$,

$$\boldsymbol{H}_k = \left.\frac{\partial \mathbf{h}}{\partial \boldsymbol{x}}\right|_{\bar{\boldsymbol{x}}_{k|k-1}, \boldsymbol{u}_k}, \tag{6.24}$$

and $\boldsymbol{K}_k$ is the Kalman gain. It is defined as

$$\boldsymbol{K}_k = \boldsymbol{P}_{k|k-1}\,\boldsymbol{H}_k{}^{\mathsf{T}}\left(\boldsymbol{H}_k\,\boldsymbol{P}_{k|k-1}\,\boldsymbol{H}_k{}^{\mathsf{T}} + \boldsymbol{R}_k\right)^{-1}, \tag{6.25}$$

being $\boldsymbol{R}_k$ the covariance of the observation noise $\boldsymbol{\nu}_k$. Note that $\boldsymbol{R}_k \in \mathbb{R}^{1\times 1}$ or $\boldsymbol{R}_k \in \mathbb{R}^{2\times 2}$, depending on q_k (6.17).

3. **Projection**. To increase the accuracy of the state estimation, it should be corrected in the case that it is outside its bounds. There are multiple ways of enforcing linear constraints in Kalman filters [130]. For this problem, a very simple and effective approach is to project the mean state vector based on its covariance. To obtain the maximum likelihood estimate of the state subject to inequality state constraints, the problem is formulated as

$$\hat{\boldsymbol{x}}_{k|k} = \underset{\boldsymbol{x}}{\arg\min}\,\big(\boldsymbol{x} - \bar{\boldsymbol{x}}_{k|k}\big)^{\mathsf{T}}\,\boldsymbol{P}_{k|k}{}^{-1}\,\big(\boldsymbol{x} - \bar{\boldsymbol{x}}_{k|k}\big), \quad \text{subject to } \boldsymbol{A}\,\boldsymbol{x} \leq \boldsymbol{b}. \tag{6.26}$$

In general, this is a quadratic programming problem. In our case, only the position needs to be constrained, which means that

$$\boldsymbol{A} = \begin{bmatrix} -1 & 0 & 0 & 0 & 0 \\ +1 & 0 & 0 & 0 & 0 \end{bmatrix}, \qquad \boldsymbol{b} = \begin{bmatrix} 0 \\ 1 \end{bmatrix}. \tag{6.27}$$

This is easily solved because both constraints cannot be active at the same time. Thus, it can be reformulated as an equality constrained quadratic programming problem,

$$\hat{\boldsymbol{x}}_{k|k} = \underset{\boldsymbol{x}}{\arg\min}\big(\boldsymbol{x} - \bar{\boldsymbol{x}}_{k|k}\big)^{\mathsf{T}}\,\boldsymbol{P}_{k|k}{}^{-1}\,\big(\boldsymbol{x} - \bar{\boldsymbol{x}}_{k|k}\big), \quad \text{subject to } \boldsymbol{A}_k\,\boldsymbol{x} = b_k, \tag{6.28}$$

where $\boldsymbol{A}_k$ and b_k correspond to the active constraint,

$$\begin{aligned} \boldsymbol{A}_k &= \begin{cases} \big[-1 \quad 0 \quad 0 \quad 0 \quad 0\big], & \text{if } \bar{z}^{\#}_{k|k} < 0 \\ \boldsymbol{0}_{0\times 5}, & \text{if } 0 \leq \bar{z}^{\#}_{k|k} \leq 1\,, \\ \big[+1 \quad 0 \quad 0 \quad 0 \quad 0\big], & \text{if } \bar{z}^{\#}_{k|k} > 1 \end{cases} \\ b_k &= \begin{cases} 0, & \text{if } \bar{z}^{\#}_{k|k} < 0 \\ \boldsymbol{0}_{0\times 1}, & \text{if } 0 \leq \bar{z}^{\#}_{k|k} \leq 1\,. \\ 1, & \text{if } \bar{z}^{\#}_{k|k} > 1 \end{cases} \end{aligned} \tag{6.29}$$

Note that the position $\bar{z}^{\#}_{k|k}$ is the first element of the state vector $\bar{\boldsymbol{x}}_{k|k}$. The solution of the problem is

$$\hat{\boldsymbol{x}}_{k|k} = \bar{\boldsymbol{x}}_{k|k} + \boldsymbol{P}_{k|k}\,\boldsymbol{A}_k{}^{\mathsf{T}}\Big(\boldsymbol{A}_k\,\boldsymbol{P}_{k|k}\,\boldsymbol{A}_k{}^{\mathsf{T}}\Big)^{-1}\big(b_k - \boldsymbol{A}_k\,\bar{\boldsymbol{x}}_{k|k}\big). \tag{6.30}$$

6.3.2 Backward filter

The complete two-pass algorithm is based on the Extended Rauch–Tung–Striebel smoother (ERTSS). Analogously to the EKF, the ERTSS is an approximated version of the recursive Bayesian smoothing [131], in which the transition function is linearized (6.21), and the probability distributions are assumed to be Gaussian,

$$\big(\boldsymbol{x}_k \mid \boldsymbol{u}_1, \ldots, \boldsymbol{u}_{k_\mathrm{f}}, \boldsymbol{y}_1, \ldots, \boldsymbol{y}_{k_\mathrm{f}}\big) \approx \boldsymbol{x}_{k|k_\mathrm{f}}^{\mathrm{ERTSS}} \sim \mathcal{N}\big(\hat{\boldsymbol{x}}_{k|k_\mathrm{f}}, \boldsymbol{P}_{k|k_\mathrm{f}}\big), \tag{6.31}$$

where k_f represents the final sample of the smoothed interval.

The algorithm includes the previous steps from the forward filter, and two additional ones that constitute the backward filter:

4. **Smoothing**. As the chosen notation already suggests, the filtered estimation at $k = k_\mathrm{f}$ is equal to the smoothed one ($\hat{\boldsymbol{x}}_{k_\mathrm{f}|k_\mathrm{f}}$, $\boldsymbol{P}_{k_\mathrm{f}|k_\mathrm{f}}$). Then, starting at k_f, past states are smoothed through a backward recursion,

$$\bar{\boldsymbol{x}}_{k|k_\mathrm{f}} = \hat{\boldsymbol{x}}_{k|k} + \boldsymbol{G}_k\,(\hat{\boldsymbol{x}}_{k+1|k_\mathrm{f}} - \bar{\boldsymbol{x}}_{k+1|k}), \tag{6.32}$$

$$\boldsymbol{P}_{k|k_\mathrm{f}} = \boldsymbol{P}_{k|k} + \boldsymbol{G}_k(\boldsymbol{P}_{k+1|k_\mathrm{f}} - \boldsymbol{P}_{k+1|k})\,\boldsymbol{G}_k{}^\mathsf{T}, \tag{6.33}$$

   where $\boldsymbol{G}_k$ is the smoother gain,

$$\boldsymbol{G}_k = \boldsymbol{P}_{k|k}\,\boldsymbol{F}_{k+1}{}^\mathsf{T}\,\boldsymbol{P}_{k+1|k}{}^{-1}. \tag{6.34}$$

   Notice that this process requires the EKF state estimates for all k, so they should be stored or recalculated.

5. **Projection**. The smoothed state estimation $\bar{\boldsymbol{x}}_{k|k}$ is projected to satisfy the state constraints, resulting in $\hat{\boldsymbol{x}}_{k|k}$. The problem statement is equivalent to the one presented in the third step of the EKF algorithm. Consequently, the derived solution, analogous to (6.30), is

$$\hat{\boldsymbol{x}}_{k|k_\mathrm{f}} = \bar{\boldsymbol{x}}_{k|k_\mathrm{f}} + \boldsymbol{P}_{k|k_\mathrm{f}}\,\boldsymbol{C}_k{}^\mathsf{T}\Big(\boldsymbol{A}_k\,\boldsymbol{P}_{k|k_\mathrm{f}}\,\boldsymbol{A}_k{}^\mathsf{T}\Big)^{-1}\big(b_k - \boldsymbol{A}_k\,\bar{\boldsymbol{x}}_{k|k_\mathrm{f}}\big), \tag{6.35}$$

   where

$$\begin{aligned}
\boldsymbol{A}_k &= \begin{cases} \big[-1 \quad 0 \quad 0 \quad 0 \quad 0\big], & \text{if } \bar{z}^{\#}_{k|k_\mathrm{f}} < 0 \\ \boldsymbol{0}_{0\times 5}, & \text{if } 0 \le \bar{z}^{\#}_{k|k_\mathrm{f}} \le 1\,, \\ \big[+1 \quad 0 \quad 0 \quad 0 \quad 0\big], & \text{if } \bar{z}^{\#}_{k|k_\mathrm{f}} > 1 \end{cases} \\
b_k &= \begin{cases} 0, & \text{if } \bar{z}^{\#}_{k|k_\mathrm{f}} < 0 \\ \boldsymbol{0}_{0\times 1}, & \text{if } 0 \le \bar{z}^{\#}_{k|k_\mathrm{f}} \le 1\,. \\ 1, & \text{if } \bar{z}^{\#}_{k|k_\mathrm{f}} > 1 \end{cases}
\end{aligned} \tag{6.36}$$

Note that the backward recursion must be computed offline, so it cannot be directly used for feedback control. However, it can be formulated and used in repetitive operations, as in the cycle-to-cycle learning strategies commonly proposed for many real devices, including the reluctance actuators under study.

6.4 Analysis

In this section, the performance of the proposed estimator is analyzed via simulations.

6.4.1 Reference simulations

The complete model presented in Chapter 2 (RAM-JA) is a continuous-time model that includes the most important electromagnetic phenomena. The derived expression for the gap reluctance (2.30) takes into account the flux fringing phenomenon. Moreover, in contrast with the basic model (RAM-FK), the dynamics of the electromagnetic force are based on the JA hysteresis model, as explained in Section 2.3.2. Regarding the mechanical subsystem, the dynamics of the movable part is given by the hybrid automaton from Fig. 2.3, where it is assumed perfectly inelastic collisions, and an ideal mass-spring-damper system. Formally,

$$\gamma = 0, \qquad F_{\text{pas}}(z, v) = k_{\text{sp}}\,(z_{\text{sp}} - z) - c_{\text{f}}\,v, \tag{6.37}$$

As shown in Section 2.5, simulations match real measurements with high accuracy. Thus, for analysis purposes, RAM-JA is considered the reference, emulating a real reluctance actuator. Its parameters are in Table 6.1.

Table 6.1: Parameters of the reference model (RAM-JA).

Parameter	Value		Parameter	Value	
m_{mov}	1.6×10^{-3}	kg	N	1200	
k_{sp}	61.8	N/m	R	48	Ω
z_{sp}	0.0192	m	k_{eddy}	1630	Ω^{-1}
c_{f}	0.8	N s/m	l_{c}	0.055	m
z_{min}	4×10^{-4}	m	A_{c}	1.26×10^{-5}	m^2
z_{max}	1.4×10^{-3}	m	M_{sat}	1.45×10^{6}	A/m
$\mathcal{R}_{\text{g},0}$	5.594×10^{6}	H^{-1}	b	2.45×10^{-3}	T
$\mathcal{R}'_{\text{g},0}$	1.105×10^{11}	H^{-1}/m	c	0.736	
k_1	1318	m^{-1}	κ	942	A/m
k_2	9.735×10^{-3}	m	α	3.66×10^{-3}	

In Fig. 6.2, we present an ideal solution of the soft-landing problem for a making (closing) and breaking (opening) cycle. In the left-hand side, the state variables are de-

picted. Equally to Section 5.3.1, the position trajectories for both operations are designed with fifth-degree polynomials (see Fig. 6.2a). As boundary conditions (5.32), the initial and final positions are set to $z_{\max}$ or $z_{\min}$ (depending on the operation type), while the velocities and accelerations are set to zero. This can be easily checked in the velocity graphic in Fig. 6.2c. The motion duration for each operation is set to $4\,\mathrm{ms}$. Fig. 6.2e shows the ϕ–$\mathcal{F}_{\mathrm{c}}$ hysteresis curve. This phenomenon is not negligible, so the lack of a proper hysteresis model in the estimator model will be a source of estimation errors even when the rest of the parameters fit perfectly the ones from RAM-JA. The right-hand side of Fig. 6.2 depicts the inputs and output of the estimator model. Fig. 6.2f presents the required coil voltage to move the actuator as desired, and it will be treated as one of the inputs of the system. We also show the discrete state in Fig. 6.2d, which is the second element of the input vector defined in (6.9), and determines the dynamic mode of the system: lower limit ($q = 1$), motion ($q = 2$) or upper limit ($q = 3$). Lastly, the output of the system is the coil current, presented in Fig. 6.2b. Note that there is an interval before the start of motion (at $t = 1\,\mathrm{ms}$ and $t = 11\,\mathrm{ms}$) that allows the coil to energize or de-energize until the magnetic force manages to compensate the spring force. Then, after the landing (at $t = 5\,\mathrm{ms}$ and $t = 15\,\mathrm{ms}$), the voltage is set to a constant value which guarantees that the mover is fixed at the desired position.

6.4.2 Compared estimators

To showcase the usefulness of the proposed estimator, it is compared with alternatives under the same conditions. All of them are based on the discrete model presented in Section 6.2. It is fully specified to match RAM-JA used as the reference. Given the definition of the passive force (6.37), the corresponding counterpart can be defined in a similar way,

$$F^{\#}_{\mathrm{pas}}(z^{\#}, v^{\#}) = k^{\#}_{\mathrm{sp}}\,(z^{\#}_{\mathrm{sp}} - z^{\#}) - c^{\#}_{\mathrm{f}}\,v^{\#}, \tag{6.38}$$

and, since $F^{\#}_{\mathrm{pas}}(z^{\#}, v^{\#}) = l_z\,F_{\mathrm{pas}}(z, v)$ (6.4), the auxiliary parameters are related to the original ones as follows:

$$k^{*}_{\mathrm{sp}} = k_{\mathrm{sp}}\,{l_z}^2, \qquad z^{\#}_{\mathrm{sp}} = \frac{z_{\mathrm{sp}} - z_{\min}}{l_z}, \qquad c^{*}_{\mathrm{f}} = c_{\mathrm{f}}\,{l_z}^2. \tag{6.39}$$

The auxiliary function $\mathcal{R}^{\#}_{\mathrm{c}}$ must also be defined. It is a scaled version of the core reluctance term $\mathcal{R}_{\mathrm{c}}$, which can be modeled based on Fröhlich–Kennelly(FK) relation, as explained Section 2.3.2. In an analogous way, it can be expressed as follows:

$$\mathcal{R}^{\#}_{\mathrm{c}}(\lambda) = \frac{\mathcal{R}^{\#}_{\mathrm{c},0}}{1 - \lambda/\lambda_{\mathrm{sat}}}, \tag{6.40}$$

where the constant $\mathcal{R}^{\#}_{\mathrm{c},0}$ is the value of the scaled reluctance when $\lambda = 0$, and λ_{sat} is the saturation value of λ. Note that the reference model does not have a core reluctance,

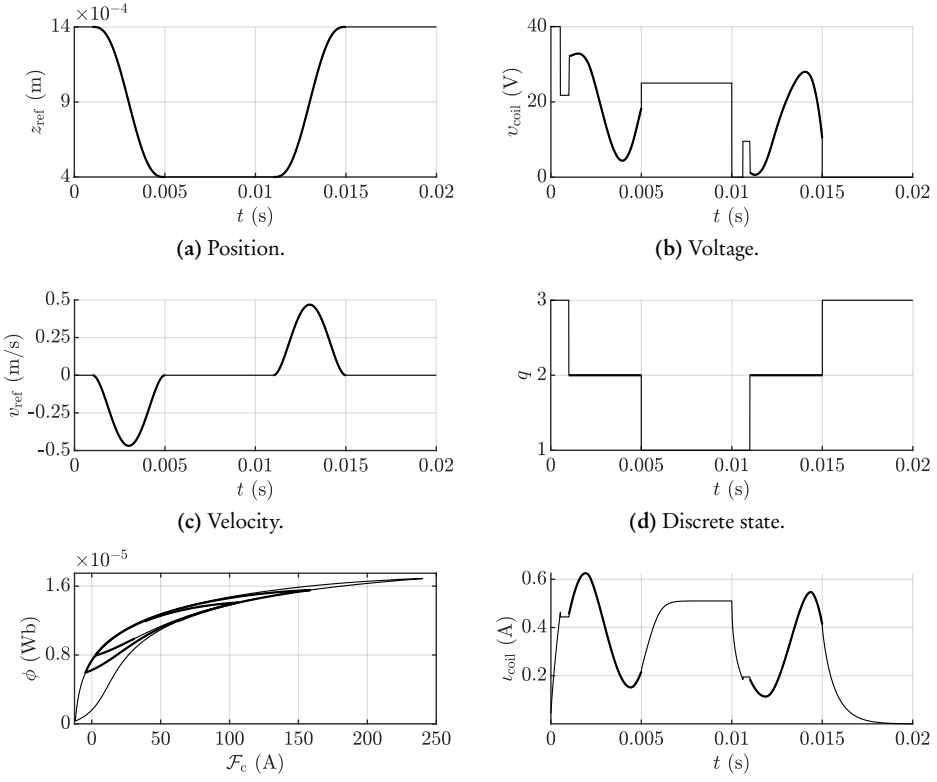

(a) Position. **(b)** Voltage. **(c)** Velocity. **(d)** Discrete state. **(e)** Magnetic flux–electromotive force. **(f)** Current.

Figure 6.2: Simulation results using RAM-JA. The wide lines correspond to the motion intervals.

so these constants cannot be directly related to the ones from Table 6.1. Instead, they are fitted to the simulation results from Section 6.4.1. To summarize, the auxiliary parameters from the discrete model are presented in Table 6.2, with their corresponding nominal values.

Four different estimators are designed based on the discrete model. They are:

- **EKF**: The first estimator is the forward filter described in Section 6.3.1.
- **ERTSS**: The second one is the complete proposal, in which the data from the forward filter is smoothed using the backward recursion presented in Section 6.3.2. As only the motion operations are of interest, the smoothing is applied only on those intervals. In that regard, for each operation, the last motion sample (in which $q_k = 2$) is treated as k_{f}, which marks the start of the backward smoothing. Then, the algorithm stops when $q_k \neq 2$.

Table 6.2: Parameters of the reduced model.

Parameter	Nominal value
$m^{\#}_{\text{mov}}$	1.6×10^{-9} kg m^2
$k^{\#}_{\text{sp}}$	6.18×10^{-8} N m
$z^{\#}_{\text{sp}}$	18.8

Parameter	Nominal value	
$c^{\#}_{\text{f}}$	8×10^{-7}	N m s
$\mathcal{R}^{\#}_{\text{c},0}$	1.75	H^{-1}
λ_{sat}	0.0238	Wb

- **ERTSS$\backslash e_\iota$**: The third estimator uses the same procedure as the previous one but with a slightly simplified model: the auxiliary state variable e_ι is set to zero,

$$\mathrm{f}_{e_\iota}(\cdot) = 0, \qquad w_{e_\iota,k} = 0. \tag{6.41}$$

- **ERTSS$\backslash e_F$**: Similarly, a fourth ERTSS is designed by changing the model. In this case, the other auxiliary variable e_F is set to zero,

$$\mathrm{f}_{e_F}(\cdot) = 0, \qquad w_{e_F,k} = 0. \tag{6.42}$$

  Note that e_F does not only represent force deviations due to parametric or discretization errors but also accounts for the normal forces during contact. As such, the transition function of the position (6.10) must also be tweaked to circumvent the removal of e_F,

$$\mathrm{f}_{z^{\#}}(\boldsymbol{x}_{k-1}, \boldsymbol{u}_k) = \begin{cases} 0, & \text{if } q_k = 1 \\ 2\, z^{\#}_k - z^{\#}_{k-1} + {T_\mathrm{s}}^2\ f^{\#}_v(z^{\#}_{k-1}, v^{\#}_{k-1}, \lambda_{k-1}, 0), & \text{if } q_k = 2\,. \\ 1, & \text{if } q_k = 3 \end{cases} \tag{6.43}$$

The comparison between EKF and ERTSS will be useful for quantifying the accuracy increase of the smoother. On the other hand, the results from ERTSS$\backslash e_\iota$ and ERTSS$\backslash e_F$ will serve to determine the overall improvement of the ERTSS estimations due to these simple modifications in the model.

6.4.3 Model parameters

To compare between the proposed and the alternative estimators, their robustness to modeling errors is analyzed. Numerous simulations are performed, in which the model parameters for the estimators are perturbed. Consider $\boldsymbol{p}$ to be the vector of perturbed parameters,

$$\boldsymbol{p} = \begin{bmatrix} m^{\#}_{\text{mov}} & k^{\#}_{\text{sp}} & z^{\#}_{\text{sp}} & c^{\#}_{\text{f}} & \mathcal{R}^{\#}_{\text{c},0} & \lambda_{\text{sat}} & \text{mean}(\mathcal{R}^{\#}_{\text{g}}) & \text{mean}(\mathcal{R}'^{\#}_{\text{g}}) \end{bmatrix}^{\mathsf{T}}. \tag{6.44}$$

Note that the average of both the gap reluctance and its partial derivative are included. Formally, their mean values are calculated with respect to the position,

$$\operatorname{mean}(\mathcal{R}_{\mathrm{g}}^{\#}) = \int_0^1 \mathcal{R}_{\mathrm{g}}^{\#}(z^{\#})\,\mathrm{d}z^{\#}, \qquad \operatorname{mean}(\mathcal{R}_{\mathrm{g}}^{\prime\#}) = \int_0^1 \mathcal{R}_{\mathrm{g}}^{\prime\#}(z^{\#})\,\mathrm{d}z^{\#}. \tag{6.45}$$

Then, each of the parameters p_i is perturbed in each run,

$$p_i = p_i^{\mathrm{nom}}\,(1+\epsilon_i), \tag{6.46}$$

being p_i^{nom} the corresponding nominal parameter value and ϵ_i the relative error, which is randomly selected in each run according to a continuous uniform probability density distribution with an interval length $\Delta\epsilon$,

$$\epsilon_i \sim \operatorname{unif}\big(1-\Delta\epsilon/2,\, 1+\Delta\epsilon/2\big). \tag{6.47}$$

The errors ϵ_7 and ϵ_8 serve to modify the mean values of the gap reluctance and its partial derivative. Then, with some simple manipulations, it is possible to derive their perturbed values for any position,

$$\mathcal{R}_{\mathrm{g}}^{\#}(z^{\#}) = \mathcal{R}_{\mathrm{g}}^{\#^{\mathrm{nom}}}(z^{\#}) + \operatorname{mean}\left(\mathcal{R}_{\mathrm{g}}^{\#^{\mathrm{nom}}}\right)\epsilon_7 + (z^{\#}-1/2)\,\operatorname{mean}\left(\mathcal{R}_{\mathrm{g}}^{\prime\#^{\mathrm{nom}}}\right)\epsilon_8, \tag{6.48}$$

$$\mathcal{R}_{\mathrm{g}}^{\prime\#}(z^{\#}) = \mathcal{R}_{\mathrm{g}}^{\prime\#^{\mathrm{nom}}}(z^{\#}) + \operatorname{mean}\left(\mathcal{R}_{\mathrm{g}}^{\prime\#^{\mathrm{nom}}}\right)\epsilon_8. \tag{6.49}$$

Apart from the model parameters, we also need to set the covariance of the process and observation noises. On the one hand, the process covariance $\boldsymbol{Q}$ is highly dependent on the errors of the parameters, so it is optimally calculated for each $\Delta\epsilon$. To simplify, the process noises are assumed uncorrelated, so $\boldsymbol{Q}$ is a diagonal matrix. On the other hand, the observation covariance $\boldsymbol{R}_k$ depends only on the measurement errors of the current. To emulate this type of error, white noise is added to the current ι_{coil} every sample of every run, with a standard deviation of $\sigma_\iota = 2\times10^{-3}$ A. Then, according to (6.17), the covariance $\boldsymbol{R}_k$ is defined as

$$\boldsymbol{R}_k = \begin{cases} {\sigma_\iota}^2, & \text{if } q_k = 2 \\ \begin{bmatrix} {\sigma_\iota}^2 & 0 \\ 0 & 0 \end{bmatrix}, & \text{if } q_k \neq 2 \end{cases}. \tag{6.50}$$

Then, the initial state is initialized in each simulation. It is assumed that both current and flux are zero at the start, so $e_{\iota 1}$ is also zero. As the coil is de-energized, the mover is initially in the upper limit, i.e. $z_1^{\#} = 1$. The initial acceleration is zero, so e_{F1} must compensate exactly the estimated force of the spring (based on the perturbed parameters $k_{\mathrm{sp}}^{\#}$ and $z_{\mathrm{sp}}^{\#}$). Ultimately, the mean state and covariance are initialized as follows:

$$\hat{\boldsymbol{x}}_{1|1} = \begin{bmatrix} 1 & 1 & 0 & 0 & -k_{\mathrm{sp}}^{\#}\,(z_{\mathrm{sp}}^{\#}-1) \end{bmatrix}^{\mathsf{T}}, \qquad \boldsymbol{P}_{1|1} = \boldsymbol{0}. \tag{6.51}$$

Note that the initial magnetic flux is not exactly zero in the reference (see Fig. 6.2e). Technically, its initial variance should be positive to account for that discrepancy. Nonetheless, for the sake of simplicity, we have decided to set it to zero.

6.4.4 Simulation results

For each one of the estimators presented in Section 6.4.2, and for different error interval lengths $\Delta\epsilon$, 10 000 Monte Carlo simulations are performed. The position from Fig. 6.2a is estimated by using the electrical signals from Fig. 6.2b and 6.2f. The chosen sampling period is 20 µs. To summarize and compare the results, normalized root-mean-square errors (NRMSE) of the position are calculated for each operation,

$$\mathrm{NRMSE}_z = \sqrt{\frac{\sum_k \left(\hat{z}_k^{\#} - z_{\mathrm{ref}}^{\#}(t_k)\right)^2}{\sum_k \left(z_{\mathrm{ref}}^{\#}(t_k)\right)^2}}, \tag{6.52}$$

where $\hat{z}_k$ is the estimated normalized position for each sample k, and $z_{\mathrm{ref}}^{\#}$ is the normalized reference position,

$$z_{\mathrm{ref}}^{\#} = \frac{z_{\mathrm{ref}} - z_{\mathrm{min}}}{l_z}. \tag{6.53}$$

Note that the position errors are zero outside the motion intervals, so only the samples k in which $q_k = 2$ are used to compute each NRMSE_z.

The errors are presented in Figs. 6.3a and 6.3b for the making and breaking operations, respectively. The advantage of the proposed ERTSS over a more traditional EKF is quite evident, with smaller errors for every $\Delta\epsilon$. There is also a notable improvement over ERTSS$\backslash \boldsymbol{e_\iota}$ and ERTSS$\backslash \boldsymbol{e_F}$, which justifies the addition of the auxiliary variables e_ι and e_F. On the one hand, e_F mainly accounts for modeling errors in the force characterization, so its usefulness is clearer for larger parameter errors. On the other hand, the main motivation for adding e_ι is to account for current errors due to the lack of a hysteresis model. Thus, as the graphics confirm, it is useful even for negligible parameter errors. The estimation of the velocity is also very important for soft-landing control, as the goal is to reduce impact velocities. Then, in an equivalent fashion, the velocity estimation errors NRMSE_v are calculated and presented in Figs 6.3c and 6.3d. The velocity errors are consistently larger, but, for $\Delta\epsilon < 10\,\%$ the proposed ERTSS are still very accurate.

To better understand why the smoother (ERTSS) is so much better than its filter counterpart (EKF), Fig. 6.4 depicts the full position evolution of the worst-case scenario for $\Delta\epsilon = 10\,\%$ (of all 10 000 ERTSS runs with 2 operation each, the one with the maximum NRMSE_z is selected). As explained in Section 6.3, the forward filter recursion of the ERTSS is precisely the EKF. The advantage of the ERTSS is that, once the landing occurs, the position estimate is corrected. Then, the backward smoothing recursion serve to refine past data based on the position correction at the contact instant.

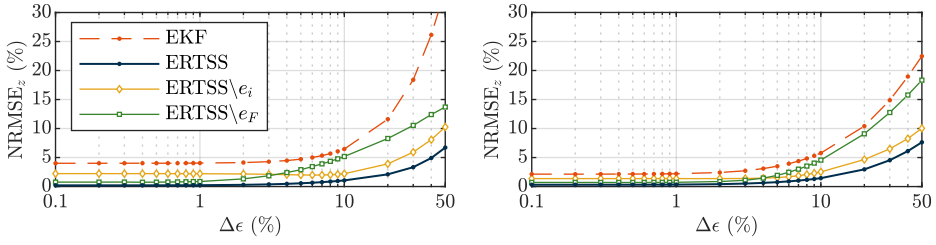

(a) Position errors (making operations).

(b) Position errors (breaking operations).

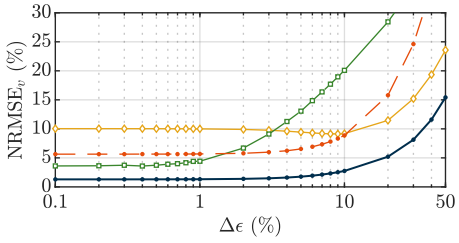

(c) Velocity errors (making operations).

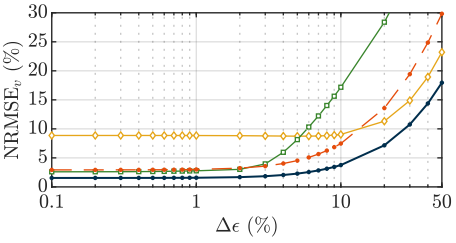

(d) Velocity errors (breaking operations).

Figure 6.3: Estimation errors in the making and breaking operations, for different interval lengths $\Delta\epsilon$. Notice the logarithmic scale of the horizontal axis.

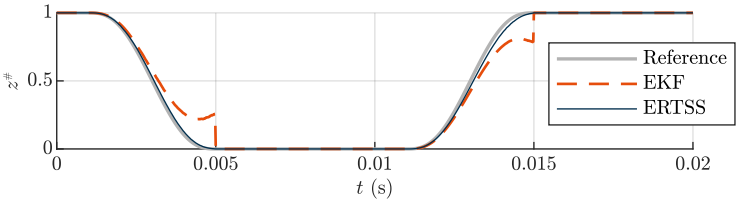

Figure 6.4: Worst-case result regarding the position estimation, for $\Delta\epsilon = 10\,\%$.

6.5 Discussion

We have proposed a position estimator for soft-landing control of short-stroke single-coil reluctance actuators. It is a Rauch–Tung–Striebel smoother, which uses the electrical signals and contact information as observable variables. To facilitate its implementation, it uses a deliberately simple model. Despite that, the simulated results show that the estimation of both position and velocity are very accurate, even with large parameter errors. This is especially evident when compared to other alternatives, proving the advantage of the novel ideas. On the one hand, the incorporation of error terms as state variables serves to estimate and correct modeling errors. On the other hand, the backward recursion exploits the information gained after the contact instant and corrects past estimates correspondingly.

We have taken advantage of all the available simulated data to optimally calculate the covariance matrices. In practice, their values should be estimated according to the available information about the actuator and its measurements, and then fine-tuned. Nevertheless, it is viable to assume that the process noises are uncorrelated, as the presented analysis has shown. In that case, the number of nonzero elements in the process noise covariance matrix is reduced to only three, simplifying the fine-tuning process.

Chapter 7

Closing

The research work for this thesis has been directed toward the soft-landing control of short-stroke reluctance actuators. Dynamical models have been proposed, based on which controllers and estimators have been designed and evaluated. This last chapter includes a summary and the main conclusions, as well as recommendations for continuing the research.

7.1 Summary and conclusions

Reluctance actuators are widely used due to their high force densities and low heat dissipation. In addition, the relatively low cost of small short-stroke single-coil reluctance actuators makes them the preferable choice for on-off switching operations in many applications. One major drawback of these and many other switching actuators is the strong impact at the end of each commutation, which provokes bouncing, mechanical wear and acoustic noise. Furthermore, the force, energy and cost efficiency of the reluctance actuators under consideration comes at the expense of some disadvantages regarding their control, mainly the highly nonlinear dependence of the magnetic force with the state variables—position and magnetic flux—, the unit-to-unit variability and the lack of position measurements for identification and control.

As stated in Section 1.2, the aim of this thesis has been the mitigation of the impact velocities by using control systems theory and techniques, taking into account the problems of limitations of this class of actuators. The main contributions and conclusions of the thesis address the research objectives: modeling, identification, control and estimation. Specifically, the first and second objectives are tackled in Chapter 2; then, Chapters 3, 4 and 5 focus on the third and central objective; and, lastly, Chapter 6 pursues the fourth objective.

Contributions, results and conclusions derived from the research work have been submitted to their publication in high-impact journals. At the time of writing, most of them are already published [23], [26], [31], one has been accepted for publication and is

available online [22], and another is under review [30]. Other contributions have been presented in international peer-reviewed conference [21], [24], [25], [27]. Additionally, two patent applications have been submitted to protect inventions related to the state estimation of reluctance actuators in cooking appliances [28], [29].

For clarity, the main conclusions of the research are divided into categories in accordance with the chapters:

7.1.1 Dynamical modeling

We have presented dynamical models of reluctance actuators, characterizing both mechanical and electromagnetic dynamics. As the models are intended for control and estimation purposes, the computationally demanding finite element method is discarded. Instead, lumped-parameter models are proposed for describing the dynamic behavior of reluctance actuators, while still taking into account the most relevant electromagnetic phenomena.

The two main contributions are the gap reluctance expression and the hysteresis model. On the one hand, flux fringing is incorporated by means of the derived gap reluctance expression, based on McLyman's factor. The generalized expression can be directly used for actuators with an arbitrary number of position-dependent and fixed gaps. On the other hand, the magnetic hysteresis characterization is based on the Jiles–Atherton model. It is usually implemented in such a way that the input is the magnetization, and the output is the magnetic flux density. In the proposed modification, however, both the magnetic flux and magnetomotive force are internal state variables. This approach makes the dynamical model directly applicable to control applications.

Regarding the mechanical subsystem, the limited range of motion of short-stroke reluctance actuators results in hybrid dynamics, with both continuous and discrete dynamic behavior. Thus, a hybrid automaton is used to model this part of the system. It is general enough to include the full spectrum of collision types, ranging from perfectly inelastic to perfectly elastic. Nevertheless, modeling the bouncing phenomenon is not deemed important in this thesis because the intention is to mitigate them by controlling an actuator before the collision event.

Two model types are presented: a basic model (RAM-FK) [21], which neglects the magnetic hysteresis; and a complete model (RAM-JA) [22], which includes the hysteresis characterization. They are both state-space representations, where every dynamical function can be computed analytically. Moreover, the input and output are, interchangeably, the coil voltage and current. Thus, they can be used for designing observers or controllers, where the voltage is the controllable input and the current is the measured output (or vice versa).

To simplify the models and their identification, a series of transformations are suggested in order to reduce the number of parameters for the electromagnetic subsystems

of both models. Then, it is shown that all the parameters of the derived reduced models are identifiable from measurements of voltage and current.

The main purpose of the model fitting has been to validate and compare the different models. As expected, RAM-FK is the most efficient but also the least accurate. On the other hand, RAM-JA adjusts much better to the experimental data. They have been compared to a state-of-the-art solution that uses the Generalized Preisach model, which requires to solve numerically the differential equation of the electromagnetic variable. It has been shown that the accuracy of the proposed RAM-JA is very similar to the state-of-the-art alternative while being much more computationally efficient.

7.1.2 Optimal control design

We have proposed a new optimal control approach to design soft-landing trajectories of actuators, and their corresponding input signals [23]. Although the contact position is considered a random variable, the system dynamics is still defined as a deterministic model, which permits formulating and solving it as a regular optimal control problem. It is also possible to include additional terms to the cost functional if it is required to optimize other concepts, e.g., the contact time or the power consumption.

One of the most direct ways of exploiting the optimal control design is in the implementation of open-loop controllers. As the main advantage of this type of control, the implementation is simple and inexpensive because it does not require measuring or estimating variables. However, the main disadvantage of open-loop control is its sensitivity to any kind of disturbance or error. Thus, to analyze its performance, a Monte Carlo method has been carried out, in which the model parameters are perturbed to emulate variability and modeling errors. In general, it is shown that the open-loop control designed with the proposed method has better performance than a conventional deterministic solution. These simulation results also show the advantage of controlling with the current instead of the voltage. In general, current-based open-loop or feedforward controllers are preferable to the voltage counterparts because the magnetic flux, magnetic force and, subsequently, the position dynamics do not depend on the coil resistance, which changes greatly with the temperature.

7.1.3 Run-to-run control

A new run-to-run (R2R) strategy for soft-landing control has been presented [25], [26]. It can be interpreted as a cycle-to-cycle adaptation of open-loop and feedforward controllers, effectively closing the loop. In contrast with conventional position feedback controllers, the R2R algorithm does not require the position, which makes it useful for applications in which position sensors or estimators are not feasible. Instead, it relies on auxiliary measurements for evaluating each commutation.

The complete algorithm has been separated into different parts, most notably the input definition and the search algorithm. On the one hand, the current has been selected as the input in order to make the controller more robust to temperature changes. Thus, a flatness-based feedforward controller has been designed that permits adapting the current signals from cycle to cycle. This is an improvement over previous works [78], which propose to use the voltage as input (see Appendix B for more details). On the other hand, the search algorithms are generalized, so they may be useful for other applications of R2R control, even outside this scenario. The main proposal is based on Bayesian optimization (BO), which has been adapted in several ways for its application in the R2R control.

The proposed control (R2R-BO) has been compared with two alternatives, that uses pattern search (PS) and Nelder–Mead (NM) methods. One important advantage of R2R-BO is that, as it uses Gaussian process regressors, it directly accounts for uncertainty and hence it is more robust. Besides, it efficiently exploits previous data to select new points and converge rapidly to an optimal solution. Simulations and experiments have been performed, showing the improvement of R2R-BO with respect to the other R2R strategies.

7.1.4 Sliding-mode control

This thesis has also explored the idea of tackling the soft landing problem through conventional position feedback control. With this type of controllers, tracking errors can theoretically be corrected during each commutation, instead of relying on cycle-to-cycle adaptation. Therefore, its main advantage over the previous solutions is its robustness to nonrepeating disturbances.

We have proposed a sliding-mode controller that does not require any information about the dynamical system, making it very versatile [27]. We have also derived the convergence criteria based on a generalized dynamical model with special attention paid to the hybrid dynamics. The convergence analysis has shown the importance of the position reference to be tracked. For simplicity, polynomial trajectories have been tested. Nonetheless, a better choice is to obtain the trajectories through optimal control design, as in Chapter 3, so that their feasibility is guaranteed—at least for the nominal system.

Concerning its implementation, the sampling rate must be large enough to track the position trajectories and achieve low impact velocities. Simulation results show that the contact velocities are significant even with sampling rates in which the tracking position errors are seemingly insignificant. Anyway, given the simplicity of the controller, the sampling rate should not be a limiting factor concerning its implementation. Instead, for many actuators, the most challenging aspect of the feedback control is the acquisition of position values in real time for the feedback loop.

7.1.5 State estimation

A new model-based state estimation approach has been presented for soft-landing tracking control of reluctance actuators [30]. It is based on RAM-FK from Chapter 2, but it is further simplified in order to facilitate its implementation. We have also proposed to use the discrete state of the hybrid system—i.e. the dynamic mode of the system—as a second input of the estimator model. This requires a sensor to know if the mover is in contact with one of its limits. It is a compromise between measuring only electrical signals and measuring directly the position. On the one hand, if only the current and voltage are measured, the estimator must be based on a more complex and accurate model, such as RAM-JA, presented in Chapter 2. This makes the model identification and estimator implementation much more challenging and expensive. On the other hand, a full position sensor would not be affordable, especially for low-cost solutions with simple reluctance actuators.

The state estimation is approached as a smoothing problem of a stochastic process, in which the state at a given time is refined by using future observation samples. The smoother estimation is considerably more accurate than the filter counterpart. Note that the smoother is not causal, so it cannot be directly used for feedback control. However, the smoothing estimations can be exploited by cycle-to-cycle learning-type strategies. For example, the impact velocities can be estimated and be used as the evaluation variables in the run-to-run control. In a more direct way, the position estimation can be used for position tracking with iterative learning control (ILC).

7.2 Recommendations for future work

There is potential to extend and improve the ideas and results presented in this thesis. Several possible directions for future research are suggested:

- The dynamical system identification is very important for the application of soft-landing controllers. On the one hand, it is essential for the design of open-loop and feedforward policies. Although run-to-run strategies can be used to correct those, good initial guesses would greatly improve their convergence rate. On the other hand, regarding position tracking, even though it is possible to design model-free feedback controllers, they still rely on position estimations when measuring the position is not feasible. The estimation precision is greatly dependent on the modeling errors. Therefore, the development of an accurate and efficient identification procedure for any reluctance actuator would be a major contribution. Ideally, it would fully characterize the system, including mechanical and electromagnetic dynamics, from easily measurable variables, e.g., the coil voltage and current. This thesis has proposed model reductions for the electromagnetic system, and an identifiability analysis provided that the position is fixed. We suggest expanding upon

this work, with identifiability analysis of the entire dynamical system, gaining insight about the required excitation and measurements for estimating every relevant parameter of the original or reduced models.

- R2R control is a combination of different components, and each one can be further investigated. Regarding the search method, the one based on Bayesian optimization (R2R-BO) proves to be the best in both simulated and experimental results. However, it is the most computationally expensive, even after the adjustments introduced. The most efficient alternative from the ones analyzed is based on the Nelder–Mead method (R2R-NM). It proves to be quite effective at exploitation, i.e., closing around the best point thus far and reaching a local minimum. However, it is not as suitable for exploration, i.e., searching the entire space for better points and thus ultimately finding the global optimum. Thus, a combination of R2R-BO and R2R-NM could be advantageous, e.g. exploring sporadically as in R2R-BO while exploiting frequently as in R2R-NM.

  Concerning the input generation, almost any type of controller can be incorporated in an R2R algorithm for its cycle-to-cycle adaptation. This thesis has parameterized the input based on open-loop input profiles and feedforward controllers because they do not rely on measuring or estimating the position. An interesting alternative that has not yet been tested is the R2R optimization of model parameters used in a position estimator—ideally a real-time observer—, whose estimations can be exploited by feedback controllers.

- Apart from the one presented in this thesis, there are many proposals of feedback controllers in the literature. For this class of actuators, the actual research interest lies in the state observer. From the point of view of stochastic estimation, smoothers have proven to be significantly more precise than filters. However, only filters can be regarded as stochastic observers, because smoothers are not causal. Thus, ways of incorporating the information of the smoothers into real-time observers should be studied. One possible approach is through a cycle-to-cycle adaptation of the observer parameters. As mentioned above, it can be based on the R2R algorithm presented in this thesis so that the model parameters are optimized for the observer instead of—or in addition to—the feedforward controller. Nonetheless, a more direct usage of the smoothing estimations is for ILC, in which the position errors during one commutation are used to adapt the input profile for the next commutation.

Appendix A

Run-to-Run Search Alternatives

In Section 4.3, we have proposed a run-to-run strategy with a search function based on the theory of Bayesian optimization. For comparison purposes, two additional search functions have been designed and are described in this appendix.

A.1 Pattern search

Pattern search (PS) is a direct-search optimization method. As such, it does not require to compute or estimate the gradient of the cost function [132]. Instead, it evaluates points following a pattern that does not depend on the cost function [133]. Although originally formulated for unconstrained optimization, it has been extended to constrained problems [134]. Recently, a constrained PS method has been adapted for R2R soft-landing control of reluctance actuators [78]. This state-of-the-the-art approach is the basis for the presented algorithm.

The mesh pattern has $2\,d + 1$ points (being d the dimension of the search space), where the starting one $\mathbf{X}_1$ is the best point so far $\boldsymbol{\chi}_{\mathbf{best}}$ (i.e., the point with the lowest cost). The remaining points $\mathbf{X}_2$, $\mathbf{X}_3$, ..., $\mathbf{X}_{2\,d+1}$ are placed around it, such that they correspond to the centers of the faces of a d-dimensional orthotope[1] whose center is $\mathbf{X}_1$. The points are selected one by one as χ^{j+1}, to be evaluated outside the search function (see Algorithm 4.1). Once the last point has been evaluated, there are two ways of updating the mesh, depending on which one is the best point.

1. **Contraction**. If the best point is still $\mathbf{X}_1$, the mesh is contracted, reducing the distance of the other points to $\mathbf{X}_1$.
2. **Expansion**. If the best point is any other $\mathbf{X}_i$, the center of the mesh moves to that point, so that $\mathbf{X}_i$ becomes the starting point of the new mesh. Also, the mesh is expanded, augmenting the distance of the other points to the new $\mathbf{X}_1$.

[1] The orthotope is a generalization of the rectangle ($d = 2$) and rectangular cuboid ($d = 3$) for any d.

The search function is described in Algorithm A.1. Following the notation introduced in Chapter 4, its inputs are the point $\boldsymbol{\chi}^j$, which has been obtained in the previous iteration, and its evaluation ψ^j. Its output is the next point $\boldsymbol{\chi}^{j+1}$. The function relies on some persistent variables, such as the matrices $\mathbf{X} \in \mathbb{R}^{d \times (2\,d+1)}$ and $\boldsymbol{\Psi} \in \mathbb{R}^{1 \times (2\,d+1)}$, which are used to store the mesh points and their corresponding evaluations. The variables are independently updated and stored for each operation type, but, to simplify the algorithm description, the distinction is omitted. It also depends on two constant coefficients for the contracting or expanding the mesh (c_{con} and c_{exp}, respectively), which must satisfy the following conditions:

$$0 < c_{\mathrm{con}} < 1, \qquad\qquad c_{\mathrm{exp}} > 1. \tag{A.1}$$

Algorithm A.1 Pattern search optimization

```
1:  function SEARCH(χ^j, ψ^j)
2:      Constant. d, c_exp, c_con, χ_lb, χ_ub, ΔX_min, ΔX_max
3:      Persistent. X, Ψ, ΔX, k
4:      Ψ_k ← ψ^j                                   ▷ Store current cost
5:      loop
6:          k ← k + 1                               ▷ Update mesh index
7:          if k > 2 d + 1 then
8:              i ← arg min_i' Ψ_i'
9:              χ_best ← X_i                        ▷ Update best point
10:             if i = 1 then
11:                 ΔX ← sat_{ΔX_min}^{ΔX_max}(c_con ΔX)    ▷ Contraction
12:             else
13:                 ΔX ← sat_{ΔX_min}^{ΔX_max}(c_exp ΔX)    ▷ Expansion
14:             end if
15:             k ← 1
16:         end if
17:         X_k ← sat_{χ_lb}^{χ_ub}(χ_best + ΔX_k)  ▷ Next mesh point
18:         if X_k ≠ X_i, ∀i < k then
19:             χ^{j+1} ← X_k
20:             return χ^{j+1}
21:         else
22:             Ψ_k ← ∞                             ▷ Skip evaluation of X_k
23:         end if
24:     end loop
25: end function
```

The first step of the algorithm is to store the last cost ψ^j in the vector Ψ. Secondly, if every point of the mesh has been evaluated and stored, the mesh is updated, expanding or contracting as required. Then, the next point to be evaluated is selected. Note that a saturation function sat is used to constrain the point to the search bounds $\boldsymbol{\chi}_{\mathbf{lb}}$ and $\boldsymbol{\chi}_{\mathbf{ub}}$. It is therefore possible that the selected point is identical to a previous one. In that case, a

new point is calculated and selected for evaluation. This last measure is an improvement over the state-of-the-art search function [78], preventing the redundant evaluation of identical points and potentially speeding up the convergence.

A.2 Nelder–Mead

For comparison purposes, an alternative search method has been developed. It is based on the Nelder–Mead (NM) simplex method, which is one of the most widely used and cited direct search methods [135]–[137]. The algorithm keeps a set of $d + 1$ evaluated points forming the vertices of a nondegenerate simplex[2]. In each iteration, one or more tasks are performed, modifying the vertices and reevaluating the function in those new points. The tasks are illustrated in Fig. A.1 for the simple case of $d = 2$. They are:

1. **Reflection**. The worst vertex (the point that corresponds to the largest function evaluation) is reflected with respect to the centroid of the remaining vertices.
2. **Expansion**. If the reflected point is the best so far, it is expanded farther from the centroid. The best one of these two is kept.
3. **Contraction**. If the reflected vertex is the worst point, a contraction is performed toward the centroid.
4. **Renewal**. If the contracted point is worse than its original, all vertices of the simplex are modified and evaluated.

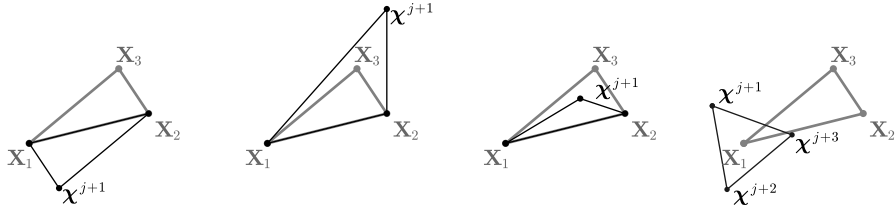

(a) Reflection. **(b)** Expansion. **(c)** Contraction. **(d)** Renewal.

Figure A.1: Tasks for updating the simplex ($d = 2$) and selecting the next point(s) to be evaluated.

In order to implement it in the R2R control, the standard algorithm is modified in several ways. The first modification is related to the last task. The standard method shrinks the simplex, fixed on the best vertex. As stated by various authors [138], [139], the shrinkage is potentially problematic because it may rapidly converge to a nonoptimal point. It is also inadvisable for optimizing stochastic functions, as the best point is never

[2]The simplex is a generalization of the triangle ($d = 2$) and tetrahedron ($d = 3$) for any d.

reevaluated. In [138] a translation is proposed such that the previous best vertex becomes the center of the new one. In our proposal, the simplex is also centered at the best point. However, instead of maintaining its shape, the vertices are recalculated so they form a randomly rotated regular simplex with the same volume. This prevents both simplex degeneracy and retention of misleadingly good evaluations due to noisy measurements.

Secondly, instead of setting a termination condition, the algorithm is designed to continually operate. Specifically, instead of terminating the optimization when the simplex volume is lesser than a chosen minimum $V_{\min}$, the simplex is prevented to be contracted below that threshold. The simplex volume V is updated in each iteration, augmenting it when expanding and reducing it when contracting, without requiring to compute it from the vertices in every iteration. Also, the actual simplex volume is not important, it is possible to initialize it to 1 and then set $V_{\min}$ in accordance.

The function is described in Algorithm A.2. Its inputs are the point $\boldsymbol{\chi}^j$, which was obtained in the previous iteration, and its evaluation ψ^j. Its output is the next point $\boldsymbol{\chi}^{j+1}$. In the process, several variables are updated inside the function: the simplex vertices $\mathbf{X} \in \mathbb{R}^{d\times(d+1)}$ and their respective evaluations $\boldsymbol{\Psi} \in \mathbb{R}^{1\times(d+1)}$, the centroid $\boldsymbol{\chi}_\mathbf{c} \in \mathbb{R}^d$, and the volume V. Normally, the NM method is presented in a sequential way with multiple evaluations per iteration. However, as stated in Algorithm 4.1, only one evaluation is needed in each function call. Thus, the current step (reflecting, expanding, contracting or rearranging) is stored in the persistent variable $s \in \{1,\, 2,\, 3,\, 4\}$. For the same reason, the index of the vertex to be evaluated is stored in the persistent variable $k \in \{1,\, 2,\, \ldots,\, (d+1)\}$. Note that all these variables are different for each operation type, but, for the sake of simplicity, that distinction is omitted. The method also depends on three constant coefficients for the reflection, expansion and contraction steps (c_{ref}, c_{exp} and c_{con}, respectively). They must satisfy the following conditions:

$$c_{\text{exp}} > 1, \qquad 0 < c_{\text{ref}} < c_{\text{exp}}, \qquad 0 < c_{\text{con}} < 1. \tag{A.2}$$

Algorithm A.2 Nelder–Mead optimization

```
1: function SEARCH(χ^j, ψ^j)
2:     Constant. d, c_ref, c_exp, c_con, V_min
3:     Persistent. X, Ψ, χ_c, V, s, k
       ▷ Update simplex X, Ψ and step s
4:     switch s
5:         case 1  ▷ Reflect
6:             if ψ^j ≤ Ψ_{d+1} then
7:                 (X_{d+1}, Ψ_{d+1}) ← (χ^j, ψ^j)
8:             end if
9:             if ψ^j < Ψ_1 then
10:                s ← 2
11:            else if ψ^j > Ψ_d then
12:                s ← 3
13:            else if ψ^j > Ψ_d then
14:                X ← RENEW(X_1, V)
15:                s ← 4
16:            end if
17:        case 2  ▷ Expand
18:            if ψ^j < Ψ_{d+1} then
19:                (X_{d+1}, Ψ_{d+1}) ← (χ^j, ψ^j)
20:            end if
21:            s ← 1
22:        case 3  ▷ Contract
23:            if ψ^j < Ψ_{d+1} then
24:                (X_{d+1}, Ψ_{d+1}) ← (χ^j, ψ^j)
25:                s ← 1
26:            else
27:                X ← RENEW(X_1, V)
28:                s ← 4
29:            end if
30:        case 4  ▷ Simplex
31:            Ψ_k ← ψ^j
32:            if k = d + 1 then
33:                s ← 1
34:                k ← 1        ▷ Initialize index
35:            end if
36:    end switch
       ▷ Find next decision vector χ^{j+1}
37:    switch s
38:        case 1  ▷ Reflect
39:            (X, Ψ) ← SORT(X, Ψ)
               ▷ Ψ_1 ≤ Ψ_2 ≤ ... ≤ Ψ_{d+1}
40:            χ_c ← Σ_{i=1}^{d} X_i / d
               ▷ Centroid of X_1, ..., X_d
41:            χ^{j+1} ← χ_c + c_ref(χ_c − X_{d+1})
42:            V ← c_ref V  ▷ Update volume
43:        case 2  ▷ Expand
44:            χ^{j+1} ← χ_c + c_exp (X_{d+1} − χ_c)
45:            V ← c_exp V  ▷ Update volume
46:        case 3  ▷ Contract
47:            χ^{j+1} ← χ_c + c_con (X_{d+1} − χ_c)
48:            V ← c_con V  ▷ Update volume
49:        case 4  ▷ Simplex
50:            χ^{j+1} ← X_j
51:            k ← k + 1          ▷ Next vertex
52:    end switch
53:    return χ^{j+1}
54: end function
```

Appendix B

Run-to-Run Voltage Control

This appendix presents an alternative input parametrization for the run-to-run method proposed in Chapter 4. Bang-bang profiles are considered for the input signals, which are more suitable for voltage control. Then, different run-to-run voltage control methods are compared through simulations.

B.1 Input generation and dynamical model

When using the voltage as input, bang-bang solutions are fitting because they are very easily parametrizable and implementable. The input profiles switch between two limiting values $u_{\min}$ and $u_{\max}$, so they can be defined from a finite set of switching instants or intervals. The simplest bang-bang profile suitable for soft-landing control is one parameterized in terms of two time intervals ($d = 2$) for each operation, as shown in Fig. B.1.

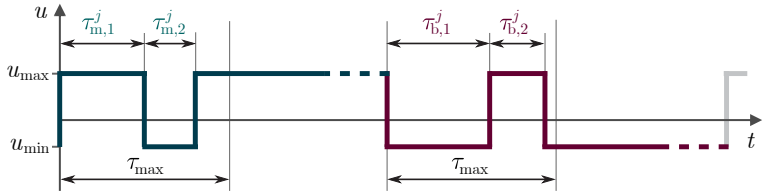

Figure B.1: Profile of the input signals for making and breaking operations of the jth iteration.

The variable time intervals are $\tau^j_{\mathrm{m/b},1}$ and $\tau^j_{\mathrm{m/b},2}$, while the constant $\tau_{\max}$ is the maximum time interval allowed for the commutation. The two interval parameters must be

related to the decision vectors $\boldsymbol{\chi}^{j}_{\mathbf{m/b}}$. They are normalized as follows:

$$\chi^{j}_{\mathrm{m/b},1} = \frac{\tau^{j}_{\mathrm{m/b},1}}{\tau_{\max}}, \qquad \chi^{j}_{\mathrm{m/b},2} = \frac{\tau^{j}_{\mathrm{m/b},2}}{\tau_{\max} - \tau^{j}_{\mathrm{m/b},1}}. \tag{B.1}$$

This way, every decision variable can conveniently be bounded to $[0, 1]$, and it is ensured that $\tau^{j}_{\mathrm{m/b},1} + \tau^{j}_{\mathrm{m/b},2} \leq \tau_{\max}$. The constant $\tau_{\max}$ must be set accordingly.

Note that, when $u_{\min} = 0$, the optimally designed soft-landing control signals that minimize the transient time follows the aforementioned bang-bang profile [62]. However, if $u_{\min} < 0$, the time-optimal voltage solutions show a bang-bang-off behavior [24]. In other words, an additional interval in which $u = 0$ would be required for each operation. However, this interval is only necessary to ensure that the current and magnetic flux do not change direction. Thus, to keep the input generation as simple as possible, an alternative solution is considered: saturating the current to prevent negative values. As discussed in Section 3.4.1, this is easily implemented with diodes or simulated with a hybrid automaton.

In that regard, the dynamical model used in the simulations is a simplified version of the one presented in Section 3.4.1, in which the eddy currents are neglected, i.e. $k_{\mathrm{eddy}} = 0$. As such, it is described by the hybrid automaton depicted in Fig. B.2. It presents six dynamic modes, with the corresponding guard conditions and reset rules. The discrete state $q \in \{1, 2, \ldots, 6\}$ designates the dynamic mode: positive magnetic flux and plunger in the lower limit, motion or the upper limit ($q = 1$, 2 or 3, respectively); or current saturated to zero and plunger in the lower limit, motion or the upper limit ($q = 4$, 5 or 6, respectively). Note that the automaton can be interpreted as a simplified version of the one from Fig. 3.2. In this case, as the eddy currents are neglected, saturating the magnetic flux to zero implies saturating also the current.

B.2 Compared search strategies

The proposed run-to-run (R2R) control is compared with two alternative strategies.

Run-to-run based on pattern search (R2R-PS)

The first one is based on the pattern search (PS) method, as explained in Appendix A.1. It requires evaluating $2\,d+1$ times in each iteration, one is the reevaluation of the previous best point and the others are evaluations around that point. As $d = 2$, it is necessary to perform 5 making and 5 breaking commutations in each iteration. The starting mesh for both operation types is

$$\mathbf{X} = \begin{bmatrix} 0.5 & 0.75 & 0.5 & 0.25 & 0.5 \\ 0.5 & 0.5 & 0.75 & 0.5 & 0.25 \end{bmatrix}. \tag{B.2}$$

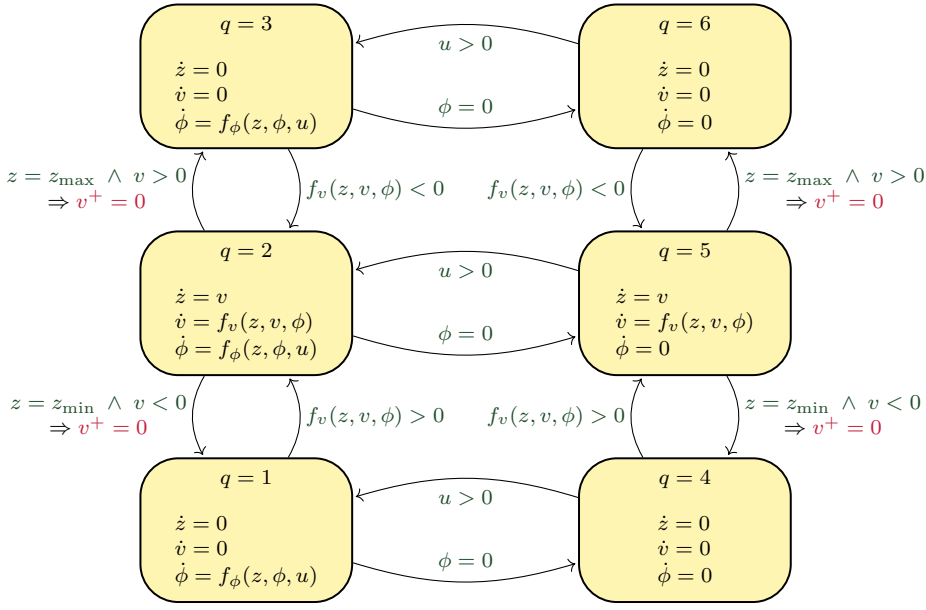

Figure B.2: Diagram of the hybrid automaton modeling the full system of the actuator, including the magnetic flux saturation to zero. Each transition between modes (yellow blocks) occurs when the corresponding guard condition (green text) is satisfied. In some transitions, the continuous state jumps according to the corresponding reset rule (red text).

Accordingly, the remaining persistent variables of Algorithm A.1 are set as follows:

$$\boldsymbol{\chi}_{\mathbf{best}} = \begin{bmatrix} 0.5 \\ 0.5 \end{bmatrix}, \quad \Delta\mathbf{X} = 0.25 \begin{bmatrix} \mathbf{0} & \boldsymbol{I} & -\boldsymbol{I} \end{bmatrix}, \quad k = 1. \tag{B.3}$$

The mesh size is halved or doubled if the new best point is the same or not, respectively, as the previous one. Overall, the constants of the PS optimization method are set as

$$c_{\text{exp}} = 2, \qquad c_{\text{con}} = 0.5, \tag{B.4}$$

$$\Delta\mathbf{X}_{\mathbf{min}} = 10^{-3} \begin{bmatrix} \mathbf{0} & \boldsymbol{I} & -\boldsymbol{I} \end{bmatrix}, \qquad \Delta\mathbf{X}_{\mathbf{max}} = \begin{bmatrix} \mathbf{0} & \boldsymbol{I} & -\boldsymbol{I} \end{bmatrix}. \tag{B.5}$$

Run-to-run based on Nelder–Mead (R2R-NM)

The second R2R control is based on the NM method. Compared to the PS method, it requires fewer evaluations per iteration. For its application in R2R control, several modifications are introduced to the algorithm, as explained in Appendix A.2. The initial points are set such that they form a regular simplex, i.e., an equilateral triangle, centered at $[0.5 \quad 0.5]^\mathsf{T}$, with every vertex at a distance of 0.5, and randomly rotated. The simplex is updated depending on three constant coefficients for its reflection, expansion and

contraction (c_{ref}, c_{exp} and c_{con} respectively). The constants of the method are set as follows:

$$V_{\min} = 0.005^d, \qquad c_{\text{ref}} = 1, \qquad c_{\text{exp}} = 2, \qquad c_{\text{con}} = 0.5. \tag{B.6}$$

Run-to-run based on Bayesian optimization (R2R-BO)

The last strategy uses a preliminary version of the BO search function presented in Section 4.3. The first difference is that the search space lower and upper bounds $\boldsymbol{\chi}_{\mathbf{lb}}$ and $\boldsymbol{\chi}_{\mathbf{ub}}$ are not adaptive, i.e. the function BOUNDS (Algorithm 4.3) is not included. Secondly, the (4.26) is not used for removing points that are far away from the bounded space. Lastly, the acquisition function is the next expected improvement (4.38), which does not consider that the evaluation variables are always nonnegative. In regards to its configuration, the first evaluated decision vector is set to $[0.5 \quad 0.5]^{\mathsf{T}}$ for both making and breaking operations. To limit the stored data, $k_{\max}$ is set to 50. Furthermore, the prior mean values and kernel hyperparameters from (4.16) are specified for each case so the optimization process works efficiently.

B.3 Simulation results

Simulations are performed to analyze the proposed R2R control and to compare the optimization algorithm with the pattern search method. To simulate the disturbance, white noise is added to the position constraints,

$$z^j_{\min} = \bar{z}_{\min} + \varepsilon^j_{z\min}, \qquad z^j_{\max} = \bar{z}_{\max} + \varepsilon^j_{z\max}, \tag{B.7}$$

where $\varepsilon^j_{z\min}$ and $\varepsilon^j_{z\min}$ are independent normal random variables with zero mean and standard deviation σ_z. The parameters for the input generation and the model are specified in Table B.1.

Table B.1: System dynamics and input parameters.

Parameter	Value	
R	55	Ω
N	1200	
$\mathcal{R}_{\text{c},0}$	2.32×10^6	H^{-1}
ϕ_{sat}	2×10^{-5}	Wb
$\mathcal{R}_{\text{g},0}$	5.594×10^6	H^{-1}
$\mathcal{R}'_{\text{g},0}$	1.105×10^{11}	H^{-1}/m
k_1	1318	m^{-1}
k_2	9.735×10^{-3}	m

Parameter	Value	
m_{mov}	1.6×10^{-3}	kg
k_{sp}	74.05	N/m
z_{sp}	1.5×10^{-2}	m
c_{f}	0	Ns/m
$\bar{z}_{\min}$	3×10^{-4}	m
$\bar{z}_{\max}$	1.3×10^{-3}	m
$u_{\min/\max}$	∓ 50	V
$\tau_{\max}$	3×10^{-3}	s

The three R2R controllers are compared through a Monte Carlo method, performing 500 simulations of 200 making and breaking commutations for each given σ_z. For the first comparison, σ_z is set to $10^{-6}\,\mathrm{m}$ and the resulting costs ψ are obtained for each commutation and each operation type. R2R-PS requires 5 commutations per iteration so, for better visualization, the results are grouped 5 by 5. In Fig. B.3, from each set of 2500 costs, the mean is displayed, as well as the interval between the 25th and 75th percentiles. R2R-PS is able to reach costs close to zero, as the 25th percentile values indicate, but the observation randomness, albeit low, slows down the convergence rate—especially in the making operation—, as the mean and 75th percentile values indicate. In contrast, the other strategies converge faster, especially the proposed R2R-BO.

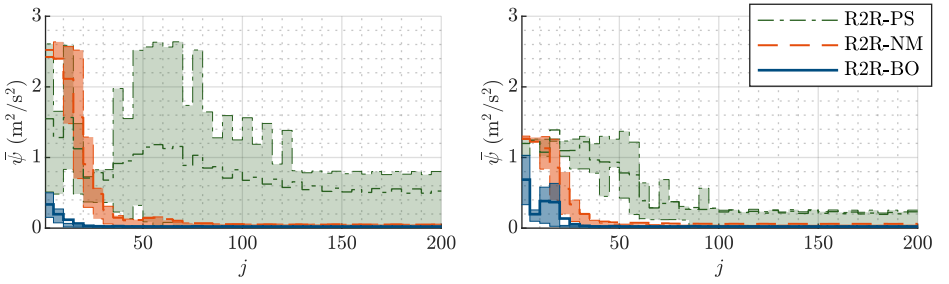

(a) Making operations. **(b)** Breaking operations.

Figure B.3: Comparison of results (mean values and 25th-75th percentile intervals) from R2R-PS, R2R-NM and R2R-BO, for $\sigma_z = 10^{-6}\,\mathrm{m}$.

For the following graphics, we display the average cost $\bar{\psi}$ for each number of commutations j,

$$\bar{\psi} = \frac{1}{j}\sum_{i=1}^{j}\psi^i. \tag{B.8}$$

$\bar{\psi} = \sum_{i=1}^{j}\psi^i/j$ It varies less abruptly, making it more suitable for increasing position deviations and eliminating the need for grouping in sets of 5. In Fig. B.4, the mean and percentile intervals of $\bar{\psi}$ are represented as a function of the number of commutations. Figs. B.4a and B.4b show the average costs for $\sigma_z = 10^{-6}\,\mathrm{m}$, obtained from the previous costs ψ (Figs. B.3a and B.3b). The σ_z is increased to $10^{-5}\,\mathrm{m}$ (Figs. B.4c and B.4d), $2\times10^{-5}\,\mathrm{m}$ (Figs. B.4e and B.4f), and $5\times10^{-5}\,\mathrm{m}$ (Figs. B.4g and B.4h). As expected R2R-BO is consistently better than R2R-PS. The R2R-BO results are very good for $\sigma_z \leq 2\times10^{-5}\,\mathrm{m}$. In particular, the R2R-BO making costs are slightly better than the breaking ones for $\sigma_z = 10^{-6}\,\mathrm{m}$ because, in this specific case, the starting point is significantly better. Despite that, for greater deviations, the breaking average costs reach lower minimums. Notice also that, although setting $\sigma_z = 5\times10^{-5}\,\mathrm{m}$ is merely a 5 % of the nominal valve travel distance, it is enough to make the impact velocities vary greatly between commutations, especially in the making operations.

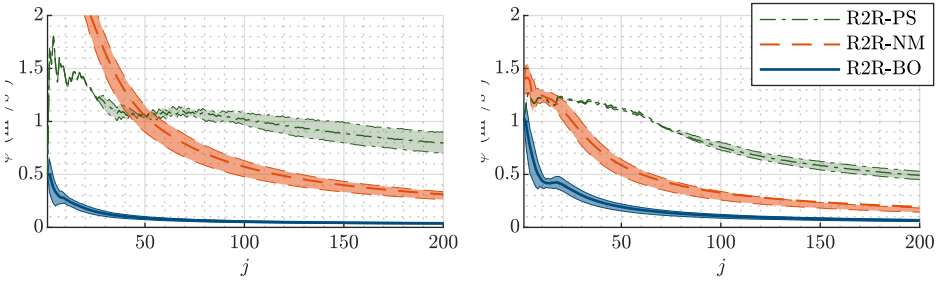

(a) Making operations ($\sigma_z = 10^{-6}$ m).

(b) Breaking operations ($\sigma_z = 10^{-6}$ m).

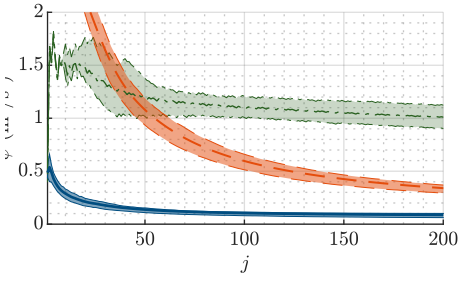

(c) Making operations ($\sigma_z = 10^{-5}$ m).

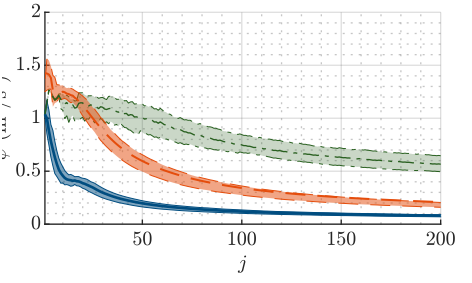

(d) Breaking operations ($\sigma_z = 10^{-5}$ m).

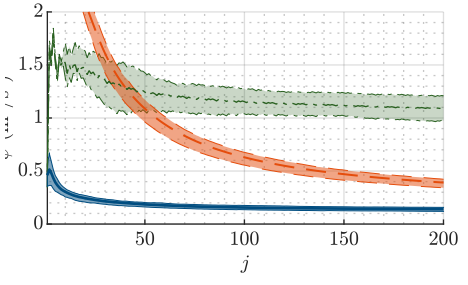

(e) Making operations ($\sigma_z = 2 \times 10^{-5}$ m).

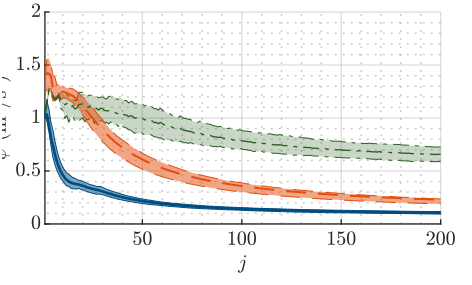

(f) Breaking operations ($\sigma_z = 2 \times 10^{-5}$ m).

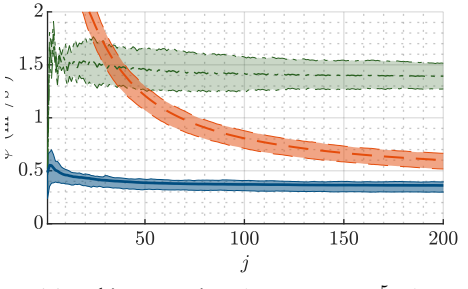

(g) Making operations ($\sigma_z = 5 \times 10^{-5}$ m).

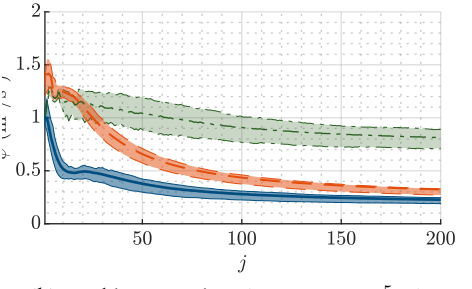

(h) Breaking operations ($\sigma_z = 5 \times 10^{-5}$ m).

Figure B.4: Comparison of results (mean values and 25th-75th percentile intervals) from R2R-PS, R2R-NM and R2R-BO, for different position deviations.

Appendix C

Dimension Reduction

This appendix details step by step the process of removing redundant decision variables for the provided example from Section 4.5.1. Then, simulated results before and after the dimension reduction are used for validation purposes.

C.1 Algorithm execution

Firstly, the sensitivities before the dimension reduction are represented in Fig. C.1. Note that the sensitivities with respect to the spring constants z_{sp} and $k_{\mathrm{sp}}^{\#}$ are very similar. The reason is that the spring resting position z_{sp} is much larger than any $z \in [z_{\min},\, z_{\max}]$, so the spring force is almost constant with respect to z. Therefore, the decision variable related to one of those parameters could be omitted. Note also that the sensitivity with respect to k_{eddy} is very low, so that decision variable could probably be discarded as well. Nevertheless, there may be other decision variables that could be removed, even if it is not readily apparent from observing the graphics. Thus, Algorithm 4.4 is executed.

In both making and breaking operations, the first decision variable to be removed is the one related to $\mathcal{R}_{\mathrm{c},0}$ ($j = 7$). The resulting $\boldsymbol{\chi}_{\setminus j}$ is

$$\boldsymbol{\chi}_{\setminus 7} = \begin{bmatrix} 108 & 31 & 25 & 23 & 26 & -111 & 0 & 106 & -7 \end{bmatrix}^{\mathsf{T}} \times 10^{-3} \tag{C.1}$$

for the making operation, and

$$\boldsymbol{\chi}_{\setminus 7} = \begin{bmatrix} 43 & 103 & 23 & 29 & -15 & -115 & 0 & 81 & -22 \end{bmatrix}^{\mathsf{T}} \times 10^{-3} \tag{C.2}$$

for the breaking operation.

These variables can be removed because their sensibilities can be approximately replicated with the other ones ($\nabla U(t)\, \boldsymbol{\chi}_{\setminus j} \approx \nabla U_k(t)$). The errors of this approximation are represented in Fig. C.2. Notice that they are bounded according to the selected tolerance $\chi_{\mathrm{tol}} = 10^{-3}$ A.

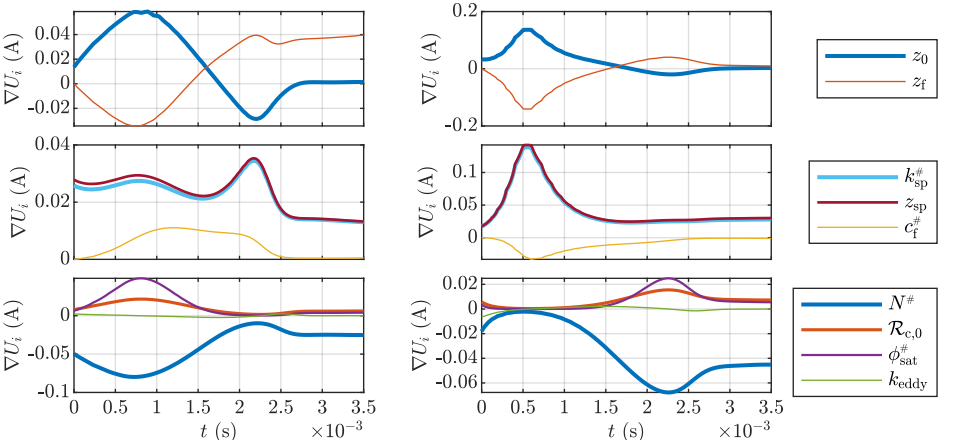

(a) Making operation. **(b)** Breaking operation.

Figure C.1: Sensitivities of the input to the decision variables ($d = 9$).

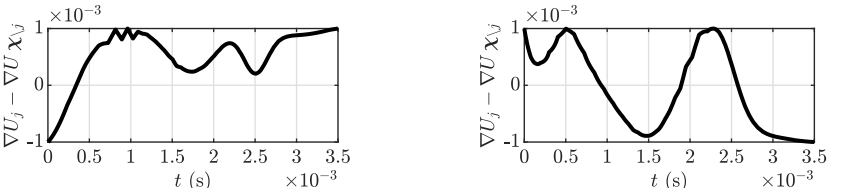

(a) Making operation. **(b)** Making operation.

Figure C.2: Sensitivity errors due to the first removed decision variable.

Once a decision variable is removed, the bounds $\theta_{\mathrm{lb}i}$ and $\theta_{\mathrm{ub}i}$ of the remaining variables χ_i are augmented, as explained in Section 4.4.2. Their sensitivities are also augmented because they are directly proportional to the corresponding bound length $(\theta_{\mathrm{ub}_i} - \theta_{\mathrm{lb}i})$. The sensitivities after the first loop iteration of the algorithm are represented in Fig. C.3. Note that, while the sensitivity related to $\mathcal{R}_{\mathrm{c},0}$ is removed, the other ones are slightly augmented to compensate for it.

After the second iteration, the 8th decision variable (related to k_eddy) is selected for removal in both operations. Specifically, the computed $\boldsymbol{\chi}_{\setminus j}$ is

$$\boldsymbol{\chi}_{\setminus 8} = \begin{bmatrix} -173 & -34 & -49 & -56 & -246 & -144 & 41 & 0 \end{bmatrix}^\mathsf{T} \times 10^{-3} \tag{C.3}$$

for the making operation, and

$$\boldsymbol{\chi}_{\setminus 8} = \begin{bmatrix} -169 & -366 & -14 & -255 & -184 & -249 & 11 & 0 \end{bmatrix}^\mathsf{T} \times 10^{-3} \tag{C.4}$$

for the breaking operation. Note that 8th element of each of these 8th dimensional decision vectors corresponds to the 9th element of the original 9th dimensional decision

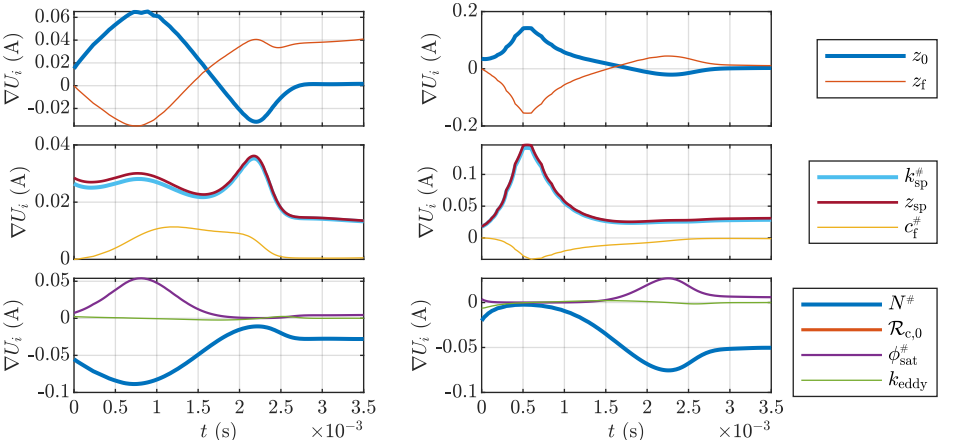

(a) Making operation. **(b)** Breaking operation.

Figure C.3: Sensitivities of the input to the decision variables ($d = 8$).

vectors. The sensitivity errors due to its removal are represented in Fig. C.4. Then, the resulting sensitivities are represented in Fig. C.5.

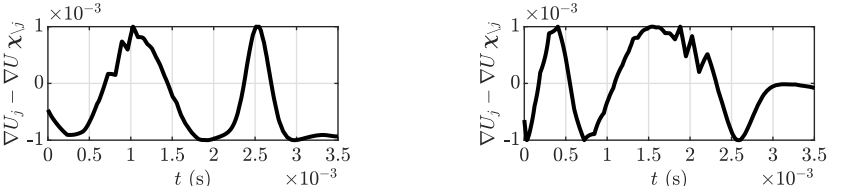

(a) Making operation. **(b)** Making operation.

Figure C.4: Sensitivity errors due to the second removed decision variable.

Lastly, after the third iteration of the algorithm, the 3rd decision variable (related to $k_\mathrm{sp}^\#$) is selected for removal. The calculated $\boldsymbol{\chi}_{\setminus j}$ is

$$\boldsymbol{\chi}_{\setminus 3} = \begin{bmatrix} -273 & -7 & 0 & 576 & 177 & -210 & 147 \end{bmatrix}^\mathsf{T} \times 10^{-3} \tag{C.5}$$

for the making operation, and

$$\boldsymbol{\chi}_{\setminus 3} = \begin{bmatrix} 52 & -226 & 0 & 473 & 39 & -211 & 141 \end{bmatrix}^\mathsf{T} \times 10^{-3} \tag{C.6}$$

for the breaking operation. The sensitivity errors due to its removal are represented in Fig. C.6.

At the end, the algorithm has removed the 3rd, 7th and 9th decision variables ($k_\mathrm{sp}^\#$, $\mathcal{R}_{\mathrm{c},0}$, k_eddy) for both operations.

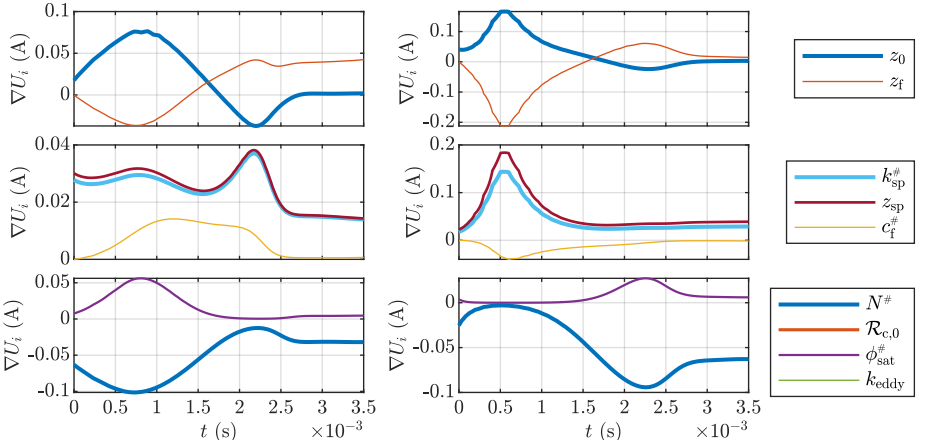

(a) Making operation. **(b)** Breaking operation.

Figure C.5: Sensitivities of the input to the decision variables ($d = 7$).

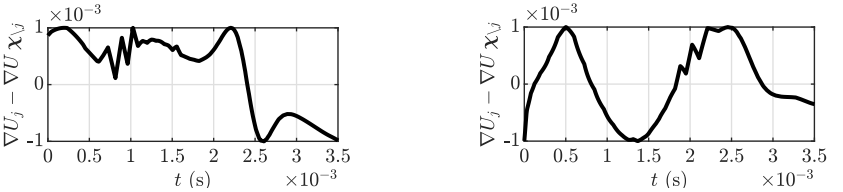

(a) Making operation. **(b)** Making operation.

Figure C.6: Sensitivity errors due to the third removed decision variable.

C.2 Run-to-run comparison

Note that the parameter reduction process is optional, the original decision vector ($d = 9$) can be used. Moreover, it is possible to use larger decision vectors, adding theoretically redundant parameters (in the presented case, the moving mass m_{mov}). However, this is not only detrimental to the convergence rate, but also to the computational requirements of the control strategy.

To showcase the effectiveness of reducing the number of decision variables, an additional simulated analysis is included in this appendix section, analogous to the one presented in Section 4.5.3. In Fig. C.7, results of R2R-BO using the full decision vector ($d = 9$) are compared with the ones using the reduced decision vector ($d = 6$). In the breaking operation, the results are quite similar, especially in the mean value. On the other hand, in the making operation, which starts with a much greater cost, the advantage of reducing d is evident.

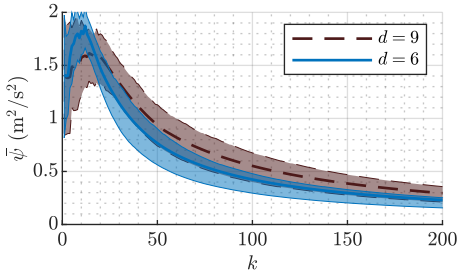

(a) Making operations ($\sigma_p = 10^{-3}$).

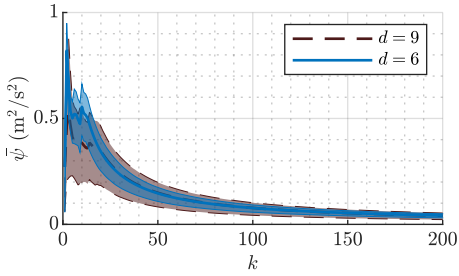

(b) Breaking operations ($\sigma_p = 10^{-3}$).

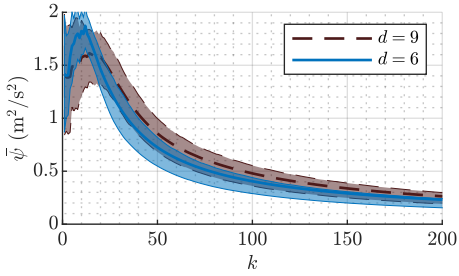

(c) Making operations ($\sigma_p = 2 \times 10^{-3}$).

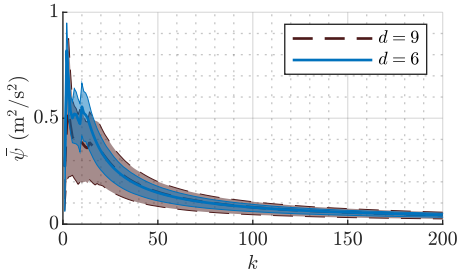

(d) Breaking operations ($\sigma_p = 2 \times 10^{-3}$).

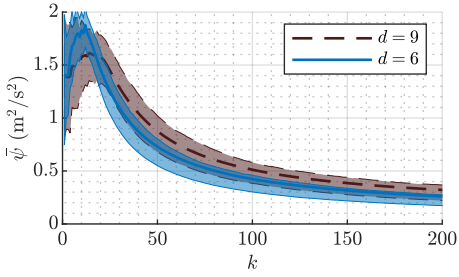

(e) Making operations ($\sigma_p = 5 \times 10^{-3}$).

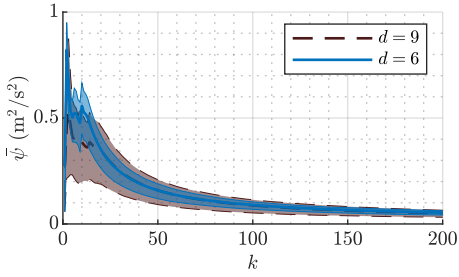

(f) Breaking operations ($\sigma_p = 5 \times 10^{-3}$).

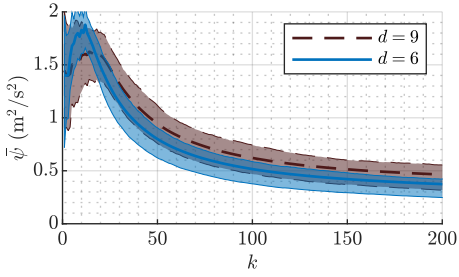

(g) Making operations ($\sigma_p = 10^{-2}$).

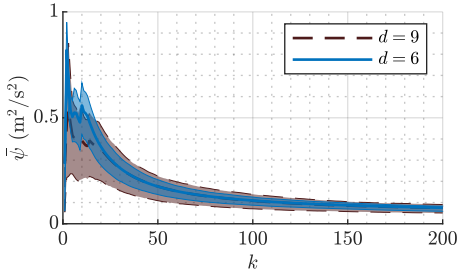

(h) Breaking operations ($\sigma_p = 10^{-2}$).

Figure C.7: Comparison of results (mean values and 25th-75th percentile intervals) from R2R-BO before and after the dimension reduction, for different σ_p.

Bibliography

[1] A. Katalenic, J. De Boeij, H. Butler, and P. P. J. Van Den Bosch, "Linearization of a current-driven reluctance actuator with hysteresis compensation," *Mechatronics*, vol. 23, no. 2, pp. 163–171, Mar. 2013. DOI: 10.1016/j.mechatronics.2013.01.004 (cit. on p. 25).

[2] X.-D. Lu and D. L. Trumper, "Ultrafast Tool Servos for Diamond Turning," *CIRP Annals*, vol. 54, no. 1, pp. 383–388, 2005. DOI: 10.1016/S0007-8506(07)60128-0 (cit. on p. 25).

[3] H. S. Lim, R. Krishnan, and N. S. Lobo, "Design and control of a linear propulsion system for an elevator using linear switched reluctance motor drives," *IEEE Transactions on Industrial Electronics*, vol. 55, no. 2, pp. 534–542, Feb. 2008. DOI: 10.1109/TIE.2007.911942 (cit. on p. 25).

[4] D. J. Kluk, M. T. Boulet, and D. L. Trumper, "A high-bandwidth, high-precision, two-axis steering mirror with moving iron actuator," *Mechatronics*, vol. 22, no. 3, pp. 257–270, Apr. 2012. DOI: 10.1016/j.mechatronics.2012.01.008 (cit. on p. 25).

[5] J. Bao, N. H. Vrijsen, B. L. Gysen, R. L. Sprangers, and E. A. Lomonova, "Optimization of the force density for medium-stroke reluctance actuators," *IEEE Transactions on Industry Applications*, vol. 50, no. 5, pp. 3194–3202, Feb. 2014. DOI: 10.1109/TIA.2014.2304586 (cit. on p. 25).

[6] X. Xue, K. W. E. Cheng, and Z. Zhang, "Model, analysis, and application of tubular linear switched reluctance actuator for linear compressors," *IEEE Transactions on Industrial Electronics*, vol. 65, no. 12, pp. 9863–9872, Dec. 2018. DOI: 10.1109/TIE.2018.2818638 (cit. on p. 25).

[7] S. Ito, S. Troppmair, B. Lindner, F. Cigarini, and G. Schitter, "Long-Range Fast Nanopositioner Using Nonlinearities of Hybrid Reluctance Actuator for Energy Efficiency," *IEEE Transactions on Industrial Electronics*, vol. 66, no. 4, pp. 3051–3059, Apr. 2019. DOI: 10.1109/TIE.2018.2842735 (cit. on p. 25).

[8] M. Naidu, S. Gopalakrishnan, and T. W. Nehl, "Fault-tolerant permanent magnet motor drive topologies for automotive X-by-wire systems," *IEEE Transactions on Industry Applications*, vol. 46, no. 2, pp. 841–848, Mar. 2010. DOI: 10.1109/TIA.2009.2039982 (cit. on p. 25).

[9] J. Acero, J. M. Burdio, L. A. Barragan, D. Navarro, R. Alonso, J. R. Ramon, F. Monterde, P. Hernandez, S. Llorente, and I. Garde, "Domestic induction appliances," *IEEE Industry Applications Magazine*, vol. 16, no. 2, pp. 39–47, Mar. 2010. DOI: 10.2165/00128413-199107960-00056 (cit. on p. 25).

[10] S. Haghbin, S. Lundmark, M. Alakula, and O. Carlson, "Grid-connected integrated battery chargers in vehicle applications: Review and new solution," *IEEE Transactions on Industrial Electronics*, vol. 60, no. 2, pp. 459–473, Feb. 2013. DOI: 10.1109/TIE.2012.2187414 (cit. on p. 25).

[11] T. C. Beh, M. Kato, T. Imura, S. Oh, and Y. Hori, "Automated Impedance Matching System for Robust Wireless Power Transfer via Magnetic Resonance Coupling," *IEEE Transactions on Industrial Electronics*, vol. 60, no. 9, pp. 3689–3698, Sep. 2013. DOI: 10.1109/TIE.2012.2206337 (cit. on p. 25).

[12] J. Pohl, M. Sethson, P. Krus, and J. O. Palmberg, "Modelling and validation of a fast switching valve intended for combustion engine valve trains," *Proceedings of the Institution of Mechanical Engineers. Part I: Journal of Systems and Control Engineering*, vol. 216, no. 2, pp. 105–116, Mar. 2002. DOI: 10.1243/0959651021541462 (cit. on p. 25).

[13] W. Hoffmann, K. Peterson, and A. G. Stefanopoulou, "Iterative learning control for soft landing of electromechanical valve actuator in camless engines," *IEEE Transactions on Control Systems Technology*, vol. 11, no. 2, pp. 174–184, Mar. 2003. DOI: 10.1109/TCST.2003.809242 (cit. on pp. 25, 91, 117).

[14] R. R. Chladny, C. R. Koch, and A. F. Lynch, "Modeling Automotive Gas-Exchange Solenoid Valve Actuators," *IEEE Transactions on Magnetics*, vol. 41, no. 3, pp. 1155–1162, Mar. 2005. DOI: 10.1109/TMAG.2004.841701 (cit. on pp. 25, 35).

[15] Y. P. Yang, J. J. Liu, D. H. Ye, Y. R. Chen, and P. H. Lu, "Multiobjective optimal design and soft landing control of an electromagnetic valve actuator for a camless engine," *IEEE/ASME Transactions on Mechatronics*, vol. 18, no. 3, pp. 963–972, Jun. 2013. DOI: 10.1109/TMECH.2012.2195728 (cit. on pp. 25, 91).

[16] A. T. van Zanten, "Evolution of electronic control systems for improving the vehicle dynamic behavior," in *Proceedings of the 6th International Symposium on Advanced Vehicle Control*, Hisoshima, Japan, Sep. 2002, pp. 7–15 (cit. on p. 25).

[17] M. Branciforte, A. Meli, G. Muscato, and D. Porto, "ANN and Non-Integer Order Modeling of ABS Solenoid Valves," *IEEE Transactions on Control Systems Technology*, vol. 19, no. 3, pp. 628–635, May 2011. DOI: 10.1109/TCST.2010.2049999 (cit. on p. 25).

[18] P. Barkan, "A Study of the Contact Bounce Phenomenon," *IEEE Transactions on Power Apparatus and Systems*, vol. PAS-86, no. 2, pp. 231–240, 1967. DOI: 10.1109/TPAS.1967.291840 (cit. on p. 25).

[19] A. G. Espinosa, J. R. R. Ruiz, and X. A. Morera, "A sensorless method for controlling the closure of a contactor," *IEEE Transactions on Magnetics*, vol. 43, no. 10, pp. 3896–3903, Oct. 2007. DOI: 10.1109/TMAG.2007.904355 (cit. on p. 25).

[20] R. M. Schmidt, G. Schitter, and J. van Eijk, "Electromechanic actuators," in *The Design of High Performance Mechatronics*, 3rd ed., Amsterdam, the Netherlands, 2011, ch. 5, pp. 243–247. DOI: 10.3233/978-1-60750-826-7-i (cit. on p. 26).

[21] E. Moya-Lasheras, C. Sagues, E. Ramirez-Laboreo, and S. Llorente, "Nonlinear Bounded State Estimation for Sensorless Control of an Electromagnetic Device," in *2017 IEEE 56th Annual Conference on Decision and Control (CDC)*, Melbourne, Australia, Dec. 2017, pp. 5050–5055. DOI: 10.1109/CDC.2017.8264407 (cit. on pp. 30, 31, 55, 146).

[22] E. Moya-Lasheras, C. Sagues, and S. Llorente, "An efficient dynamical model of reluctance actuators with flux fringing and magnetic hysteresis," *Mechatronics*, vol. 74, Apr. 2021. DOI: 10.1016/j.mechatronics.2021.102500 (cit. on pp. 30, 146).

[23] E. Moya-Lasheras, E. Ramirez-Laboreo, and C. Sagues, "Probability-Based Optimal Control Design for Soft Landing of Short-Stroke Actuators," *IEEE Transactions on Control Systems Technology*, vol. 28, no. 5, pp. 1956–1963, Jun. 2019. DOI: 10.1109/TCST.2019.2918479 (cit. on pp. 31, 145, 147).

[24] E. Ramirez-Laboreo, E. Moya-Lasheras, and C. Sagues, "Optimal open-loop control policies for a class of nonlinear actuators," in *2019 18th European Control Conference (ECC)*, Naples, Italy, Jun. 2019, pp. 3261–3266. DOI: 10.23919/ECC.2019.8795785 (cit. on pp. 31, 84, 146, 158).

[25] E. Moya-Lasheras, E. Ramirez-Laboreo, and C. Sagues, "A Novel Algorithm Based on Bayesian Optimization for Run-to-Run Control of Short-Stroke Reluctance Actuators," in *2019 18th European Control Conference (ECC)*, Naples, Italy, Jun. 2019, pp. 1103–1109. DOI: 10.23919/ECC.2019.8795949 (cit. on pp. 31, 146, 147).

[26] E. Moya-Lasheras and C. Sagues, "Run-to-Run Control With Bayesian Optimization for Soft Landing of Short-Stroke Reluctance Actuators," *IEEE/ASME Transactions on Mechatronics*, vol. 25, no. 6, pp. 2645–2656, Dec. 2020. DOI: 10.1109/TMECH.2020.2987942 (cit. on pp. 31, 145, 147).

[27] E. Moya-Lasheras, E. Ramirez-Laboreo, and C. Sagues, "Model-Free Sliding-Mode Controller for Soft Landing of Reluctance Actuators," in *21st IFAC World Congress 2020*, Berlin, Germany, Jul. 2020 (cit. on pp. 31, 146, 148).

[28] S. Llorente Gil, E. Moya Lasheras, E. J. Ramirez Laboreo, and C. Sagües Blázquiz, "Domestic appliance device", WO/2019/106488, 2019 (cit. on pp. 31, 146).

[29] J. Ballester Castañer, J. Corral Ricalde, S. Llorente Gil, E. Moya Lasheras, J. S. Ochoa Torres, E. Placer Maruri, E. J. Ramirez Laboreo, J. Rivera Peman, C. Sagües Blázquiz, and D. Serrano García, "Gas cooking appliance device," WO/2019/220247, 2019 (cit. on pp. 31, 146).

[30] E. Moya-Lasheras, J. M. Schellekens, and C. Sagues, "Rauch–Tung–Striebel Smoother for Control of Short-Stroke Reluctance Actuators," under review (cit. on pp. 31, 146, 149).

[31] E. Ramirez-Laboreo, E. Moya-Lasheras, and C. Sagues, "Real-Time Electromagnetic Estimation for Reluctance Actuators," *IEEE Transactions on Industrial Electronics*, vol. 66, no. 3, pp. 1952–1961, Mar. 2019. DOI: 10.1109/TIE.2018.2838077 (cit. on pp. 32, 55, 59, 145).

[32] A. M. Pawlak and T. W. Nehl, "Transient finite element modeling of solenoid actuators: The coupled power electronics, mechanical, and magnetic field problem.," *IEEE Transactions on Magnetics*, vol. 24, no. 1, pp. 270–273, Jan. 1988. DOI: 10.1109/20.43909 (cit. on p. 35).

[33] G. Zhai, Q. Wang, W. Yang, and H. Liang, "Permanent-Magnet Equivalent Model of Calculating Relay's Static Attractive Torque Characteristics by Finite Element Method," *IEEE Transactions on Magnetics*, vol. 48, no. 9, pp. 2467–2471, Sep. 2012. DOI: 10.1109/TMAG.2012.2196705 (cit. on p. 35).

[34] E. Ramirez-Laboreo and C. Sagues, "Reluctance actuator characterization via FEM simulations and experimental tests," *Mechatronics*, vol. 56, pp. 58–66, Dec. 2018. DOI: 10.1016/j.mechatronics.2018.10.009 (cit. on pp. 35, 58).

[35] N. C. Cheung, K. W. Lim, and M. F. Rahman, "Modelling a linear and limited travel solenoid," in *Proceedings of IECON '93 - 19th Annual Conference of IEEE Industrial Electronics*, vol. 3, Maui, Hawaiian Islands, USA, Nov. 1993, pp. 1567–1572. DOI: 10.1109/IECON.1993.339304 (cit. on p. 35).

[36] M. Taghizadeh, A. Ghaffari, and F. Najafi, "Modeling and identification of a solenoid valve for PWM control applications," *Comptes Rendus Mécanique*, vol. 337, no. 3, pp. 131–140, Mar. 2009. DOI: 10.1016/J.CRME.2009.03.009 (cit. on p. 35).

[37] E. Ramirez-Laboreo, C. Sagues, and S. Llorente, "A New Model of Electromechanical Relays for Predicting the Motion and Electromagnetic Dynamics," *IEEE Transactions on Industry Applications*, vol. 52, no. 3, pp. 2545–2553, May 2016. DOI: 10.1109/TIA.2016.2518120 (cit. on pp. 35, 45).

[38] T. Braun, J. Reuter, and J. Rudolph, "Observer Design for Self-Sensing of Solenoid Actuators With Application to Soft Landing," *IEEE Transactions on Control Systems Technology*, vol. 27, no. 4, pp. 1720–1727, Jul. 2019. DOI: 10.1109/TCST.2018.2821656 (cit. on pp. 35, 129).

[39] N. H. Vrijsen, J. W. Jansen, and E. A. Lomonova, "Prediction of Magnetic Hysteresis in the Force of a Prebiased E-Core Reluctance Actuator," *IEEE Transactions on Industry Applications*, vol. 50, no. 4, pp. 2476–2484, Jul. 2014. DOI: 10.1109/TIA.2013.2296653 (cit. on p. 35).

[40] M. Ruderman, "Stroke-dependent magnetic hysteresis modeling in proportional solenoids using parametric Gaussian-mixture Preisach distribution," in *IEEE/ASME International Conference on Advanced Intelligent Mechatronics, AIM*, Besançon, France, Jul. 2014, pp. 1587–1591. DOI: 10.1109/AIM.2014.6878310 (cit. on p. 35).

[41] I. MacKenzie and D. Trumper, "Real-time Hysteresis Modeling of a Reluctance Actuator Using a Sheared-Hysteresis-Model Observer," *IEEE/ASME Transactions on Mechatronics*, vol. 21, no. 1, pp. 4–16, Feb. 2016. DOI: 10.1109/TMECH.2015.2513769 (cit. on p. 35).

[42] E. Ramirez-Laboreo, M. G. L. Roes, and C. Sagues, "Hybrid Dynamical Model for Reluctance Actuators Including Saturation, Hysteresis and Eddy Currents," *IEEE/ASME Transactions on Mechatronics*, vol. 24, no. 3, pp. 1396–1406, Jun. 2019. DOI: 10.1109/TMECH.2019.2906755 (cit. on pp. 35, 57, 59, 60, 63).

[43] S. Rosenbaum, M. Ruderman, T. Ströhla, and T. Bertram, "Use of Jiles–Atherton and Preisach Hysteresis Models for Inverse Feed-Forward Control," *IEEE Transactions on Magnetics*, vol. 46, no. 12, pp. 3984–3989, Dec. 2010. DOI: 10.1109/TMAG.2010.2071391 (cit. on pp. 35, 36).

[44] D. C. Jiles and D. L. Atherton, "Theory of ferromagnetic hysteresis," *Journal of Magnetism and Magnetic Materials*, vol. 61, no. 1–2, pp. 48–60, Sep. 1986. DOI: 10.1016/0304-8853(86)90066-1 (cit. on pp. 36, 46).

[45] S. Bobbio, G. Milano, C. Serpico, and C. Visone, "Models of magnetic hysteresis based on play and stop hysterons," *IEEE Transactions on Magnetics*, vol. 33, no. 6, pp. 4417–4426, Nov. 1997. DOI: 10.1109/20.649875 (cit. on p. 36).

[46] R. G. Harrison, "Modeling High-Order Ferromagnetic Hysteretic Minor Loops and Spirals Using a Generalized Positive-Feedback Theory," *IEEE Transactions on Magnetics*, vol. 48, no. 3, pp. 1115–1129, Mar. 2012. DOI: 10.1109/TMAG.2011.2170846 (cit. on p. 36).

[47] F. Liorzou, B. Phelps, and D. L. Atherton, "Macroscopic Models of Magnetization," *IEEE Transactions on Magnetics*, vol. 36, no. 2, pp. 418–428, Mar. 2000. DOI: 10.1109/20.825802 (cit. on p. 36).

[48] E. Lwithwaite, "Magnetic equivalent circuits for electrical machines," *Proceedings of the Institution of Electrical Engineers*, vol. 114, no. 11, p. 1805, Nov. 1967. DOI: 10.1049/piee.1967.0344 (cit. on p. 37).

[49] D. K. Cheng, "Static magnetic fields," in *Field and Wave Electromagnetics*, 2nd ed., Reading, MA, United States, 1989, ch. 6, pp. 251–257 (cit. on p. 37).

[50] N. H. Vrijsen, "Magnetic Hysteresis Phenomena in Electromagnetic Actuation Systems," PhD thesis, Eindhoven University of Technology, 2014. DOI: 10.6100/IR780946 (cit. on p. 38).

[51] E. Ramirez-Laboreo, "Modeling and Control of Reluctance Actuators," PhD thesis, Universidad de Zaragoza, 2019 (cit. on pp. 38, 40).

[52] H. Wenzl, F. Straußberger, T. Braun, S. Wirtensohn, L. Kiltz, J. Reuter, and H. Aschemann, "Comparison and Identifiability Analysis of Friction Models for the Dither Motion of a Solenoid," in *2018 23rd International ConferencRosenbaum2010e on Methods and Models in Automation and Robotics, MMAR 2018*, Miedzyzdroje, Poland, Aug. 2018, pp. 321–326. DOI: 10.1109/MMAR.2018.8485888 (cit. on p. 40).

[53] R. Goebel, R. G. Sanfelice, and A. R. Teel, "Hybrid dynamical systems," *IEEE Control Systems Magazine*, vol. 29, no. 2, pp. 28–93, Apr. 2009. DOI: 10.1109/MCS.2008.931718 (cit. on pp. 42, 93).

[54] C. W. T. McLyman, "DC Inductor Design, Using Gapped Cores," in *Transformer and Inductor Design Handbook*, 4th ed., Dec. 2011, ch. 8, p. 11. DOI: 10.1201/b10865-8 (cit. on p. 43).

[55] D. Jiles, "Magnetic Properties," in *Introduction to Magnetism and Magnetic Materials*, 3rd ed., Boston, Massachusetts, USA, Sep. 2015, ch. 5, pp. 147–168. DOI: 10.1201/b18948-14 (cit. on p. 44).

[56] N. Sadowski, N. Batistela, J. Bastos, and M. Lajoie-Mazenc, "An Inverse Jiles–Atherton Model to Take Into Account Hysteresis in Time-Stepping Finite-Element Calculations," *IEEE Transactions on Magnetics*, vol. 38, no. 2, pp. 797–800, Mar. 2002. DOI: 10.1109/20.996206 (cit. on p. 46).

[57] D. C. Jiles and D. L. Atherton, "Ferromagnetic Hysteresis," *IEEE Transactions on Magnetics*, vol. 19, no. 5, pp. 2183–2185, Sep. 1983. DOI: 10.1109/TMAG.1983.1062594 (cit. on p. 46).

[58] J. Dormand and P. Prince, "A family of embedded Runge–Kutta formulae," *Journal of Computational and Applied Mathematics*, vol. 6, no. 1, pp. 19–26, Mar. 1980. DOI: 10.1016/0771-050X(80)90013-3 (cit. on p. 63).

[59] C. Robert Koch, A. F. Lynch, and R. R. Chladny, "Modeling and Control of Solenoid Valves for Internal Combustion Engines," *IFAC Proceedings Volumes*, vol. 35, no. 2, pp. 197–202, Dec. 2002. DOI: 10.1016/s1474-6670(17)33941-1 (cit. on p. 65).

[60] M. Montanari, F. Ronchi, and C. Rossi, "Trajectory Generation for Camless Internal Combustion Engine Valve Control," in *IEEE International Symposium on Industrial Electronics*, Rio de Janeiro, Brazil, Jun. 2003, pp. 454–459. DOI: 10.1109/ISIE.2003.1267292 (cit. on p. 65).

[61] T. Braun, J. Reuter, and J. Rudolph, "Flatness-Based Feed-Forward Control Design for Solenoid Actuators Considering Eddy Currents," in *8th IFAC Symposium on Mechatronic Systems*, vol. 52, Vienna, Austria, Sep. 2019, pp. 567–572. DOI: 10.1016/j.ifacol.2019.11.736 (cit. on p. 65).

[62] T. Glück, W. Kemmetmüller, and A. Kugi, "Trajectory optimization for soft landing of fast-switching electromagnetic valves," *IFAC Proceedings Volumes*, vol. 44, no. 1, pp. 11 532–11 537, Sep. 2011. DOI: 10.3182/20110828-6-IT-1002.01822 (cit. on pp. 65, 158).

[63] A. Fabbrini, A. Garulli, and P. Mercorelli, "A Trajectory Generation Algorithm for Optimal Consumption in Electromagnetic Actuators," *IEEE Transactions on Control Systems Technology*, vol. 20, no. 4, pp. 1025–1032, Jul. 2012. DOI: 10.1109/TCST.2011.2159006 (cit. on p. 65).

[64] B. Borovic, A. Q. Liu, D. Popa, H. Cai, and F. L. Lewis, "Open-loop versus closed-loop control of MEMS devices: choices and issues," *Journal of Micromechanics and Microengineering*, vol. 15, no. 10, pp. 1917–1924, Aug. 2005. DOI: 10.1088/0960-1317/15/10/018 (cit. on p. 66).

[65] H. Sumali, J. E. Massad, D. A. Czaplewski, and C. W. Dyck, "Waveform design for pulse-and-hold electrostatic actuation in MEMS," *Sensors and Actuators, A: Physical*, vol. 134, no. 1, pp. 213–220, Feb. 2007. DOI: 10.1016/j.sna.2006.04.041 (cit. on p. 66).

[66] M. S. Allen, J. E. Massad, R. V. Field, and C. W. Dyck, "Input and Design Optimization Under Uncertainty to Minimize the Impact Velocity of an Electrostatically Actuated MEMS Switch," *Journal of Vibration and Acoustics*, vol. 130, no. 2, p. 021 009, Feb. 2008. DOI: 10.1115/1.2827981 (cit. on p. 66).

[67] J. C. Blecke, D. S. Epp, H. Sumali, and G. G. Parker, "A Simple Learning Control to Eliminate RF-MEMS Switch Bounce," *Journal of Microelectromechanical Systems*, vol. 18, no. 2, pp. 458–465, Apr. 2009. DOI: 10.1109/JMEMS.2008.2007243 (cit. on p. 66).

[68] A. Jain, P. R. Nair, and M. A. Alam, "Strategies for dynamic soft-landing in capacitive microelectromechanical switches," *Applied Physics Letters*, vol. 98, no. 23, pp. 20–23, Jun. 2011. DOI: 10.1063/1.3598960 (cit. on p. 66).

[69] D. S. Naidu, "Pontryagin Minimum Principle," in *Optimal Control Systems*, 4, 1st ed., vol. 124, Boca Raton, FL, 2003, ch. 6, pp. 252–259. DOI: 10.1201/9781315214429-6 (cit. on p. 66).

[70] D. H. Jacobson, S. B. Gershwin, and M. M. Lele, "Computation of Optimal Singular Controls," *IEEE Transactions on Automatic Control*, vol. AC-15, no. 1, pp. 67–73, Feb. 1970. DOI: 10.1109/TAC.1970.1099360 (cit. on p. 72).

[71] J. Kierzenka and L. F. Shampine, "A BVP Solver Based on Residual Control and the MATLAB PSE," *ACM Transactions on Mathematical Software*, vol. 27, no. 3, pp. 299–316, Sep. 2001. DOI: 10.1145/502800.502801 (cit. on p. 79).

[72] C. Tai and T. C. Tsao, "Control of an electromechanical actuator for camless engines," in *Proceedings of the 2003 American Control Conference*, vol. 4, Denver, Colorado, USA, Jun. 2003, pp. 3113–3118. DOI: 10.1109/acc.2003.1244007 (cit. on p. 91).

[73] K. S. Peterson and A. G. Stefanopoulou, "Extremum seeking control for soft landing of an electromechanical valve actuator," *Automatica*, vol. 40, no. 6, pp. 1063–1069, Jun. 2004. DOI: 10.1016/j.automatica.2004.01.027 (cit. on p. 91).

[74] M. Benosman and G. M. Atinç, "Multi-Parametric Extremum Seeking-based Learning Control for Electromagnetic Actuators," in *2013 American Control Conference*, Washington, D.C., USA, 2013, pp. 1914–1919. DOI: 10.1080/00207179.2014.964779 (cit. on p. 91).

[75] Y. Wang, F. Gao, and F. J. Doyle, "Survey on iterative learning control, repetitive control, and run-to-run control," *Journal of Process Control*, vol. 19, no. 10, pp. 1589–1600, Dec. 2009. DOI: 10.1016/j.jprocont.2009.09.006 (cit. on p. 91).

[76] E. Sachs, R. S. Guo, S. Ha, and A. Hu, "Process Control System for VLSI Fabrication," *IEEE Transactions on Semiconductor Manufacturing*, vol. 4, no. 2, pp. 134–144, May 1991. DOI: 10.1109/66.79725 (cit. on p. 91).

[77] J. Moyne, E. del Castillo, and A. M. Hurwitz, *Run-to-Run Control in Semiconductor Manufacturing*, 1st ed. Boca Raton, Florida, USA, 2000, p. 368. DOI: 10.1201/9781420040661 (cit. on p. 91).

[78] E. Ramirez-Laboreo, C. Sagues, and S. Llorente, "A New Run-to-Run Approach for Reducing Contact Bounce in Electromagnetic Switches," *IEEE Transactions on Industrial Electronics*, vol. 64, no. 1, pp. 535–543, Jan. 2017. DOI: 10.1109/TIE.2016.2605622 (cit. on pp. 91, 92, 110, 148, 151, 153).

[79] C. C. Palerm, H. Zisser, L. Jovanovič, and F. J. Doyle, "A run-to-run control strategy to adjust basal insulin infusion rates in type 1 diabetes," *Journal of Process Control*, vol. 18, no. 3-4, pp. 258–265, Mar. 2008. DOI: 10.1016/j.jprocont.2007.07.010 (cit. on p. 91).

[80] M. Crose, J. S. I. Kwon, A. Tran, and P. D. Christofides, "Multiscale modeling and run-to-run control of PECVD of thin film solar cells," *Renewable Energy*, vol. 100, pp. 129–140, Jan. 2017. DOI: 10.1016/j.renene.2016.06.065 (cit. on p. 91).

[81] X. Tang, C. Zou, T. Wik, K. Yao, Y. Xia, Y. Wang, D. Yang, and F. Gao, "Run-to-Run Control for Active Balancing of Lithium Iron Phosphate Battery Packs," *IEEE Transactions on Power Electronics*, vol. 35, no. 2, pp. 1499–1512, Feb. 2020. DOI: 10.1109/TPEL.2019.2919709 (cit. on p. 91).

[82] R. Ganesan, T. K. Das, and K. M. Ramachandran, "A Multiresolution Analysis-Assisted Reinforcement Learning Approach to Run-by-Run Control," *IEEE Transactions on Automation Science and Engineering*, vol. 4, no. 2, pp. 182–193, Apr. 2007. DOI: 10.1109/TASE.2006.879915 (cit. on p. 91).

[83] A. Di Gaeta, C. I. Hoyos Velasco, and U. Montanaro, "Cycle-by-cycle adaptive force compensation for the soft-landing control of an electro-mechanical engine valve actuator," *Asian Journal of Control*, vol. 17, no. 5, pp. 1707–1724, Jul. 2015. DOI: 10.1002/asjc.988 (cit. on p. 91).

[84] B. Srinivasan, D. Bonvin, E. Visser, and S. Palanki, "Dynamic optimization of batch processes: II. Role of measurements in handling uncertainty," *Computers & Chemical Engineering*, vol. 27, no. 1, pp. 27–44, Jan. 2003. DOI: 10.1016/S0098-1354(02)00117-5 (cit. on p. 92).

[85] L. M. Rios and N. V. Sahinidis, "Derivative-free optimization: a review of algorithms and comparison of software implementations," *Journal of Global Optimization*, vol. 56, no. 3, pp. 1247–1293, Jul. 2013. DOI: 10.1007/s10898-012-9951-y (cit. on p. 92).

[86] B. Srinivasan, C. Primus, D. Bonvin, and N. Ricker, "Run-to-run optimization via control of generalized constraints," *Control Engineering Practice*, vol. 9, no. 8, pp. 911–919, Aug. 2001. DOI: 10.1016/S0967-0661(01)00051-X (cit. on p. 92).

[87] H. Abdelrahman, F. Berkenkamp, J. Poland, and A. Krause, "Bayesian Optimization for Maximum Power Point Tracking in Photovoltaic Power Plants," in *2016 European Control Conference (ECC)*, Aalborg, Denmark, Jun. 2016, pp. 2078–2083. DOI: 10.1109/ECC.2016.7810598 (cit. on p. 95).

[88] A. Baheri, S. Bin-Karim, A. Bafandeh, and C. Vermillion, "Real-time control using Bayesian optimization: A case study in airborne wind energy systems," *Control Engineering Practice*, vol. 69, pp. 131–140, Dec. 2017. DOI: 10.1016/j.conengprac.2017.09.007 (cit. on p. 95).

[89] C. E. Rasmussen and C. K. I. Williams, "Regression," in *Gaussian Processes for Machine Learning*, 2005, ch. 2, pp. 13–19. DOI: 10.7551/mitpress/3206.003.0005 (cit. on pp. 95, 97).

[90] N. D. Lawrence, M. W. Seeger, and R. Herbrich, "Fast Sparse Gaussian Process Methods: The Informative Vector Machine," in *Advances in Neural Information Processing Systems 15*, S. Becker, S. Thrun, and K. Obermayer, Eds., Vancouver, British Columbia, Canada, Dec. 2002, pp. 609–616 (cit. on p. 100).

[91] R. Kalman, "On the general theory of control systems," *IFAC Proceedings Volumes*, vol. 1, no. 1, pp. 491–502, Aug. 1960. DOI: 10.1016/s1474-6670(17)70094-8 (cit. on p. 102).

[92] M. Fliess, J. Lévine, P. Martin, and P. Rouchon, "Flatness and defect of nonlinear systems: introductory theory and examples," *International Journal of Control*, vol. 61, no. 6, pp. 1327–1361, Jun. 1995. DOI: 10.1080/00207179508921959 (cit. on p. 103).

[93] J. A. Nelder and R. Mead, "A Simplex Method for Function Minimization," *The Computer Journal*, vol. 7, no. 4, pp. 308–313, Jan. 1965. DOI: 10.1093/comjnl/7.4.308 (cit. on p. 110).

[94] J. Tsai, C. R. Koch, and M. Saif, "Cycle Adaptive Feedforward Approach Controllers for an Electromagnetic Valve Actuator," *IEEE Transactions on Control Systems Technology*, vol. 20, no. 3, pp. 738–746, May 2012. DOI: 10.1109/TCST.2011.2126575 (cit. on p. 110).

[95] K. W. Lim, N. C. Cheung, and M. F. Rahman, "Proportional control of a solenoid actuator," in *Proceedings of IECON'94 - 20th Annual Conference of IEEE Industrial Electronics*, vol. 3, Bologna, Italy, Sep. 1994, pp. 2045–2050. DOI: 10.1109/IECON.1994.398134 (cit. on pp. 117, 129).

[96] P. Mercorelli, "A Lyapunov-based Adaptive Control Law for an Electromagnetic Actuator," *2013 AASRI Conference on Intelligent Systems and Control 2013*, vol. 4, pp. 96–103, Jan. 2013. DOI: 10.1016/j.aasri.2013.10.016 (cit. on pp. 117, 129).

[97] C. Tai and T. C. Tsao, "Control of an electromechanical camless valve actuator," in *Proceedings of the 2002 American Control Conference*, Anchorage, Alaska, USA, May 2002, pp. 262–267. DOI: 10.1109/acc.2002.1024814 (cit. on pp. 117, 129).

[98] M. Montanari, F. Ronchi, and C. Rossi, "Nonlinear Control of an Electromechanical Valve Actuator," *IFAC Proceedings Volumes*, vol. 37, no. 22, pp. 179–184, Apr. 2004. DOI: 10.1016/s1474-6670(17)30341-5 (cit. on pp. 117, 129).

[99] N. E. Kahveci and I. V. Kolmanovsky, "Control Design for Electromagnetic Actuators Based on Backstepping and Landing Reference Governor," in *5th IFAC Symposium on Mechatronic Systems*, vol. 43, Cambridge, Massachusetts, USA, Oct. 2010, pp. 393–398. DOI: 10.3182/20100913-3-US-2015.00051 (cit. on pp. 117, 129).

[100] M. Benosman and G. M. Atinç, "Extremum seeking-based adaptive control for electromagnetic actuators," *International Journal of Control*, vol. 88, no. 3, pp. 517–530, Oct. 2015. DOI: 10.1080/00207179.2014.964779 (cit. on pp. 117, 129).

[101] F. Deschaux, F. Gouaisbaut, and Y. Ariba, "Magnetic force modelling and nonlinear switched control of an electromagnetic actuator," in *IEEE 58th Conference on De- cision and Control (CDC 2019)*, Nice, France, Dec. 2019, pp. 1416–1421. DOI: 10.1109/CDC40024.2019.9030113 (cit. on pp. 117, 129).

[102] D. L. Trumper, S. M. Olson, and P. K. Subrahmanyan, "Linearizing control of magnetic suspension systems," *IEEE Transactions on Control Systems Technology*, vol. 5, no. 4, pp. 427–438, Jul. 1997. DOI: 10.1109/87.595924 (cit. on pp. 117, 129).

[103] C. Robert Koch, A. F. Lynch, and S. K. Chung, "Flatness-based automotive solenoid valve control," *IFAC Proceedings Volumes*, vol. 37, no. 13, pp. 817–822, Sep. 2004. DOI: 10.1016/S1474-6670(17)31326-5 (cit. on pp. 117, 129).

[104] S. K. Chung, C. R. Koch, and A. F. Lynch, "Flatness-Based Feedback Control of an Automotive Solenoid Valve," *IEEE Transactions on Control Systems Technology*, vol. 15, no. 2, pp. 394–401, Mar. 2007. DOI: 10.1109/TCST.2006.886440 (cit. on pp. 117, 129).

[105] R. R. Chladny and C. R. Koch, "Flatness-Based Tracking of an Electromechanical Variable Valve Timing Actuator With Disturbance Observer Feedforward Compensation," *IEEE Transactions on Control Systems Technology*, vol. 16, no. 4, pp. 652–663, Jul. 2008. DOI: 10.1109/TCST.2007.912121 (cit. on pp. 117, 129).

[106] R. Gill, A. Wahrburg, O. Craciun, K. Listmann, and C. Reuber, "Model Based Landing Control for a Bistable Electromagnetic Actuator with Discontinuous Dynamics," in *2015 IEEE Conference on Control Applications (CCA)*, Sydney, Australia, Sep. 2015, pp. 1479–1485. DOI: 10.1109/CCA.2015.7320820 (cit. on pp. 117, 129).

[107] J.-J. E. Slotine and W. Li, "Sliding Control," in *Applied Nonlinear Control*, vol. 199, Englewood Cliffs, New Jersey, USA, 1991, ch. 7, pp. 276–290 (cit. on p. 117).

[108] F. Malaguti and E. Pregnolato, "Proportional Control of On/off Solenoid Operated Hydraulic Valve by Nonlinear Robust Controller," in *Proceedings of the IEEE International Symposium on Industrial Electronics*, vol. 2, L'Aquila, Italy, Jul. 2002, pp. 415–419. DOI: 10.1109/isie.2002.1026322 (cit. on p. 117).

[109] M. Di Bernardo, S. Santini, A. Di Gaeta, C. I. Hoyos Velasco, and U. Montanaro, "Model-Based Soft Landing Control of an Electromechanical Engine Valve Actuator," in *Dynamic Systems and Control Conference*, vol. 2, Fort Lauderdale, Florida, USA, Sep. 2012, pp. 87–94. DOI: 10.1115/DSCC2012-MOVIC2012-8526 (cit. on p. 117).

[110] J.-H. Lee, Y.-W. Yun, H.-W. Hong, and M.-K. Park, "Control of spool position of on/off solenoid operated hydraulic valve by sliding-mode controller," *Journal of Mechanical Science and Technology*, vol. 29, no. 12, pp. 5395–5408, Dec. 2015. DOI: 10.1007/s12206-015-1141-7 (cit. on p. 117).

[111] X. Zhao, L. Li, J. Song, C. Li, and X. Gao, "Linear Control of Switching Valve in Vehicle Hydraulic Control Unit Based on Sensorless Solenoid Position Estimation," *IEEE Transactions on Industrial Electronics*, vol. 63, no. 7, pp. 4073–4085, Jun. 2016. DOI: 10.1109/TIE.2016.2541080 (cit. on p. 117).

[112] J. Fang, X. Wang, J. Wu, S. Yang, L. Li, X. Gao, and Y. Tian, "Modeling and Control of A High Speed On/Off Valve Actuator," *International Journal of Automotive Technology*, vol. 20, no. 6, pp. 1221–1236, Dec. 2019. DOI: 10.1007/s12239-019-0114-8 (cit. on p. 117).

[113] P. Eyabi and G. Washington, "Modeling and sensorless control of an electromagnetic valve actuator," *Mechatronics*, vol. 16, no. 3–4, pp. 159–175, Apr. 2006. DOI: 10.1016/j.mechatronics.2005.11.008 (cit. on p. 117).

[114] A. Levant, "Sliding order and sliding accuracy in sliding-mode control," *International Journal of Control*, vol. 58, no. 6, pp. 1247–1263, Mar. 1993. DOI: 10.1080/00207179308923053 (cit. on p. 118).

[115] M. F. Rahman, N. C. Cheung, and K. W. Lim, "Converting a Switching Solenoid to a Proportional Actuator," *IEEJ Transactions on Industry Applications*, vol. 116, no. 5, pp. 531–537, Sep. 1996. DOI: 10.1541/ieejias.116.531 (cit. on p. 129).

[116] M. Di Bernardo, A. Di Gaeta, C. I. Hoyos Velasco, and S. Santini, "Energy-Based Key-On Control of a Double Magnet Electromechanical Valve Actuator," *IEEE Transactions on Control Systems Technology*, vol. 20, no. 5, pp. 1133–1145, Sep. 2012. DOI: 10.1109/TCST.2011.2162332 (cit. on p. 129).

[117] P. Mercorelli, "An Antisaturating Adaptive Preaction and a Slide Surface to Achieve Soft Landing Control for Electromagnetic Actuators," *IEEE/ASME Transactions on Mechatronics*, vol. 17, no. 1, pp. 76–85, Feb. 2012. DOI: 10.1109/TMECH.2010.2089467 (cit. on p. 129).

[118] J. R. Van Dam, B. L. Gysen, E. A. Lomonova, and M. Dhaens, "Soft-landing control of low-energy solenoid valve actuators," in *2018 13th International Conference on Ecological Vehicles and Renewable Energies, EVER 2018*, Monte-Carlo, Monaco, May 2018, pp. 1–5. DOI: 10.1109/EVER.2018.8362372 (cit. on p. 129).

[119] F. Deschaux, F. Gouaisbaut, and Y. Ariba, "Nonlinear control for an uncertain electromagnetic actuator," in *2018 IEEE Conference on Decision and Control (CDC)*, Miami Beach, Florida, USA, Dec. 2018, pp. 2316–2321. DOI: 10.1109/CDC.2018.8618914 (cit. on p. 129).

[120] T. Glück, W. Kemmetmüller, C. Tump, and A. Kugi, "A novel robust position estimator for self-sensing magnetic levitation systems based on least squares identification," *Control Engineering Practice*, vol. 19, no. 2, pp. 146–157, Feb. 2011. DOI: 10.1016/j.conengprac.2010.11.003 (cit. on p. 129).

[121] M. F. Rahman, N. N. C. Cheung, K. W. Lim, and Khiang Wee Lim, "Position estimation in solenoid actuators," *IEEE Transactions on Industry Applications*, vol. 32, no. 3, pp. 552–559, May 1996. DOI: 10.1109/28.502166 (cit. on p. 129).

[122] N. König and M. Nienhaus, "A Solution to Ambiguities in Position Estimation for Solenoid Actuators by Exploiting Eddy Current Variations," *Sensors*, vol. 20, no. 12, p. 3441, Jun. 2020. DOI: 10.3390/s20123441 (cit. on p. 129).

[123] R. R. Chladny and C. R. Koch, "A Magnetic Flux-Based Position Sensor for Control of an Electromechanical VVT Actuator," in *2006 American Control Conference*, Minneapolis, Minnesota, USA, Jun. 2006, pp. 3978–3983. DOI: 10.1109/acc.2006.1657340 (cit. on p. 129).

[124] J. C. Renn and Y. S. Chou, "Sensorless plunger position control for a switching solenoid," *JSME International Journal, Series C: Mechanical Systems, Machine Elements and Manufacturing*, vol. 47, no. 2, pp. 637–645, Jun. 2004. DOI: 10.1299/jsmec.47.637 (cit. on p. 129).

[125] P. Mercorelli, "A Hysteresis Hybrid Extended Kalman Filter as an Observer for Sensorless Valve Control in Camless Internal Combustion Engines," *IEEE Transactions on Industry Applications*, vol. 48, no. 6, pp. 1940–1949, Nov. 2012. DOI: 10.1109/TIA.2012.2226193 (cit. on p. 129).

[126] F. Straußberger and J. Reuter, "Position Estimation in Electro-Magnetic Actuators Taking into Account Hysteresis Effects," in *7th IFAC Symposium on Mechatronic Systems*, vol. 49, Loughborough University, Leicestershire, UK, Sep. 2016, pp. 206–212. DOI: 10.1016/j.ifacol.2016.10.549 (cit. on p. 130).

[127] L. Verlet, "Computer Experiments on Classical Fluids. I. Thermodynamical Properties of Lennard-Jones Molecules," *Physical Review*, vol. 159, no. 1, pp. 98–103, Jul. 1967. DOI: 10.1103/PhysRev.159.98 (cit. on p. 132).

[128] H. E. Rauch, F. Tung, and C. T. Striebel, "Maximum likelihood estimates of linear dynamic systems," *AIAA Journal*, vol. 3, no. 8, pp. 1445–1450, Aug. 1965. DOI: 10.2514/3.3166 (cit. on p. 133).

[129] R. E. Kalman, "A New Approach to Linear Filtering and Prediction Problems," *Journal of Basic Engineering*, vol. 82, no. 1, pp. 35–45, Mar. 1960. DOI: 10.1115/1.3662552 (cit. on p. 133).

[130] D. Simon, "Kalman filtering with state constraints: a survey of linear and nonlinear algorithms," *IET Control Theory and Applications*, vol. 4, no. 8, pp. 1303–1318, Aug. 2010. DOI: 10.1049/iet-cta.2009.0032 (cit. on p. 135).

[131] H. Cox, "On the Estimation of State Variables and Parameters for Noisy Dynamic Systems," *IEEE Transactions on Automatic Control*, vol. 9, no. 1, pp. 5–12, Jun. 1964. DOI: 10.1109/TAC.1964.1105635 (cit. on p. 136).

[132] R. Hooke and T. A. Jeeves, "'Direct Search' Solution of Numerical and Statistical Problems," *Journal of the Association for Computing Machinery (ACM)*, vol. 8, no. 2, pp. 212–229, Apr. 1961. DOI: 10.1145/321062.321069 (cit. on p. 151).

[133] V. Torczon, "On the Convergence of Pattern Search Algorithms," *SIAM Journal on Optimization*, vol. 7, no. 1, pp. 1–25, Feb. 1997. DOI: 10.1137/S1052623493250780 (cit. on p. 151).

[134] R. M. Lewis and V. Torczon, "Pattern Search Algorithms for Bound Constrained Minimization," *SIAM Journal on Optimization*, vol. 9, no. 4, pp. 1082–1099, Jan. 1999. DOI: 10.1137/S1052623496300507 (cit. on p. 151).

[135] J. C. Lagarias, J. A. Reeds, M. H. Wright, and P. E. Wright, "Convergence Properties of the Nelder–Mead Simplex Method in Low Dimensions," *SIAM Journal on Optimization*, vol. 9, no. 1, pp. 112–147, 1998. DOI: 10.1137/S1052623496303470 (cit. on p. 153).

[136] T. G. Kolda, R. M. Lewis, and V. Torczon, "Optimization by direct search: New perspectives on some classical and modern methods," *SIAM Review*, vol. 45, no. 3, pp. 385–482, 2003. DOI: 10.1137/S003614450242889 (cit. on p. 153).

[137] F. Gao and L. Han, "Implementing the Nelder-Mead simplex algorithm with adaptive parameters," *Computational Optimization and Applications*, vol. 51, no. 1, pp. 259–277, May 2012. DOI: 10.1007/s10589-010-9329-3 (cit. on p. 153).

[138] R. R. Ernst, "Measurement and Control of Magnetic Field Homogeneity," *Review of Scientific Instruments*, vol. 39, no. 7, pp. 998–1012, Jul. 1968. DOI: 10.1063/1.1683586 (cit. on pp. 153, 154).

[139] R. R. Barton and J. S. Ivey, "Modifications of the Nelder-Mead Simplex Method for Stochastic Simulation Response Optimization," in *1991 Winter Simulation Conference*, Phoenix, AZ, USA, Dec. 1991, pp. 945–953. DOI: 10.1109/wsc.1991.185709 (cit. on p. 153).